ResearchGate

See discussions, stats, and author profiles for this publication at: https://www.researchgate.net/publication/352742935

Recent Development of Intelligent Shunt Fault Classifier for Nigeria 33kV Power Lines

Chapter · June 2021

DOI: 10.9734/bpi/nupsr/v9

CITATIONS
0

READS
286

2 authors:

Peter Mbamaluikem
The Federal Polytechnic, Ilaro
17 PUBLICATIONS **62** CITATIONS
SEE PROFILE

Ayokunle Awelewa
Covenant University
72 PUBLICATIONS **577** CITATIONS
SEE PROFILE

All content following this page was uploaded by Peter Mbamaluikem on 20 December 2021.

The user has requested enhancement of the downloaded file.

Newest Updates in Physical Science Research

Vol. 9

B P International

Newest Updates in Physical Science Research

Vol. 9

Newest Updates in Physical Science Research

Vol. 9

India ▪ United Kingdom

B P International

Editor(s)

Dr. Thomas F. George

Chancellor / Professor,
Department of Chemistry and Physics, University of Missouri-St. Louis One University
Boulevard St. Louis, USA.
Email: tfgeorge@umsl.edu;

FIRST EDITION 2021

ISBN 978-93-91312-26-8 (Print)
ISBN 978-93-91312-34-3 (eBook)
DOI: 10.9734/bpi/nupsr/v9

© Copyright (2021): Authors. The licensee is the publisher (B P International).

Contents

Preface

This book covers key areas of physical science research. The contributions by the authors include bulk modulus, micro-hardness, semiconductors, electro-negativity, glass ceramic, radioactive waste, crystallization temperature, crystalline phase, ladder-type four-level system, time-dependent resonant three-step absorption, time-dependent perturbation theory, three different light pulses, acoustic optics, Bragg diffraction, spatial filters, Raman diffraction, MATLAB, superfluid helium, boiling, recovery heat flux, two-fluid model, heat and mass transfer, superconductivity, magnetism, magnetic force, c*urie point,* Gill’s electronic theory, *complex normed space, generalized angle, complex Hilbert space, energy literacy, assessment framework, physics education, artificial neural network, fault detection, fault classification, transmission line, distance protection, driver fatigue, alerting effect, clustering, differential entropy. This book contains various materials suitable for students, researchers and academicians in the field of physical science research.*

Print ISBN: 978-93-91312-26-8, eBook ISBN: 978-93-91312-34-3

Determining the Bulk Modulus and Microhardness of Tetrahedral Semiconductors

Sanjay Kumar Gorai[1*]

DOI: 10.9734/bpi/nupsr/v9/2123F

ABSTRACT

From electronegativity and principal quantum number of II-VI, III-V semiconductors, a general empirical formula for calculating bulk modulus (B) and microhardness (H) was discovered. Constant C1, which appears in the expression of bulk modulus, as well as constants C2 and C3, which appear in the expression of microhardness and the exponent M, have the following values. The numerical values of C1,C2, C3 and M are respectively 206.6, 8.234, 1.291, -1.10 for II-VI 72.4, 31.87, 7.592, -0.95 for III-V semiconductors. The chemical bonding behaviour of constituent atoms in these semiconductors can be accurately reflected by both electro-negativity and principal quantum number. The measured bulk modulus and microhardness values are very similar to the reported results. The results of this research would aid in the development of new semiconductor materials as well as the investigation of their mechanical properties.

Keywords: Bulk modulus; microhardness; semiconductors; electro-negativity.

1. INTRODUCTION

Because of their growing scientific and technical applications, interest in studying various properties of binary tetrahedral semiconductors has grown in recent years [1-5]. However, the bulk modulus and microhardness of these materials have rarely been studied. Kumar et al. [6-7] proposed an empirical relationship for binary tetrahedral semiconductors between bulk modulus, microhardness, and plasmon energy using plasmon energy. Reddy et al. [8-9] proposed an empirical relationship between electronegativity and semiconductor bulk modulus. However, Verma and Sharma [10-12] proposed an empirical relationship using the ionic charge model when determining bulk modulus and microhardness of semiconductors, taking into account that both plasmon energy and the ionic charge model depend on the number of valence electrons. Various theories have been developed to calculate the energy gaps and ionicity of binary tetrahedral semiconductors, which have drawn considerable interest of researchers [13-16] in recent years, to understand various properties of these compounds. In this study, Electronegativity has been used to determine the bulk modulus and microhardness of these materials considering that it delineates the capability of an atom in a molecule to attract bonding electrons [17-18]. The principal quantum number is also used as a input parameter to estimate the bulk modulus and microhardness of these materials.

2. METHODOLOGY

The bulk modulus of any material depends on the volume of its constituent atoms. The bulk modulus of any material depends on the valence electron gas pressure completely determine the resistance of atoms to compression. This compression of an atom is closely related to two parameters. One parameter is the electronegativity value which is the attracting power of the electronegativity value which is the attracting power of effective nuclear charge to valence electrons in outer orbitals. The larger the EN value the more tightly the nuclei hold the valence and smaller the bulk modulus. Since it is a measure of the stiffness or of the energy required to produce a given deformation. The higher the bulk modulus, the stiffer is the crystal. This deformation is the distortion of the outer electronic shell.

---

[1] *Department of Physics, Tata College Chaibasa, Westsingbhum 833201, Jharkhand, India.*
**Corresponding author: E-mail: shreyagorai@gmail.com;*

The distortion produced in a crystal is related with the principal quantum number of constituent atoms in a material. The larger the principal quantum number, the longer the distance between the nuclei and valence electrons, and the larger electronic polarisability and hence higher bulk modulus. The electronegativity and principal quantum number both are very useful parameter in understanding the nature of chemical bonding and predict mechanical properties like bulk modulus and microhardness of tetrahedral semiconductors. For II-VI and III-V semiconductors the bulk modulus is assumed to be correlated to is the average principal quantum number $\eta_{av} = (n_A + n_{B \diagup 2})$ of valence electrons of atoms A and B and χ_A and χ_B are electronegativities of atoms A and B respectively. For II-VI and III-V semiconductors the bulk modulus is empirically expressed as

$$B=C_1 \left(\frac{\eta_{av}}{\sqrt{\chi_A \chi_B}} \right)^M \text{ .... (1)} \quad B=LH+O \text{ .... (2)} \quad H=C_2 \left(\frac{\eta_{av}}{\sqrt{\chi_A \chi_B}} \right)^M -C_3 \qquad (3)$$

where C1 and M have values 206.6,-1.09 for II-VI and 72.4,-0.95 for III-V semiconductors respectively.

Table 1. Bulk modulus of tetrahedral semiconductors

Compounds	$\frac{\eta_{av}}{\sqrt{\chi_A \chi_B}}$	**Cal.Eq. (1)**	**Exp. Ref.[17]**	**Ref. [6]**	**Ref. [16]**	**Ref. [17]**	**Ref. [18]**	**Ref. [19]**	**Ref. [20]**	**% deviation**
1	2	3	4	5	6	7	8	9	10	11
$A^{II}B^{IV}$										
BeO	1	206.6		265.12	291					
BeS	1.57	125.78		111.81	132					
BeSe	1.98	97.45		97.29	109					
BeTe	2.48	76.07		71.54	80					
ZnO	1.67	117.52		139.78	149					
ZnS	2.45	77.09	77	77.8		90	44.7	61	75.21	0.1283
ZnSe	2.93	63.32	62	68.07		75	39.1	58	65.7	2.1373
ZnTe	3.55	51.27	51	58.24		59	32.3	54	61.46	0.5331
CdS	2.98	62.1	62	59.35		69	36.5	66	61.6	0.2538
CdSe	3.51	51.91	53	51.57		60	32.8	60	58.9	2.047
CdTe	4.19	42.72	42	44.01		47	27.5	56	41.6	1.7292
HgS	3.35	54.64		43.07						
HgSe	3.9	46.23		59.07						
HgTe	4.61	38.46		51.39						
MgTe	3.26	56.31		42.15						
Average % deviation						14.98	38.21	14.34	6.91	1.04
$A^{III}B^{VI}$										
BN	0.84	203.45		218.52						
BP	1.32	132.43		164.33						
BAs	1.64	107.75		137.61		87				
AlN	1.26	138.41				79				
AlP	1.89	94.16	86	88.47	87	57				9.4965
AlAs	2.29	78.46	77	77.71	79					1.9067
AlSb	2.81	64.60	58	56.32	57					1.388
GaN	1.51	116.54		169.14		84.5				
GaP	2.21	81.16	89	86.63	87	74.5				8.804
GaAs	2.62	69.04	75	73.2	77	56.9				7.936
GaSb	3.16	57.78	57	53.12	58					1.3817
InN	1.89	94.16		117.75						
InP	2.7	67.10	71	66.8	67	65.6				5.489
InAs	3.15	57.96	60	59.73	61	59.5				3.397
InSb	3.76	48.99	47	47.3	47	46.7				4.2344
Average %deviation			*2.15*	*2.84*		*2.35*				4.89

Table 2. Microhardness of tetrahedral semiconductors

Compounds	$\frac{\eta_{av}}{\sqrt{\chi_A \chi_B}}$	Cal.Eq. (2)	Exp. Ref.[21]	Ref.[6]	Ref.[23]	% deviation
1	2	3	4	5	6	7
BeO	1	6.94	9.1-12.7	8.21		23.7363
BeS	1.57	3.72		3.01		
BeSe	1.98	2.59		2.52		
BeTe	2.48	1.74		1.64		
ZnO	1.67	3.39	3.9,4.8	3.96	4.6	13.0769
ZnS	2.45	1.78	1.7,2.8,3.5	1.86	3.3	4.706
ZnSe	2.93	1.23	1.3-1.8	1.52	1.7	5.3846
ZnTe	3.55	0.75	0.8-1.1	1.19	1.0	6.25
CdS	2.98	1.19	1.2,1.22	1.23	1.1	0.8333
CdSe	3.51	0.78	0.7-1.2	0.96	0.8	11.29
CdTe	4.19	0.41	0.4-0.64	0.71	0.5	2.5
HgS	3.35	0.89		1.22		
HgSe	3.9	0.55		0.96		
HgTe	4.61	0.24		0.65		
MgTe	3.26	0.95		0.68		
Average % deviation				25.41	30.75	8.48
$A^{III}B^{VI}$						
BN	0.84	30.02	30.02	29.57	45.8	12.4781
BP	1.32	16.89	16.89	20.81	32.3	45.5161
BAs	1.64	12.33	12.33	16.5	24.2	35.1053
AlN	1.26	18	18			
AlP	1.89	9.816	9.816	5.5	10.9	78.473
AlAs	2.29	6.914	6.914	5	6.3	44.042
AlSb	2.81	4.351	4.351	4		08.775
GaN	1.51	13.95	13.95			
GaP	2.21	7.412	7.412	9.45		21.5661
GaAs	2.62	5.172	5.172	7.5		28.1667
GaSb	3.16	3.091	3.091	4.48		31.0045
InN	1.89	9.816	9.816			
InP	2.7	4.813	4.813	4.3		17.39
InAs	3.15	3.123	3.123	3.84		5.3636
InSb	3.76	1.464	1.464	2.2		34.545
Average % deviation				25.898	25.88	21.42

Plendl et al. [19] have shown that B=KH, where K is the constant. Instead of using single proportionality factor which has not been sufficient to yield acceptable values of B and H ,in this paper two proportionality factor have been used which gives better fit to measured values . In equation 2, L and O are constants. The numerical values of L and O are respectively 25.09,32.31 for II=VI,5.409,41.07for IIIV semiconductors. Using above Equation (1) and Equation (2) the microhardness have been estimated by the following relation: In equation 3 where C2 , C3 and M are the constants. The numerical values of C2, C3 and M are respectively 8.234,1.291,1.10 for II-VI 31.87,7.592,0.95 for III-V semiconductors respectively. Using Equation (3) the microhardness of materials have been estimated and listed in Table 2 along with the results of experimental values and earlier researchers.

3. RESULTS AND DISCUSSION

Bulk modulus and microhardness is estimated using Equation (1) and Equation (3) for binary tetrahedral semiconductors. The estimated values are given in Table 1 and Table 2 along with the results of earlier researchers [20-24] for the comparison. It is observed that the calculated values are in better agreement with the experimental data. The results also agree closely with the values reported for these compounds by earlier workers [19-24]. The percentage deviation is given in Table 1 and Table 2. The average percentage deviation of B and H is 1.09, 8.48 and 4.89, 21.42 for II-VI and III-V binary tetrahedral semiconductors. The minimum average percentage deviation in present approach indicates that empirical relation is better than earlier approach [6,19-27]. The higher value of average percentage deviation of bulk modulus of III-V semiconductors may be to scattered data of elastic constants and bond length.

4. CONCLUSION

The proposed empirical expression helps to estimate the bulkmodulus and microhardness of binary and ternary semiconductors in terms of electronegativity value and the average principal quantum number of valence electrons. The calculated values of these parameters are presented in Table 1 and Table 2 respectively. The inclusion of electronegativity and principal quantum number has some bearing on the concept chemical bonding. From this study it is possible to correlate bulk modulus and microhardness with the nature of bonding of the materials.These two parameters electronegativity and average principal quantum number delineates the structure –property relationship in solid state sciences.

COMPETING INTERESTS

Author has declared that no competing interests exist.

REFERENCES

1. Shay JL, Wernic JH. Ternary chalcopyrite semiconductors growth. In: Electronic properties and application, pergamon press, New York; 1975.
2. Kazmerski LL. Ternary Compound thin film solar cells. Nuovo Cimento. 20 2013; 1983.
3. Deab SK, Zunger A. Ternary multinary compounds. Mater. Res. Soc Conf. Proc. 1987;37.
4. Yan C, Xue D. Synthesize of Designed Templates for Novel Semiconductors materials with hollow structure. Funct. Mater. Lett. 2008;1:37.
5. Zhu Y. Insight into the structure and formation of Titanioum oxide Nanotubes. Funct. Mater. Lett. 2008;1239.
6. Kumar V, Shrivastava AK, Jha Vijeta. Bulk modulus and microhardness of tetrahedral semiconductors. J. Physics and Chemistry of Solids. 2010;71:1513.
7. Kumar V, Prasad GM, Chandra D. Microhardness of $A^{N-1}B^{N+1}C_2^{8-N}$ Chalcopyrite Semiconductors. Phys. Status. Solidi b170. 1992;77.
8. Reddy RR, Ahammed YN, Rama Gopal K, Rao TVR. Microhardness of $A^{N-1}B^{N+1}C_2^{8-N}$ Chalcopyrite Semiconductors. Infrared Phys. & Tech. 1998;3955.
9. Reddy RR, Nazeer AY, Rama, Gopal K, Rao TVR, Abdul Azeem P, Reddy MP. Coorelation between optical basicity, electronegativity and electronic polarisability for some oxides and oxysalts. Optical Materials. 1999;12(4),425-428.
10. Verma AS. Phys. Stat. Sol (b). Correlation between ionic charge and the optical properties of zinc blende and complex structured solids. 2009;246:192.
11. Verma AS, Sharma D. Dielectric constants of $A^{I}B^{III}C_2^{VI}$ and $A^{II}B^{IV}C_2^{V}$ chalcopyrite semiconductors. Phys. Scr. 2007;76:22.
12. Verma AS. Bond stretching force constants of $A^{I}B^{III}C_2^{VI}$ and $A^{II}B^{IV}C_2^{V}$ chalcopyrite semiconductors. Solid State Commun. 2009;149:1236.
13. Kumar GS. Analysis of Ionicity using plasmon energy and electro negativity difference of binary tetrahedral semiconductors and ionic compounds. Research Journal of Physical Sciences.
14. Kumar V, Shrivastava AK, Jha V. Bulk modulus and microhardness of tetrahedral semiconductors. Journal of Physics and Chemistry of Solids. 2010;71(11):1513-20.
15. Ahmad S, Ashraf M, Ahmad A, Singh DV. Electronic and optical properties of semiconductor and alkali halides. Arabian Journal for Science and Engineering. 2013;38(7):1889-94.

16. Asikuzun E, Ozturk O. Theoretical and experimental approaches to measuring mechanical properties of Zn 1− x Co x O binary tetrahedral bulk semiconductors. Journal of Materials Science: Materials in Electronics. 2018;29(10):7971-8.
17. Li K, Xue D. Anew set of electronegativity scale for trivalent lanthanides. Phys. Status. Solidi B. 2007;2441982.
18. Xue D, Zuo S, Ratajczak H. Electronegativity and structural characteristics of lanthanides J. Phys. Status. Solidi B. Physica B. 2004;352:99.
19. Plendl JN, Mitra SS, Gielisse P. Compressibility, cohesive energy and hardness of Non-metallic solids,1965;12:367.
20. Neumann H. Microhardness scaling and bulk modulus –microhardness relationship in $A^{II}B^{IV}C_2^{V}$ chalcopyrite compounds. Cryst. Res. Technol. 1988;23:97.
21. Cohen ML. Analytic relalation between bulk moduli and lattice constants. Phys. Rev. B. 1985;35:7988.
22. Lam PK, Cohen ML, Martinez G. Calculation of bulk moduli of diamond and zinc blende solids. Phys. Rev. B. 1987;35:9190.
23. Douri Y. Al, Abid H, Aourag H. Coorelation between the bulk modulus and charge density in semiconductors. Physica B. 2001;305:186.
24. Douri Y, Al, Abid H, Aourag H. Calculation of bulk moduli semiconductor compounds. Physica B. 2002;322:179.
25. Lide DR. Hand book Chemistry and Physics, 80 th ed., CRC Press; 1999-2000.
26. Weber MJ. Hand book of optical materials, CRC Publication; 2003.
27. Garbato L, Rucci A. Microhardness of ternary chalcopyrite semiconductors, Philos. Mag. 1977;35:1685.

Biography of author(s)

Sanjay Kumar Gorai
Department of Physics, Tata College Chaibasa, Westsingbhum 833201, Jharkhand, India.

Research and Academic Experience:
25 years of Teaching
20 years of Research

Research Area: Solid state physics

Number of Published papers: 15

Special Award: Featured in Bibliography in Marguis who’s who in 2013.

© Copyright (2021): Author(s). The licensee is the publisher (B P International).

DISCLAIMER
This chapter is an extended version of the article published by the same author(s) in the following conference proceeding.
Journal of Physics: Conference Series, 365: 012013, 2012.

Print ISBN: 978-93-91312-26-8, eBook ISBN: 978-93-91312-34-3

The Impact of Crystal Growth Temperature on Zr Reach Crystalline Phase Formation in a Nuclear Waste Confinement Glass Ceramic

Dalila Moudir[1*], Nour-El-Hayet Kamel[1], Abdelbaki Benmounah[2], Yasmina Mouheb[1], Rafika Souag[2], Boudjmaa Bezzazi[2], Fairouz Aouchiche[1], Ziane Kamel[1] and Soumia Kamariz[1]

DOI: 10.9734/bpi/nupsr/v9/9368D

ABSTRACT

Many glass ceramics could be used to contain radioactive waste. This is the case with glasses that contain radiation-resistant ceramics such as zirconolites, pyrochlores, or pyroxenes. This study investigates the effect of crystal growth temperature on the formation of the following phases in a nuclear glass ceramic system: Al_2O_3-SiO_2-CaO-MgO-ZrO_2-TiO_2. The materials with six contents of ZrO_2, ranging from 1.00 to 6.40 m.%, are synthesized by a discontinuous method, consisting in a double-melting at 1,350°C, followed by both a nucleation at 564°C, and a crystal growth treatment at: 900, 100 and 1,100°C. The morphology of the materials as a whole reveals a glassy feature with an opaque aspect. A different crystallisation process can also be seen from the bulk to the surface. The X-ray diffraction (XRD) analysis of glass ceramics reveals that the main identified crystalline skeletons are those of 2M-zirconolite, CaZrTi2O7, and ZrO2, depending on the ZrO2 content of the materials and the crystal-growth temperature. Due to the complexity of the oxide mixture, the material with the middle content in ZrO2 (4.5 m. %) and crystallised at the middle value of Tc (1,010°C) shows the greatest content in zirconolite (87%), doped with either lanthanides or alcalin-earth elements.The temperature of 1,010°C appears to be more selective in terms of 2M-zirconolite formation.

Keywords: Glass ceramic; radioactive waste; crystallization temperature; XRD; crystalline phase.

1. INTRODUCTION

A significant research area is the implementation of specific sequestration matrix designed to confine specific radionuclides. The industrial solution currently used for the confinement of radiotoxic elements found in nuclear waste consists of incorporating them into a system glass:SiO_2-Al_2O_3-B_2O_3-Na_2O. This confinement is not specific, but it does have a good loading ability and excellent long-term behaviour [1].

Various mineral matrices for the specific disposal of many radioisotopes produced from nuclear waste, particularly, for minor actinides (Mac), and fission products "lanthanides" (FP), include ceramics, such as zircon-titanates (zirconolite), zirconates (zirconia, stabilized zirconia, and phosphates (apatite, monazite) [2,3].

Glasses and glass-ceramics belong to advanced functional materials. Their electrical, mechanical, thermal, and optical properties depend significantly on the local structure of the glass-host [4,5]. The structure and properties can be changed drastically during the transformation from glasses to glass-ceramics under the heat treatment process [6,7]. The ceramics elaborating processes are difficult to

---

[1] *Algiers Nuclear Research Centre, Division of Nuclear Techniques, P.O.Box: 399, Alger-RP, Algiers, Algeria.*
[2] *Research Unit on Materials, Processes and Environment (URMPE), University M'hamed Bouguerra, Avenue de l'indépendance, 35000, Boumerdès, Algeria.*
**Corresponding author: E-mail: dalilamoudir@yahoo.fr;*

implement to date, and many glass-ceramics are also under study. They consist of crystals homogeneously distributed in a glass matrix, and exhibit increased performances compared to alumino-borosilicate glasses.

Research on glass-ceramics (noted: GC) matrices for radioactive waste (RW) sequestration can benefit from both glass technology and interesting confinement properties of crystalline ceramic phases [8,9].

In this study, we have synthesized a ZrO_2-rich glass-ceramic by a discontinuous method, consisting in a double-melting at 1,350°C, followed by both a crystallization and crystal-growth, treatments at 564 and 1,010°C, respectively. In order to access the influence of the crystal-growth temperature on the nature of the germs born in the bulk of the GC materials, pellets of variable contents in ZrO_2 are ceramized at three crystal-growth temperatures (Tc), namely: 900, 1,010 and 1,100°C during 3 h. The crystalline phases analysis formed in the materials is performed by X-ray diffraction (XRD).

2. EXPERIMENTS

The general GC mixtures chemical composition is inspired from previous research studies [10]. The samples are prepared with the following ZrO_2 mass contents: 1.00, 2.49, 3.50, 4.50, 5.00, 5.70 and 6.40 m. % (Table 1).

Table 1. Chemical composition of the synthesized GC materials

Oxide (m.%)	Content (%)						
ZrO_2	1.000	2.487	3.500	4.500	5.000	5.700	6.400
Al_2O_3	12.948	12.948	12.948	12.948	12.948	12.948	12.948
B_2O_2	0.782	0.782	0.782	0.782	0.782	0.782	0.782
BaO	0.586	0.586	0.586	0.586	0.586	0.586	0.586
CaO	11.487	11.487	11.487	11.487	11.487	11.487	11.487
CeO_2	3.113	3.113	3.113	3.113	3.113	3.113	3.113
CrO_3	0.391	0.391	0.391	0.391	0.391	0.391	0.391
Er_2O_3	1.281	1.281	1.281	1.281	1.281	1.281	1.281
Fe_2O_3	1.281	1.281	1.281	1.281	1.281	1.281	1.281
K_2O	0.978	0.978	0.978	0.978	0.978	0.978	0.978
La_2O_3	0.489	0.489	0.489	0.489	0.489	0.489	0.489
Li_2O	4.105	4.105	4.105	4.105	4.105	4.105	4.105
MgO	2.500	2.500	2.500	2.500	2.500	2.500	2.500
MnO_2	0.195	0.195	0.195	0.195	0.195	0.195	0.195
MoO_3	2.737	2.737	2.737	2.737	2.737	2.737	2.737
Nd_2O_3	1.173	1.173	1.173	1.173	1.173	1.173	1.173
NiO	0.586	0.586	0.586	0.586	0.586	0.586	0.586
P_2O_5	0.391	0.391	0.391	0.391	0.391	0.391	0.391
Pr_6O_{11}	0.098	0.098	0.098	0.098	0.098	0.098	0.098
SiO_2	47.427	45.940	44.927	43.927	43.427	42.727	42.027
Ta_2O_5	0.195	0.195	0.195	0.195	0.195	0.195	0.195
TiO_2	4.790	4.790	4.790	4.790	4.790	4.790	4.790
V_2O_5	0.098	0.098	0.098	0.098	0.098	0.098	0.098
WO_3	0.782	0.782	0.782	0.782	0.782	0.782	0.782
Y_2O_3	0.489	0.489	0.489	0.489	0.489	0.489	0.489
Yb_2O_3	0.098	0.098	0.098	0.098	0.098	0.098	0.098
Total	100.00	100.00	100.00	100.00	100.00	100.00	100.00

The employed commercial reagents were: Al_2O_3 (Fluka), B_2O_3 (Purity ≥ 99%), CaO (Merck, ≥ 97%), CeO_2 (Aldrich, 99.999%), CrO_3 (Merck, ≥ 99%), Fe_2O_3 (Merck, ≥ 99%), K_2CO_3 (Merck, ≥ 99%), Li_2O (Merck, ≥ 99%), MgO (Flucka, ≥ 97%), MnO_2 (Merck), MoO_3 (Merck, ≥ 99.5%), Nd_2O_3 (Fluka, ≥ 99.9%), P_2O_5 (Merck, ≥ 98%), Pr_6O_{11} (Merck, ≥ 99%), SiO_2 (Prolabo), Ta_2O_5 (Merck, ≥ 99%), TiO_2 (Merck, ≥ 99%),V_2O_5 (Labosi), WO_3 (Merck), Y_2O_3 (Merck, ≥ 99%), Yb_2O_3 (Aldrich, 99.9%), ZrO_2

(Aldrich, 99%). REE elements' oxides are dried over night at 1,000 °C, and the other oxides at 400 °C, for the same time. BaO, Er_2O_3, La_2O_3 and NiO are prepared by calcination at 450°C of $BaNO_3$ (Fluka, 99.6%), $ErN_3O_9{\cdot}5H_2O$ (Acros Organics, 99.9%), $La(NO_3)_3{\cdot}6H_2O$ (Fluka, 99.99%), and $Ni(NO_3)_2{\cdot}6H_2O$ (Fluka, 99.6%), respectively.

The GC synthesis is carried out by a double-melting at 1,350 °C. This is necessary to ensure a complete homogenization of the oxides mixture, to guarantee isotrope properties of the final products. The melts are poured in a graphite cylindrical mold to obtain pellets. The nucleation step is carried out at a nucleation temperature (Tn) of the parent glass, chosen as the glass transition temperature measured by differential thermal analysis (Tg) plus 30 °C (Tn = Tg + 30). Tn = 564 °C for 2 h. the crystal growth treatment (Tc) is performed at: 900, 1,010 and 1,100 °C for 3 h, for the whole. The GC materials are cooled to the ambient air.

For the six studied compositions glasses, X-ray diffraction (XRD) analysis was conducted by a Philips X'Pert PRO apparatus, operating at CuKα1 wavelength ($\lambda K\alpha 1$ = 0.15406 nm). The analytical parameters were as follow: V = 40 kV and I = 40 mA; a 2θ scanning from 3° to 80°. The XRD data were collected at room temperature on milled and sieved glass samples, with a mean size of 80 µm. For this, a 5657 Gmbh Retsch automatic agath mortar was used. The crystalline phase(s) identification was done using the Philips X'Pert plus 2004 software [11].

3. RESULTS AND DISCUSSION

3.1 Characterization of the Materials

The GC phase's identification was performed by XRD analysis, on thin blades from the bulk of the samples to avoid surface effects in the GC [12].

For the three Tc heat treatments and for the GC six chemical compositions studied, the XRD spectra are gathered in Figs. 1-7.

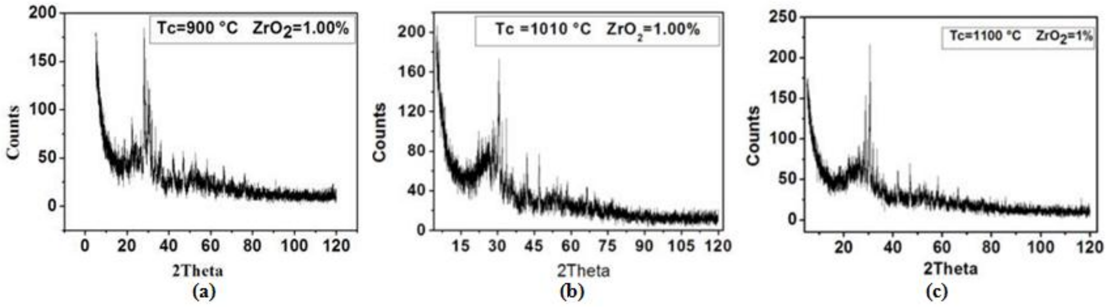

Fig. 1. Diffractogram of the GC with 1 m.% ZrO_2 content. (a) Tc = 900°C, (b) Tc = 1,010°C and (c) Tc = 1,100°C

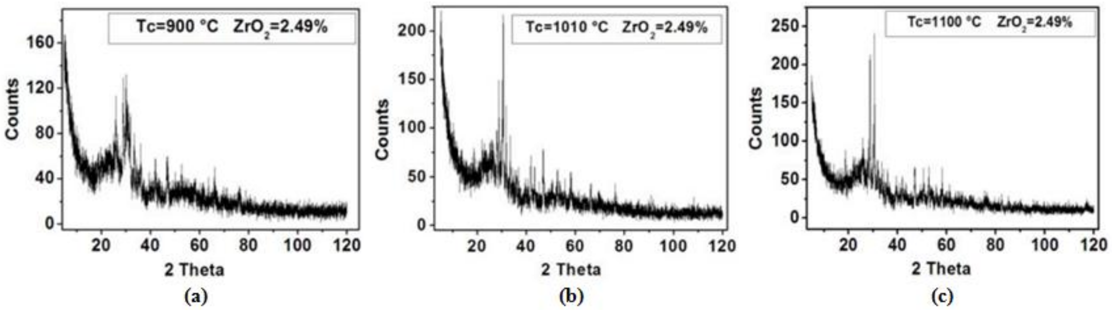

Fig. 2. Diffractogram of the GC with 2.49 m.% ZrO_2 content. (a) Tc = 900°C, (b) Tc = 1,010°C and (c) Tc = 1,100°C

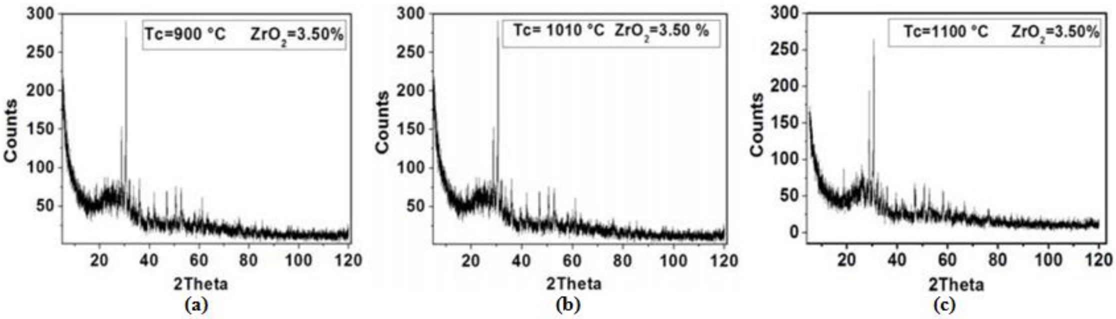

Fig. 3. Diffractogram of the GC with 3.50 m.% ZrO$_2$ content. (a) Tc = 900°C, (b) Tc = 1,010°C and (c) Tc = 1,100°C

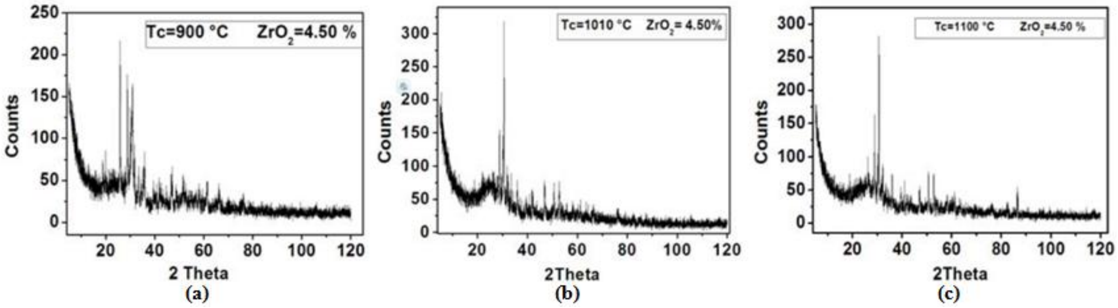

Fig. 4. Diffractogram of the GC with 4.50 m.% ZrO$_2$ content. (a) Tc = 900°C, (b) Tc = 1,010°C and (c) Tc = 1,100°C

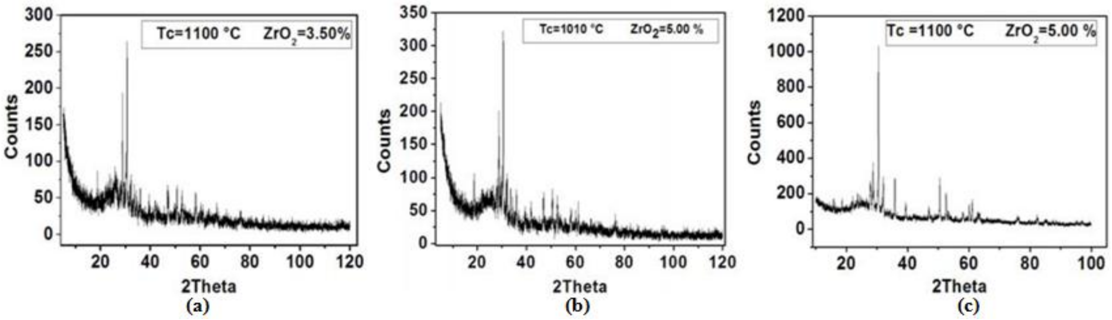

Fig. 5. Diffractogram of the GC with 5.00 m.% ZrO$_2$ content. (a) Tc = 900°C, (b) Tc = 1,010°C and (c) Tc = 1,100°C

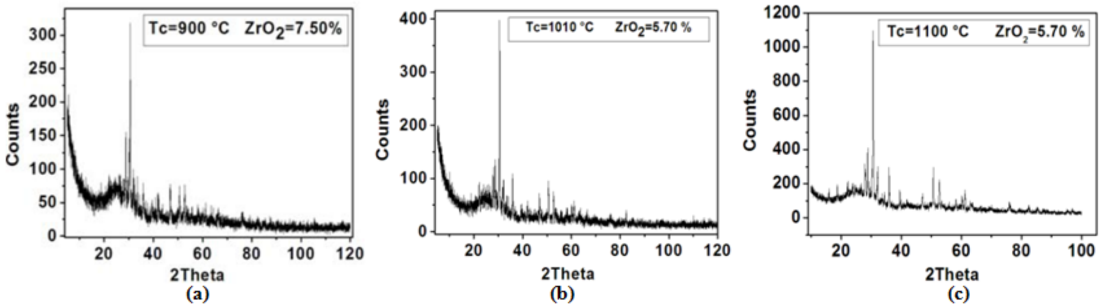

Fig. 6. Diffractogram of the GC with 5.70 m.% ZrO$_2$ content. (a) Tc = 900°C, (b) Tc = 1,010°C and (c) Tc = 1,100°C

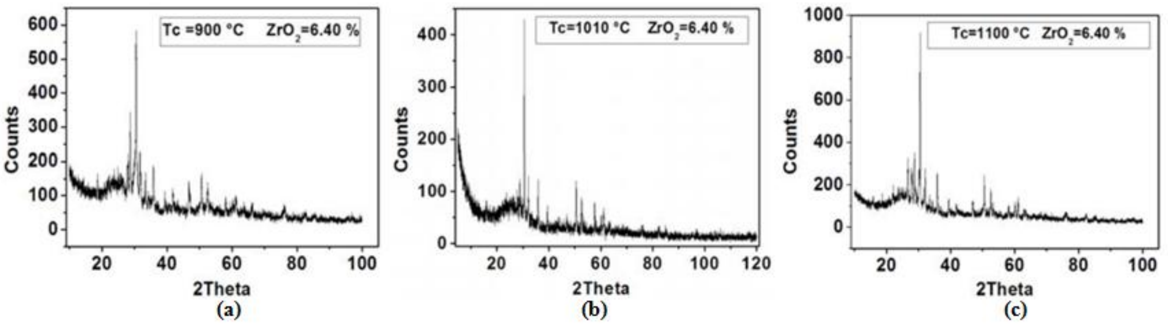

Fig. 7. Diffractogram of the GC with 6.40 m.% ZrO_2 content. (a) Tc = 900°C, (b) Tc = 1,010°C and (c) Tc = 1,100°C

At the lowest crystal-growth temperature of 900 °C, and for the lowest levels of ZrO_2 in the GCs, there are few Zr-containing phases (especially zirconolite $CaZrTi_2O_7$) in the germinated crystals: $CaZrTi_2O_7$ (JCPDS: 00-034-0167), ZrO_2 (JCPDS: 01-073-1441), $ZrTiO_4$ (JCPDS: 01-074-1504), $Nd_2 (Ce_{0.05}Zr_{0.95})_2O_7$ (JCPDS:01-078-1619), ZrTi) O_4 (JCPDS:01-080-1783), (Ca0.85Nd0.075Zr0.075) (Nd0.075Zr0.775Ti0.15) (Ti2O7) (JCPDS: 01-081-1491), $ZrO_{1.95}$ (JCPDS: 01-081-1544), $Zr_{0.86}Y_{0.14}O_{1.93}$ (JCPDS: 01-082-1243), $Ca_{0.15}Zr_{0.85}O_{1.85}$ (JCPDS: 01-084-1829).

They reach a significant concentration, when the content of ZrO_2 in the ceramic reaches 3.50%.

At the intermediate temperature of crystallization (1,010°C), the Zr-reach phases are the main crystalline germs in the materials, even for the lowest content in of ZrO_2 (1%).

However, it is only over 2.49 m. % of ZrO_2 in the GC material that the zirconolite skeleton $CaZrTi_2O_7$ appears with a significant concentration. The most VC materials contain over 65 m. % of zirconolite jointly with other additive Zr-containing phases.

For Tc = 1,100°C, the most crystals formed in the bulk of the GC materials are Zr oxides for the whole of ZrO_2 contents in the materials, with a great content in 2M-zirconolite over 4.5 m.% of ZrO_2 in the GC matrices.

3.2 Discussion

Loiseau and Caurant et al. [13] have synthesized Zr-rich GC materials. They report the co-existence of germs of zirconolite and ZrO_2 fluorine crystals, with a Tc temperature of 1,000 °C. The fluorine structure shows a very muddled distribution of Ca^{2+}, Zr^{4+} and Ti^{4+} cations in zirconolite. This muddle distribution is attenuated when Tc increases [14].

For the present study, the zirconolite is the main formed phase in the bulk of the GC materials for the Tc temperature of 1,010°C, which is near this given by Loiseau and Caurant et al. [13] despite the differences in the nature of the GC materials and the synthesis parameters.

The best crystal-growth treatment in term of selectivity toward the 2M-zirconolite formation seems to be that of 1,010°C.

One can conclude that the lowest crystal-growth temperature Tc = 900°C does not favor the germination of Zr-rich phases, particularly zirconolite. The intermediate Tc temperature of 1,010°C, leads to the greatest selective formation of zirconolite in the GC materials.

However, 900 and 1,100°C also lead to the germination of radiation resistant phases rich in Zr, and thus may ensure a double-confinement of the lanthanides and actinides present in the radioactive waste solution [13].

4. CONCLUSIONS

In this study, we performed the synthesis and characterization of Zr-reach GC materials dedicated for the confinement of radioactive waste. The parent glass is an aluminosilicate glass in the system: SiO_2-Al_2O_3-CaO-MgO-ZrO_2-TiO_2.

The synthesis method is based on a double melting at 1,350°C, followed by a nucleation at 564 °C and a crystal growth at: 900, 1,010 and 1,100°C. The obtained results allow concluding that the GC materials exhibit typical properties compared to those of the glass matrix, because they contain highly self-irradiation resistant phases, such as zirconolite. Thus, these materials are potential candidates as nuclear waste forms for double-containment of actinides and lanthanides. For the whole of the studied chemical compositions of the materials, and for the three chosen Tc treatments, a Zr-reach crystalline phase, the 2M-zirconolite ($CaZrTi_2O_7$), was identified by XRD analysis, with high levels over 60% for the lowest ZrO_2 content in the materials. Minor phases as zirconia (ZrO_2) and zircon ($ZrSiO_4$) are also observed.

The highest content in zirconolite (87%) is reached for the GC with 4.5 m.% of ZrO_2. The lowest crystallization temperature (900°C) does not promote the germination of Zr-rich phases, especially zirconolite. This is intermediate crystal-growth temperature of 1,010°C, which leads to the greatest selectivity in zirconolite ceramic germination. However, the crystal-growth temperatures of 1,010 and 1,100°C also result in germination of Zr-reach radiation resistant phases.

COMPETING INTERESTS

Authors have declared that no competing interests exist.

REFERENCES

1. Jouan A, Francillon NJ, Moncouyoux JP. Vitrification of radioactive high-level waste in France. Status and Perspectives Source: Glass. 1997;3(4):4-10.
2. Glasser FP. The role of ceramics, cement and glass in the immobilization of radioactive wastes, British Ceramic Transactions Journal. 1985;84(1):1-8.
3. Donald IW, Metcalfe BL, Taylor RNJ. The immobilization of high level radioactive wastes using ceramics and glasses. Journal of Materials Science. 1997;32(22):5851-5887.
4. Shaaban KS, Wahab EA, Shaaban ER, Mahmoud SA. Investigation of crystallization and mechanical characteristics of glass and glass-ceramic with the compositions x Fe 2 O 3-35SiO 2-35B 2 O 3-10Al 2 O 3-(20− x) Na 2 O. Journal of Materials Engineering and Performance. 2020;29(7):4549-58.
5. Sołtys M, Górny A, Pisarska J, Pisarski WA. Electrical and optical properties of glasses and glass-ceramics. Journal of Non-Crystalline Solids. 2018;498:352-63.
6. Komatsu T. Design and control of crystallization in oxide glasses. Journal of Non-Crystalline Solids. 2015;428:156-75.
7. Li L, Wang F, Liao Q, Wang Y, Zhu H, Zhu Y. Synthesis of phosphate based glass-ceramic waste forms by a melt-quenching process: The formation process. Journal of Nuclear Materials. 2020;528:151854.
8. Hayward PJ. The use of glass ceramics for immobilising high level wastes from nuclear fuel recycling. Glass Technologie. 1988;29(4):122-136.
9. Hayward PJ. Glass-ceramics in radioactive waste forms for the future. Elsevier Science Publishers B. V. 1988;427-493.
10. Kamel N, Moudir D, Kamel Z, Djerridi A, Mouhamou S, Benmounah A, et al. Effect of the Ce content on a nuclear waste glassy matrix in the system: SiO_2-Al_2O_3-CaO-MgO-ZrO_2-TiO_2, synthesized at a low melting temperature. Journal of Materials Science and Engineering A. 2013;3(4):209-223.
11. JCPDS Data Philips X'Pert High Score Package, Diffraction data CD-ROM. International Center for Diffraction Data, Newtown Square PA; 2004.
12. Jenkins R, Snyder RL. Introduction to X-ray powder diffraction, Wiley, Interscience; 1996.

13. Loiseau P, Caurant D, Majerus O, Baffier N, Fillet C. Crystallization study of (TiO_2, ZrO_2)-rich SiO_2-Al_2O_3-CaO glasses Part I: Preparation and characterization of zirconolite-based glass-ceramics. Journal of Materials Science. 2003;38:843-852.
14. Vance ER, Ball CJ, Blackford MG, Cassidy DJ, Smith KL. Crystallisation of zirconolite from an alkoxide precursor. Journal of Nuclear Materials. 1990;175:58-66.

© Copyright (2021): Author(s). The licensee is the publisher (B P International).

DISCLAIMER

This chapter is an extended version of the article published by the same author(s) in the following journal.
Journal of Materials Science and Engineering B, 4(8): 220-225, 2014.

Print ISBN: 978-93-91312-26-8, eBook ISBN: 978-93-91312-34-3

Study on Time-Dependent Absorption Theory of Three Light Pulses in a Ladder-Type Four-Level System

I. Rebane[1*]

DOI: 10.9734/bpi/nupsr/v9/9837D

ABSTRACT

The time-dependent theory of the absorption of three light pulses with an arbitrary duration in ladder-type four-level systems is proposed. The pulses are in resonance with the corresponding transitions. By using the time-dependent perturbation theory the spectral and temporal behaviour of the probability that the fourth level is excited at the moment *t* is found. We calculate and analyse the cases where the frequencies of the maxima of the two of three light pulses are fixed and the maximum of the remaining pules varies. Widths of possible absorption lines depend on different parameters. On the whole, three or four lines may exist, one of them corresponds to coherent contribution and the others do not.

Keywords: Ladder-type four-level system; time-dependent resonant three-step absorption; time-dependent perturbation theory; three different light pulses.

1. INTRODUCTION

Multistep absorption/excitation has been investigated in many ways and also both monochromatic light and light pulses have been used [1-9]. In [9] the possible time dependent two-step absorption spectra of two light pulses are theoretically investigated by using the simplest model for matter and in the case of an arbitrary duration of absorbed light pulses from monochromatic light to ultrashort pulses.

Thereby, we note that if at the two-step absorption in the three-level system the monochromatic light with the frequency ω_1 is absorbed at the first step $0\rightarrow1$, then in the spectrum where the frequency ω_1 is fixed and the frequency ω_2 of the maximum of the second light pulse (which is absorbed at the second step $1\rightarrow2$) varies, there exists one line whose width is determined by the rate of energy relaxation of the second excited level 2 and by the spectral width of the second pulse. In our opinion, this is exactly the same situation as in [7]. We note that if at the first step of the absorption the light pulse is absorbed and/or the pure phase relaxation of the first excited level exists, the second line is added to the aforementioned spectrum. The width of this line depends on the rates of the energy relaxations of both excited levels 1 and 2, the rate of the pure phase relaxation and on the spectral width of the second pulse, but not on the spectral width of the first pulse. On the other hand, the width of the initial line, in addition to the aforementioned parameters, depends on the spectral width of the first pulse. This line corresponds to the coherent contribution of the spectrum [3]. We note that the linewidths depend on the timeframes between the pulses and the time *t* as well.

In this paper the three-step absorption of three light pulses in a four-level system (the pulses are in resonance with the corresponding transitions) is observed to analyse which absorption lines are possible at all and which parameters their widths depend on. Different limit cases are studied also analytically. The interaction with the environment (phonons) is taken into account phenomenologically

---

[1] *National Institute of Chemical Physics and Biophysics, Akadeemia tee 23, 12618, Tallinn, Estonia.*
**Corresponding author: E-mail: rebaneinna@gmail.com;*

via the relaxation constants of the electronic levels. The presented model holds for impurity centers at low temperatures with weak electron-phonon coupling.

2. PROBABILITY OF THREE STEP TRANSITION

The process started from ground level 0. Resonance conditions are $\omega_1 \approx \Omega_{01}$, $\omega_2 \approx \Omega_{12}$, and $\omega_3 \approx \Omega_{23}$ where Ω_{01}, Ω_{12}, and Ω_{23} are the frequencies of the transitions 0→1, 1→2, and 2→3, and ω_1, ω_2 and ω_3 are the frequencies of the maxima of the pulses.

Let us find the probability that at time t the system is in the final state applying time dependent perturbation theory. First we find the amplitude of the probability. For general consideration we need formulas, where the initial state of the system consists of the electromagnetic field and matter is given at initial time $t_0 = -\infty$. In this case we can use any shapes of exciting pulses of light.

The system is described by Hamiltonian

$$\hat{H} = \hat{H}_{CR} + \hat{V} = \hat{H}_C + \hat{H}_R + \hat{V}. \tag{1}$$

At the initial time t_0 the system is in the state

$$\left|\psi(t_0)\right\rangle = \left|\psi_C(t_0)\right\rangle \left|\psi_R(t_0)\right\rangle. \tag{2}$$

In Eq. (1) $\hat{H}_C$ is the Hamiltonian of matter, $\hat{H}_R$ is the Hamiltonian of the electromagnet field, $\hat{V}$ is the Hamiltonian of interaction and in Eq. (2) $\left|\psi_C(t_0)\right\rangle$ and $\left|\psi_R(t_0)\right\rangle$ are the initial states of matter and the electromagnetic field.

The characteristic states and eigenvalues of these Hamiltonians are the following:

$$\hat{H}_{CR}\left| j\right\rangle = E_j \left| j\right\rangle, \quad \hat{H}_C\left|i\right\rangle = E_i\left|i\right\rangle, \quad \hat{H}_R\left|\omega\right\rangle = \omega\left|\omega\right\rangle. \tag{3}$$

The initial state of matter:

$$\left|\psi_C(t_0)\right\rangle = \sum_{i'} b_{i'}\left|i'\right\rangle \exp\left(-iE_{i'}t_0\right) \tag{4}$$

and the initial state of electromagnetic field (three light pulses):

$$\begin{aligned}\left|\psi_R(t_0)\right\rangle = &\int_{-\infty}^{\infty} d\omega B_1(\omega-\omega_1)\exp(-i\omega t_0)\int_{-\infty}^{\infty} d\omega' B_2(\omega'-\omega_2)\exp(-i\omega' t_0)\\ &\times\int_{-\infty}^{\infty} d\omega'' B_3(\omega''-\omega_3)\exp(-i\omega'' t_0)\left|\omega,\omega',\omega''\right\rangle,\end{aligned} \tag{5}$$

where

$$\int_{-\infty}^{\infty} d\omega\left|B_1(\omega)\right|^2 = 1, \quad \int_{-\infty}^{\infty} d\omega'\left|B_2(\omega')\right|^2 = 1 \quad \int_{-\infty}^{\infty} d\omega''\left|B_3(\omega'')\right|^2 = 1. \tag{6}$$

Eq. (6) describe normalization conditions of three single photon wave packages with maxima at frequencies ω_1, ω_2 and ω_3, correspondingly.

The amplitude of the probability to find the system at time $t \geq t_0$ in the state $|j\rangle$ according to the Hamilton equation is

$$\begin{aligned} c_j(t) &= \langle j|\exp\left[-i(t-t_0)\hat{H}\right]|\psi(t_0)\rangle \\ &= \sum_{i'}\int_{-\infty}^{\infty} d\omega \int_{-\infty}^{\infty} d\omega' \int_{-\infty}^{\infty} d\omega'' \langle j|\exp\left[-i(t-t_0)\hat{H}\right]|i'\rangle|\omega,\omega',\omega''\rangle b_{i'}\exp(-iE_{i'}t_0) \\ &\times B_1(\omega-\omega_1)B_2(\omega'-\omega_2)B_3(\omega''-\omega_3)\exp\left[-i(\omega+\omega'+\omega'')t_0\right] \\ &= \sum_{j'}\langle j|\exp\left[-i(t-t_0)\hat{H}\right]|j'\rangle b_{j'}\exp(-iE_{j'}t_0). \end{aligned} \tag{7}$$

Let us take into account that at y ≥ 0

$$\exp\left(-iy\hat{H}\right) = \exp\left(-iy\hat{H}_{CR}\right)T\exp\left[-i\int_0^y ds\hat{V}(s)\right], \tag{8}$$

where $\hat{V}(s) = \exp\left(is\hat{H}_{CR}\right)\hat{V}\exp\left(-is\hat{H}_{CR}\right)$, T is the operator of chronological arranging, which puts the operators from right to left in the order of increasing *s*. To go to limit $t_0 \rightarrow -\infty$ the decay of the characteristic states of the Hamiltonian $\hat{H}_{CR}$ have to be taken into account. Then the amplitude $c_j(t)$ can be approximately presented as follows

$$\begin{aligned} c_j(t) \approx \sum_{n=1}^{\infty}(-i)^n \sum_{j_1,j_2,\ldots,j_n}{}' \int_{t_0}^{t} dt_1 \int_{t_0}^{t_1} dt_2 \ldots \int_{t_0}^{t_{n-1}} dt_n \exp\left[-i\left(E_j - i\gamma_j\right)(t-t_1)\right]\langle j|\hat{V}|j_1\rangle \\ \times\exp\left[-i\left(E_{j_1}-i\gamma_{j_1}\right)(t_1-t_2)\right]\langle j_1|\hat{V}|j_2\rangle\ldots\langle j_{n-1}|\hat{V}|j_n\rangle b_{j_n}\exp\left(-iE_{j_n}t_n\right), \end{aligned} \tag{9}$$

where γ_j is the decay constant of the state $|j\rangle$ and the apostrophe means that the terms with the coinciding numbers of states are omitted. This formula can be used for all values of t_0 including $-\infty$ only if the interaction is small enough.

Here we assume that the final state does not coincide the with initial state ($b_j = 0$), the integration variables t_1, t_2, …, t_n are the times of the transitions of the amplitude of the probability from one characteristic state of Hamiltonian $\hat{H}$ into the other, and the differences $t - t_1$, $t_1 - t_2$, … $t_{n-1} - t_n$, and $t_n - t_0$ determine time intervals during which the amplitude of the probability is in state $|j\rangle$, $|j_1\rangle$, ..., $|j_{n-1}\rangle$ and $|j_n\rangle$ correspondingly.

To describe the process with the three photons the term of the third order of the expansion is needed:

$$c_j(t) \approx -i \sum_{j_1, j_2, j_3}{}' \int_{t_0}^{t} dt_1 \int_{t_0}^{t_1} dt_2 \int_{t_0}^{t_2} dt_3 \exp\left[-i\left(E_j - i\gamma_j\right)(t - t_1)\right] \langle j|\hat{V}|j_1\rangle \exp\left[-i\left(E_{j_1} - i\gamma_{j_1}\right)(t_1 - t_2)\right]$$
$$\times \langle j_1|\hat{V}|j_2\rangle \exp\left[-i\left(E_{j_2} - i\gamma_{j_2}\right)(t_2 - t_3)\right] \langle j_2|\hat{V}|j_3\rangle b_{j_3} \exp\left(-iE_{j_3} t_3\right). \tag{10}$$

Since

$$\begin{gathered} E_j - i\gamma_j = E_i - i\gamma_i, \quad E_{j_1} - i\gamma_{j_1} = E_{i_1} - i\gamma_{i_1} + \omega'', \\ E_{j_2} - i\gamma_{j_2} = E_{i_2} - i\gamma_{i_2} + \omega' + \omega'', \; E_{j_3} = E_{i_3} + \omega + \omega' + \omega'' \end{gathered} \tag{11}$$

Then

$$c_j(t) \approx -i \sum_{i_1, i_2, i_3}{}' \int_{-\infty}^{\infty} d\omega \int_{-\infty}^{\infty} d\omega' \int_{-\infty}^{\infty} d\omega'' \int_{t_0}^{t} dt_1 \int_{t_0}^{t_1} dt_2 \int_{t_0}^{t_2} dt_3 \exp\left[-i\left(E_i - i\gamma_i\right)(t - t_1)\right]$$
$$\times \langle i|\langle 0|\hat{V}|\omega''\rangle|i_1\rangle \exp\left[-i\left(E_{i_1} - i\gamma_{i_1} + \omega''\right)(t_1 - t_2)\right] \langle i_1|\langle \omega''|\hat{V}|\omega', \omega''\rangle|i_2\rangle$$
$$\times \exp\left[-i\left(E_{i_2} - i\gamma_{i_2} + \omega' + \omega''\right)(t_2 - t_3)\right] \langle i_2|\langle \omega', \omega''|\hat{V}|\omega, \omega', \omega''\rangle|i_3\rangle \tag{12}$$
$$\times b_{i_3} \exp\left[-i\left(E_{i_3} + \omega + \omega' + \omega''\right)t_3\right] B_1(\omega - \omega_1) B_2(\omega' - \omega_2) B_3(\omega'' - \omega_3).$$

Let us introduce the single photon matrix elements

$$\begin{gathered} v_{\omega_1} = \langle \omega', \omega''|\hat{V}|\omega, \omega', \omega''\rangle, \\ v_{\omega_2} = \langle \omega''|\hat{V}|\omega', \omega''\rangle, \quad v_{\omega_3} = \langle 0|\hat{V}|\omega''\rangle, \end{gathered} \tag{13}$$

and the functions $B_i(t)$ which determine time profiles of the pulses:

$$B_i(\omega) = \int_{-\infty}^{\infty} dt \exp(i\omega t) B_i(t). \tag{14}$$

In the end we get

$$c_j(t) \approx -i \sum_{i_1, i_2, i_3}{}' \int_{-\infty}^{t} dt_1 \int_{-\infty}^{t_1} dt_2 \int_{-\infty}^{t_2} dt_3 \exp\left[-i\left(E_i - i\gamma_i\right)(t - t_1)\right] \langle i|v_{\omega_3}|i_1\rangle \exp\left[-i\left(E_{i_1} - i\gamma_{i_1}\right)(t_1 - t_2)\right]$$
$$\times \langle i_1|v_{\omega_2}|i_2\rangle \exp\left[-i\left(E_{i_2} - i\gamma_{i_2}\right)(t_2 - t_3)\right] \langle i_2|v_{\omega}|i_3\rangle b_{i_3} \exp\left(-iE_{i_3} t_3\right) \varepsilon_1(t_3) \varepsilon_2(t_2) \varepsilon_3(t_1), \tag{15}$$

where

$$\varepsilon_i(t) = \exp\left(-i\omega_i t\right) B_i(t). \tag{16}$$

In Eq. (16) it is assumed that the pulses are quasi-monochromatic, i.e. $B_i(t)$ are slowly changing functions in comparison with exp(-i$\omega_i t$).

To get the probability it is necessary to average the quantity $|c_i(t)|^2$ over the initial states and to summarize over the final states. In conditions of thermal equilibrium

$$\left\langle b_{i_3}^{*} b_{i'_3} \right\rangle_C = n_{i_3} \delta_{i_3 i'_3}, \quad n_{i_3} = \frac{1}{Z} \exp\left(-E_{i_3}/kT\right) \tag{17}$$

In Eq.(17) Z is the statistic sum, T is temperature and $\langle \cdots \rangle$ is the mark of averaging over ensemble. Taking the preceding into account, we get

$$\begin{gathered} W(t) \approx \sum_{i,i_3} n_{i_3} \sum_{i_1,i_2,i'_1,i'_2} \int_{-\infty}^{t} dt_1 \int_{-\infty}^{t} dt'_1 S_3(t_1,t'_1) \int_{-\infty}^{t_1} dt_2 \int_{-\infty}^{t'_1} dt'_2 S_2(t_2,t'_2) \\ \times \int_{-\infty}^{t_2} dt_3 \int_{-\infty}^{t'_2} dt'_3 \langle i_3 | v_{\omega_1}^{+} | i'_2 \rangle \exp\left[i\left(E_{i'_2} - i\gamma_{i'_2}\right)(t'_2 - t'_3)\right] \langle i'_2 | v_{\omega_2}^{+} | i'_1 \rangle \\ \times \exp\left[i\left(E_{i'_1} - i\gamma_{i'_1}\right)(t'_1 - t'_2)\right] \langle i'_1 | v_{\omega_3}^{+} | i \rangle \exp\left[-iE_i (t'_1 - t_1) - \gamma_i (2t - t_1 - t'_1)\right] \\ \times \langle i | v_{\omega_3} | i_1 \rangle \exp\left[-i\left(E_{i_1} - i\gamma_{i_1}\right)(t_1 - t_2)\right] \langle i_1 | v_{\omega_2} | i_2 \rangle \\ \times \exp\left[-i\left(E_{i_2} - i\gamma_{i_2}\right)(t_2 - t_3)\right] \langle i_2 | v_{\omega_1} | i_3 \rangle \exp\left[-iE_{i_3} (t_3 - t'_3)\right] S_1(t_3,t'_3). \end{gathered} \tag{18}$$

Here

$$S_i\left(t_j,t'_j\right) = \left\langle \varepsilon_i^{*}\left(t_j\right) \varepsilon_i\left(t'_j\right) \right\rangle_R \tag{19}$$

are the correlation functions of the absorbed pulses, $\langle \cdots \rangle_R$ denotes averaging over states of pulses. The functions $S_i(t_j,t'_j)$ are considerably different from zero in the region $|t_j|$, $|t'_j| \le \Delta_i^{-1}$, where Δ_i is the spectral width of pulse i. If the pulse is coherent, its duration is determined by the time Δ_i^{-1}.

Taking into account that $E_i |i\rangle = \hat{H}_C |i\rangle$ and introducing the operator of damping $\gamma_i |i\rangle = \hat{\gamma} |i\rangle$, the Eq. (18) can be rewritten in the form (see also [10, 11]:

$$W(t) = \int_{-\infty}^{t} dt_1 \int_{-\infty}^{t} dt'_1 S_3(t_1,t'_1) \int_{-\infty}^{t_1} dt_2 \int_{-\infty}^{t'_1} dt'_2 S_2(t_2,t'_2) \int_{-\infty}^{t_2} dt_3 \int_{-\infty}^{t'_2} dt'_3 F(t,t_1,t'_1,t_2,t'_2,t_3,t'_3) S_1(t_3,t'_3), \tag{20}$$

Where

$$\begin{gathered} F(t,t_1,t'_1,t_2,t'_2,t_3,t'_3) = \langle v_{\omega_1}^{+} \exp\left[i\left(\hat{H}_C + i\gamma\right)(t'_2 - t'_3)\right] v_{\omega_2}^{+} \exp\left[i\left(\hat{H}_C + i\gamma\right)(t'_1 - t'_2)\right] \\ \times v_{\omega_3}^{+} \exp\left[-i\hat{H}_C (t'_1 - t_1) - \gamma(2t - t_1 - t'_1)\right] v_{\omega_3} \exp\left[-i\left(\hat{H}_C - i\gamma\right)(t_1 - t_2)\right] v_{\omega_2} \\ \times \exp\left[-i\left(\hat{H}_C - i\gamma\right)(t_2 - t_3)\right] v_{\omega_1} \exp\left[-i\hat{H}_C (t_3 - t'_3)\right] \rangle_C . \end{gathered} \tag{21}$$

At the end this probability $W(t)$ decreases to zero with the increase of the time t.

3. MODEL

To simplify the calculations, the light pulses are taken coherent and of a single-sided exponential shape. The corresponding correlation functions are

$$\begin{aligned} S_1(t_3,t'_3) &= \theta(t_3-\tau_1)\theta(t'_3-\tau_1)\Delta_1 \exp[i\omega_1(t_3-t'_3)-\Delta_1(t_3+t'_3-2\tau_1)/2], \\ S_2(t_2,t'_2) &= \theta(t_2-\tau_2)\theta(t'_2-\tau_2)\Delta_2 \exp[i\omega_1(t_2-t'_2)-\Delta_2(t_2+t'_2-2\tau_2)/2], \\ S_3(t_1,t'_1) &= \theta(t_1-\tau_3)\theta(t'_1-\tau_3)\Delta_3 \exp[i\omega_2(t_1-t'_1)-\Delta_3(t_1+t'_1-2\tau_3)/2], \end{aligned} \tag{22}$$

where $\theta(x)$ is Heaviside step function, τ_1, τ_2 and τ_3 are the time moments when the pulses begin to pass through the impurity centre, Δ_1, Δ_2 and Δ_3 are the FWHM spectral widths of the pulses.

In our elementary model the phase relaxation and the phonon wings are not taken into account, the relaxation processes of the excited levels 1, 2 and 3 are described by the rates of energy relaxation γ_1, γ_2 and γ_3. Thus the interaction with phonons is taken into account phenomenologically via the relaxation constants of the electronic levels.

Then the correlation function of the four-level system is

$$\begin{aligned} F\,(t,t_1,t'_1,t_2,t'_2\,t_3,t'_3) = C\ \exp[-\gamma_3(2t-t_1-t'_1)/2-i\Omega_{23}(t_1-t'_1)-\gamma_2(t_1+t'_1-t_2-t'_2)/2 \\ -i\Omega_{12}(t_2-t'_2)-\gamma_1(t_2+t'_2-t_3-t'_3)/2-i\Omega_{01}(t_3-t'_3)], \end{aligned} \tag{23}$$

where C is a constant.

In summary we have twelve parameters/variables which have influence on the spectra (Δ_1, Δ_2, Δ_3, τ_2 - τ_1, τ_3 - τ_2, t - τ_3, ω_1 - Ω_{01}, ω_2 - Ω_{12}, ω_3 - Ω_{23}, γ_1, γ_2 and γ_3).

2.1 Monochromatic Light

Using monochromatic light at all three steps of the absorption process, i.e. in Eq. (22) the FWHM spectral widths of the pulses $\Delta_1 = \Delta_2 = \Delta_3 = 0$ (stationary case). Then

$$W \approx \frac{1}{\left[(\Omega_{01}-\omega_1)^2+\gamma_1^2/4\right]} \frac{1}{\left[(\Omega_{01}+\Omega_{12}-\omega_1-\omega_2)^2+\gamma_2^2/4\right]} \frac{1}{\left[(\Omega_{01}+\Omega_{12}+\Omega_{23}-\omega_1-\omega_2-\omega_3)^2+\gamma_3^2/4\right]} \tag{24}$$

In Eq. (24) the first term describes the absorption of light with frequency ω_1 between the levels 0→1, the second term describes the absorption of light with frequency ω_1 + ω_2 between the levels 0 →2, and the third term describes the absorption of light with frequency ω_1 + ω_2 + ω_3 between the levels 0→3.

In the case where the frequencies ω_1 and ω_2 are fixed and the frequency ω_3 varies, only the line between the levels 0 →3 exists, which corresponds to coherent contribution. The width of this line depends only on the rate of energy relaxation γ_3 of the final state 3. It is so only in this model. If we take into account the phase relaxation of the levels 1 and 2, other two lines appear which correspond to non-coherent contribution. If the light is not monochromatic, i.e. spectral widths of the coherent pulses $\Delta_1 \neq 0$, $\Delta_2 \neq 0$ and $\Delta_3 \neq 0$, then these other two lines appear even though the phase relaxation is not taken into account (see Chapter 6). In [9] it has been shown that the ratio of non-coherent and coherent parts, i.e. ratio of luminescence and scattering of resonant secondary radiation (the process between levels 0→1→0, the second order of perturbation theory) is determined by the ratio of the rates of the phase relaxation and the rate of the energy relaxation of excited level 1.

2.2 Ultrashort Pulses

Here $x \equiv \Omega_{01} - \omega_1$, $y \equiv \Omega_{12} - \omega_2$, and $z \equiv \Omega_{23} - \omega_3$.

1. The first pulse is much shorter than the relaxation time of the second level γ_1. Then

$$S_1(t_3,t'_3) \approx \delta(t_3-\tau_1)\delta(t'_3-\tau_1)\exp[i\omega_1(t_3-t'_3)], \tag{25}$$

$$W(t) = \int_{\tau_1}^{t} dt_1 \int_{\tau_1}^{t} dt'_1 S_3(t_1,t'_1) \int_{\tau_1}^{t_1} dt_2 \int_{\tau_1}^{t'_1} dt'_2 S_2(t_2,t'_2) F(t,t_1,t'_1,t_2,t'_2,\tau_1,\tau_1). \tag{26}$$

Eq. (26) describes two-step absorption between levels 1→2→3. The initial level 1 is excited at the time moment τ_1. In our model with correlation functions from Eq. (22) and (23) the probability is the following:

$$\begin{aligned}
W(t) \approx & \frac{1}{\left[y^2+(\Delta_2+\gamma_1-\gamma_2)^2/4\right]}\Bigg\{\frac{\exp[-\gamma_1(\tau_2-\tau_1)]}{\left[z^2+(\Delta_3+\gamma_2-\gamma_3)^2/4\right]} \\
& \times[\ \exp(-\gamma_2(\tau_3-\tau_2)-\gamma_3(t-\tau_3))+\exp(-\Delta_3(t-\tau_3)-\gamma_2(t-\tau_2)) \\
& -2\cos(z(t-\tau_3))\exp(-(\Delta_3+\gamma_3)(t-\tau_3)/2-\gamma_2(t+\tau_3-2\tau_2)/2)] \\
& +\frac{1}{\left[(y+z)^2+(\Delta_2+\Delta_3+\gamma_1-\gamma_3)^2/4\right]} \\
& \times[\ \exp(-\Delta_2(\tau_3-\tau_2)-\gamma_1(\tau_3-\tau_1)-\gamma_3(t-\tau_3))+\exp(-\Delta_2(t-\tau_2)-\Delta_3(t-\tau_3)-\gamma_1(t-\tau_1)) \\
& -2\cos((y+z)(t-\tau_3))\exp(-\Delta_2(t+\tau_3-2\tau_2)/2-\Delta_3(t-\tau_3)/2-\gamma_1(t+\tau_3-2\tau_1)/2-\gamma_3(t-\tau_3)/2)] \\
& -\Bigg[\frac{\exp(iy(\tau_3-\tau_2))}{(iz\ +(\Delta_3+\gamma_2-\gamma_3)/2)(-i(y+z)+(\Delta_2+\Delta_3+\gamma_1-\gamma_3)/2)} \\
& \times(\exp(-\gamma_2(\tau_3-\tau_2)/2-\gamma_3(t-\tau_3)/2)-\exp(-iz(t-\tau_3)-\Delta_3(t-\tau_3)/2-\gamma_2(t-\tau_2)/2)) \\
& \times(\exp(-\Delta_2(\tau_3-\tau_2)/2-\gamma_1(\tau_3+\tau_2-2\tau_1)/2-\gamma_3(t-\tau_3)/2) \\
& -\exp(i(y+z)(t-\tau_3)-\Delta_2(t-\tau_2)/2-\Delta_3(t-\tau_3)/2-\gamma_1(t+\tau_2-2\tau_1)/2))+c.c.]\}.
\end{aligned} \tag{27}$$

2. When the second pulse is ultrashort

$$S_2(t_2,t'_2) \approx \delta(t_2-\tau_2)\delta(t'_2-\tau_2)\exp[i\omega_2(t_2-t'_2)], \tag{28}$$

Then

$$W(t) = \int_{\tau_2}^{t} dt_1 \int_{\tau_2}^{t} dt'_1 S_3(t_1,t'_1) \int_{-\infty}^{\tau_2} dt_3 \int_{-\infty}^{\tau_2} dt'_3 F(t,t_1,t'_1,\tau_2,\tau_2,t_3,t'_3) S_1(t_3,t'_3). \tag{29}$$

Here we have multiplication of two one-step processes: 0→1 and 2→3, in the latter case level 2 is excited at moment τ_2. In our model the probability is the following:

$$
\begin{aligned}
W(t) \approx{} & \frac{1}{\left[x^2+\left(\Delta_1-\gamma_1\right)^2/4\right]}\left\{\exp\left[-\Delta_1\left(\tau_2-\tau_1\right)\right]+\exp\left[-\gamma_1\left(\tau_2-\tau_1\right)\right]\right. \\
& \left.-2\cos\left[x\left(\tau_2-\tau_1\right)\right]\exp\left[-(\Delta_1+\gamma_1)(\tau_2-\tau_1)/2\right]\right\} \\
& \times\frac{1}{\left[z^2+\left(\gamma_2+\Delta_3-\gamma_3\right)^2/4\right]}\left\{\exp\left[-\gamma_2\left(t-\tau_2\right)-\Delta_3\left(t-\tau_3\right)\right]+\exp\left[-\gamma_2\left(\tau_3-\tau_2\right)-\gamma_3\left(t-\tau_3\right)\right]\right. \\
& \left.-2\cos\left[z\left(t-\tau_3\right)\right]\exp\left[-\gamma_2\left(t+\tau_3-2\tau_2\right)/2-\left(\Delta_3+\gamma_3\right)\left(t-\tau_3\right)/2\right]\right\}.
\end{aligned}
\tag{30}
$$

3. In the case where the third pulse is ultrashort

$$
S_3(t_1,t'_1)\approx\delta(t_1-\tau_3)\delta(t'_1-\tau_3)\exp[i\omega_3(t_1-t'_1)]
\tag{31}
$$

And

$$
W(t)=\int_{-\infty}^{\tau_3}dt_2\int_{-\infty}^{\tau_3}dt'_2S_2\left(t_2,t'_2\right)\int_{-\infty}^{t_2}dt_3\int_{-\infty}^{t'_2}dt'_3F\left(t,\tau_3,\tau_3,t_2,t'_2,t_3,t'_3\right)S_1\left(t_3,t'_3\right).
\tag{32}
$$

Here two-step absorption 0→1→2 takes place. In our model the probability is the following:

$$
\begin{aligned}
W(t) \approx{} & \frac{\exp\left[-\gamma_3\left(t-\tau_3\right)\right]}{\left[x^2+\left(\Delta_1-\gamma_1\right)^2/4\right]}\left\{\frac{1}{\left[y^2+\left(\Delta_2+\gamma_1-\gamma_2\right)^2/4\right]}\right. \\
& \times\left[\exp\left(-\gamma_1\left(\tau_2-\tau_1\right)-\gamma_2\left(\tau_3-\tau_2\right)\right)+\exp\left(-\Delta_2\left(\tau_3-\tau_2\right)-\gamma_1\left(\tau_3-\tau_1\right)\right)\right. \\
& \left.-2\cos\left(y\left(\tau_3-\tau_2\right)\right)\exp\left(-(\Delta_2+\gamma_2)\left(\tau_3-\tau_2\right)/2-\gamma_1\left(\tau_2+\tau_3-2\tau_1\right)/2\right)\right] \\
& +\frac{1}{\left[\left(x+y\right)^2+\left(\Delta_1+\Delta_2-\gamma_2\right)^2/4\right]} \\
& \times\left[\exp\left(-\Delta_1\left(\tau_2-\tau_1\right)-\gamma_2\left(\tau_3-\tau_2\right)\right)+\exp\left(-\Delta_1\left(\tau_3-\tau_1\right)-\Delta_2\left(\tau_3-\tau_2\right)\right)\right. \\
& \left.-2\cos\left(\left(x+y\right)\left(\tau_3-\tau_2\right)\right)\exp\left(-\Delta_1\left(\tau_2+\tau_3-2\tau_1\right)/2-\Delta_2\left(\tau_3-\tau_2\right)/2-\gamma_2\left(\tau_3-\tau_2\right)/2\right)\right] \\
& -\left[\frac{\exp\left(\left(ix-\left(\Delta_1+\gamma_1\right)/2\right)\left(\tau_2-\tau_1\right)\right)}{\left(iy+\left(\Delta_2+\gamma_1-\gamma_2\right)/2\right)\left(-i\left(x+y\right)+\left(\Delta_1+\Delta_2-\gamma_2\right)/2\right)}\right. \\
& \times\left(\exp\left(-\gamma_2\left(\tau_3-\tau_2\right)/2\right)-\exp\left(\left(-iy-\left(\Delta_2+\gamma_1\right)/2\right)\left(\tau_3-\tau_2\right)\right)\right) \\
& \left.\left.\times\left(\exp\left(-\gamma_2\left(\tau_3-\tau_2\right)/2\right)-\exp\left(\left(i\left(x+y\right)-\left(\Delta_1+\Delta_2\right)/2\right)\left(\tau_3-\tau_2\right)\right)\right)+c.c.\right]\right\}.
\end{aligned}
\tag{33}
$$

3. RESULTS

Subsequently, $\tau_1=0$, $T_1\equiv\tau_2-\tau_1$, $T_2\equiv\tau_3-\tau_2$, $x\equiv\Omega_{01}-\omega_1$, $y\equiv\Omega_{12}-\omega_2$, and $z\equiv\Omega_{21}-\omega_3$.

In Figs. 1 - 3 we analyzed the case where z is variable, x and y are fixed and chosen different from Fig. 1. Dependence of the probability $W(t)$ on $z\equiv\Omega_{23}-\omega_3$ at the fixed value of $x=-15\gamma_3$, $y=-10\gamma_3$ for different values of Δ_2 (in γ_3). $\Delta_1=0.1\gamma_3$, $\Delta_3=\gamma_3$, $\gamma_1=5\gamma_3$, $\gamma_2=5\gamma_3$, $T_1=10^{-7}\gamma_3^{-1}$, $T_2=0.1\gamma_3^{-1}$, $t=1.1\gamma_3^{-1}$. All curves are normalized to 1.

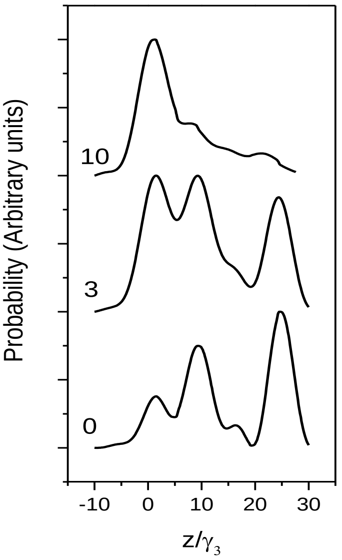

Fig. 1. Dependence of the probability $W(t)$ on $z \equiv \Omega_{23} - \omega_3$ at the fixed value of $x = -15\gamma_3$, $y = -10\gamma_3$ for different values of Δ_2 (in γ_3). $\Delta_1 = 0.1\gamma_3$, $\Delta_3 = \gamma_3$, $\gamma_1 = 5\gamma_3$, $\gamma_2 = 5\gamma_3$, $T_1 = 10^{-7}\gamma_3^{-1}$, $T_2 = 0.1\gamma_3^{-1}$, $t = 1.1\gamma_3^{-1}$. All curves are normalized to 1.

In Fig. 1 the dependence of the spectrum on the parameter Δ_2 at fixed time t is presented. We get three lines with maxima at $z = -(x + y)$, $z = -y$ and $z = 0$. The location of the maximum of the first line from the right at $z = -(x + y)$ ($\omega_3 = \Omega_{01} + \Omega_{12} + \Omega_{23} - \omega_1 - \omega_2$) shows that the three pulses are absorbed together so that $x + y + z = 0$ ($\omega_1 + \omega_2 + \omega_3 = \Omega_{01} + \Omega_{12} + \Omega_{23}$) without excitation of the levels 1 and 2 and therefore this is the coherent contribution. The locations of the maxima of the other two lines at $z = -y$ ($\omega_3 = \Omega_{12} + \Omega_{23} - \omega_2$) and $z = 0$ ($\omega_3 = \Omega_{23}$) show that the absorption takes place correspondingly 0→1→3 and 0→1→2→3 or 0→2→3 and therefore these are not coherent contributions. In the first case the second and the third pulses are absorbed together from level 1. With the increase of the spectral width of the second pulse Δ_2 the intensity of the line at $z = 0$ increases and the intensities of the other lines decrease.

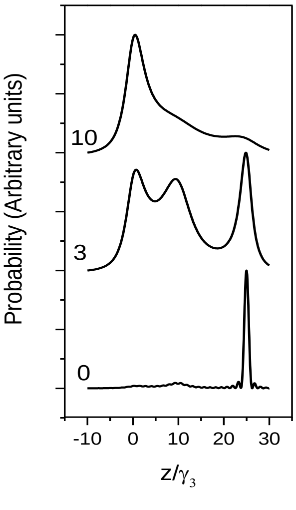

Fig. 2. Dependence of the probability $W(t)$ on $z \equiv \Omega_{23} - \omega_3$ at the fixed value of $x = -15\gamma_3$, $y = -10\gamma_3$ for different values of Δ_2 (in γ_3). $\Delta_1 = 0.1\gamma_3$, $\Delta_3 = \gamma_3$, $\gamma_1 = 5\gamma_3$, $\gamma_2 = 5\gamma_3$, $T_1 = 10^{-7}\gamma_3^{-1}$, $T_2 = 0.1\gamma_3^{-1}$, $t = 5.1\gamma_3^{-1}$. All curves are normalized to 1

In Fig. 2 comparison with Fig. 1 time *t* is much longer. In this case the line width of the line with maximum at $z = -(x + y)$ (corresponds to the coherent contribution) diminishes, the limit width of this line is determined by the spectral widths of the pulses Δ_1, Δ_2 and Δ_3 and with the energy relaxation constant γ_3 of the excited electronic level 3. From certain time *t* with the increase of time *t* the intensity and the width of the lines decrease. In Fig. 2 curve 1 ($\Delta_2 = 0$) is enlarged compared to the corresponding curve 1 in Fig. 1 3.2 times.

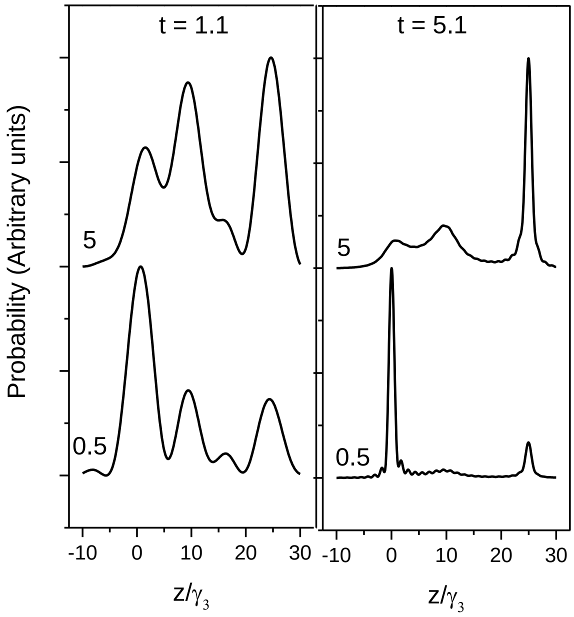

Fig. 3. Dependence of the probability $W(t)$ on $z \equiv \Omega_{23} - \omega_3$ at the fixed value of $x = -15\gamma_3$, $y = -10\gamma_3$ for different values of γ_2 (in γ_3) and t (in γ_3^{-1}). $\Delta_1 = 0.1\gamma_3$, $\Delta_2 = \gamma_3$, $\Delta_3 = \gamma_3$, $\gamma_1 = 5\gamma_3$, $\gamma_2 = 5\gamma_3$, $T_1 = 10^{-7}\gamma_3^{-1}$, $T_2 = 0.1\gamma_3^{-1}$. All curves are normalized to 1

In Fig. 3 the dependence of the spectrum on the parameter γ_2 at different time *t* is presented.
The analysis of these three figures and the other spectra with different parameters shows that the limit width of the line with maximum at $z = -y$ is determined by the spectral widths of the pulses Δ_2 and Δ_3, and by the energy relaxation constants γ_1 and γ_3. The limit width of the line with maximum at $z = 0$ is determined by the spectral width of the pulse Δ_3 and by the energy relaxation constants γ_2 and γ_3.
In the case of our correlation functions of the excitation pulses the limit values of FWHM of the lines are the following (ω_1 and ω_2 (i.e. *x* and *y*) are fixed):

$$\begin{aligned}
&\sigma_{\max\, at\, z=0} \equiv \lim_{|t-\tau_3|\to\infty} \sigma_{z=0}(T,t) = \gamma_2 + |\Delta_3 - \gamma_3| \quad (the\ non-coherent\ contribution),\\
&\sigma_{\max\, at\, z=-y} \equiv \lim_{|t-\tau_3|\to\infty} \sigma_{z=-y}(T,t) = \gamma_1 + \Delta_2 + |\Delta_3 - \gamma_3| \quad (the\ non-coherent\ contribution),\\
&\sigma_{\max\, at\, z=-x-y} \equiv \lim_{|t-\tau_3|\to\infty} \sigma_{z=-x-y}(T,t) = \Delta_1 + \Delta_2 + |\Delta_3 - \gamma_3| \quad (the\ coherent\ contribution).
\end{aligned} \tag{34}$$

The other parameters influence only the intensities of these lines.

The analysis shows that in the general case, where the spectral widths of the pulses Δ_1, Δ_2 and Δ_3 are comparable with the energy relaxation constants γ_1, γ_2 and γ_3, if the frequency of the maximum of the first pulse ω_1 (ω_2, ω_3 are fixed) is variable three lines with the maxima at $x = 0$, $x = -y$, $x = -y - z$ exist in the spectra. In the case where the frequency of the maximum of the second pulse ω_2 (ω_1, ω_3 are fixed) is variable four lines with the maxima at $y = 0$, $y = -x$, $y = -z$, $y = -x - z$ exist in the spectra.

In Figs. 4 – 6 the spectral widths of light pulses Δ_1, Δ_3, the time intervals T_1, T_2, the time t and the relaxation constants γ_1, γ_2 and γ_3 are the same.

In Fig. 4 the dependence of the probability $W(t)$ on the frequency of the maximum of the first pulse ω_1 is calculated, the other frequencies ω_2, ω_3 are fixed and the quantities $\omega_2 - \Omega_{12}$, $\omega_3 - \Omega_{23}$ are chosen different from zero to separate possible lines spectroscopically.

In Fig. 5 the dependence of the probability $W(t)$ on the frequency of the maximum of the second pulse ω_2 is presented, the other frequencies ω_1, ω_3 are fixed.

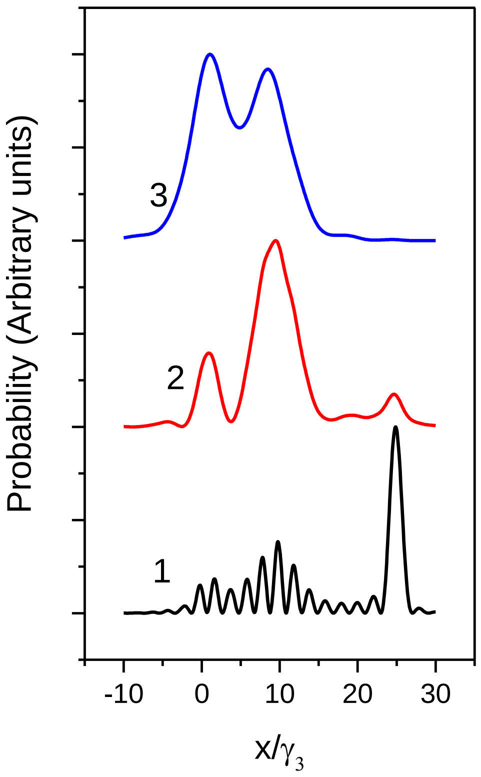

Fig. 4. Probability $W(t)$ for different values of Δ_2, $x \equiv \Omega_{01} - \omega_1$ is variable. $y = -10\gamma_3$, $z = -15\gamma_3$. Curve 1 – $\Delta_2 = 0$, curve 2 – $\Delta_2 = 3\gamma_3$, curve 3 – $\Delta_2 = 10\gamma_3$. $\Delta_1 = 0.1\gamma_3$, $\Delta_3 = \gamma_3$, $\gamma_1 = \gamma_2 = 5\gamma_3$, $T_1 = T_2 = \gamma_3^{-1}$, $t = 5.1\gamma_3^{-1}$. Curves are normalized to 1.

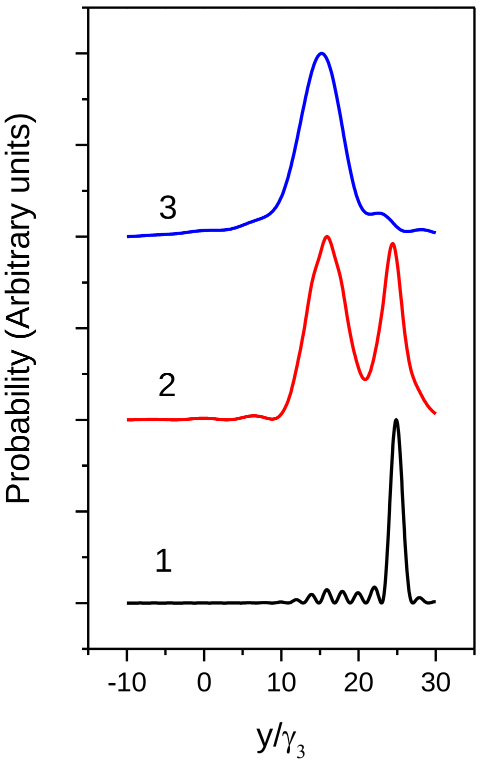

Fig. 5. Probability $W(t)$ for different values of Δ_2, $y \equiv \Omega_{12} - \omega_2$ is variable. $x = -15\gamma_3$, $z = -10\gamma_3$. Curve 1 – $\Delta_2 = 0$, curve 2 – $\Delta_2 = 3\gamma_3$, curve 3 – $\Delta_2 = 10\gamma_3$. The other parameters are the same as in Fig. 4. Curves are normalized to 1.

In Fig. 6 the dependence of the probability $W(t)$ on the frequency of the maximum of the third pulse ω_3 is calculated, the other frequencies ω_1, ω_2 are fixed. At different values of the spectral width of the second pulse Δ_2 different lines exist. When the frequency ω_1 is variable, then the possible maximums of the lines are at $x = 0$, $x = -y$ (in Fig. 4 $x = 10\gamma_3$) and $x = -y - z$ (in Fig. 4 $x = 25\gamma_3$). When the frequency ω_2 is variable, the possible maximums of the lines are at $y = 0$, $y = -x$ (in Fig. 5 $y = 15\gamma_3$), $y = -z$ and $y = -x - z$ (in Fig. 5 $y = 25\gamma_3$). Finally, when the frequency ω_3 is variable, the possible maximums of the lines are at $z = 0$, $z = -y$ and $z = -x - y$ (in Fig. 6 $z = 25\gamma_3$).

The widths of the different lines depend on different parameters (Table 1). It can be seen from the Table that if z varies, the width of the line with the maximum at $z = 0$ depends on the parameters γ_2, γ_3 and Δ_3; the width of the line with the maximum at $z = -y$ depends on the parameters γ_1, γ_3, Δ_2 and Δ_3; the width of the line with the maximum at $z = -x - y$ depends on the parameters γ_3, Δ_1, Δ_2 and Δ_3.

In the case, where the monochromatic light ($\Delta_1 = 0$) is used at the first step of the absorption (0→1) in the spectrum where x varies, all three lines remain, in the spectrum where y varies the lines with the maximums at $y = -x$ and $y = -x - z$ remain, and in the spectrum where z varies the lines with the maximums at $z = 0$ and $z = -x - y$ remain.

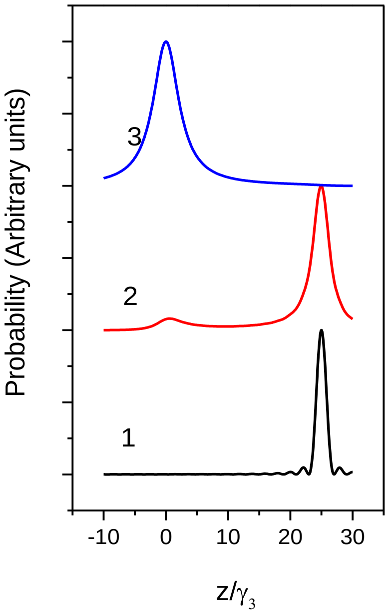

Fig. 6. Probability $W(t)$ for different values of Δ_2, $z \equiv \Omega_{23} - \omega_3$ is variable. $x = -15\gamma_3$, $y = -10\gamma_3$. Curve 1 – $\Delta_2 = 0$, curve 2 – $\Delta_2 = 3\gamma_3$, curve 3 – $\Delta_2 = 10\gamma_3$. The other parameters are the same as in Fig. 4. Curves are normalized to 1.

Fig. 7 shows the case where $y \equiv \Omega_{12} - \omega_2$ varies, in which all four possible lines are visible.

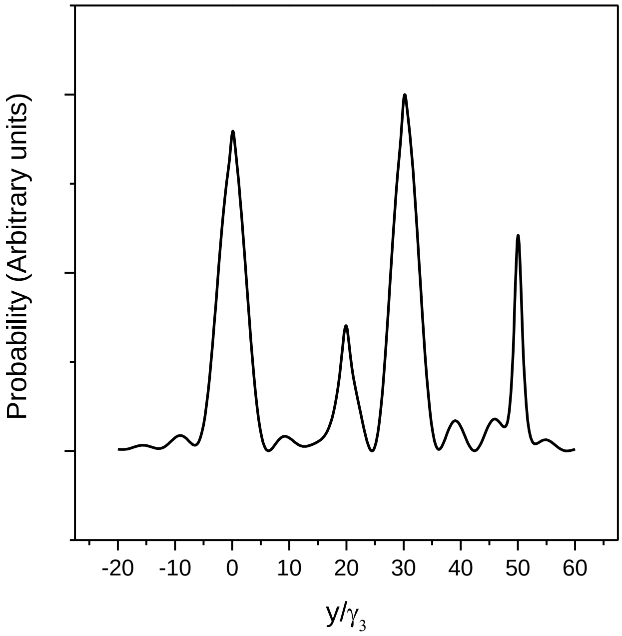

Fig. 7. Probability $W(t)$ in the case where all four lines exist, $y \equiv \Omega_{12} - \omega_2$ is variable. $x = -30\gamma_3$, $z = -20\gamma_3$, $\Delta_1 = \Delta_2 = \Delta_3 = \gamma_1 = \gamma_2 = \gamma_3$, $T_1 = 2\gamma_3^{-1}$, $T_2 = \gamma_3^{-1}$, $t = 10.1\gamma_3^{-1}$. Curve is normalized to 1.

If, additionally, the monochromatic light is used at the second step of the absorption ($1 \rightarrow 2$) in the spectrum where z is a variable, the line with the maximum at $z = 0$ disappears as well.

Note, that the lines for which the equation $x + y + z = 0$ applies are the coherent parts of the spectrums. Furthermore, the widths of all lines depend on the timespans T_1, T_2 and the time t. In general, with the increase of T_1, T_2 and t the lines become narrower.

Table 1. The dependence of the widths of different lines on different parameters

Locations of the maximums of the lines	**$\Delta_1 \neq 0$, $\Delta_2 \neq 0$, $\Delta_3 \neq 0$**	**$\Delta_1 = 0$, $\Delta_2 \neq 0$, $\Delta_3 \neq 0$**	**$\Delta_1 = \Delta_2 = 0$, $\Delta_3 \neq 0$**	**$\Delta_1 = \Delta_2 = \Delta_3 = 0$**
***x* varies**				
$x = 0$	γ_1, Δ_1	γ_1	γ_1	γ_1
$x = -y$	γ_2, Δ_1, Δ_2	γ_2, Δ_2	γ_2	γ_2
$x = -y - z$	γ_3, Δ_1, Δ_2, Δ_3	γ_3, Δ_2, Δ_3	γ_3, Δ_3	γ_3
***y* varies**				
$y = 0$	γ_1, γ_2, Δ_2	-	-	-
$y = -x$	γ_2, Δ_1, Δ_2	γ_2, Δ_2	γ_2	γ_2
$y = -z$	γ_1, γ_3, Δ_2, Δ_3	-	-	-
$y = -x - z$	γ_3, Δ_1, Δ_2, Δ_3	γ_3, Δ_2, Δ_3	γ_3, Δ_3	γ_3
***z* varies**				
$z = 0$	γ_2, γ_3, Δ_3	γ_2, γ_3, Δ_3	-	-
$z = -y$	γ_1, γ_3, Δ_2, Δ_3	-	-	-
$z = -x - y$	γ_3, Δ_1, Δ_2, Δ_3	γ_3, Δ_2, Δ_3	γ_3, Δ_3	γ_3

4. CONCLUSIONS

The time-dependence theory of three-step absorption of three different light pulses with an arbitrary duration in the electronic four-level model is proposed. The probability that the fourth level is excited at the time moment t is found to be depending on the time delays between the pulses T_1 and T_2, the spectral widths of the pulses Δ_1, Δ_2 and Δ_3 and the energy relaxation constants γ_1, γ_2 and γ_3 of the excited electronic levels 1, 2 and 3. The time dependent perturbation theory is applied.

In the calculations the pulses are taken as coherent and of a single-sided exponential shape, ω_1, ω_2 and ω_3 are the frequencies of the maximums, 0, T_1 and $T_1 + T_2$ are the time moments when the pulses begin to pass through the impurity centre. The resonance conditions are $\omega_1 \approx \Omega_{01}$, $\omega_2 \approx \Omega_{12}$ and $\omega_3 \approx \Omega_{23}$ where Ω_{01}, Ω_{12} and Ω_{13} are the frequencies of the transitions $0 \rightarrow 1$, $1 \rightarrow 2$ and $2 \rightarrow 3$.

In the general case, where the spectral widths of the pulses Δ_1, Δ_2 and Δ_3 are comparable with the energy relaxation constants γ_1, γ_2 and γ_3, three lines may exist in the spectra in the cases where ω_1 or ω_3 are variable (corresponding ω_2 and ω_3 or ω_1 and ω_2 are fixed, Fig. 4 and 6). In the case where ω_2, is variable there may exist four lines (ω_1 and ω_3 are fixed, Fig. 7). An analysis shows that the widths of the possible lines depend on different parameters (Table).

This work was supported by the Estonian Ministry of Education and Research through the Research Funding “Femtosecond multiphotonics: From quantitative spectroscopy to quantum optics”, PRG661.

COMPETING INTERESTS

Author has declared that no competing interests exist.

REFERENCES

1. Yan Yi J, Fried LE, Mukamel S. J. Phys. Chem. 1989;93:8149.
2. Yan Yi J, Mukamel S. Phys. Rev. A. 1990;41:6485.

3. Gelin MF, Egorova D, Pisliakov AV, Domcke W. Chem. Phys. Letters. 2004;391:234.
4. Dobryakov AL, Kovalenko SA, Ernsting NP. J. Chem. Phys. 2005;123:044502.
5. Librantz A FH, Tarelho LVG, Gomes L, Ranieri IM. Exacta, São Paulo. 2006;4:179.
6. Dobryakov AL, Perez Lustres JL, Kovalenko SA, Ernsting NP. Chem. Phys. 2008;347:127.
7. Tanasittikosol M, Carr C, Adams CS, Wetherill KJ. Phys. Rev.A . 2012;85:033830.
8. Carr C, Tanasittikosol M, Sargsyan A, Sarkisyan D, Adams CS, Weatherill K. J Opt. Lett. 2012;37:3858.
9. Rebane I. Physics Letters A. 2015;379:2135.
10. Hau-Riege SP. Nonrelativistic Quantum X-Ray Physics (Weinheim: Wiley-VCH). 2015;133-158.
11. Rebane I. Proc. Estonian Acad. Sci. 66 1; Rebane I IOP Conf. Series: J. Physics. 2017;833:012023

Biography of author(s)

Dr. I. Rebane
National Institute of Chemical Physics and Biophysics, Akadeemia tee 23, 12618, Tallinn, Estonia.

She was born on August 12, 1953, and is a senior research fellow in the Estonian National Institute of Chemical Physics and Biophysics and has held that position since 2020. From 1976 to 2020, she worked as a researcher and as a senior research fellow in the Institute of Physics of the Estonian Academy of Sciences (now part of the University of Tartu, Faculty of Science and Technology). She completed her undergraduate studies in Theoretical Physics in the University of Tartu in 1976 and received her PhD in 1981 from the Institute of Physics of the Estonian Academy of Sciences. Her research is mainly focused on the theory of absorption of light pulses in multilevel systems, single molecule spectroscopy, theory of spectral hole burning by light pulses and theory of time dependent resonant secondary emission spectra. During her long career, Rebane has written more than 100 articles.

© Copyright (2021): Author(s). The licensee is the publisher (B P International).

DISCLAIMER
This chapter is an extended version of the article published by the same author(s) in the following conference proceeding.
Journal of Physics: Conf. Series 833,012023;2017.

Print ISBN: 978-93-91312-26-8, eBook ISBN: 978-93-91312-34-3

Determination of Acousto-Optic Spatial Filters Diffracted Light at Zeroth-Order Using MATLAB Analysis

Elham Jasim Mohammad[1*]

DOI: 10.9734/bpi/nupsr/v9/10395D

ABSTRACT

This paper introduces the essentials of acousto-optics with the theory and applications using MATLAB. There are some software used to process acousto-optics filter and the implementation details of any acousto-optics algorithm are inaccessible. Our work is focused on software used to solving the coupled equations in Bragg diffraction by creating MATLAB function for use in Bragg regime and acoustic-optic spatial filtering and employing mainly the MATLAB program for solving this problem. We review the role of acousto-optic and spatial filtering for high-pass spatial filtering. Classically, acousto-optic interactions comprise scattering of photons by energetic phonons into higher and lower orders. Standard weak interaction theory describes diffraction in the Bragg regime as the propagation of a uniform plane wave of light through a uniform plane wave of sound, resulting in the well known first- and zeroth-order diffraction. We investigate Raman-Nath diffraction corresponding to near-Bragg diffraction. A result shows the dependence of various scattered orders on the incident angle/Bragg angle illustrating the Bessel function dependence.

Keywords: Acousto optics; bragg diffraction; spatial filters; raman diffraction; matlab.

1. INTRODUCTION

Acousto-optics devices are used in laser equipment for electronic control of the intensity and position of the laser beam. In this paper, we will explain the theory and application of acousto-optics filter. Acousto-optics interaction occurs in all optical mediums when an acoustic wave and a laser beam are present in the medium [1]. Acousto-optics effect magnitude has a strong dependence on the angle of light incidence and the wavelength of optical radiation. An important characteristic of the effect is the Bragg angle [2]. When an acoustic wave is launched into the optical medium, it generates a refractive index wave that behaves like a sinusoidal grating. An incident laser beam passing through this granting will diffract the laser beam into several orders. With appropriate design, the first order beam has the highest efficiency. Its angular position is linearly proportional to the acoustic frequency, so that the higher the frequency, the larger the diffracted angle [1].

Currently, an acousto-optics method of light beams regulation find wide applications in many areas of science and technology. The interest in the diffraction of light by ultrasonic waves may be explained by the advantages of acousto-optics in regulation of non-coherent optical beams as well as of rays generated by lasers. In modern optics, medical diagnostics technologies [3], optical engineering, and laser technology, the acousto-optics methods have been successfully applied for the control of the amplitude, frequency, phase, and polarization of coherent optical signals. The diffraction of optic beams by acoustic waves has also been used for the regulation of direction of light propagation. Due to high reliability, quick action, efficiency of operation, and simplicity of design, the acousto-optics instruments can be recommended for use in modern systems of intelligent optics and in novel generations of devices providing processing of optical information in real time [4].

---

[1] *Mustansiriyah University, Collage of Science, Physics Department, Baghdad, Iraq.*
**Corresponding author: E-mail: elham.jasim@uomustansiriyah.edu.iq*

In general, good operation parameters of the acousto-optics cells have made it possible to use them as spatial frequency filters in optical information processing systems. Such filters possess a number of advantages in comparison with processing instruments of other types. For example, acousto-optics filters are not critical in terms of the place of their installation in an optical system. Moreover, they can be electronically tuned in real time by direct modulation of the amplitude and frequency of acoustic waves resulting in the desired quick and reliable processing of optical beams.

However, a number of acute problems exist in the field of electronic control of optical signals that are not yet solved by modern science and technology. One of the problems is the necessity to find a simple way to quickly and efficiently regulate parameters of non-collimated optical rays and optical beams forming images in coherent light [4].

2. ACOUSTO-OPTICS EFFECT

Acousto-optic effect, also known in the scientific literature as acousto-optic interaction or diffraction of light by acoustic waves, was first predicted by *Brillouin* in 1921 and experimentally revealed by Lucas, Biquard and Debye, Sears in 1932 [5].

The acousto-optics effect is a specific case of photo elasticity, where there is a change of a material's permittivity, ε, due to a mechanical strain$\mathrm{a}$. Photoelasticity is the variation of the optical indicatrix coefficients B_i caused by the strain a_j given by [6]:

$$\Delta B_i = p_{ij} a_j \tag{1}$$

Where p_{ij} is the photoelastic tensor with components, $\mathrm{i}, \mathrm{j} = 1,2, \ldots .6$ specifically in the acousto-optics effect, the strains a_j is a result of the acoustic wave which has been excited within a transparent medium. This then gives rise to the variation of the refractive index. For a plane acoustic wave propagating along the *z* axis, the change in the refractive index can be expressed as [6]:

$$n(z,t) = n + \Delta n \, cos(\omega t - kz) \tag{2}$$

where, *n* is the undisturbed refractive index, ω is the angular frequency, k is the wave number, and Δn is the amplitude of variation in the refractive index generated by the acoustic wave, and is given as [6]:

$$\Delta n = -\frac{1}{2} n^3 p_{ij} a_j \tag{3}$$

The generated refractive index, gives a diffraction grating moving with the velocity given by the speed of the sound wave in the medium. Light which then passes through the transparent material, is diffracted due to this generated refraction index, forming a prominent diffraction pattern. This diffraction pattern corresponds with a conventional diffraction grating at angles $\emptyset_m$ from the original direction, and is given by [6]:

$$\Lambda \, sin(\emptyset_m) = m\lambda \tag{4}$$

Where, λ is the wavelength of the optical wave, Λ is the wavelength of the acoustic wave and m is the integer order maximum. Light diffracted by an acoustic wave of a single frequency produces two distinct diffraction types. These are Raman-Nath diffraction and Bragg diffraction [6].

Raman-Nath diffraction is observed with relatively low acoustic frequencies, typically less than 10 MHz, and with a small acousto-optics interaction length, ℓ, which is typically less than 1cm. This type of diffraction occurs at an arbitrary angle of incidence, $\emptyset_{inc}$.

In contrast, Bragg diffraction occurs at higher acoustic frequencies, usually exceeding 100 MHz. The observed diffraction pattern generally consists of two diffraction maxima; these are the zeroth and the first orders. However, even these two maxima only appear at definite incidence angles close to the

Bragg angle, $\emptyset_B$. The first order maximum or the Bragg maximum is formed due to a selective reflection of the light from the wave fronts of ultrasonic wave. The Bragg angle is given by the expression [6]:

$$sin\emptyset_B = -\frac{\lambda f}{2n_i v}\left[1 + \frac{v^2}{\lambda^2 f^2}(n_i^2 - n_d^2)\right] \tag{5}$$

where λ is the wavelength of the incident light wave (in a vacuum), f is the acoustic frequency, v is the velocity of the acoustic wave, n_i is the refractive index for the incident optical wave, and n_d is the refractive index for the diffracted optical waves.

In general, there is no point at which Bragg diffraction takes over from Raman-Nath diffraction. It is simply a fact that as the acoustic frequency increases, the number of observed maxima is gradually reduced due to the angular selectivity of the acousto-optics interaction.

Traditionally, the type of diffraction, Bragg or Raman-Nath, is determined by the conditions Q >> 1 and Q << 1 respectively, where Q is given by [7]:

$$Q = \frac{2\pi\lambda\ell f^2}{nv^2} = \frac{2\pi\lambda_0 L}{n\Lambda^2} \tag{6}$$

Which Q is known as the Klein-Cook parameter, where λ_0 is the wavelength of the laser beam, n is the refractive index of the crystal, L is the distance the laser beam travels through the acoustic wave and Λ is the acoustic wavelength [8].

Q<<1, this is the Raman-Nath regime (Fig. 1 (a)). The laser beam is incident roughly normal to the acoustic beam and there are several diffraction orders (... -2 -1 0 1 2 3 ...) with intensities given by Bessel functions [8].

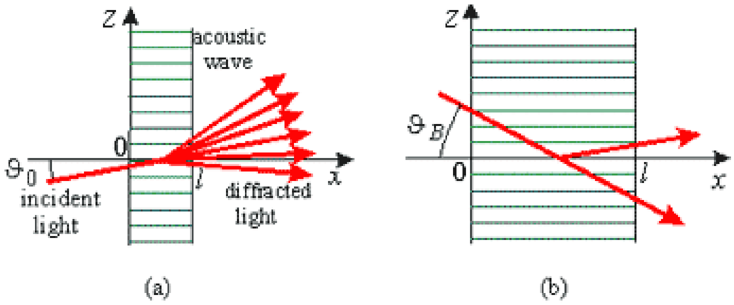

Fig. 1. Diffraction of Raman-Nth (a) and Bragg (b) [8]

Q>>1, this is the Bragg regime (Fig. 1 (b)). At one particular incidence angle, only one diffraction order is produced the others are annihilated by destructive interference.

In the intermediate situation, an analytical treatment isn't possible and a numerical analysis would need to be performed by computer. Most acousto-optics devices operate in the Bragg regime, the common exception being acousto-optics mode lockers and Q-switches [8].

Since, in general, only the first order diffraction maximum is used in acousto-optics devices, Bragg diffraction is preferable due to the lower optical losses. However, the acousto-optics requirements for Bragg diffraction limit the frequency range of acousto-optics interaction. As a consequence, the speed of operation of acousto-optics devices is also limited [1].

2.1 Acousto-Optics Filters

There are two types of the acousto-optics filters, collinear and non-collinear filters depending on geometry of acousto-optics interaction. Here we consider only non-collinear filters based on the TeO_2

single crystal [9]. The polarization of the incident light can be either ordinary or extraordinary. For the definition, we assume ordinary polarization. By tuning the frequency of the acoustic wave, the desired wavelength of the optical wave can be diffracted acousto-optically. Input light need not be polarized for a non-collinear design. Un-polarized input light is scattered into orthogonally polarized beams separated by the scattering angle for the particular design and wavelength. If the optical design provides an appropriate beam block for the un scattered light, then two beams (images) are formed in an optical pass-band that is nearly equivalent in both orthogonally linearly polarized output beams (differing by the Stokes and Anti-Stokes scattering parameter) [1].

2.2 Brief Description

The refractive index of an optical medium is altered by the presence of sound. Sound therefore modifies the effect of the medium on light; i.e., sound can control light (Fig. 2). Many useful devices make use of this acousto-optics effect; these include optical modulators, switches, deflectors, filters, isolators, frequency shifters, and spectrum analyzers. Sound is a dynamic strain involving molecular vibrations that take the form of waves which travel at a velocity characteristic of the medium (the velocity of sound) [10].

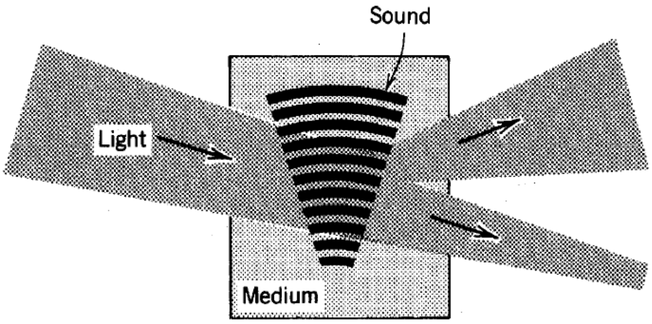

Fig. 2. Sound modifies the effect of an optical medium on light [11]

As example, a harmonic plane wave of compressions and rarefactions in a gas is pictured in Fig. 3.

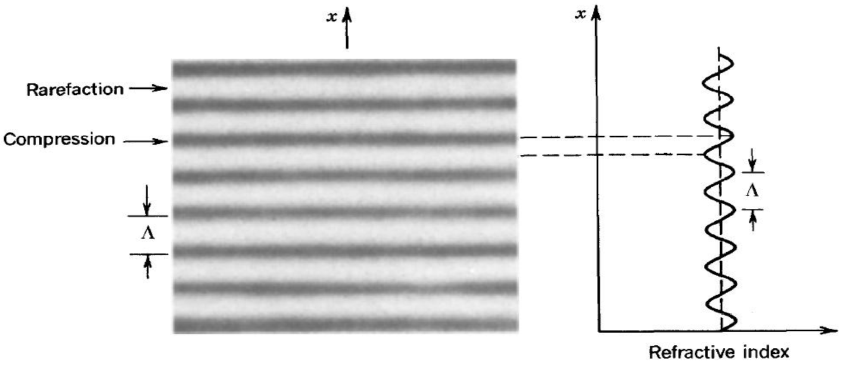

Fig. 3. Variation of refractive index accompanying a harmonic sound wave. The pattern has a period A, the wavelength of sound, and travels with the velocity of sound [10]

In those regions where the medium is compressed, the density is higher and the refractive index is larger; where the medium is rarefied, its density and refractive index are smaller. In solids, sound involves vibrations of the molecules about their equilibrium positions, which alter the optical polarize ability and consequently the refractive index.

An acoustic wave creates a perturbation of the refractive index in the form of a wave. The medium becomes a dynamic graded-index medium an inhomogeneous medium with a time-varying stratified refractive index. The theory of acousto-optics deals with the perturbation of the refractive index caused by sound, and with the propagation of light through this perturbed time-varying inhomogeneous medium [10].

Since optical frequencies are much greater than acoustic frequencies, the variations of the refractive index in a medium perturbed by sound are usually very slow in comparison with an optical period. There are therefore two significantly different time scales for light and sound. As a consequence, it is possible to use an adiabatic approach in which the optical propagation problem is solved separately at every instant of time during the relatively slow course of the acoustic cycle, always treating the material as if it were a static (frozen) inhomogeneous medium. In this quasi-stationary approximation, acousto-optics becomes the optics of an inhomogeneous medium (usually periodic) that is controlled by sound [10].

The simplest form of interaction of light and sound is the partial reflection of an optical plane wave from the stratified parallel planes representing the refractive-index variations created by an acoustic plane wave (Fig. 4) [10].

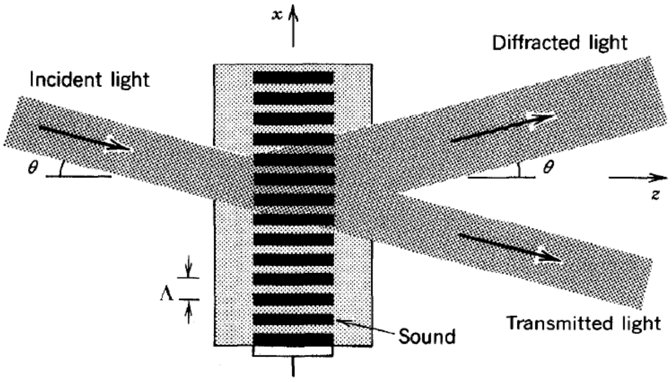

Fig. 4. Bragg diffraction: an acoustic plane wave acts as a partial reflector of light (a beam splitter) when the angle of incidence 0 satisfies the Bragg condition [10]

A set of parallel reflectors separated by the wavelength of sound Λ will reflect light if the angle of incidence θ satisfies the Bragg condition for constructive interference [9]: $sin\theta = \frac{\lambda}{2\Lambda}$, where λ is the wavelength of light in the medium [11]. This form of light-sound interaction is known as Bragg diffraction, Bragg reflection, or Bragg scattering. The device that effects it is known as a Bragg reflector, a Bragg deflector, or a Bragg cell [10].

The principle of operation of the filters is based on the dependence of the diffracted light wavelength on the acoustic frequency. Conventional applications using acousto-optics interactions have been extensively confined to signal. The best way to understand image processing using acousto-optics is through the use of spatial transfer function, which describes acousto-optics interaction between the sound and the incident optical image decomposed in terms of the angular plane wave spectrum of the light field.

We now define ξ which is the normalized distance inside the acousto-optics cell, and $\xi = 1$ signifies the exit plane of the cell [12]. We define one more important variable called the Q parameter or the Klien-Cook parameter in acousto-optics. ϕ_B Bragg angle and δ represent the deviation of the incident plane wave away from the Bragg angle. By limiting case to two diffracted orders and the case of zeroth-order light, we decompose the incident field into plane waves with different amplitudes propagating in direction defined by: $\emptyset' = \delta \times \emptyset_B$.

Raman-Nath diffraction given as:

$$\frac{d\psi_m}{d\xi} = -j\frac{\alpha}{2}e^{-j\frac{1}{2}Q\xi\left[\frac{\phi_{inc}}{\phi_B}+(2m-1)\right]}\psi_{m-1} - j\frac{\alpha}{2}e^{j\frac{1}{2}Q\xi\left[\frac{\phi_{inc}}{\phi_B}+(2m-1)\right]}\psi_{m+1} \tag{7}$$

And the Raman-Nath solution is:

$$\psi_m = (-j)^m\psi_{inc}J_m(\alpha\xi) \tag{8}$$

The plane wave amplitude of the zeroth-order light when a plane wave ψ_{inc} is incident at ψ' away from the nominally Bragg angle of incidence is given in below equation:

$$\psi_0(\xi) = \psi_{inc}e^{-j\delta Q\xi/4}\left\{cos[\left(\frac{\delta Q}{4}\right)^2 + \left(\frac{\alpha}{2}\right)^2]^{\frac{1}{2}}\xi + j\frac{\delta Q}{4}\frac{sin[\left(\frac{\delta Q}{4}\right)^2+(\alpha/2)^2]^{1/2}\xi}{[\left(\frac{\delta Q}{4}\right)^2+(\alpha/2)^2]^{1/2}}\right\} \tag{9}$$

Where α is the peak phase delay, hence we can define the so-called transfer function of the zeroth-order light as follows:

$$H_0(\delta) = \frac{\psi_0(\xi)|_{\xi=1}}{\psi_{inc}} \tag{10}$$

Where $\psi_0(\xi)|_{\xi=1}$ is the result from equation (10) evaluated at the exit of the Bragg cell. This definition of the transfer function permits us to relate the input (incident) spectrum, $\Psi_{inc}(k_{x'})$, to the output (zeroth-order) spectrum, $\Psi_0(k_{x'})$, as [12]:

$$\Psi_{inc}(k_{x'}) = \Psi_{inc}(k_{x'})H_0(\delta) \tag{11}$$

Where $\Psi_{inc}(x')$ and $\Psi_0(x')$ are the field distribution of the incident light and that of the zeroth-order light, respectively and $k_{x'}$ representing the transform variables. Finally, the concept of spatial filtering becomes clear when we relate the spatial frequency $k_{x'}$ along x' to ϕ' by [12]:

$$\Psi_0(k_{x'}) = \Psi_{inc}(k_{n'})H_0(k_{x'}\Lambda/\pi) \tag{12}$$

As $\phi' = \delta \times \emptyset_B$ and $\emptyset_B = \lambda_0/2\Lambda$ eq. (13) can now be written in terms of spatial frequency if we use the above derived relationship such that: $\delta = k_{x'}\Lambda/\pi$.

$$k_{x'} = k_0\,sin(\phi') \approx k_0\emptyset' = k_0\delta\emptyset_B = \pi\delta/\Lambda \tag{13}$$

The spatial distribution $\psi_0(x')$ is then given by:

$$\psi_0(x') = \frac{1}{2\pi}\int_{-\infty}^{\infty}\Psi_{inc}(k_{x'})H_0(k_{x'}\Lambda/\pi)exp(-jk_{x'}x')dk_{x'} \tag{14}$$

Equation (14) determines the profile of the scattered zeroth-order field, $\psi_0(x')$, from any arbitrary incident field, $\psi_{inc}(x')$, in the presence of the acoustic field. Using equation (12) and equation (14), the amplitude of the zeroth-order diffracted light written in a full 2D version, $\psi_0(x')$, at the exit of the Bragg cell, can be approximately written as [13]:

$$\psi_0(x,y) = \left(A - B\frac{\partial}{\partial x}\right)\psi_{inc}(x,y) \tag{15}$$

3. RESULTS AND DISCUSSION

We proceed with the acousto-optics spatial filter. In this paper results, we used the transfer function formalism to demonstrate some numerical results obtained by MATLAB where, after we calculate the diffracted intensities involving deferent diffracted orders in up shifted Bragg interaction, we have created a MATLAB function for deferent coupled differential equations, and then used equation (7) to investigate Raman-Nath diffraction and equation (8) to investigate Raman-Nath solution. Explain the phenomenon of high-pass filtering or edge enhancement in the zeroth-order diffracted light theoretically from the transfer function directly from equation (9) and then the zeroth-order beam has been spatially filtered by the transfer function. In the first, corresponding to near-Bragg diffraction. We used equation (7) to investigate Raman-Nath diffraction. Fig. 5 shows the dependence of various scattered orders on the incident angle/Bragg angle illustrating the Bessel function dependence. Fig. 6 illustrates non-ideal Raman-Nath diffraction for normal incidence.

Note that, the true zeros, which are the characteristic of the Bessel functions for the ideal case, disappear for large value of incident angle/Bragg angle. When the interaction length *L* (distance the laser beam travels through the acoustic wave) is short enough so that the accumulated of phase mismatch is small. This is called the Raman-Nath or Debey-Sears region and is characterized by the simultaneous existence of many scattered orders. For a special condition on the angle of incidence and the angle of diffraction into the ± 1 orders, namely $\emptyset_{\pm 1} = -\emptyset_0$, there is a phase synchronism between the 0 and -1 orders, and between the 0 and $+1$ orders. When $\emptyset_{\pm 1} = -\emptyset_0$, this means that the zeroth order and the diffracted order propagate symmetrically with respect to the sound wave fronts. The angle of incidence of the zeroth order in this case is according $\emptyset_{\pm 1} = -\emptyset_0$.

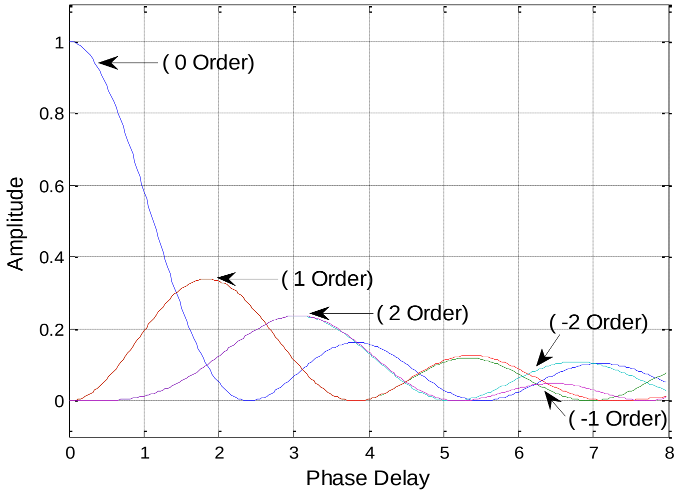

Fig. 5. Amplitude of diffracted orders in the ideal Raman-Nath regime. The (-1 order) and (1 orders) are overlapped. Also, the (-2 order) and (2 orders) are overlapped. Raman-Nath diffraction

The amplitude of the various diffracted orders, therefore, show the same functional dependence as the corresponding orders of the Bassel functions on the phase delay. This behavior is depicted in Fig. 5 and Fig. 6 for the first three lowest orders.

In Bragg region, the interaction length is long enough so that the accumulated phase mismatch for all diffracted orders other than the ± 1 render their intensiies negligible. The only constructive interference can occur for the +1 or the -1 orders. The criterion for this region is just the opposite of that defining the Raman-Nath region. As we discussed before, it is of great interest for practical applications of acoustc-optics interaction theory to consider small deviations from the phase synchronism condition characterizing this bragg region. Such casess can be due to either in the sound frequency or due to changes in the angle of incidence in such a way that it no longer satisfies the Bragg condition. Finally, in the near Bragg region we consider the transition region is difficult to treat analytically and, consequently, the condition for operation in the Bragg regime is rather vague. It is often possible, however, to define the Bragg region more accurately by specifying the maximum percentage of light diffracted into the first order in interaction of the kind carried out by Klein an Cook.

They performed numerical calculations of the amount of light diffracted as a function of the parameter Q, so that for the ideal Bragg case, all the light would have been diffracted. Figs 7, 8 and 9 shows the incident, the zeroth-order beams and the pure differentiation results respectively. Fig 7 shows its magnitude of zeroth-order transfer function as a function of spatial frequency.

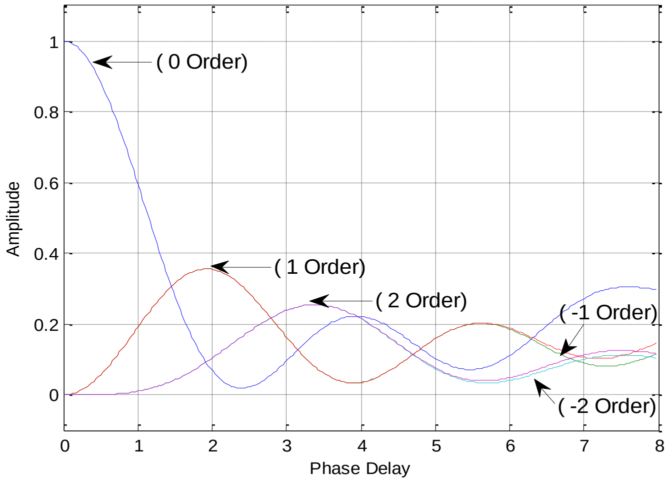

Fig. 6. Amplitude of diffracted orders in non-ideal Raman-Nath regime, the (-1 order) and (1 orders) are overlapped. Also, the (-2 order) and (2 orders) are overlapped. Non-ideal Raman-Nath diffraction for normal incidence

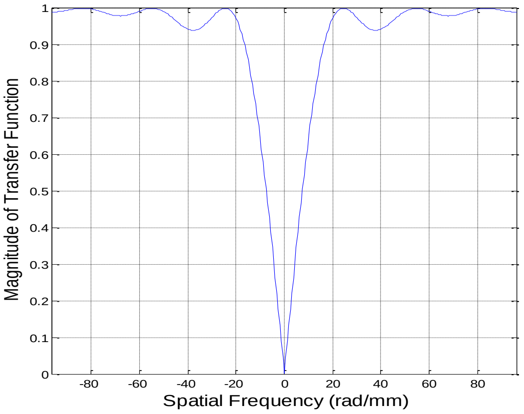

Fig. 7. The incident beams, magnitude of zeroth-order transfer function (length of square= 1mm)

Fig. 8 shows the profile of incident beam and the output zeroth-order beam profile and Fig. 9 shows that the left edge of the square has been emphasized. Both edges of the square image have been extracted equally along the x-direction. Selective edge extraction, that is, either only the left edge of the image or the right edge of the image, can be performed when we change the sound pressure through incidence angle.

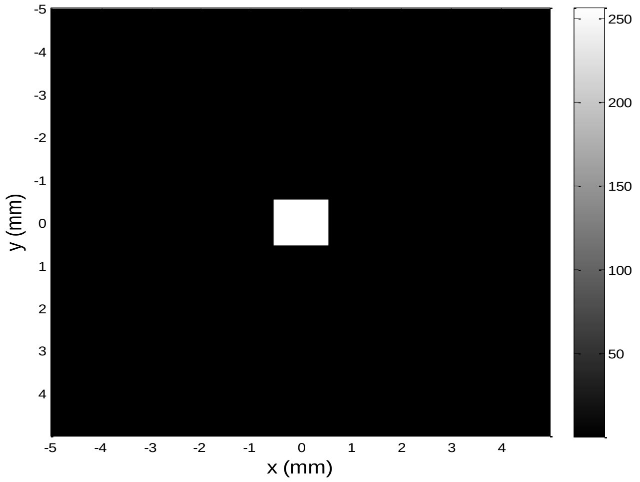

Fig. 8. The zeroth-order beams, profile of incident beam (length of square= 1mm)

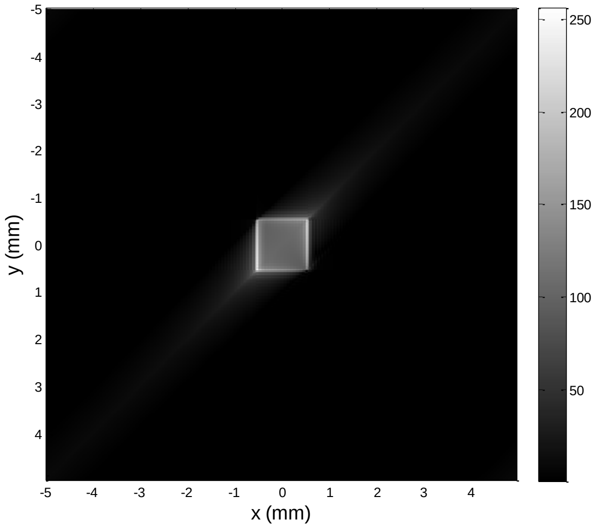

Fig. 9. The pure differentiation beams, profile of zeroth-order output beam (length of square= 1mm)

4. CONCLUSIONS

This paper is, in general, devoted to the theoretical study of the acousto-optics selection of optical spatial frequencies. The Bragg diffraction occurs at higher acoustic frequencies and the observed diffraction pattern generally consists of two diffraction maxima; these are the zeroth and the first orders, these two maxima only appear at definite incidence angles close to the Bragg angle. The first order maximum or the Bragg maximum is formed due to a selective reflection of the light from the wave. An optical filter is completely described by its frequency response, which is information on how the amplitude and phase is acted for each frequency component. This is most often given in the form of a complex valued transfer function. The standard weak interaction theory describes diffraction in the Bragg regime as the propagation of a uniform plane wave of light through a uniform plane wave of sound, resulting in the well-known first- and zeroth-order diffraction.

COMPETING INTERESTS

Author has declared that no competing interests exist.

REFERENCES

1. Joseph N. New Studies of Acousto_Optic Interaction, Arthur Lakes Library, colorado School of Mines, Golden, Colorado. 1998;80401:T3669 8.
2. Vladimir B, Maxim K, Sergey M, Vladimir M. Acousto-Optic Cells with Phased-Array Transducers and Their Application in Systems of Optical Information Processing, Materials 2021;14:451.
   Available: https://doi.org/10.3390/ma14020451, 2021.
3. Zaichenko KV, Gurevich BS. Application of acousto-optic tunable filters inthe devices of skin cancer diagnostics," Proc. SPIE 11585, Biophotonics—Riga. 2020;115850K
   DOI: 10.1117/12.2581750.
4. Voloshinov, Vitaly B. Two-dimensional selection of optical spatial frequencies by acousto-optic methods", Optical Engineering; 2002.
5. Balakshy VI. Acousto-optics cell as a filter of spatial frequencies, J. Commun. Techn. & Electronics. 1984;29:1610-1616.
6. en.wikipedia.org.
7. Bahaa EA, Malvin CT. Fundamentals of Photonics", Book, Chapter 20 Acousto-Optics, ISBNs: 0-471-83965-5 (Hardback); 0-471-2-1374-8 (Electronic), John Wiley & Sons, Inc; 1991.
8. Xia P, et al. Characterization of vascular endothelial growth factor's effect on the activation of protein kinase C, its isoforms, and endothelial cell growth. J Clin Invest. 1996;98(9):2018-2026.
9. acoustooptics.phys.msu.su.
10. Saleh. Acousto-Optics", Wiley Series in Pure and Applied Optics; 1991.
11. ShaoQun Z, "Femtosecond pulse laser scanning using Acousto Optic Deflector", Science in China Series G Physics Mechanics and Astronomy; 2009.
12. Bogumil BJ, Partha PB, Anna S. Acousto-Optics and Applications IV; 2001.
13. Acousto-Optics. Encyclopedia of Physical Science and Technology; 2004.

Biography of author(s)

Dr. Elham Jasim Mohammad, Assistant Professor
Mustansiriyah University, Collage of Science, Physics Department, Baghdad, Iraq.

She was born in Iraq and obtained a Ph.D. degree in Optoelectronic Sciences from the Physics Department, College of Science, Mustansiriyah University, her M.S. degree in Image Process, Physics Science from the Department of Physics/ College of Science/ Mustansiriyah University and she received B.S. degree in Physical Science from the Department of Physics/ College of Science, Mustansiriyah University. Currently, she works as an Assistant Professor in the Department of Physics/ College of Science, Mustansiriyah University, Baghdad, Iraq.

© Copyright (2021): Author(s). The licensee is the publisher (B P International).

DISCLAIMER
This chapter is an extended version of the article published by the same author(s) in the following conference proceeding.
IOP Conf. Series: Materials Science and Engineering, 454,012134,2018.

Print ISBN: 978-93-91312-26-8, eBook ISBN: 978-93-91312-34-3

Recovery Heat Flux at Superfluid Helium Film Boiling on the Cylindrical Heaters in Different Conditions

Yu Yu Puzina[1*] and A. P. Kryukov[1]

DOI: 10.9734/bpi/nupsr/v9/9939D

ABSTRACT

The set of two equations for determination of the recovery heat flux density is presented. Pressure distribution in the liquid determined by the hydrostatic difference, Laplace pressure jump on the vapor-liquid interface, the non-equilibrium effects in the vapor film is taken into account in one of them. The correct correlation for the normal component of momentum flux density tensor obtained on the base of two-fluid model was used at deriving this equation. Second equation describes heat transfer in helium II by the Gorter-Mellink semi-empirical theory. Various simplifications and special cases are analyzed. Experimental data on the boiling of superfluid helium under various conditions are interpreted on the base formulated mathematical model. Good enough agreement between the calculated and experimental results takes place.

Keywords: Superfluid helium; boiling; recovery heat flux; two-fluid model; heat and mass transfer.

1. INTRODUCTION

Superconductor magnet is usually cooled by normal liquid helium (He I), however higher cryostability could be obtained in superfluid helium (He II). Superconductor cooled by He II shows a larger critical current and recovery current than those in He I. Furthermore, pressurized superfluid helium has better cooling properties than saturated one has.

Superfluid helium is successfully used as a magnets coolant of modern particle accelerators, reactors of controlled thermonuclear synthesis and cooling of space telescopes. Two reasons determine the use of this working fluid as a coolant for superconducting devices: low operating temperature, which increases the reliability of such systems, and improved heat exchange indicators. Helium II spontaneously penetrates into various cavities of the magnet windings, while its large specific heat capacity and high heat transfer efficiency in the liquid can provide powerful stabilization from thermal interference.

The thermal stability of superconducting wires depends strongly upon the heat transfer to the coolant. In fact, pressure is an important factor on the heat transfer to superfluid helium. The direct experimental data about peak and recovery heat fluxes and vapor film behavior can give important information about critical parameters for high field system emergency mode. Superconducting engineering still relies heavily on liquid helium heat transfer efficiency model of calculations.

Based on the two-fluid hydrodynamics, an analog of the famous Rayleigh-Plesset equation for the dynamics of a spherical vapor bubble in superfluid helium is derived in [1]. Due to two-fluid nature of He-II and the specific form of the momentum flux density tensor some new effects in the evolution of the interface boundary position, absent in ordinary fluids, appear. The application of two-fluid

---

[1] *Department of Low Temperature National Research University, Moscow Power Engineering Institute, 14 Krasno kazarmennaya, Moscow, 111250 Russia.*
**Corresponding author: E-mail: Puzina2006@inbox.ru*

approach to describe heat and mass transfer processes [1] gave the authors an idea to use it for model [2] further development.

For the classical liquid new experimental results on the influence of the size of the heater and the heating rate on the minimum critical heat flux were presented in [3]. The experiments and numerical simulations demonstrate how the minimum critical heat flux is computed for a given case. In addition, it was demonstrated that the minimum critical heat flux does not depend on the size of the heater at atmospheric pressure when the size of the heater is larger than 1 mm. The derived theoretical approach finds applications in the design of the systems based on high-temperature superconductors.

Some useful considerations for the superfluid helium were found in [4]. The research aim was to establish a theoretical framework for the analysis of the transient behaviour of vapour bubbles resulting from superfluid helium boiling under the conditions of microgravity. As long as the volume of a bubble is small in comparison with the volume of a container, the dynamics of the surrounding liquid and interface momentum transfer seem to be the dominant factors determining the pace of bubble growth.

The experimental data about recovery heat flux was received in [5] and presented in [6] also among others. The corresponding model is developed in the following part. Experimental studies of the He-II boiling on the surfaces of the cylindrical heaters in a bulk of He-II and under constrained conditions were also conducted [7]. Visualization of helium-II film boiling was first performed when observed from the end of a cylindrical heater. These experiments show that the noiseless film boiling is observed in a free volume and in the constrained conditions.

Thermal measurement and visualization study results were compared for the case of the narrow parallel channel in He II [8]. Even in the narrow channel, the several film boiling modes exist same as in open bath. In the narrow channel, the unstable film boiling mode region of the weakly subcooled and the noisy film boiling was smaller than that in open bath. The unique boiling state in the narrow parallel channel is the quasi-nucleation boiling state. According to the visualization results, the vapor repeats generation and collapse intermittently appears around the lambda pressure.

Noisy film boiling was found to occur in a small rectangular duct with periodic oscillation of temperature and sound generation [9]. The periodic oscillation strongly depends on the helium pressure and the heat flux. It becomes smaller with higher heat power and larger with higher pressure. Experiments of superfluid helium flow in a channel with a monodisperse backfill were carried out [10] and show the oscillation of interface surface and liquid column at different parameters also.

Consequently at the all investigations and practical use the recovery heat flux is the minimum heat flux for the existence of vapor film and it is an upper bound for stable cryostabilization. At this the aim of this study is to develop of traditional approach for calculation of the recovery heat flux with taken into account heat mass transfer peculiarities in superfluid helium. This development can be useful for the next describing of the vapor-liquid dynamics.

2. BOILING IN LARGE VOLUME

The following problem statement of the superfluid helium film boiling in a large volume is considered (Fig. 1). The boiling is silent. Cylindrical heater of radius R_w is immersed in the superfluid helium at the depth h. A smooth vapour film is formed that is coaxial to the heater. The recovery process takes place when the vapor film collapses into the liquid at the heat flux $q_w = q_R$. Above the free surface of the liquid constant pressure P_b is maintained so the liquid is in equilibrium with the vapor $P_b = P_S(T_b)$.

The base approach is presented in paper [2]. Here is the development of this approach with surface tension and boundary conditions on the vapor-liquid interface based on two-fluid model.

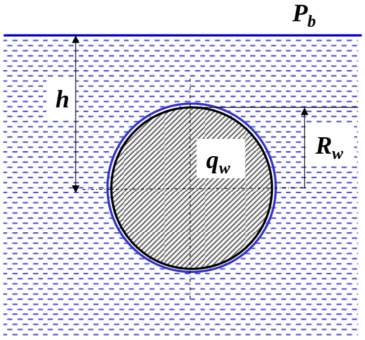

Fig. 1. Schematic diagram of the problem

2.1 Boundary Conditions

The interface surface in continuum mechanics is considered as geometry object with zero thickness, which separate two phase with significantly different properties. In the common case interface is permeable for the muss, momentum and energy flux. For the control volume around point on the interface (Fig. 2) we can write a system of conservation equations [11]. For simplicity, we assume that the mass flux is zero. The phases are viscous and heat-conducting. Denote the normal to the interface as *x*, then

$$\Pi_{xx}'' - \Pi_{xx}' = 2\sigma H \,, \tag{1}$$

where Π_{xx} is the normal component of the momentum flux density tensor, σ is the surface tension, and *H* is the average curvature of the surface.

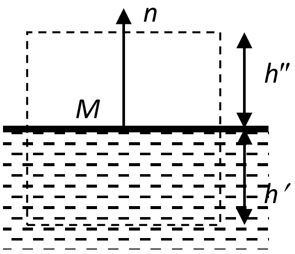

Fig. 2. Control volume in the vicinity of a point on the interface

The rate of surface pulse occurrence in the absence of a tangential tension gradient along the surface

$$\Pi_{xy}'' - \Pi_{xy}' = 0 \,, \tag{2}$$

where Π_{xy} is the tangent component of the momentum flux density tensor.

For a classical fluid, the expanded form of writing the momentum flux density tensor is as follows:

$$\Pi_{xx} = \rho\tilde{u}_x\tilde{u}_x + p - \tau_{xx} \,, \tag{3}$$

$$\Pi_{xy} = \rho\tilde{u}_x\tilde{u}_y - \tau_{xy} \,, \tag{4}$$

where u_x is the velocity of the medium normal to the surface, u_y - velocity of the medium in the direction tangent to the surface, p is the pressure, τ - tensor of viscous stresses, sign tilde indicates the definition of velocity in its own reference frame.

If we take the no-slip condition at the interface, that is

$$\tilde{u}_y{}'' - \tilde{u}_y{}' = 0\,, \tag{5}$$

$$\tau_{xy}{}'' - \tau_{xy}{}' = 0\,, \tag{6}$$

Then neglecting the mass flux on the interface it turns out

$$\left(p'' - p'\right) - \left(\tau_{xx}{}'' - \tau_{xx}{}'\right) = 2\sigma H\,. \tag{7}$$

Newton's generalized law of viscous friction

$$\tau_{kl} = \mu\left(\frac{\partial u_k}{\partial x_l} + \frac{\partial u_l}{\partial x_k} - \frac{2}{3}\frac{\partial u_m}{\partial x_m}\delta_{kl}\right), \tag{8}$$

Where μ is the dynamic viscosity, allows us to determine the normal component of the viscous stress tensor for an incompressible fluid as

$$\tau_{xx} = 2\mu\frac{\partial u_x}{\partial x}\,. \tag{9}$$

Thus, we can write the compatibility condition for the *x*-normal to the surface

$$\left(P'' - P'\right) - \left(\frac{4}{3}\mu''\frac{\partial \tilde{u}_x{}''}{\partial x} - 2\mu'\frac{\partial \tilde{u}_x{}'}{\partial x}\right) = 2\sigma H\,. \tag{10}$$

However, for superfluid helium, the momentum flux density tensor according the two-fluid hydrodynamics [12] is written as follows:

$$\prod\nolimits_{ik} = \rho_n \tilde{u}_{ni}\tilde{u}_{nk} + \rho_s \tilde{u}_{si}\tilde{u}_{sk} + p\delta_{ik}\,, \tag{11}$$

where u_n is the velocity of the normal component, u_s is the velocity of the superfluid component, ρ_n is the density of the normal component, ρ_s is the density of the superfluid component, δ_{ik} is the Kronecker symbol.

At the phase interface, the mass flow is equal to zero:

$$j_x = \rho_n \tilde{u}_{nx} + \rho_s \tilde{u}_{sx} = 0\,, \tag{12}$$

Then the normal component of the viscous stress tensor corresponds to the velocity of the normal component u_n:

$$\tau_{xx} = 2\mu'\frac{\partial u_{nx}}{\partial x}\,. \tag{13}$$

Normal component of momentum flux density tensor

$$\Pi_{xx} = \rho_n \left[1 + \frac{\rho_n}{\rho_s}\right] \tilde{u}_{nx}{}^2 + P' - 2\mu' \frac{\partial \tilde{u}_{nx}}{\partial x}. \tag{14}$$

Compatibility condition for the normal momentum flux density tensor:

$$\left(P'' - P'\right) - \left(\frac{4}{3}\mu'' \frac{\partial u_x{}''}{\partial x} - 2\mu' \frac{\partial u_{nx}}{\partial x}\right) - \rho_n \left[1 + \frac{\rho_n}{\rho_s}\right] u_{nx}{}^2 = 2\sigma H. \tag{15}$$

Tangent tensor of the momentum flux density

$$\Pi_{xy} = \rho_n \left(1 + \frac{\rho_n}{\rho_s}\right) \tilde{u}_{nx} \tilde{u}_{ny} - \mu' \left(\frac{\partial u_{nx}}{\partial y} + \frac{\partial u_{ny}}{\partial x}\right). \tag{16}$$

The non-slip conditions are formulated for the normal component:

$$u_y{}'' - u_{ny} = 0, \tag{17}$$

$$\mu'' \left(\frac{\partial u_x}{\partial y} + \frac{\partial u_y}{\partial x}\right) - \mu' \left(\frac{\partial u_{nx}}{\partial y} + \frac{\partial u_{ny}}{\partial x}\right) = 0. \tag{18}$$

Thus, in conjugate problems with the He-II – vapour interface, new type of boundary conditions should be exploited to close the system of conservation equations. For the steady interface it is equations (15) and (16).

3. EQUATIONS AND SIMPLIFICATIONS

The application of the model [2], describing the method of calculating the recovery heat flux for superfluid helium boiling, to the considered problem, allows us to obtain a system of equations. The peculiarity of present paper is taking into account capillary force on the vapour-liquid interface and boundary conditions on the interface.

The pressure in the fluid P' is determined by the hydrostatic difference:

$$P' = P_b + \rho' g h. \tag{19}$$

Where ρ' – liquid density, g – gravity acceleration.

The vapor pressure P'' in the film is determined by the non-equilibrium boundary condition obtained by solving of the kinetic Boltzmann equation for evaporation-condensation problems [13]. The relationship between the actual vapor pressure near the phase interface P'', the pressure $P_s(T_1)$ corresponding to saturation lines of the vapour-liquid interface temperature T_1 and the heat flux density on it q_R is the following:

$$P'' = P_S(T_1) + \frac{0.44 q_R}{\sqrt{2 R_h T_1}}. \tag{20}$$

Where R_h – individual gas constant for helium.

The correlation (20) was received for absence of mass flux density on the vapor-liquid interface. The conditions which satisfy (20) must be the minimum heat flux at which film boiling can occur, a value equal to the recovery heat flux density.

We use (15) to write the boundary condition on the interfacial surface at the velocity of the phase boundary equal to zero. In addition vapor film is steady, therefore vapor velocity is equal zero, and the term due to the viscosity forces in (15) disappears:

$$\left(P''-P'\right)+2\mu'\frac{\partial u_{nr}}{\partial r}-\rho_n\left[1+\frac{\rho_n}{\rho_s}\right]{u_{nr}}^2=\frac{\sigma}{R_w}. \tag{21}$$

In this case, the velocity of normal movement is determined from the ratio:

$$q=\rho' S T u_n. \tag{22}$$

where *S* is the entropy of the liquid. Heat transfer in a liquid is described on the basis of the Gorter-Mellink theory of mutual friction [14]:

$$\frac{dT}{dr}=-f_i(T)q^n. \tag{23}$$

where $f_i(T)$ is the empirical parameter of the Gorter – Mellink mutual friction in the temperature range $T_b \div T_1$. Usually, when calculating the exponent in equation (24), it is assumed to be $n = 3$ [2]. As noted in [15], the best agreement with the experiment is achieved at $n = 3.4$, but [16] states: "it has been shown experimentally that the exponent varies from about 3 to almost 4 when the temperature reaches the λ-point, i.e. T_λ".

Integration of (23) gives the following. Due to the law of energy conservation $q_R R_w = qr$, where *r* - the current radius in the liquid, *q* – heat flux density at this distance from the axis of the cylindrical coordinate system. This correlation is substituted to the (23):

$$\frac{dT}{dr}=-f_i(T)\frac{q^n {R_w}^n}{r^n}. \tag{24}$$

Then integrating (24)

$$\int_{T_1}^{T_b}\frac{dT}{f_i(T)}=-{q_R}^n{R_w}^n\int_{R_w}^{\infty}\frac{dr}{r^n}. \tag{25}$$

At this

$$\int_{T_1}^{T_b}\frac{dT}{f_i(T)}=-\int_{T_b}^{T_1}\frac{dT}{f_i(T)}=-\frac{T_1-T_b}{f(T)}, \tag{26}$$

where $f(T)=\dfrac{T_1-T_b}{\int_{T_b}^{T_i}\dfrac{dT}{f_i(T)}}$. As a result, we get

$$-\frac{T_1-T_b}{f(T)}=\frac{q_R{}^n R_w{}^n}{(n-1)r^{n-1}}\Bigg|_{R_w}^{\infty}=-\frac{q_R{}^n R_w{}^n}{(n-1)R_w{}^{n-1}}=-\frac{q_R{}^n R_w}{(n-1)}. \tag{27}$$

And the final is

$$T_1-T_b=f(T)\frac{q_R{}^n R_w}{(n-1)}. \tag{28}$$

Then expressing the velocity from equation (22), and temperature gradient from (23) we obtain the following for the liquid – vapor boundary:

$$\begin{aligned}\frac{\partial u_n}{\partial r}\bigg|_{r=R_w}&=\frac{\partial}{\partial r}\left(\frac{q}{\rho' ST}\right)\bigg|_{r=R_w}=\frac{1}{\rho' S}\frac{\partial}{\partial r}\left(\frac{q}{T}\right)\bigg|_{r=R_w}=\\&=\frac{1}{\rho' ST^2}\left(\frac{\partial q}{\partial r}T-\frac{\partial T}{\partial r}q\right)\bigg|_{r=R_w}=\frac{1}{\rho' ST^2}\left(T\frac{\partial}{\partial r}\frac{q_R R_w}{r}+f(T)q^{n+1}\right)\bigg|_{r=R_w}=\cdot\\&=\frac{1}{\rho' ST^2}\left(-Tq_R R_w\frac{1}{r^2}+f(T)q_R{}^{n+1}\right)\bigg|_{r=R_w}=\frac{q_R}{\rho' ST_1^2}\left(f(T)q_R{}^n-\frac{T_1}{R_w}\right)\end{aligned} \tag{29}$$

The difference between saturation pressers is transformed using the Clapeyron-Clausius equation and equation (28):

$$P_S(T_1)-P_b=P_S(T_1)-P_S(T_b)=\frac{L(T_1-T_b)}{T\left(\dfrac{1}{\rho''}-\dfrac{1}{\rho'}\right)}=\frac{L\rho''}{T_b}f(T)\frac{q_R{}^n R_w}{(n-1)}=\frac{f(T)}{(n-1)}q_R{}^n R_w\frac{L\cdot P_b}{R_h T_b{}^2}. \tag{30}$$

Where *L* is latent heat of evaporation for helium.

Then, the common equations are formulated. Vapor pressure *P″* from equation (20) and liquid pressure *P′* from equation (19), pressure difference $P_s(T_1)$–P_b from (30), velocity gradient from (29) are substituting to (21). The system of equations (19) – (30) is reduced to the following equation with respect to q_R:

$$\begin{aligned}&\frac{0.44q_R}{\sqrt{2R_hT_1}}+\frac{f(T)}{(n-1)}q_R{}^n R_w\frac{L\cdot P_b}{R_hT_b{}^2}+\frac{2\mu' q_R}{\rho' ST_1{}^2}\left(f(T)q_R{}^n-\frac{T_1}{R_w}\right)-\\&-\rho' gh-\rho_n\left[1+\frac{\rho_n}{\rho_s}\right]\left(\frac{q_R}{\rho' ST_1}\right)^2=\frac{\sigma}{R_w}\end{aligned}\;. \tag{31}$$

In this case, the temperature of the interfacial surface T_1 is determined from the ratio (28). So, the common solution is two equations (31) and (28) with two unknown variables q_R and T_1.

If we assume that the change in the temperature of the superfluid helium can be ignored ($T_1 \approx T_b$), as if $f(T)=0$ then equations (19)-(21) reduces to the following form:

$$\frac{0.44q_R}{\sqrt{2R_hT_b}}-2\mu'\frac{q_R}{\rho' ST_bR_w}-\rho' gh-\rho_n\left[1+\frac{\rho_n}{\rho_s}\right]\left(\frac{q_R}{\rho' ST_b}\right)^2=\frac{\sigma}{R_w}. \tag{32}$$

This equation is a quadratic equation with respect to the recovery heat flux density.

Earlier [17], solutions were obtained taking into account changes in the temperature of the liquid, but without peculiarities of boundary conditions on the interface He-II - vapor:

$$\frac{0.44q_R}{\sqrt{2R_h\left(T_b+\frac{f(T)}{(n-1)}q_R{}^nR_w\right)}}+\frac{f(T)}{(n-1)}q_R{}^nR_w\frac{r\cdot P_b}{R_hT_b{}^2}-\rho'gh=\frac{\sigma}{R_w} \tag{33}$$

and with the assumption of a constant temperature of the liquid

$$q_R=2.27\sqrt{2R_hT_b}\left(\rho'gh+\frac{\sigma}{R_w}\right). \tag{34}$$

We will consider below how various factors influence the value of the recovery heat flux density. In experimental works [5,6], systematic studies of the recovery heat flux on various samples of cylindrical geometry were carried out. Further, we will use the results of this work for comparison with the calculations.

4. RESULTS AND DISCUSSION

The calculation results of the recovery heat flux density q_R for the experimental data [5] with different heater sizes d_w and different immersion depth h show that agreement is achieved quite satisfactory. The dependencies of recovery heat flux q_R on immersion depth h for cylindrical heater of diameter $d = 2$ mm are presented on Fig. 3 for different approaches to calculations. These lines were received at the degree indicator $n = 3.2$ as the best for describing experimental data. As for calculation this figure shows that the best agreement with the experimental data is achieved for the full equation (31) taking into account peculiarities of the main heat and mass transfer processes in the superfluid helium and corresponding boundary conditions.

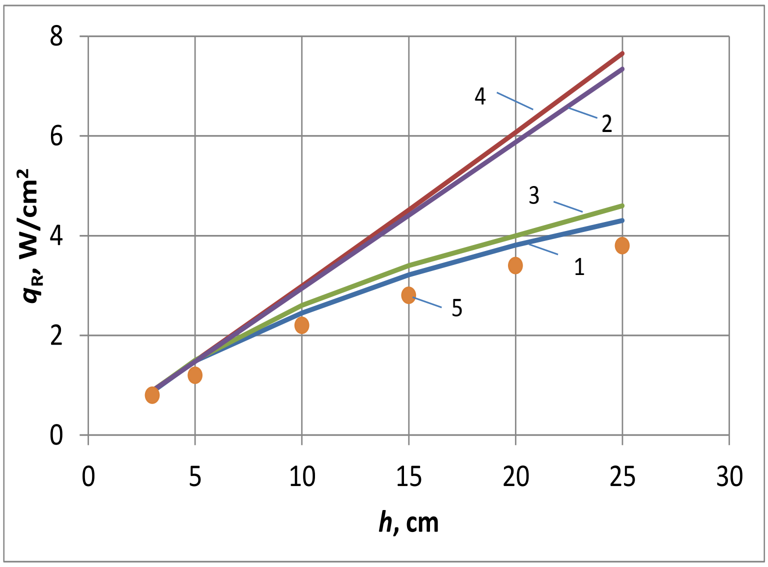

Fig. 3. Comparison of experimental and calculation data (T_b = 1.97K, d = 2 mm): 1 – eq. (31), 2 – eq. (32), 3 – eq. (33), 4 – eq. (34), 5 – experimental points

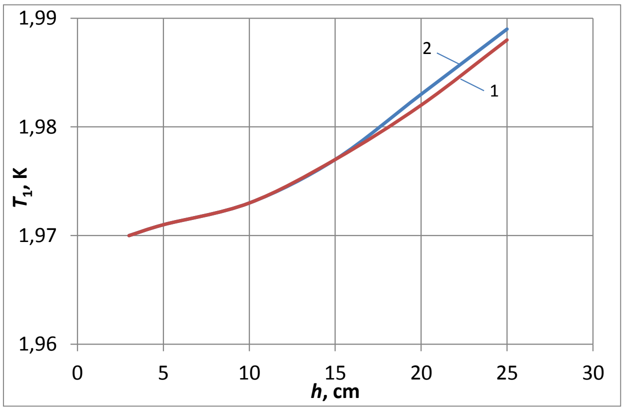

Fig. 4. Vapor-liquid interface temperature dependence on heater immersion (T_b = 1.97K, d = 2 mm): 1 – eq. (31), (28), 2 – eq. (33), (28)

The dependencies of vapour-liquid interface temperature are presented on Fig. 4. These dependencies were received as the result of solution systems of equations. As we can see from Fig. 4 temperature difference in liquid is less than 0.02K for chosen parameters. But as we can see from Fig. 3 this difference may affect on the results for heat flux densities and corresponding one. For example this factor may explain occurring of noise film boiling at the large immersion depth. Difference between two types of calculation from equations (28), (31) and equations (28), (33) is not quite big but the formulation of the right boundary conditions for liquid-vapor interface can be useful for the class of problem with superfluid helium boiling.

The dependencies of recovery heat flux q_R on immersion depth h for cylindrical heater of diameter d = 0.05 mm are presented on Fig. 5 for different approaches to calculations. Instead of previously result all lines are near experimental points as for small immersion depth as for big enough. At this it is necessary to note, that this line are almost linear, due to the small heater diameter.

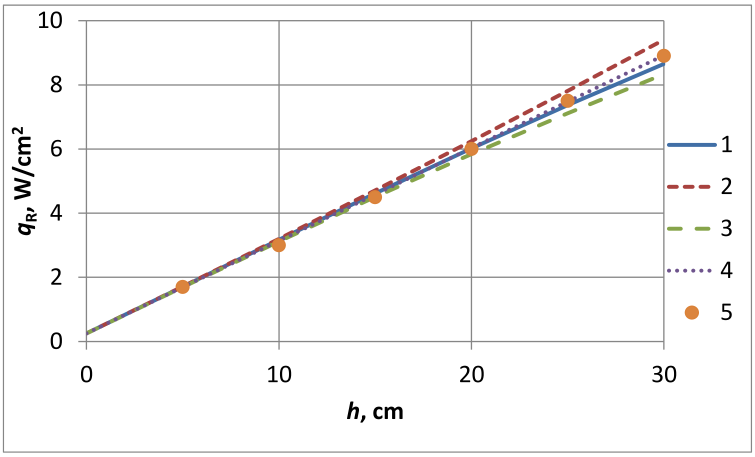

Fig. 5. Comparison of experimental and calculation data (T_b = 1.91K, d_w = 0.05 mm): 1 – eq. (31), 2 – eq. (32), 3 – eq. (33), 4 – eq. (34), 5 – experimental points

The dependencies of recovery heat flux density q_R on bath temperature T_b for cylindrical heater od diameter d = 0.8 mm are presented on Fig. 6 for different approaches to calculations. From these lines we can find that for temperature near λ-point there is necessary to analyse heat transfer in superfluid helium and change in the interface temperature. For the large heater immersion depth the difference between two approaches to calculation is more than for small.

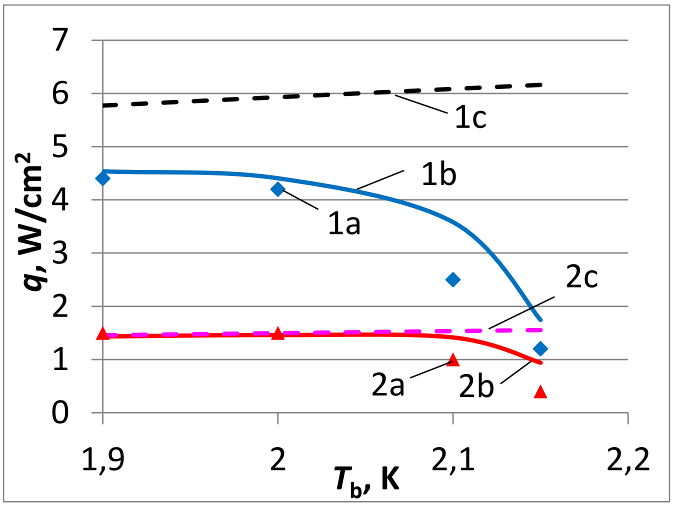

Fig. 6. The dependence of the recovery heat flux q on the temperature of the bath T_b at different immersion depths for a cylindrical heater d_w = 0.8 mm: 1 – immersion depth h = 20 cm, 2 – immersion depth h = 5 cm; a - experimental data (points); b - according to the system of equations (31), (28) at n=3.2; c - according to equation (34)

Therefore, when calculating the processes of heat and mass transfer during the film boiling of helium-II on a cylindrical heater, it is necessary to take into account normal and superfluid motion especially near the vapour-liquid interface. Non-equilibrium effects near vapour-liquid interface determine the formation of the vapor film, relationship of heat flux and vapour pressure and saturation line. The calculation of temperature increase in superfluid helium due heat transfer and formulating of heat balance in liquid can be made on the base the Gorter-Mellink theory.

3.1 Boiling of Superfluid Helium in Microgravity

In experiments [18], the conditions of microgravity were ensured by the free fall of the container in a pipe with a height of 122 m, the pressure in which was at the level of 50 Pa. The experiment lasted approximately 4.7 s, during which the level of microgravity was $g_0 = 10^{-5}g$.

To create a single bubble in helium-II, a microheater of manganine wire with an outer diameter of 0.05 mm and a length of 1.88 mm was placed in the cryostat. Heater was fixed on both sides by two superconducting monofilaments. The heat load of the heater was measured by a four-wire circuit. Most of the heat was released in the manganin part, even when the superconducting wires were partially in the vapor bubble. The direct current was switched on simultaneously with the onset of free fall and remained on during the entire time of microgravity (until the start of braking).

During the experiment, a single vapor bubble was formed on the heater surface, which grew to a size of (6÷10) mm in diameter at a bath temperature of 1.9K. The size dependence of the vapor film on the time was calculated by the area occupied by the vapor in the frames of the video.

The problem of superfluid helium boiling in microgravity corresponds to Fig. 1. However, vapor film on the heater surface is formed in ideal spherical shape as shown by experimental data [18]. But the recovery heat flux can be estimated for cylindrical geometry.

The level of microgravity in experiments [18] was $g_0 = 10^{-5}g$. The estimate shows that the hydrostatic pressure difference can be neglected $\rho' g_0 h \approx 7 \cdot 10^{-4}$ Pa. The capillary pressure difference is $\frac{\sigma}{R_w} \approx 12.4$ Pa at the heater radius $R_w \approx 2.5 \cdot 10^{-5}$ m.

Then equation (31) in microgravity is transformed to the following

$$\frac{0.44q_R}{\sqrt{2R_hT_1}}+\frac{f(T)}{(n-1)}{q_R}^nR_w\frac{L\cdot P_b}{R_h{T_b}^2}+\frac{2\mu' q_R}{\rho' S{T_1}^2}\left(f(T){q_R}^n-\frac{T_1}{R_w}\right)- \\ -\rho_n\left[1+\frac{\rho_n}{\rho_s}\right]\left(\frac{q_R}{\rho' ST_1}\right)^2=\frac{\sigma}{R_w} \quad . \tag{35}$$

And equation (34) is transformed to the next one

$$q_R=2.27\sqrt{2R_hT_b}\left(\frac{\sigma}{R_w}\right). \tag{36}$$

On the Fig. 7 there are two dependencies of recovery heat flux on bath temperature for two approaches to calculation. As we can see the difference between two lines is quiet small (several units), and the value of the recovery heat flux is less than for earth gravity by an order of magnitude (see Figs. 3, 5). At the same time dependencies is almost linear for small heater as for microgravity as at the full gravity conditions.

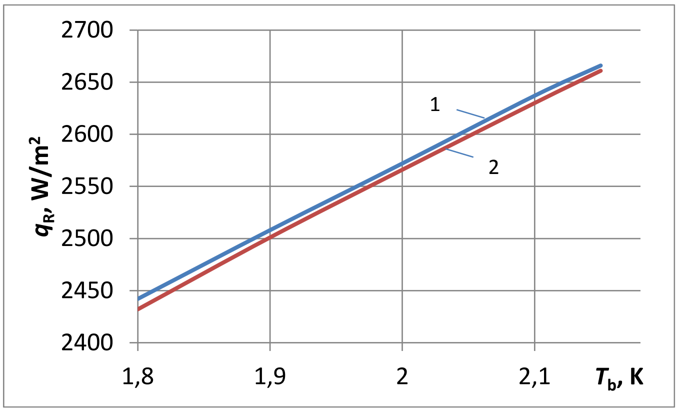

Fig. 7. Recovery heat flux dependence on temperature for microgravity (d_w = 0.05 mm): 1 – eq. (35), (28); 2 – eq. (36)

At this we can conclude that recovery heat flux is determined by the capillary force in microgravity instead of laboratory conditions where the hydrostatic pressure plays main role. As we can see from Figs. 3, 5 the corresponding values for free volume lies in the range of (1÷8) W/cm^2, that in 4÷32 times more than in microgravity. Therefore corresponding values of peak heat flux should be also less for microgravity. In experiments [19] heat flux density for vapor film growing was (1.7÷5.5) W/cm^2. This value is consistent in order with data [5, 6] presented on Figs. 3, 5.

4. CONCLUSION

The calculation method for recovery heat flux at film boiling of superfluid helium is developed based on continuum mechanics and molecular kinetic theory. The peculiarities of heat transfer in superfluid helium are considered based on the two-fluid model for boundary conditions and semi-empirical theory of Gorter-Mellink. The surface tension is taking into account also, that is an important factor for small heater and microgravity conditions. The experimental data were analyzed. Comparison of calculation and experimental data is good enough. At this, presented method is satisfactory described the known experimental data.

Recovery heat flux at microgravity [18] is determined by the capillary force and smaller by an order than for full gravity.

ACKNOWLEDGEMENTS

This work was supported by the Russian Science Foundation (project No. 19-19-00321).

COMPETING INTERESTS

Authors have declared that no competing interests exist.

REFERENCES

1. Nemirovskii SK. Physical review B. 2020;102:064511.
2. Kryukov AP, SW Van Sciver. Cryogenics. 1981;21:525.
3. Delov MI, Kuzmenkov DM, Lavrukhin AA, Kutsenko KV. International Journal of Heat and Mass Transfer. 2020;157:119941.
4. Grunt K et al. International Journal of Heat and Mass Transfer. 2019;134:1073.
5. Spiridonov AG. Experimental investigations of heat transfer with superfluid helium (PhD MPEI); 1981.
6. Ametistov EV, Grigoryev VA. Heat transfer with He-II (Energoatomizdat); 1986.
7. Korolyov PV, Kryukov AP, Puzina Yu Yu, Yachevsky IA. Journal of Physics: Conf. Series.2020;1675:012059.
8. Takada S, Kobayashi H, Murakami M, Kimura N. IOP Conf. Series: Materials Science and Engineering. 2020;755:012142.
9. Eikoku Y, Ishida K,Iwamoto A, Tsuji Y. Journal of Low Temperature Physics. 2019;196:6.
10. Korolyov PV, Kryukov AP, Puzina Yu Yu, Yachevsky IA. Journal of Physics: Conf. Series. 2020;1683:022017
11. Labuntsov DA, Yagov VV. Mechanics of two-phase system (Publishing house of MPEI); 2007.
12. Landau LD. Hydrodynamics (Fizmathlit); 2000.
13. Muratova TM, Labuntsov DA. High Temperature. 1969;7:959.
14. Gorter C J, Mellink J H 1949 Physica XV 285
15. Lebrun Ph, Tavian L. Proceedings of the CAS-CERN Accelerator School: Superconductivity for Accelerators. 2013;CERN–2014–005.
16. Van Sciver SW. Helium cryogenics (Springer-Verlag New York); 2012.
17. Puzina Yu Yu, Kryukov AP. Journal of Physics: Conf. Series. 2019;1370:012018
18. Takada S et al. Cryogenics. 2018;89:157.
19. Korolyov PV, Puzina Yu Yu. Journal of Physics: Conf. Series. 2017;891:012018.

Biography of author(s)

Yu Yu Puzina
Department of Low Temperature National Research University, Moscow Power Engineering Institute, 14 Krasno kazarmennaya, Moscow, 111250 Russia.

Presently, she is an Assistant professor and the Head of Department of Low Temperatures of Moscow Power Engineering Institute (Moscow Power Engineering Institute, Krasnokazarmennaya 14, Moscow 111250, Russia. She served as an Engineer (2005-2017) in Department of Low Temperatures and a Lecturer(2017-2018) in Department of Low Temperatures. She obtained Diploma of Docent (equivalent of Associate professor) in cryogenics in 2020, Degree of Technical Sciences (Ph.D. equivalent), thesis: “Peculiarities of the transfer processes on the interfacial surfaces of vapor-liquid” in 2005, Diploma in Low temperature Engineering and Physics (equivalent of Ms. Degree), Moscow Power Engineering Institute (MPEI) in 2002. Her Professional Interests include Heat and Mass Transfer, Non-equilibrium Effects in Transport Phenomena at Interface Surfaces, Molecular Physics, Fluid Dynamics, Boiling of He II (Superfluid Helium), and Cryogenics. She has 64 Publications in the national and international journal.

A. P. Kryukov
Department of Low Temperature National Research University, Moscow Power Engineering Institute, 14 Krasno kazarmennaya, Moscow, 111250 Russia.

Research and Academic Experience: He is the professor of Low Temperatures Department, National Research University Moscow Power Engineering Institute (1992-Present), Received Degree of Doctor of Technical Sciences (D Sci(Eng)) in 1991, Chief of Computer Simulation Laboratory in Institute for High Performance Computing and Data bases (IHPC) (Moscow Branch of IHPC) (1996-2001), Visiting Scholar at Wisconsin University (Madison, USA) (1980-1981).

Research Area: Heat and Mass Transfer. Non-equilibrium Effects in Transport Phenomena at Interface Surfaces. Molecular Physics. Fluid Dynamics. Cryogenics, including transfer processes in He II. Vacuum Science and Technologies.

Number of Published papers: 204.

Special Award: He is the Honorary Worker of Higher Professional Education of the Russian Federation during 2015.

Any other remarkable point(s): He is also a Member of National Committee on Heat and Mass Transfer of Russian Academy of Sciences (2007-present)

© Copyright (2021): Author(s). The licensee is the publisher (B P International).

DISCLAIMER
This chapter is an extended version of the article published by the same author(s) in the following conference proceeding.
Journal of Physics: Conference Series, 1370: 012018, 2019.

Print ISBN: 978-93-91312-26-8, eBook ISBN: 978-93-91312-34-3

$\mathrm{B} \propto \frac{1}{\mathrm{T}}$ and Meissner Effect 1933 Re-explained by Gill's Electronic Theory of Magnetism 1964

Avtar Singh Gill[1*]

DOI: 10.9734/bpi/nupsr/v9/9867D

ABSTRACT

Curie point is reached according to Gill's electronic theory of magnetism 1964 because of the *increased inter-atomic distance* at a certain high temperature for a particular metal which makes it impossible for some exposed electrons of a ferromagnetic atom to latch onto the exposed protons of the next atom to cause magnetization. This *Curie point* could be increased by applying a stronger external magnetic field.

Meissner effect 1933 refers to the *lateral expulsion or squeezing out* of an otherwise constant total magnetic flux from within the magnet to the outside on cooling of the magnet to a critical temperature as it results in less internal space. It will be shown that *the concept of internal plus external magnetic flux as a constant is wrong* and an alternative explanation will be presented to explain the Meissner experiment results obtained in 1933 with the help of Gill's electronic theory of magnetism 1964 (*the re-explained Meissner effect*).

Gill's electronic theory of magnetism shows that the reduced inter-atomic distance of the magnetized chain inside the magnetized tin cylinder on cooling will result in a greater number of electrons of one atom to latch onto the protons of the next atom and so on. This increased magnetic force of attraction between exposed electrons and protons of adjacent magnetized atoms will prevent any expulsion of the increased intra-magnetic force along its lateral length. *There is greater magnetization of the tin cylinders resultant magnetic poles at the two ends due to reduced inter-atomic distance due to cooling resulting in the development of a stronger external magnetic force around the tin cylinder, with no change in the external applied external magnetic force and this is the correct Meissner effect.*

Levitation of the electron dependent north magnetic pole of a magnet in the Meissner experiment due to a dense layer of electrons on the tin surface will be addressed.

Superconductivity will be explained by super-cooling leading to a greatly reduced inter-atomic distance leading to easy flow of the free outer valence electrons as they are experiencing near zero resistance while flowing from one atom to the next. These outer free electrons in a superconducting supercooled state will experience equal force from neighboring consecutive proton masses of consecutive atoms and thus are able to move freely with zero resistance.

Keywords: Gill's electronic theory; superconductivity; curie point; magnetic force; electrical forces.

1. INTRODUCTION

A better understanding of physics leads to better applications. While dealing with magnetism, we are dealing with two forces from the two poles of a magnet [1,2]. The negative or north magnetic pole N will repel another negative or north magnetic pole N and the positive or south magnetic pole S will repel another positive or south magnetic pole S and the negative or north magnetic pole N will attract the positive or south magnetic pole S. *Gill's electronic theory of magnetism (1964)* shows that the magnetic force is a combination of the electron dependant and proton dependant forces from the two magnetic poles and the relative motion between the very same two forces produce an electric current.

---

[1] *Maimonides Medical Center, Brooklyn, New York, USA.*
**Corresponding author: E-mail: avtargillmd@aol.com;*

Pierre Curie while dealing with magnetism at high temperatures brought up the Curie point and Curie's law [3,4]. The author has similar results with dot product equations which have been further elaborated with the application of Gill's electronic theory of magnetism.

The Walther Meissner and Robert Ochsenfeld experiment 1933 while dealing with temperatures approaching absolute zero obtained results which were explained as lateral expulsion of magnetic flux known as the *Meissner effect* [5]. Gill's electronic theory of magnetism 1964 [6] explains the magnetic configuration of the tin cylinder atoms under the influence of an electromagnet. It is further explained why there cannot be any lateral expulsion of internal magnetic forces although internal magnetic forces increase with cooling [7-9]. The overall increase in external magnetic forces around a tin cylinder without any expulsion of magnetic flux from within is because of increased magnetization of its magnetic ends because of cooling.

A. Einstein in 1905 [10] and Richard Feynman in 1943 expressed concern about asymmetry between the magnetic force and the electrical forces and the same is resolved with the application of Gill's electronic theory of magnetism 1964.

2. METHOD

Gill's electronic theory of magnetism 1964 will be summarized and its application will help in explaining the Curie point and its variation with change of applied external magnetic force. Next, Gill's electronic theory of magnetism 1964 will be applied to the Meissner experiment 1933 and the results will be explained. It will be shown that there is *no lateral expulsion of magnetic flux (Meissner effect),* but there is development of extra magnetic flux/force from the magnetic ends due to decreased inter-atomic distance in the tin cylinder due to cooling with all other factors remaining unchanged. It will be explained how a decreased inter-atomic distance due to cooling makes it easier for a larger number of inner electrons of one magnetized atom to latch on to the protons of the next magnetized atom and so on and we have a larger number of exposed inner electrons $(\boldsymbol{n})$ with a negative torque $(-\boldsymbol{\tau})$ at one end as the negative or north magnetic pole N and an equal larger number of exposed protons $(\boldsymbol{n})$ at the other end with a positive torque $(+\boldsymbol{\tau})$ as the positive or south magnetic pole S of the tin cylinder. This leads to extra magnetic force manifestation on the outside. *It will be explained why magnetic flux cannot be pushed out of the lateral tin surface after cooling.* Superconductivity will be explained along with a presentation of stages of magnetism.

3. GILL'S ELECTRONIC THEORY OF MAGNETISM (1964)

Gill's electronic theory of magnetism (1964) is based on the structure of the atom and explains how the positively charged protons and the negatively charged electrons of an atom are responsible for both magnetism and electrical forces.

In the diagrams that follow in this article, we are using a simplified version of the structure of an atom with a large black proton mass and small red inner electrons. *Please note that the outer free valence electrons (not shown) take part mainly in electrical current flow.*

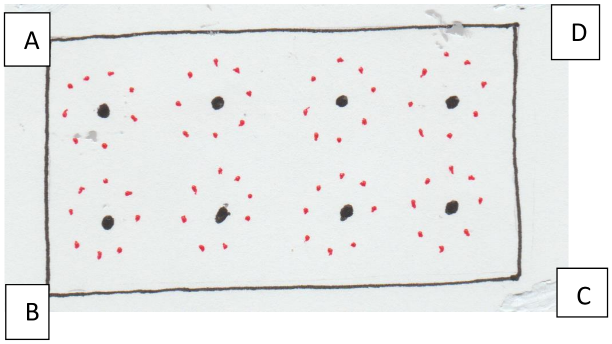

Fig. 1a.

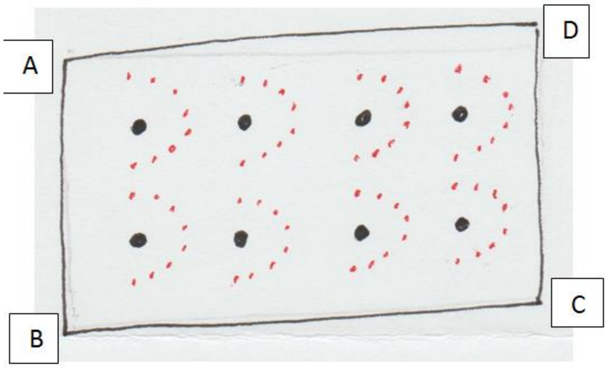

Fig. 1b.

Fig. 1a. Shows neutral iron atoms in the un-magnetized state
Fig. 1b. Shows the change in position of the inner electrons on magnetization
● *Large black dots-protons*
● *Small red dots-electrons*

Fig. 1b shows the change in position of the inner electrons on magnetization. If the displaced magnetized electrons have a negative torque $(-\boldsymbol{\tau})$, then the exposed protons at the other end of the magnetized atom will have a positive torque $(+\boldsymbol{\tau})$ and vice versa. This chain continues with the magnetic ends manifesting as the exposed negatively torqued $(-\boldsymbol{\tau})$ electron based negative or north magnetic pole N and the exposed oppositely torqued $(+\boldsymbol{\tau})$ proton based positive or south magnetic pole S of the magnet.

Gill's electronic theory of magnetism 1964 shows the neutral iron atoms in Fig. 1a are magnetized in Fig. 1b and CD has become the negative or north magnetic pole N with a negatively torqued $(-\boldsymbol{\tau})$ non-moving charge $-\boldsymbol{ne}$ of the magnet and AB has become the positive or the south magnetic pole S of the magnet with an opposite positively torqued $(+\boldsymbol{\tau})$ non-moving charge $+\boldsymbol{ne}$ where $\boldsymbol{n}$ is the number of exposed inner electrons at one end and equals the number of exposed protons at the other end.

The neutral atoms in Fig. 1a have become magnetized atoms in Fig. 1b by undergoing a change in configuration and each atom also has developed an opposing torque between its own electrons and protons to give the magnetized atoms a cork-screw effect.

In Gill's electronic theory of magnetism, magnetic force $\boldsymbol{B}$ is the force of attraction between

(1) the exposed inner electron based negative or north magnetic pole N and
(2) the exposed proton based positive or south magnetic pole S.

The application of Gill's electronic theory of magnetism 1964 in Fig. 1b shows that *the magnetic force comprises of two forces (positive and negative)* emanating from the proton dependent south magnetic pole and the electron dependent north magnetic pole of reconfigured magnetized atoms.

Experiment- A physicist showed me the following experiment in 1965. On a wooden table, spread some coarse iron filings and in the middle of the iron filings, place a magnet.

In Fig. 2a we see a bar magnet with iron filings arranged along magnetic field lines. According to Gill's electronic theory of magnetism, each magnetic field line is a combination of negative electron dependent force from the north magnetic pole and the positive proton dependent force from the south magnetic pole.

In Fig. 2b, a wooden non-magnetic obstruction Z is placed on one side on the iron filings. The iron filings crumple on both sides of Z in zones X and Y. *If the magnetic force was a single force, the iron filings should have crumpled in Zone X or Zone Y only.*

Thus, the magnetic force is combination of the proton dependent positive and the electron dependent negative forces from the two poles of a magnet seen both diagrammatically and experimentally.

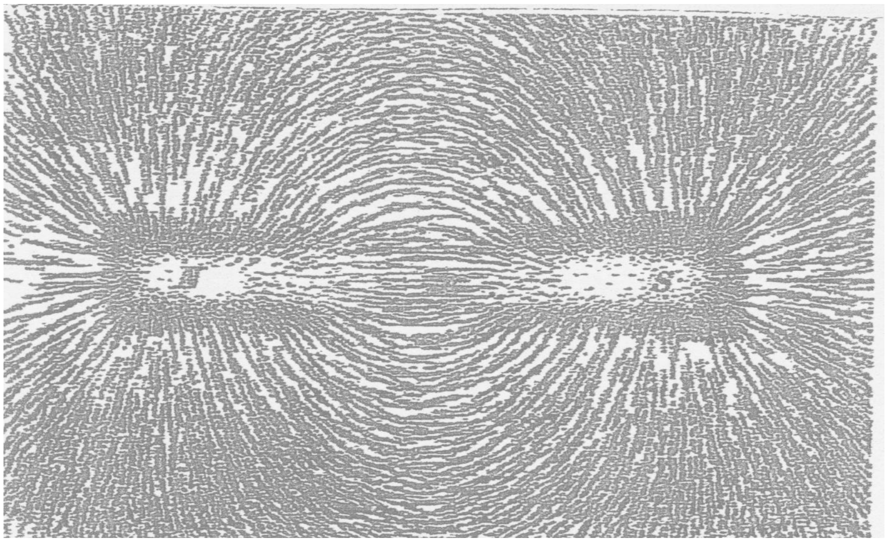

Fig. 2a.

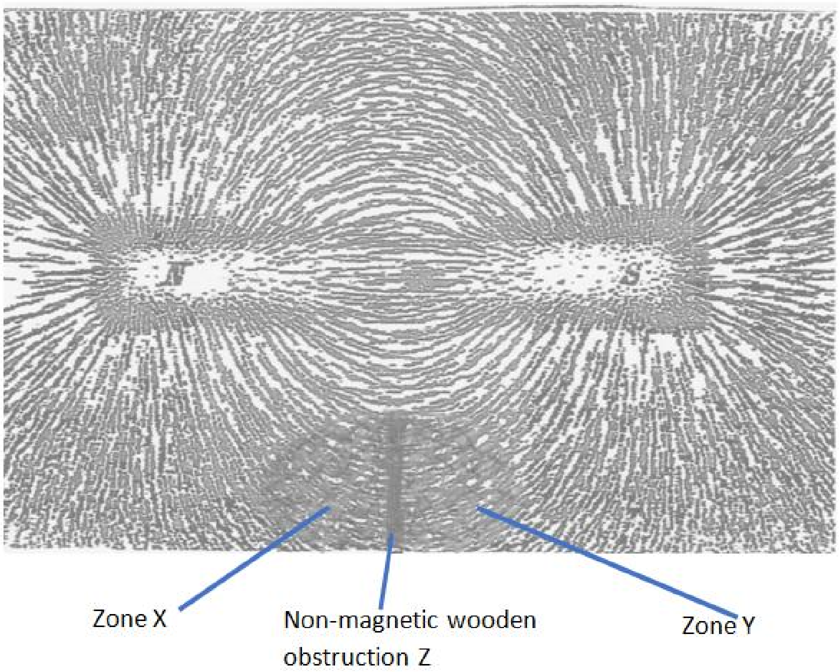

Fig. 2b.

4. CURIE POINT AND GILL'S ELECTRONIC THEORY OF MAGNETISM 1964

Fig. 3 is a magnet based on Gill's electronic theory of magnetism (1964). The *inter-atomic distance between the center of one atom and the center of the next atom is* $\boldsymbol{d}$ meters. In the magnetized state, some of the inner electrons with a negative clockwise torque $(-\boldsymbol{\tau})$ of an atom can latch onto the exposed protons with a positive anti-clockwise torque $(+\boldsymbol{\tau})$ of the next atom and so on and we have the south magnetic pole due to exposed protons with a positive anti-clockwise torque $(+\boldsymbol{\tau})$ and the north magnetic pole due to the exposed inner electrons with a negative clockwise torque $(-\boldsymbol{\tau})$ or vice versa. *If the inter-atomic distance increases beyond a certain* $\boldsymbol{d}$ *meters as indicated by temperature above the Curie point or Curie temperature* $\boldsymbol{Tc}$*, then magnetization is not possible as the exposed inner electrons of one atom are not able to latch onto the exposed protons of the next atom.*

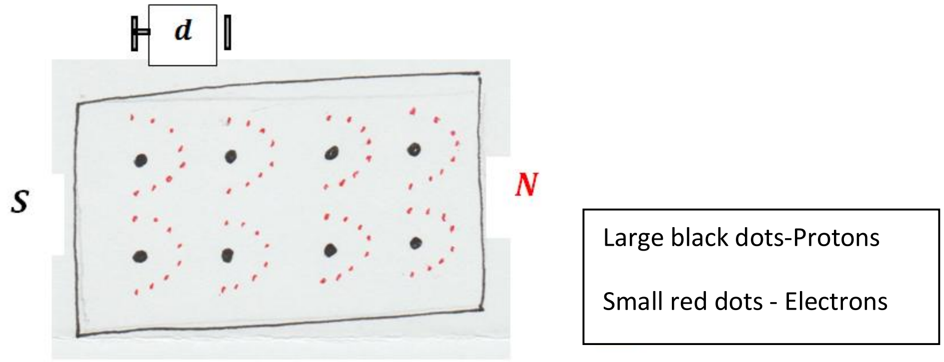

Fig. 3.

There are two factors affecting the extent of magnetization of Fig. 3:

a-*the external magnetic force*: The greater applied external magnetic force will result in a larger number of inner electrons latching on to the exposed protons of the next atom and so on, until we have exposed inner electrons at one end behaving as the negative or north magnetic pole N with a negative torque $(-\boldsymbol{\tau})$ and exposed protons at the other end behaving as the positive or south magnetic pole S with a positive torque $(+\boldsymbol{\tau})$.

b-*the inter-atomic distance*: As the inter-atomic distance $\boldsymbol{d}$ meters becomes smaller with cooling, it will result in a larger number of inner electrons of one atom to link with the exposed protons of the next atom and so on until we have a larger number of exposed inner electrons at one end as the north magnetic pole N and an equal larger number of exposed protons at the other end of the magnet as the south magnetic pole S.

When the temperature is raised, the inter-atomic distance $\boldsymbol{d}$ meters will increase.

$$\boldsymbol{d} = \boldsymbol{d}_0(\boldsymbol{1} + \boldsymbol{\mu}.\,°\boldsymbol{K})$$

where $\boldsymbol{d}_0$ meters is the inter-atomic distance at $0°\boldsymbol{K}$.
$\boldsymbol{K}$ is the temperature on the Kelvin scale.
μ is the coefficient of expansion of the metal.

Magnetizing force of attraction $\boldsymbol{F}$ between an inner electron $(-e)$ of one magnetized atom and the exposed proton $(+e)$ of the next magnetized atom when there is a distance $\boldsymbol{d}\ meters$ between them is

$\boldsymbol{F} = \frac{\boldsymbol{k}(+e)(-e)}{\boldsymbol{d}^2} = -\frac{\boldsymbol{k}e^2}{\boldsymbol{d}^2}\ newtons$. (Coulomb's law with $\boldsymbol{k}$ as the Coulomb's constant)

Gill's electronic theory of magnetism 1964 explains that the negative force from the exposed inner electron $(-e)$ because of a clockwise negative torque $(-\boldsymbol{\tau})$ of a magnetized atom has a clockwise spin and the positive force from the exposed proton $(+e)$ because of an anti-clockwise positive torque $(+\boldsymbol{\tau})$ of the next magnetized atom has an anti-clockwise spin or vice versa depending on how you look at it. These two positive and negative forces with opposite spins will entwine with each other and attract.

As the inter-atomic distance $\boldsymbol{d}$ meters becomes larger with warming, it will result in a smaller number of inner electrons of one atom to link with the exposed protons of the next atom and so on until we have smaller number of exposed inner electrons at one end as the north magnetic pole N and an equal smaller number of exposed protons at the other end of the magnet as the south magnetic pole S.

Curie point $(\boldsymbol{Tc})$ is a certain high temperature at which $\boldsymbol{d}$ meters has increased so much that no electrons of one atom are able to latch onto the protons of the next atom and the magnet becomes de-magnetized or is unable to magnetize.

$\boldsymbol{Tc = 1041°K}$ for Iron.

Thus, at $\boldsymbol{1041°K}$, the $\boldsymbol{Tc}$ for iron, the inter-atomic distance $\boldsymbol{d}$ has increased so much that the inner electrons of one atom are unable to latch onto the exposed protons of the next atom and the ferromagnet is demagnetized or cannot be magnetized.

If the length of the magnet in Fig. 3 is $\boldsymbol{D}$ meters and the total number of exposed electrons $-\boldsymbol{e}$ at the north magnetic pole is $\boldsymbol{n}$ which is also equal to the exposed protons $+\boldsymbol{e}$ at the south magnetic pole, then the expressed total magnetic force/flux which will travel around the magnet (the positive force towards the electron based negative or north magnetic pole N and the negative force towards the proton based south magnetic pole S) towards the two magnetic poles is

$$Total\ magnetic\ force\ \boldsymbol{F} = \frac{\boldsymbol{kn(+e)n(-e)}}{\boldsymbol{D^2}} = -\frac{\boldsymbol{kn^2e^2}}{\boldsymbol{D^2}}\ newtons.$$

An increased external applied magnetic force $\boldsymbol{B}$ will help this latching of the inner electrons of one atom to the protons of the next atom sequentially at temperatures above the Curie point and so the Curie point can be raised by increasing the external applied magnetic force.

Curie point $(\boldsymbol{Tc})$ increase is directly proportional to the increase in external applied magnetic force $\boldsymbol{B}$.

$$\boldsymbol{Tc} \uparrow \infty\ \boldsymbol{external\ B} \uparrow\ .$$

$$\boldsymbol{D = D_0(1 + \mu.°K)}$$

where $\boldsymbol{D_0}$ meters is the length of the magnet at $0°\boldsymbol{K}$.
$\boldsymbol{K}$ is the temperature on the Kelvin scale.
μ is the coefficient of expansion of the metal.
$\boldsymbol{D}$ meters, the length of the magnet is directly proportional to the absolute temperature $\boldsymbol{T}$ on the Kelvin scale.

$$\boldsymbol{D} \infty \boldsymbol{T}\ .$$

From the above discussion, we conclude that the resulting magnetizing force $\boldsymbol{F}$ is directly proportional to the external magnetizing force $\boldsymbol{B}$ and inversely proportional to the absolute temperature.

$\mathrm{F} \infty\ \mathrm{B}$ and $\mathrm{F} \infty \frac{1}{\mathrm{T}}$ or $\mathrm{F} \infty \frac{\mathrm{B}}{\mathrm{T}}$ or

$$\mathrm{F} = \mathrm{C}.\frac{\mathrm{B}}{\mathrm{T}} \tag{1}$$

*Where **C** is a material specific constant and resulting magnetizing force $\boldsymbol{F}$ is a dot product derived with the help of Coulomb's law.*

Discussion: Pierre Curie who experimented at high temperatures came up with **Curie's law**:

$$M = C.\frac{B}{T}$$

Where M is the resulting magnetization
B is the magnetic field in teslas
T is the absolute temperature in kelvins and
C is a material-specific Curie constant.

According to Pierre Curie, below the Curie temperature, neighboring magnetic spins align in a ferromagnet even if there is no externally applied magnetic field. Above the Curie temperature, the magnetic spins are randomly aligned unless an external magnetic field is applied.

According to Gill's electronic theory of magnetism 1964, the exposed inner electrons of one reconfigured magnetized atom latch onto the exposed protons of the next magnetized atom owing to an opposing torque (τ) between them and so onward. Above the Curie point, due to the increased inter-atomic distance, that latching on is not possible and we have a demagnetized state. As the temperature is lowered to at or below the Curie point, the latching on and magnetization will set in and a further decrease in temperature will result in greater latching on and greater magnetization.

***Equation 1** is like the derivation by Pierre Curie known as Curie's law except that we use dot product calculations while applying Gill's electronic theory of magnetism.*

The above concept holds good from the Curie temperature $\boldsymbol{Tc}$ all the way up to the super-cooled critical temperature experiment of Walther Meissner 1933.

5. WALTHER MEISSNER AND ROBERT OCHSENFELD EXPERIMENT 1933

In 1933, Walther Meissner and Robert Ochsenfeld conducted an experiment shown below and concluded that the magnetic flux was expelled from inside a cooled piece of tin to the outside due to less space inside because of cooling, erroneously presuming that the total magnetic flux inside the tin cylinder and outside it was a constant independent of the temperature of the tin *(Meissner effect).*

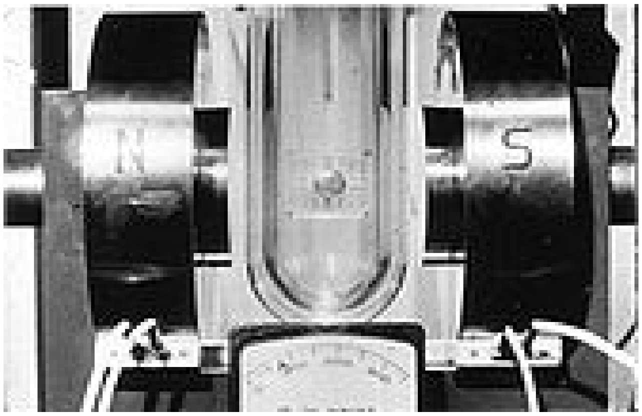

A tin cylinder—in a Dewar flask filled with liquid helium—has been placed between the poles of an electromagnet. The magnetic field is about 8 milliteslas.

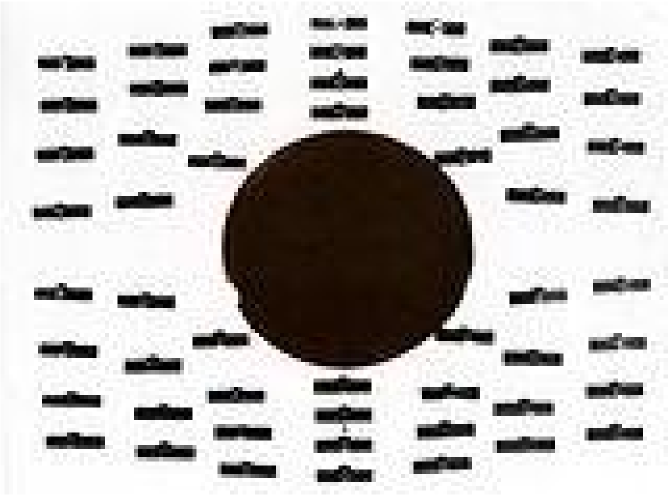

T=4.2 K, B=8 mT. Tin is in the normally conducting state. The compass needles indicate that magnetic flux permeates the cylinder.

The cylinder has been cooled from 4.2 K to 1.6 K. The current in the electromagnet has been kept constant, but the tin became superconducting at about 3 K.

Fig. 4 is a diagram showing the Meissner effect due to cooling to $< 3.72°K$. Magnetic field lines, represented as arrows, are excluded from a superconductor when it is below its critical temperature.

The Meissner effect shown above is based on the *exclusion principle* for lack of any other explanation. There is this constant external magnetic field $\boldsymbol{B}$ from the electromagnet applied to the tin cylinder in the liquid helium flask. Cooling of the tin to the critical temperature and below results in decreased inter-atomic space and the magnetic field lines inside the tin gets expelled for lack of space.

The author disagrees with the above Meissner effect explanation and applies Gill's electronic theory of magnetism 1964 to the Meissner experiment 1933 to explain the results as follows.

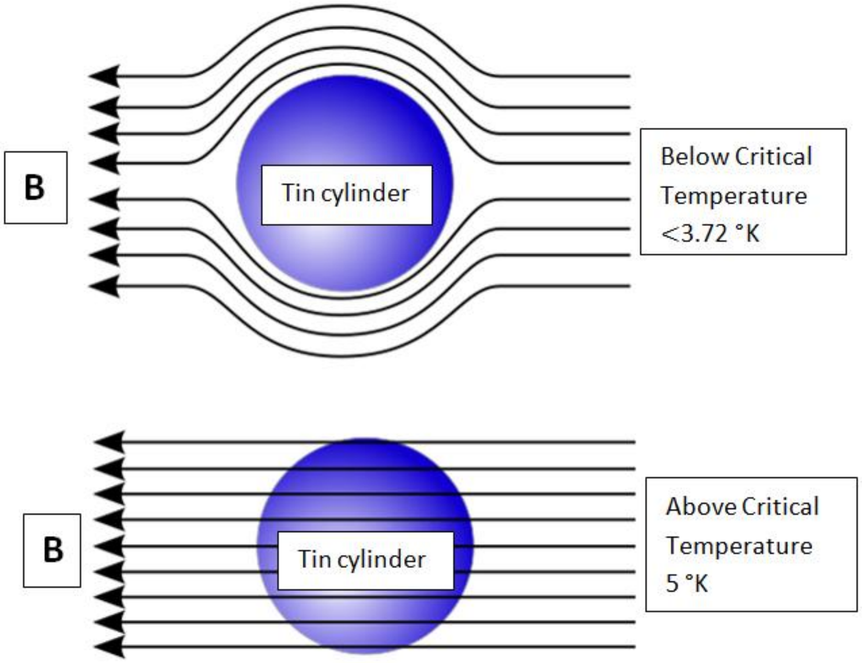

Fig. 4.

A word about Gill's electronic theory of magnetism 1964 as we move further.

Why $(+e)$ and $(-e)$ forces spin

Applying Gill's electronic theory of magnetism 1964 to the following electro-magnetic experiment shows how and why the two forces spin and entwine while they head for the opposite source.

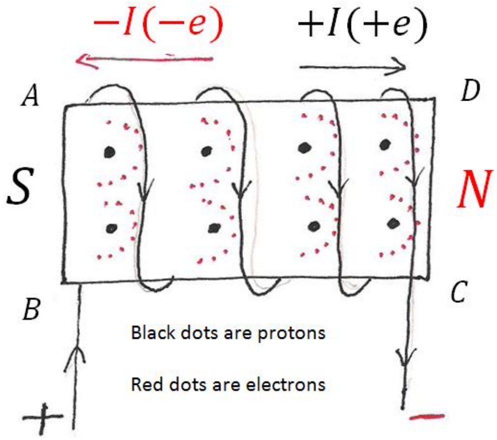

Fig. 4a

Gill's electronic theory of magnetism 1964 has been applied to a piece of iron as it is magnetized by a direct electric current coil as shown in Fig. 4a.

The negative free valence electrons $(-e)$ as they flow as a negative electric current in the coil in the negative direction towards AB act on the iron piece inside the coil and lead to an exposure of protons by attraction at the positive or south magnetic pole S and these exposed protons at the magnetic end have also *developed a positive torque* $(+\tau)$ by attraction in the direction of the circular electron flow in the electro-magnetic coil.

The same negative free valence electrons $(-e)$ as they flow in the electric coil causes the exposed inner electrons of atoms in the iron piece inside the electric coil to be repelled sequentially towards CD to become the negative or north magnetic pole N and these exposed inner electrons have *developed a negative torque* $(-\tau)$ by repulsion from the circular electron flow in the electro-magnetic coil.

The atoms in the iron piece are getting *sequentially magnetized* and at every inter-atomic intra-magnetic level there is an exposed proton $(+e)$ based south magnetic pole S with a positive torque $(+\tau)$ facing an exposed inner electron $(-e)$ based north magnetic pole N with a negative torque $(-\tau)$ of the next atom.

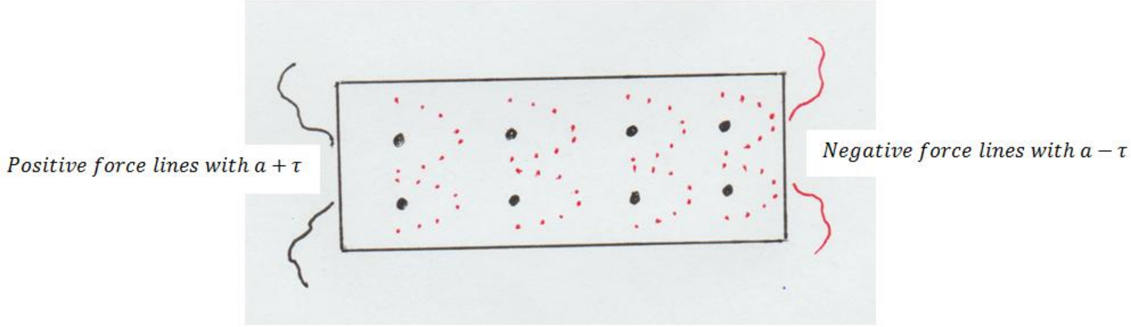

Fig. 4b. At the start of magnetization

In Fig. 4b, at the start of magnetization at $t = 0\ seconds$, the negative forces are coming out from the exposed inner electron $(-e)$ based negative or north magnetic pole N and these negative forces are experiencing a negative torque $(-\tau)$ passed on from the negative torque $(-\tau)$ of the exposed inner electron based negative or north magnetic pole N.

The exposed proton $(+e)$ based positive or south magnetic pole S has the positive forces coming out with a positive torque $(+\tau)$ passed on from the positive torque $(+\tau)$ of the exposed protons of the positive or south magnetic pole S.

These negative and positive forces also exist at the inter-atomic intra-magnetic level when magnetized and even inside the magnet there is a much greater coulombs force of attraction as the coulombs force law is applicable.

These negative forces with a negative torque $(-\tau)$ from N travel towards the positive or south magnetic pole S and the positive forces with a positive $(+\tau)$ torque from S travel towards the negative magnetic pole N and owing to their opposing torque they entwine to manifest as a single magnetic force *erroneously called the single fundamental force of magnetism.*

In above Fig. 4c at $t > 0\ seconds$, the negative forces are coming out of the negative or north magnetic pole N with a negative torque $(-\tau)$ and are headed for the exposed positive or south magnetic pole S and the positive forces are coming out of the exposed south magnetic pole S with a positive torque $(+\tau)$ and are headed for the negative or north magnetic pole N.

The intra-magnetic force will get stronger with cooling owing to decreased inter-atomic distance *and no magnetic flux whatsoever can be expelled laterally.* Cooling will facilitate increased magnetization as the electrons and protons of neighboring atoms get closer to each other and this will manifest from the exposed magnetic ends only.

The magnetic force of attraction is a combination of the negative force from the north magnetic pole N with a negative torque $-\tau$ and the positive force from the south magnetic pole S with a positive torque $+\tau$.

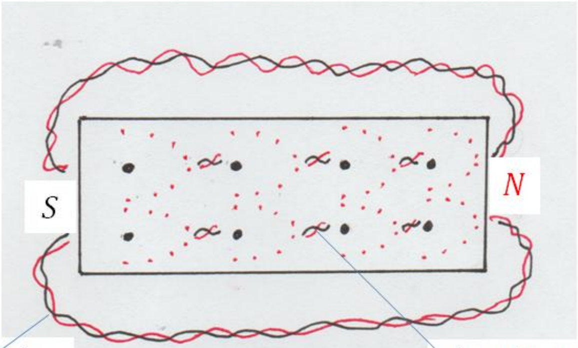

The two forces entwine to manifest as the magnetic force

The two forces also entwine sequentially at the intra-magnetic inter-atomic level

Fig. 4c. Magnetized

Owing to the opposing torque between the forces from the negative or north magnetic pole N and from the positive or south magnetic pole S, these two forces of attraction entwine with each other as in Fig. 4c and appear to be a single magnetic force of attraction both:

1 - at the inter-magnetic intra-magnetic level, this attractional force gets stronger with cooling due to decreased inter-atomic distance and no lateral expulsion of magnetic flux possible although greater magnetization possible. [1]
2 - at the extra-magnetic level it does manifest from the two ends of a magnet as the magnetic force/flux.

6. LINE DIAGRAMS OF MEISSNER EXPERIMENT PLUS GILL'S ELECTRONIC THEORY OF MAGNETISM

In Fig. 5a and Fig. 5b, we have the tin cylinder immersed in a Dewar flask with liquid helium. An electromagnet with a constant magnetic field $\boldsymbol{B}$ is placed across the Dewar flask.

The large red arrows show the overall direction of the negative electron dependant counterclockwise electric current around the electro-magnet. According to Gill's electronic theory of magnetism, it causes each magnetized atom to have some of its inner electrons repelled towards the negative or north magnetic pole N and these electrons also develop a clockwise torque $(-\boldsymbol{\tau})$ due to repulsion from the counterclockwise flowing electrons as an electric current. The exposed protons at the other end of each magnetized atom will have a counter-clockwise positive torque $(+\boldsymbol{\tau})$ due to the counter-clockwise force of attraction from the flowing electron dependant electric current. We thus have an electron dependant negative or north magnetic pole $\boldsymbol{N}$ with a negative torque $(-\boldsymbol{\tau})$ and a proton dependant positive or south magnetic pole $\boldsymbol{S}$ with a positive torque $(+\boldsymbol{\tau})$ of the electro-magnet.

These magnetized north and south poles of the electromagnet cause a similar change in the atoms of the tin cylinder and we have a south magnetic pole in the tin towards the north magnetic pole of the electromagnet and a north magnetic pole towards the south magnetic pole of the electromagnet. The magnetic force/flux around the cylinder will be proportional to the number of exposed inner electrons at its north magnetic pole which is equal to the number of exposed protons at its south magnetic pole. The decreasing inter-atomic distance with cooling will cause greater magnetization as explained by applying Gill's electronic theory of magnetism which causes greater external magnetic force as seen in the above experiment. Magnetic flux cannot be expelled laterally from inside the magnetized tin cylinder as will be explained.

---

[1] *refer Meissner effect re-explained with Gill's electronic theory of magnetism 1964 by author in ARJPS 2018.*

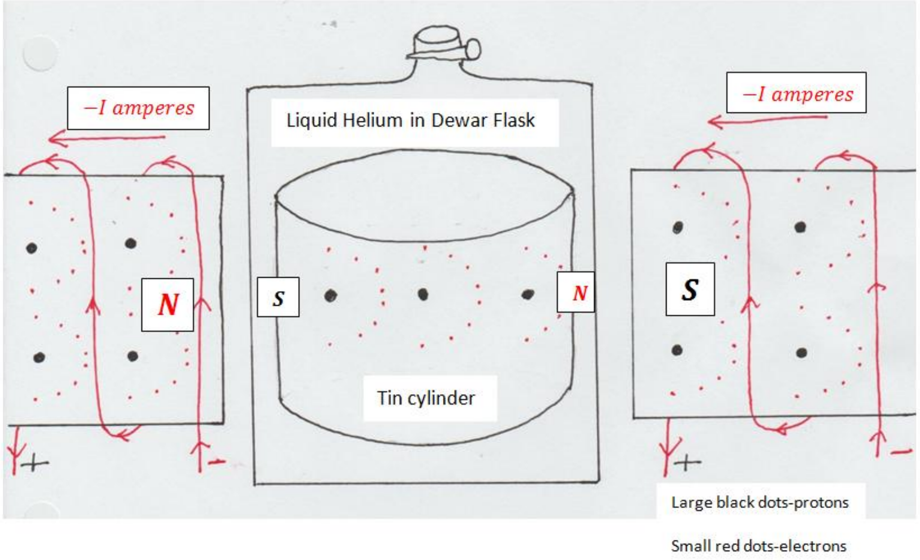

Fig. 5a. (view from front)

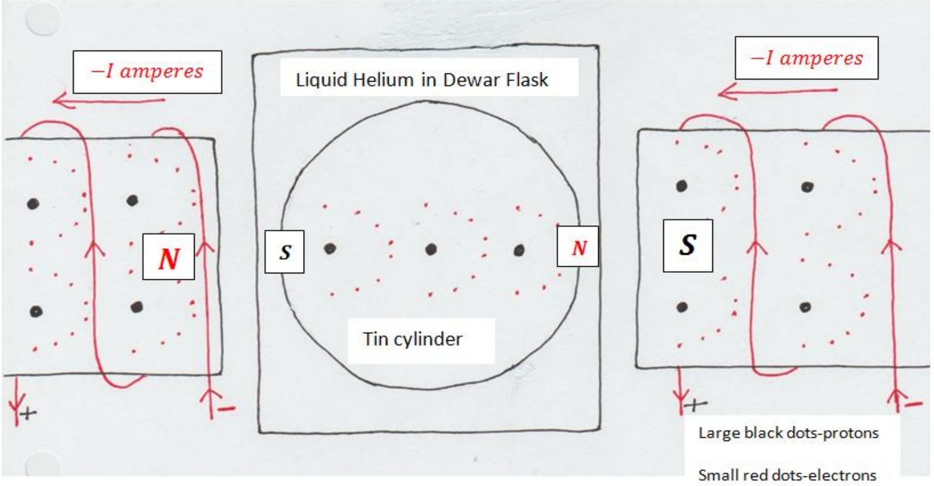

Fig. 5b. (view from the top)

7. INTRA-MAGNETIC BEHAVIOR OF NEIGHBORING MAGNETIZED ATOMS

When the above metal (tin) is being magnetized in a magnetic field and is cooled, the inter-atomic distance $\boldsymbol{d}$ meters will decrease due to cooling.

$$\boldsymbol{d} = \boldsymbol{d}_0(\mathbf{1} + \boldsymbol{\mu}.\,°\boldsymbol{K})$$

$\boldsymbol{d}_0$ meters is the inter-atomic distance at 0°$\boldsymbol{K}$.
$\boldsymbol{K}$ is temperature on the Kelvin scale.
μ is the coefficient of expansion of the metal.
$\boldsymbol{d}$ meters is the inter-atomic distance at a particular temperature.

Due to the super-cooling with liquid helium, $\boldsymbol{d}$ decreases significantly and applying Gill's electronic theory of magnetism 1964:

(a)-inner electrons of one atom will have greater ease to latch onto the protons of the next atom and so on along with an opposing torque between the electrons and the protons of each magnetized atom.
(b)-larger number of inner electrons of each atom will latch onto the protons of the next atom and so on resulting in greater magnetization.

The smaller the *inter-atomic distance* $\boldsymbol{d}$, which happens with lowering the temperature of the tin cylinder in the Meissner experiment, the easier it is for more of the inner electrons of one atom to latch onto the protons of the next atom and so on when subjected to the same external applied magnetic force $\boldsymbol{B}$**.** Also, because of the decreased $\boldsymbol{d}$, a greater number of inner electrons of each atom will latch on to the protons of the next atom and so on and result in greater magnetization of the tin cylinder without any change in the external applied magnetic $\boldsymbol{B}$ and this is what causes the Meissner effect.

8. INTRA-MAGNETIC BEHAVIOR OF MAGNETIZED NEIGHBORING PROTON AND ELECTRON

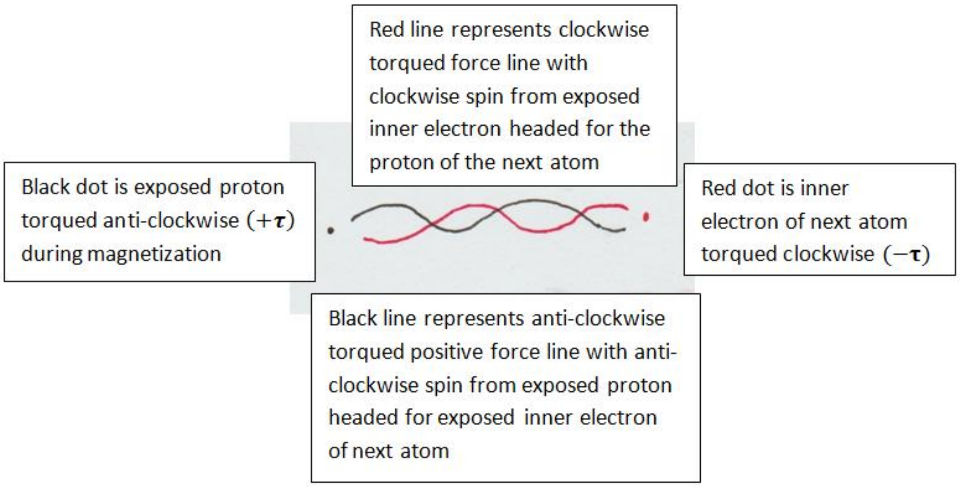

Red line represents clockwise torqued force line with clockwise spin from exposed inner electron headed for the proton of the next atom

Black dot is exposed proton torqued anti-clockwise $(+\boldsymbol{\tau})$ during magnetization

Red dot is inner electron of next atom torqued clockwise $(-\boldsymbol{\tau})$

Black line represents anti-clockwise torqued positive force line with anti-clockwise spin from exposed proton headed for exposed inner electron of next atom

Fig. 6.

Fig. 6 is a diagrammatic representation of how the negative force from an internally exposed magnetized clockwise negatively torqued $(-\boldsymbol{\tau})$ electron $(-e)$ of an atom with a clockwise spin entwines with the positive force from an internal anti-clockwise oppositely torqued $(+\boldsymbol{\tau})$ exposed proton $(+e)$ of the next atom with an anti-clockwise spin inside the magnet. Applying Coulomb's law, the magnetizing force of attraction $\boldsymbol{F}$ between the exposed proton of an atom and the exposed inner electron of the next atom at an inter-atomic distance $\boldsymbol{d}$ meters is

$$F = \frac{k(+e)(-e)}{d^2} = -\frac{ke^2}{d^2} newtons$$

where $\boldsymbol{k}$ **is** the coulomb's constant.

If the number of magnetized atoms at each level of magnetization along the length of the magnet is $\boldsymbol{n}$ and one inner electron of one atom is connected by the opposing forces to the proton of the next magnetized atom, then the total force between the magnetized atoms at each inter-atomic level is

$$F = \frac{kn(+e)n(-e)}{d^2} = -\frac{kn^2e^2}{d^2} newtons \qquad \textbf{Equation (2)}$$

As the temperature drops during cooling, d decreases further and n increases as more electrons of each atom can latch onto the next atoms exposed protons, the above equation shows that this binding magnetic force F increases further and there is no possibility of this stronger binding inter-atomic intra-magnetic force between electrons and protons of neighboring atoms from being expelled laterally from inside the magnet as the Meissner effect.

9. EXTRA-MAGNETIC BEHAVIOR OF EXPOSED PROTON AND INNER ELECTRON DEPENDANT MAGNETIC FORCES

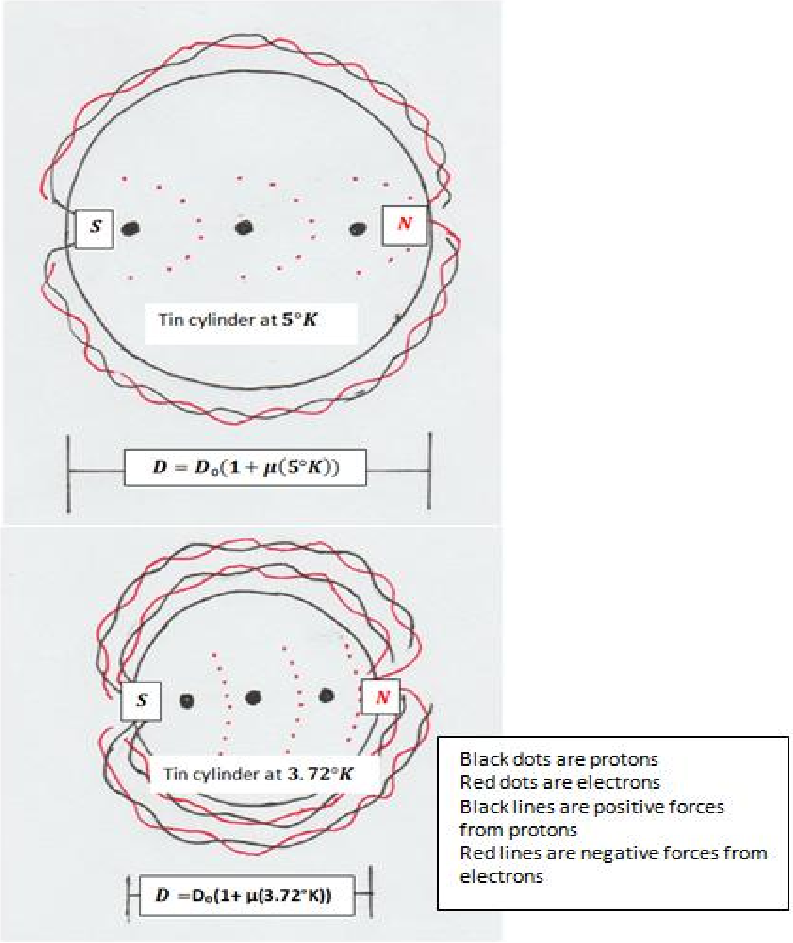

Fig. 7. Above shows the same tin cylinder in two stages of super-cooling at $5°K$ and $.72°K$

$\boldsymbol{D}$ represents the diameter of the tin cylinder in meters which keeps on decreasing with cooling.

As $\boldsymbol{D}_0$ meters is the diameter of the tin cylinder at absolute zero temperature of $°\boldsymbol{K}$.

$\boldsymbol{D} = \boldsymbol{D}_0(\mathbf{1} + \boldsymbol{\mu}(\mathbf{5}°\boldsymbol{K}))$ meters at $\mathbf{5}°\boldsymbol{K}$ and
$\boldsymbol{D} = \boldsymbol{D}_0(\mathbf{1} + \boldsymbol{\mu}(\mathbf{3.72}°\boldsymbol{K}))$ meters at $\mathbf{3.72}°\boldsymbol{K}$ where
$\boldsymbol{\mu}$ is the coefficient of thermal expansion of tin.

The coefficient of thermal expansion of grey tin between room temperature and $-\mathbf{130}°\boldsymbol{C}$ or $\mathbf{143}°\boldsymbol{K}$ is **4.7×10^{-6} per degree** $°\boldsymbol{K}$ and we may use this value in the Meissner experiment.

Fig. 7 represents the temporary magnetization of the tin cylinder when it is placed between the two poles of an electro-magnet in the Meissner experiment. At the critical temperature of about $\mathbf{3.72°K}$, a much larger number of electrons of each atom latch onto the exposed protons of the next atom. This temperature drop results in an increased intra-magnetic force and an increased extra-magnetic force from the two magnetic ends without any change in the applied external electro-magnetic force $\mathbf{B}$ which is constant. *There is no lateral expulsion of any magnetic flux from within the tin cylinder as the Meissner effect*.

If $\boldsymbol{n}$ is the number of exposed inner electrons $(-\boldsymbol{e})$ with a negative torque $(-\boldsymbol{\tau})$ as the negative or north magnetic pole N and an equal number of exposed protons $(+\boldsymbol{e})$ with a positive torque $(+\boldsymbol{\tau})$ as the positive or south magnetic pole S, then the external magnetic force spreads around the tin cylinder half circumference between the two magnetic poles $(\boldsymbol{\pi}.\frac{\boldsymbol{D}}{\mathbf{2}}\ \boldsymbol{meters})$.

As these two magnetic poles are at a direct distance $= \boldsymbol{D}_0(\mathbf{1} + \boldsymbol{\mu}°\boldsymbol{K})$, applying Coulomb's law, the external magnetizing force around the tin cylinder is

$$\boldsymbol{F} = \frac{\boldsymbol{kn(-e)n(+e)}}{\boldsymbol{D^2}} = \frac{\boldsymbol{kn(-e)n(+e)}}{(\boldsymbol{D}_0(\mathbf{1}+\boldsymbol{\mu}°\boldsymbol{K}))^2}\ newtons = -\frac{\boldsymbol{kn^2e^2}}{(\boldsymbol{D}_0(\mathbf{1}+\boldsymbol{\mu}°\boldsymbol{K}))^2} newtons$$

$$\mathbf{1}\boldsymbol{e} \approx \mathbf{1.6} \times \mathbf{10^{-19}}\ Coulombs$$

$$Coulombs\ constant\ \boldsymbol{k} = \mathbf{8.99} \times \mathbf{10^9}\boldsymbol{Nm^2C^{-2}}.$$

$\boldsymbol{\mu}$ is the coefficient of thermal expansion for tin is **4.7 × 10^{-6} per degree** $\boldsymbol{°K}$ **.**

$\boldsymbol{°K}$ represents the absolute temperature on the kelvin scale and
$\boldsymbol{D} = \boldsymbol{D}_0(\mathbf{1} + \boldsymbol{\mu}°\boldsymbol{K})$ is the diameter of the tin cylinder at that temperature.

Thus, the flux/magnetic force seen around the tin cylinder is directly proportional to the square of number of exposed protons at one end, which is also equal to the square of the number of exposed inner electrons at the other end $(\boldsymbol{n^2})$ and is inversely proportional to the square of the diameter of the tin cylinder $(\boldsymbol{D}^2)$.

$$\boldsymbol{F} \infty\, \boldsymbol{n^2} \text{ and } \infty\ \frac{\mathbf{1}}{(\boldsymbol{D}_0(\mathbf{1}+\boldsymbol{\mu}°\boldsymbol{K}))^2}\ .$$

As the absolute temperature $\boldsymbol{°K}$ decreases, the external magnetizing force $\boldsymbol{F}$ increases**.**

The same tin cylinder when cooled to $\mathbf{3.72}\boldsymbol{°K}$ which is the critical temperature, a maximal number of the inner electrons of each magnetized atom latch onto the exposed protons of the next atom and so on and we have an increased magnetic force from the two magnetic poles of the tin cylinder manifesting around the tin cylinder.

The external magnetizing force $\boldsymbol{F} = \frac{\boldsymbol{kn(+e)n(-e)}}{(\boldsymbol{D}_0(\mathbf{1}+\boldsymbol{\mu}°\boldsymbol{K}))^2} = -\frac{\boldsymbol{kn^2e^2}}{(\mathbf{D}_0(\mathbf{1}+\boldsymbol{\mu}°\mathbf{K}))^2} newtons$ **Equation (3)**

With decreasing temperature, the resultant diameter of the tin cylinder $\boldsymbol{D} = \boldsymbol{D}_0(\mathbf{1} + \boldsymbol{\mu}°\boldsymbol{K})$ keeps on decreasing resulting in an increase in the external magnetizing force.

As $\boldsymbol{D}$ is much larger than $\boldsymbol{d}$**,** **Equation (3)** is a small fraction of **Equation (2)**, but the larger intra-magnetic binding force is used up for binding the electrons and protons of the neighboring magnetized atoms. However, **Equation (3)** is enough to explain the increase in external magnetic force on cooling as seen in the Meissner experiment in 1933 and there is no need to resort to the lateral expulsion of magnetic flux to explain the Meissner effect.

The decreased temperature also causes a decreased inter-atomic distance $\mathbf{d}$ which causes an increased number of electrons of one magnetized atom to latch onto the exposed protons of the next magnetized atom resulting in an increased $\mathbf{n}$ which causes an increased external magnetic force at the critical temperature on the outside of the tin cylinder without any lateral expulsion of the intra-magnetic force called the Meissner effect.

At the critical temperature, the inter-atomic distance $\boldsymbol{d}$ has decreased significantly and **Equation (2)** shows that the binding force between the exposed inner electrons of one magnetized atom and the exposed protons of the next magnetized atom is maximal and this stronger internal magnetic force has been used as a binding force and cannot be laterally expelled or *squeezed out as a Meissner effect.*

Please note that $\boldsymbol{n}$ depends on:

-the external applied magnetic force $\boldsymbol{B}$ (which is a constant in the Meissner experiment) and
-is inversely related to the inter-atomic distance inside the tin cylinder which depends on the temperature of the tin cylinder.

Thus, we will have a greater number of exposed electrons at one end of the tin piece torqued in clockwise direction $(-\boldsymbol{\tau})$ manifesting as a clockwise spinning negative force and an equal greater number of exposed protons at the other end of the tin piece torqued in the anti-clockwise direction $(+\boldsymbol{\tau})$ manifesting as an anti-clockwise spinning positive force.

This results in a greater magnetic force effect on the outside as shown in Fig. 7 as the *Meissner effect*, without any magnetic flux being pushed out along the lateral length of the super-cooled tin cylinder at the critical temperature.

10. SUPERCONDUCTIVITY

Superconductivity is a phenomenon of zero electrical resistance occurring in certain materials called **superconductors**, when cooled below a characteristic critical temperature. It was discovered by Dutch physicist Heike Kamerlingh Onnes on April 8, 1911 in Leiden. In a superconductor, the resistance drops abruptly to zero when the material is cooled below its critical temperature. An electric current through a loop of superconducting wire can persist indefinitely with no power source.

Superconductivity will result when due to super-cooling below the critical temperature, the inter-atomic distance of the conductor decreases so that adjacent atoms merge with each other. In this situation, the free valence electrons are almost equidistant from the protons of neighboring atoms and will flow with zero resistance for an indefinite period.

The inter-atomic distance $\boldsymbol{d}$ at a temperature on the Kelvin scale is given by

$$\boldsymbol{d} = \boldsymbol{d}_0(\boldsymbol{1} + \boldsymbol{\mu}°\boldsymbol{K})$$

$\boldsymbol{d_0}$ is the inter-atomic distance at $\boldsymbol{0°K}$.
$\boldsymbol{°K}$ is temperature in Kelvins.
$\boldsymbol{\mu}$ is the coefficient of expansion of the conducting material.

On increasing the temperature of a wire, the inter-atomic distance $\boldsymbol{d}$ increases and there is greater resistance to the flow of outer free electrons or electric current.
Electrical resistance $\boldsymbol{R}$ in Ohms is directly proportional to the absolute temperature $\boldsymbol{°K}$ on the Kelvin scale.

$$Resistance\ \boldsymbol{R}\ (Ohms) \infty\ Temperature\ \boldsymbol{°K}\ (Kelvin\ scale)$$

Cooling the above wire will decrease the inter-atomic distance $\boldsymbol{d}$ and in a supercooled state, there will be no inter-atomic gap and there will be *zero resistance* to the flow of the outer free electrons (electric current) and at or below a critical temperature, we have a super-conducting wire. At this critical temperature, the outer free valence electrons are almost equidistant from the protons of the neighboring atoms due to an absent gap between the atoms and will be able to move with zero resistance across atoms and we will have a *superconductivity state.*

Superconductivity is inversely proportional to the absolute temperature on the Kelvin scale.

$$Superconductivity \infty \frac{1}{°K}$$

From the above discussion, based on Gill's electronic theory of magnetism 1964, we conclude that magnetic susceptibility is directly proportional to the applied magnetic field and it is inversely proportional to the absolute temperature on the Kelvin scale.

11. DISCUSSION

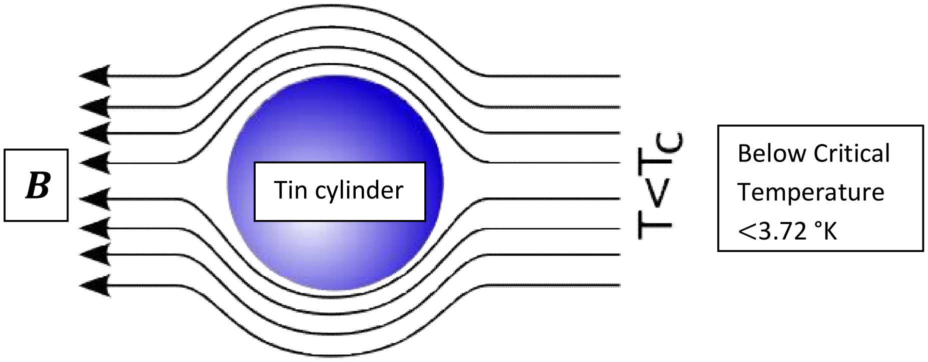

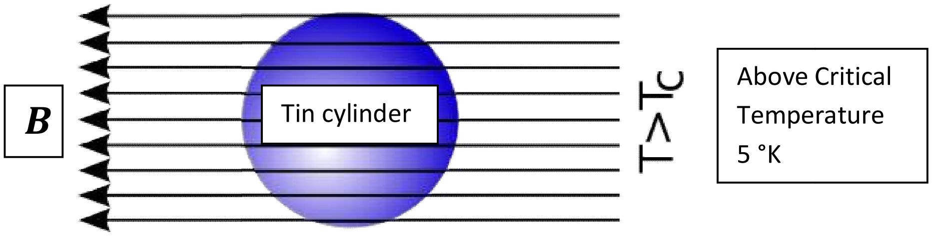

Above is a repeat diagram of Fig. 4 showing the *Meissner effect* due to cooling to $< 3.72°K$. Magnetic field lines, represented as arrows, are excluded from a superconductor when it is below its critical temperature.

Gill's electronic theory of magnetism explains how the magnetic strength in a material can vary with temperature when everything else is a constant.

Meissner applied the conservation of magnetic flux concept by a superconductor and concluded that when the interior field decreases, the exterior field increases and called it the Meissner effect.

The notion of conservation of magnetic flux to explain the increased magnetic flux by expulsion of internal magnetic flux below a critical superconducting temperature as shown in Fig. 4 is wrong. A superconductor with little or no magnetic field within it is said to be in the Meissner state is not a correct concept.

This conservation of magnetic flux without considering the change in the intra-magnetic and outer or extra-magnetic forces due to change in inter-atomic distance of the tin atoms caused by temperature change and its effect on the magnetic force is a mistake.

It has been explained that the even stronger intra-magnetic binding forces due to cooling as calculated by ***Equation 2*** *cannot be expelled as a magnetic flux and there is no Meissner effect.* The increase in external magnetic force outside the tin cylinder is due to cooling of the tin cylinder with liquid helium in the Meissner experiment 1933 as calculated by **Equation 3** and there is no expulsion of magnetic flux from within the tin cylinder to without as a Meissner effect.

Applying Gill's electronic theory of magnetism, the atoms of the tin cylinder have undergone a temporary magnet like change in configuration because of the external applied electromagnetic force. Thus, just by lowering the temperature, we have increased internal magnetic forces in a sequential manner as explained above which are even more strongly merged with neighboring magnetized atoms and cannot be expelled and *the tin cylinder undergoes greater magnetization due to reduced inter-atomic distance manifested at its magnetic ends. It is this greater magnetization which is seen as an increased external magnetic effect or Meissner Effect.*

The levitation of the electron dependent negative or north magnetic pole *N* of a magnet above the super-cooled tin cylinder is because of the dense layer of electrons on the surface of the tin cylinder cooled to the critical temperature.

11.1 Temperature Dependant Stages of Magnetization

Combining Pierre Curies high temperature experiments with the Walther Meissner and Robert Ochsenfeld low temperature experiment 1933 and applying Gill's electronic theory of magnetism 1964 we get the following stages of magnetism:

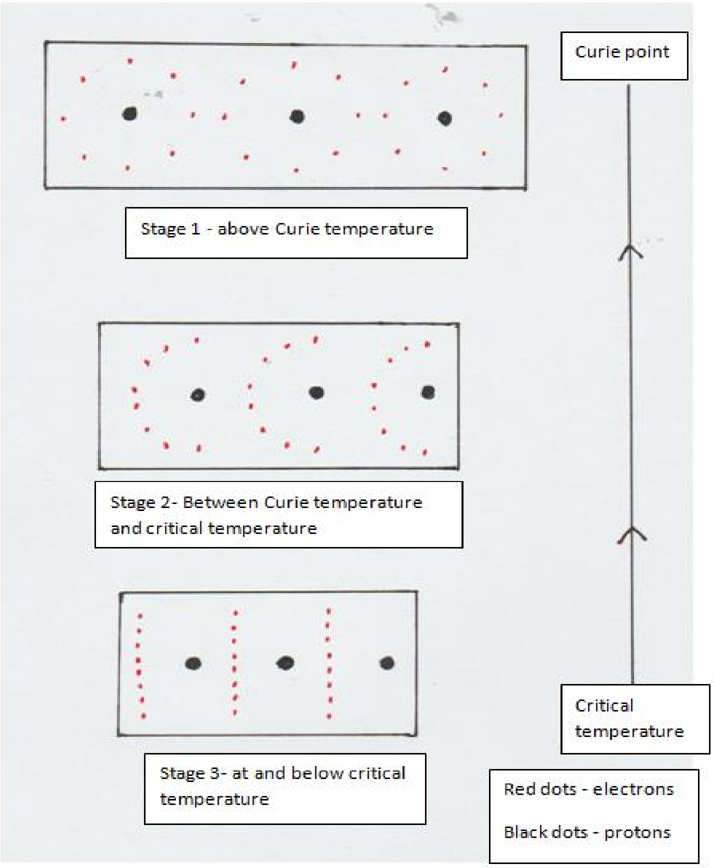

Fig. 8. $\left(B \infty \frac{1}{T}\right)$

In Fig. 8, we have the same metal showing differing magnetic behavior at different temperatures with the same external applied magnetic force $\boldsymbol{B}$ *according to Gill's electronic theory of magnetism 1964.*

Stage 1: This is at and above the Curie temperature and the neighboring atoms due to the increased inter-atomic distance are not able to latch onto one another to behave as a magnet.

Stage 2: Between the Curie temperature and the critical temperature for that material, the exposed inner electrons of a magnetized atom can latch onto the exposed protons of the next atom. There is also an increasing magnetization along with reduction of electrical resistance as the inter-atomic distance keeps on decreasing with decreasing temperature.

Stage 3: At the critical temperature for the material, a larger number of inner electrons of one atom can latch onto the exposed protons of the next atom, as there is no gap between the atoms due to the low temperature. In a super-cooled state, when the atoms of that material have no or minimal gap between them, the outer free valence electrons will flow as an electrical current against zero resistance once started as an electrical flow. The outer free valence electrons can move across these atoms which have no or minimal gap as an indefinite electric current once started due to zero resistance and we have the super-conducting state.

According to Gill's electronic theory of magnetism 1964, the increased magnetic force observed outside the tin cylinder is due to the increased magnetization of the tin due to decreased inter-atomic distance due to lowering of the temperature. Even though the external applied magnetic field $\boldsymbol{B}$ is the same, due to the decreased inter-atomic distance $\boldsymbol{d}$, a larger number of inner electrons of a magnetized atom of tin latch onto the next magnetized atom sequentially and we have a larger number of exposed inner electrons at the north magnetic pole of the magnetized tin and a larger number of exposed protons at the south magnetic pole of the tin piece. *Thus, we have an increased magnetic force outside the tin piece just by cooling without any change in the applied external magnetic field* $\boldsymbol{B}$ *and without any expulsion of the intra-magnetic force from the magnetized tin.*

The **London equations** developed by brothers Frietz and Heinz London in 1935 offered the simplest meaningful description of superconducting phenomena by trying to explain the *non-existent Meissner effect.*

It has been explained in this article that a material does not exponentially expel any internal magnetic fields or magnetic flux as it has been called as it crosses the superconducting threshold. Rather, a decrease in the inter-atomic distance $\boldsymbol{d}$ will prevent any magnetic flux from being expelled to the outside. There might be minimal surface activity as explained by Andre Marie Ampere in 1823 [11] but no expulsion or squeezing out of magnetic flux or Meissner effect.

12. CONCLUSION

Gill's electronic theory of magnetism has helped in explaining that the *Meissner effect* is because of increased external magnetic force around the tin cylinder on cooling. This is due to the increased magnetization due to the decreased temperature causing the decreased inter-atomic distance in the tin cylinder and there is *no expulsion or squeezing out of magnetic flux (Meissner effect) in the 1933 Meissner experiment as previously postulated.*

Curie point and its variability because of a change in the external applied magnetic force and/or temperature has been explained with Gill's electronic theory of magnetism along with some dot product equations.

Superconductivity and levitation of a magnet have been discussed. The relation between electric current and electromagnetic fields around a superconductor has been explained with the help of Gill's electronic theory of magnetism 1964.

Gill's electronic theory of magnetism 1964 explains the interaction between the magnetic forces and the electrical forces and does away with the *asymmetry issue* raised by A. Einstein in 1905 and Richard Feinmann in 1943.

ACKNOWLEDGMENTS

I am grateful to physicist Professor Amitabha Mukherjee (former head of department of Physics, Delhi University) for going over this article with me.

COMPETING INTERESTS

Author has declared that no competing interests exist.

REFERENCES

1. Large Increase of the Curie Temperature by Aymeric Sadoc, Bernard Mercey, Charles Simon, Dominique Grebille, Wilfrid Prellier, and Marie-Bernadette Lepetit
2. Pierre Curie-Biography Nobelprize.org. Nobel Media AB; 2014. Retrieved 14 March 2013.
3. A Treatise on Electricity and Magnetism by James Clerk Maxwell; 1851.
4. Thermal Expansion of Grey Tin by J.Thewlis & A.R.Davley
5. Meissner effect from Wikipedia.
6. Faraday's iron ring experiment 1831 explained with Gill's electronic theory of magnetism 1964 by author ARJPS 2017.
7. The Theory of Superconductivity, Nikolaĭ Nikolaevich Bogoliubov; 1963.
8. The Discovery of Superconductivity Dirk van Delft and Peter Kas.
9. Coulomb's law by Charles Augustin de Coulomb; 1784.
10. Theoretical remark on the superconductivity of metals by A. Einstein
11. Ampère's circuital law by Andre Marie Ampere 1823.

Biography of author(s)

Dr. Avtar Singh Gill
Maimonides Medical Center, Brooklyn, New York, USA.

He is a Delhi University medical graduate who later moved to USA and completed his fellowship in Cardiac Anesthesia from the famous Mount Sinai School of Medicine, New York and is currently working as an Anesthesiologist at Maimonides Medical Center, Brooklyn, New York. As a teenager, he has presented Gill's electronic theory of magnetism in 1964 under his pen name Thakar for which he was awarded a Science Talent Search Certificate in 1965. Delhi University physicist friends have been pushing him towards physics research which he has been doing on again and off again and most of his weekends and vacations for the last few years have been put to useful physics research. He is satisfied that six of his physics related research papers have been accepted with no rejection after a double-blind peer review and maybe seen in the volumes in the American Research Journal of Physics in the last few years under his name.

© Copyright (2021): Author(s). The licensee is the publisher (B P International).

DISCLAIMER

This chapter is an extended version of the article published by the same author(s) in the following journal.
American Research Journal of Physics, 4(1): 1-14, 2018.

Chapter 7

Print ISBN: 978-93-91312-26-8, eBook ISBN: 978-93-91312-34-3

Study on the Complex Angle in Normed Spaces

Volker W. Thürey^{1*}

DOI: 10.9734/bpi/nupsr/v9/9802D

ABSTRACT

We consider a generalized angle in complex normed vector spaces. Its definition corresponds to the definition of the Euclidean angle in real inner product spaces. Not surprisingly it yields complex values as 'angles'. This 'angle' has some simple properties, which are known from the usual angle in real inner product spaces. To do ordinary Euclidean geometry real angles are necessary. We show that even in a complex normed space there are many pure real valued 'angles'. The situation improves yet in inner product spaces. There we can use the theory of orthogonal systems to find many pairs of vectors with real angles, and to do geometry which is based on principles which are already known by the Greeks 2000 years ago.

Keywords: Complex normed space; generalized angle; complex Hilbert space.

We deal with complex vector spaces X provided with a norm $||\cdot||$. To initiate the following constructions we begin with the special case of an inner product space $(X, < . \,|\, . >)$ over the complex field $\mathbb{C}$. It is well known that the inner product can be expressed by the norm, namely for $\vec{x}, \vec{y} \in X$ we can write

$$< \vec{x} \mid \vec{y} > = \frac{1}{4} \cdot \left[\, ||\vec{x}+\vec{y}||^2 - ||\vec{x}-\vec{y}||^2 \;+ \mathbf{i} \cdot \left(\, ||\vec{x}+\mathbf{i}\cdot\vec{y}||^2 - ||\vec{x}-\mathbf{i}\cdot\vec{y}||^2 \,\right) \,\right] ,$$

where the symbol '**i**' means the imaginary unit.

For two vectors $\vec{x}, \vec{y} \neq \vec{0}$ it holds $< \vec{x} \mid \vec{y} > = ||\vec{x}|| \cdot ||\vec{y}|| \cdot < \frac{\vec{x}}{||\vec{x}||} \mid \frac{\vec{y}}{||\vec{x}||} >$. We use both facts to generate a continuous product in all complex normed vector spaces $(X, ||\cdot||)$, which is just the inner product in the special case of a complex inner product space.

Definition 1. *Let $\vec{x}, \vec{y}$ be two arbitrary elements of X. In the case of $\vec{x} = \vec{0}$ or $\vec{y} = \vec{0}$ we set $< \vec{x} \mid \vec{y} > := 0$, and if $\vec{x}, \vec{y} \neq \vec{0}$ (i.e. $||\vec{x}|| \cdot ||\vec{y}|| > 0$) we define the complex number*

$$< \vec{x} \mid \vec{y} > :=$$

$$||\vec{x}|| \cdot ||\vec{y}|| \cdot \frac{1}{4} \cdot \left[\left\| \frac{\vec{x}}{||\vec{x}||} + \frac{\vec{y}}{||\vec{y}||} \right\|^2 - \left\| \frac{\vec{x}}{||\vec{x}||} - \frac{\vec{y}}{||\vec{y}||} \right\|^2 + \mathbf{i} \cdot \left(\left\| \frac{\vec{x}}{||\vec{x}||} + \mathbf{i} \cdot \frac{\vec{y}}{||\vec{y}||} \right\|^2 - \left\| \frac{\vec{x}}{||\vec{x}||} - \mathbf{i} \cdot \frac{\vec{y}}{||\vec{y}||} \right\|^2 \right) \right] .$$

□

It is easy to show that the product fulfils the conjugate symmetry ($< \vec{x}|\vec{y} > = \overline{< \vec{y}|\vec{x} >}$), where $\overline{< \vec{y}|\vec{x} >}$ means the complex conjugate, the positive definiteness ($< \vec{x}|\vec{x} > \geq 0$ and also $< \vec{x}|\vec{x} > = 0$ only for $\vec{x} = \vec{0}$), and the homogeneity for pure real numbers, ($< r \cdot \vec{x} \mid \vec{y} > = r \cdot < \vec{x} \mid \vec{y} >$), and the homogeneity for pure imaginary numbers, ($< r \cdot \mathbf{i} \cdot \vec{x} \mid \vec{y} > = r \cdot \mathbf{i} \cdot < \vec{x} \mid \vec{y} >$), for $\vec{x}, \vec{y} \in X$, $r \in \mathbb{R}$. We express the norm of $\vec{x}$ by $||\vec{x}|| = \sqrt{< \vec{x} \mid \vec{x} >}$. Further we have the identity $< e^{\mathbf{i}\cdot\varphi} \cdot \vec{x} \mid \vec{x} > = e^{\mathbf{i}\cdot\varphi} \cdot < \vec{x} \mid \vec{x} >$, but for different $\vec{x}, \vec{y} \in X$ generally it holds the inequality $< e^{\mathbf{i}\cdot\varphi} \cdot \vec{x} \mid \vec{y} > \neq e^{\mathbf{i}\cdot\varphi} \cdot < \vec{x} \mid \vec{y} >$.

---

[1] *Hegelstr. 101, 28201 Bremen, Germany.*
Corresponding author: E-mail: volker@thuerey.de;

If we switch for a moment to real inner product spaces $(X, <.\,|\,.>_{real})$ we have for all $\vec{x}, \vec{y} \neq \vec{0}$ the usual Euclidean angle

$$\angle_{Euclid}(\vec{x},\vec{y}) \;=\; \arccos\left(\frac{<\vec{x}\,|\,\vec{y}>_{real}}{\|\vec{x}\|\cdot\|\vec{y}\|}\right) \;=\; \arccos\left(\frac{1}{4}\cdot\left[\left\|\frac{\vec{x}}{\|\vec{x}\|}+\frac{\vec{y}}{\|\vec{y}\|}\right\|^2 - \left\|\frac{\vec{x}}{\|\vec{x}\|}-\frac{\vec{y}}{\|\vec{y}\|}\right\|^2\right]\right),$$

which can be defined in terms of the norm, too.

For two vectors $\vec{x}, \vec{y} \neq \vec{0}$ from a complex normed vector space $(X, \|\cdot\|)$ we are able to define an 'angle' which coincides with the definition of the Euclidean angle in real inner product spaces.

Definition 2. *Let $\vec{x}, \vec{y}$ be two elements of $X\backslash\{\vec{0}\}$. We define the complex number*

$$\angle(\vec{x},\vec{y}) \;:=\; \arccos\left(\frac{<\vec{x}\,|\,\vec{y}>}{\|\vec{x}\|\cdot\|\vec{y}\|}\right).$$

This number $\angle(\vec{x},\vec{y}) \in \mathbb{C}$ is called the angle of the pair $(\vec{x},\vec{y})$. □

We state that the angle $\angle(\vec{x},\vec{y})$ is defined for all $\vec{x}, \vec{y} \neq \vec{0}$. Since we deal with complex vector spaces it is not surprisingly that we get complex numbers as 'angles'. For the definition we need the extension of the cosine and arccosine functions on complex numbers. We use two subsets $\mathcal{A}$ and $\mathcal{B}$ of the complex plane $\mathbb{C}$, where

$$\begin{aligned}\mathcal{A} \;&:=\; \{x+\mathbf{i}\cdot y \;\in\mathbb{C}\mid 0<x<\pi,\; y\in\mathbb{R}\} \;\cup\; \{0,\pi\}, \text{ and}\\ \mathcal{B} \;&:=\; \mathbb{C}\backslash\{r\in\mathbb{R}\mid r<-1 \text{ or } r>+1\}.\end{aligned}$$

We have two known homeomorphisms $\cos:\mathcal{A}\xrightarrow{\cong}\mathcal{B}$ and $\arccos:\mathcal{B}\xrightarrow{\cong}\mathcal{A}$. The cosines of the 'angles' are out of the 'complex square' $\mathcal{SQ} := \{r+\mathbf{i}\cdot s\in\mathbb{C}\mid -1\leq r,s\leq +1\}\subset\mathcal{B}$. The values of the 'angles' are from its image $\arccos(\mathcal{SQ})$, which forms a symmetric hexagon (with concave sides) in $\mathcal{A}$. Its center is $\pi/2$, two vertices are 0 and π. A third is, for instance

$$\arccos(1+\mathbf{i}) \;=\; \frac{\pi}{2}-\frac{1}{2}\cdot\left[\arccos\left(\sqrt{5}-2\right)+\mathbf{i}\cdot\log\left(\sqrt{5}+2+2\cdot\sqrt{\sqrt{5}+2}\right)\right] \;\approx\; 0.90-\mathbf{i}\cdot 1.06\,.$$

This 'angle' $\angle$ has eight comfortable properties (`An` 1) - (`An` 8) which are known from the Euclidean angle in real inner product spaces.

Theorem 1. *In a complex normed space $(X,\|\cdot\|)$ the angle $\angle$ has the following properties:*

- *(`An` 1)* $\angle$ *is a continuous map from $\left(X\backslash\{\vec{0}\}\right)^2$ onto a subset of $\arccos(\mathcal{SQ})\subset\mathcal{A}$.*
  For elements $\vec{x},\vec{y}\neq\vec{0}$ it holds that
- *(`An` 2)* $\angle(\vec{x},\vec{x})=0$,
- *(`An` 3)* $\angle(-\vec{x},\vec{x})=\pi$,
- *(`An` 4)* $\angle(\vec{x},\vec{y})=\overline{\angle(\vec{y},\vec{x})}$,
- *(`An` 5) for real numbers $r,s>0$ we have $\angle(r\cdot\vec{x},s\cdot\vec{y})=\angle(\vec{x},\vec{y})$,*
- *(`An` 6)* $\angle(-\vec{x},-\vec{y})=\angle(\vec{x},\vec{y})$,
- *(`An` 7)* $\angle(\vec{x},\vec{y})+\angle(-\vec{x},\vec{y})=\pi$.
- *(`An` 8) For any two linear independent vectors $\vec{x},\vec{y}$ of $(X,\|\cdot\|)$ there is a continuous injective map $\Theta:\;\mathbb{R}\longrightarrow\mathcal{A},\;\; t\mapsto\angle(\vec{x},\vec{y}+t\cdot\vec{x})$. The limits are*
  $\lim_{t\to-\infty}\,\Theta(t)=\pi$ *and* $\lim_{t\to\infty}\,\Theta(t)=0$.

In the following table we note some angles and their cosines. We choose two elements $\vec{x}, \vec{y} \neq \vec{0}$ of a complex normed space $(X, \|\cdot\|)$, and six suitable real numbers a, b, r, s, v, w, with $-\frac{\pi}{2} \leq a, v \leq \frac{\pi}{2}$ and $-1 \leq r, s \leq 1$, such that

$$\angle(\vec{x},\vec{y}) = \tfrac{\pi}{2} + a + \mathbf{i}\cdot b \in \mathcal{A},$$
$$\cos(\angle(\vec{x},\vec{y})) = \cos\left(\tfrac{\pi}{2} + a + \mathbf{i}\cdot b\right) = r + \mathbf{i}\cdot s \in \mathcal{B}, \quad \text{and}$$
$$\angle(\mathbf{i}\cdot\vec{x},\vec{y}) = \tfrac{\pi}{2} + v + \mathbf{i}\cdot w \in \mathcal{A}.$$

Note that the cosines of all angles in the table (third column) have the same modulus $\sqrt{r^2+s^2}$.

pair of vectors	their angle $\angle$	the cosine of $\angle$	the angle for $\vec{x} = \vec{y}$	its cosine for $\vec{x} = \vec{y}$
$(\vec{x},\vec{y})$	$\frac{\pi}{2} + a + \mathbf{i}\cdot b$	$r + \mathbf{i}\cdot s$	0	1
$(-\vec{x},\vec{y})$	$\frac{\pi}{2} - a - \mathbf{i}\cdot b$	$-r - \mathbf{i}\cdot s$	π	-1
$(\vec{y},\vec{x})$	$\frac{\pi}{2} + a - \mathbf{i}\cdot b$	$r - \mathbf{i}\cdot s$	0	1
$(-\vec{y},\vec{x})$	$\frac{\pi}{2} - a + \mathbf{i}\cdot b$	$-r + \mathbf{i}\cdot s$	π	-1
$(\mathbf{i}\cdot\vec{x},\vec{y})$	$\frac{\pi}{2} + v + \mathbf{i}\cdot w$	$-s + \mathbf{i}\cdot r$	$\frac{\pi}{2} - \mathbf{i}\cdot\log\left[\sqrt{2}+1\right]$	$\mathbf{i}$
$(\vec{y},\mathbf{i}\cdot\vec{x})$	$\frac{\pi}{2} + v - \mathbf{i}\cdot w$	$-s - \mathbf{i}\cdot r$	$\frac{\pi}{2} + \mathbf{i}\cdot\log\left[\sqrt{2}+1\right]$	$-\mathbf{i}$
$(\vec{x},\mathbf{i}\cdot\vec{y})$	$\frac{\pi}{2} - v - \mathbf{i}\cdot w$	$s - \mathbf{i}\cdot r$	$\frac{\pi}{2} + \mathbf{i}\cdot\log\left[\sqrt{2}+1\right]$	$-\mathbf{i}$
$(\mathbf{i}\cdot\vec{y},\vec{x})$	$\frac{\pi}{2} - v + \mathbf{i}\cdot w$	$s + \mathbf{i}\cdot r$	$\frac{\pi}{2} - \mathbf{i}\cdot\log\left[\sqrt{2}+1\right]$	$\mathbf{i}$

With given two non-zero vectors $\vec{x}, \vec{y} \in X$ we consider as before the angle $\angle(\vec{x},\vec{y}) = \frac{\pi}{2} + a + \mathbf{i}\cdot b$ with suitable real numbers a, b. Now we express the complex number $\angle(\mathbf{i}\cdot\vec{x},\vec{y})$ in dependence of a and b. For the presentation the real valued cosine and hyperbolic cosine are used, and their inverses arccosine and area hyperbolic cosine. We need the signum function and the natural logarithm. We use abbreviations like cos, cosh, arccos, arcsin, arcosh, sinh, log and sgn.

The result is as follows:

Theorem 2. *In a complex normed space* $(X, \|\cdot\|)$ *we take two elements* $\vec{x}, \vec{y} \neq \vec{0}$. *We assume the angle* $\angle(\vec{x},\vec{y}) = \frac{\pi}{2} + a + \mathbf{i}\cdot b \in \mathcal{A}$, *i.e.* $-\frac{\pi}{2} \leq a \leq \frac{\pi}{2}$. (*If* $a = -\frac{\pi}{2}$ *or* $a = \frac{\pi}{2}$ *since* $\angle(\vec{x},\vec{y}) \in \mathcal{A}$ *it follows* $b = 0$.) *We get*

$$\angle(\mathbf{i}\cdot\vec{x},\vec{y}) \;=\; \frac{\pi}{2} + \frac{1}{2}\cdot\left[-\operatorname{sgn}(b)\cdot\arccos(\mathsf{H}_-) + \mathbf{i}\cdot\operatorname{sgn}(a)\cdot\operatorname{arcosh}(\mathsf{H}_+)\right],$$

with the abbreviations H_- *and* H_+, *where*

$$\begin{aligned}\mathsf{H}_\pm := & \sqrt{\left[\cos^2\left(\frac{\pi}{2}+a\right) + \cosh^2(b) - 2\right]^2 + 4\cdot\cos^2\left(\frac{\pi}{2}+a\right)\cdot\cosh^2(b)} \\ & \pm\left[\cos^2\left(\frac{\pi}{2}+a\right) + \cosh^2(b) - 1\right].\end{aligned}$$

It is worthwhile to look at special cases. We consider a real angle $\angle(\vec{x},\vec{y}) = \frac{\pi}{2} + a$ (i.e. $b = 0$), and an angle on the vertical axis $x = \frac{\pi}{2}$, this means $\angle(\vec{x},\vec{y}) = \frac{\pi}{2} + \mathbf{i}\cdot b$ (i.e. $a = 0$).

Corollary 1. *For a pure real angle* $\angle(\vec{x},\vec{y}) = \frac{\pi}{2} + a$ *with* $-\frac{\pi}{2} \leq a \leq \frac{\pi}{2}$, *i.e.* $b = 0$, *we get a complex angle* $\angle(\mathbf{i}\cdot\vec{x},\vec{y})$ *with a real part* $\pi/2$,

$$\begin{aligned}\angle(\mathbf{i}\cdot\vec{x},\vec{y}) \;&=\; \frac{\pi}{2} + \mathbf{i}\cdot\frac{1}{2}\cdot\operatorname{sgn}(a)\cdot\operatorname{arcosh}\left[2\cdot\cos^2\left(\frac{\pi}{2}+a\right) + 1\right] \\ &=\; \frac{\pi}{2} + \mathbf{i}\cdot\operatorname{sgn}(a)\cdot\log\left[\;\sqrt{\cos^2\left(\frac{\pi}{2}+a\right) + 1} + \left|\cos\left(\frac{\pi}{2}+a\right)\right|\;\right].\end{aligned}$$

Corollary 2. *For an angle* $\angle(\vec{x},\vec{y}) = \frac{\pi}{2} + \mathbf{i}\cdot b$ (*i.e.* $a = 0$) *we get a pure real angle* $\angle(\mathbf{i}\cdot\vec{x},\vec{y})$,

$$\begin{aligned}\angle(\mathbf{i}\cdot\vec{x},\vec{y}) &= \frac{\pi}{2} - \frac{1}{2}\cdot\operatorname{sgn}(b)\cdot\arccos[3 - 2\cdot\cosh^2(b)]\\ &= \frac{\pi}{2} - \frac{1}{2}\cdot\operatorname{sgn}(b)\cdot\arccos[2-\cosh(2\cdot b)] \;=\; \frac{\pi}{2} - \arcsin[\sinh(b)] \;=\; \arccos[\sinh(b)]\,.\end{aligned}$$

Now we consider pairs $(\vec{x},\vec{y})$ with a real valued angle $\angle(\vec{x},\vec{y})$. For a complex normed vector space $(X, \|\cdot\|)$ we define the set of pairs

$$\mathcal{R}_X^{\bullet} := \{(\vec{x},\vec{y}) \mid \vec{x},\vec{y}\in X,\ \vec{x},\vec{y}\neq\vec{0},\ \text{and } \angle(\vec{x},\vec{y})\in\mathbb{R}\}.$$

Let us take two vectors $\vec{x},\vec{y}\neq\vec{0}$. We can prove that there is a real number $\varphi\in[0,2\pi]$ such that $(e^{\mathbf{i}\cdot\varphi}\cdot\vec{x}\,,\vec{y})\in\mathcal{R}_X^{\bullet}$, i.e. the pair has a pure real angle $\angle(e^{\mathbf{i}\cdot\varphi}\cdot\vec{x}\,,\,\vec{y})$.

This fact ensures the existance of many real valued angles even in complex normed spaces. The situation improves further in the special case of complex vector spaces provided with an inner product $< . \mid . >$.

The properties of complex inner product spaces $(X, < . \mid . >)$ have been studied extensively, and such spaces have many applications in technology and physics.

To do ordinary Euclidean geometry we need real valued angles. The idea is simple. We take an orthogonal basis T of $(X, < . \mid . >)$, and we generate $\mathcal{L}(\mathbb{R})(\mathsf{T})$, the set of all finite real linear combinations of elements of T. Let

$$\mathcal{L}(\mathbb{R})(\mathsf{T}) := \left\{\sum_{i=1}^{k} r_i\cdot\vec{x}_i \mid k\in\mathbb{N},\ r_1,r_2,\ldots,r_k\in\mathbb{R},\ \vec{x}_1,\vec{x}_2,\ldots,\vec{x}_k\in\mathsf{T}\right\}.$$

If X is a Hilbert space, i.e. it is complete, we even can use Cauchy sequences (only with real coefficients) from elements of T. It means that we can take the closure $\overline{\mathcal{L}(\mathbb{R})(\mathsf{T})}$ of $\mathcal{L}(\mathbb{R})(\mathsf{T})$ in X. This generates a real linear subspace $\overline{\mathcal{L}(\mathbb{R})(\mathsf{T})}$ of X, where all angles are real.

After that we can consider complex inner product spaces X of finite complex dimension $n\in\mathbb{N}$. Their real dimension is $2\cdot n$, and we state that the maximum dimension of a real subspace of X with all-real angles is n. The real span $\mathcal{L}(\mathbb{R})(\mathsf{T})$ of an orthogonal basis $\mathsf{T}\subset X$ yields an example.

Finally we can demonstrate that real angles are useful to do classical Euclidean geometry. We still use complex inner product spaces $(X, <\cdot\mid\cdot>)$, and we have three well known theorems of the usual geometry. Let $\vec{x},\vec{y}\neq\vec{0}$ be elements of X. We obtain the following three identities

- $\angle(\vec{x},\vec{y}) = \angle(\vec{x},\vec{x}+\vec{y}) + \angle(\vec{x}+\vec{y},\vec{y})$, (*Addition of angles*),
- $\angle(\vec{x},\vec{y}) + \angle(-\vec{x},\vec{y}-\vec{x}) + \angle(-\vec{y},\vec{x}-\vec{y}) = \pi$, (*The sum of inner angles of a triangle is* π),
- $\|\vec{x}-\vec{y}\|^2 = \|\vec{x}\|^2 + \|\vec{y}\|^2 - 2\cdot\|\vec{x}\|\cdot\|\vec{y}\|\cdot\cos(\angle(\vec{x},\vec{y}))$, (*The ‘Law of Cosines’*),

if and only if the angle $\angle(\vec{x},\vec{y})$, and therefore all angles in the above terms are pure real.

ACKNOWLEDGEMENTS

We like to thank Prof. Dr. Eberhard Oeljeklaus, Jeremy Goodsell and Franziska Brown for a careful reading of the paper and suggesting some improvements, as well Wilfried Henning for technical aid.

COMPETING INTERESTS

Author has declared that no competing interests exist.

REFERENCES

[1] Diminnie CR, Andalafte EZ, Freese RW. Angles in normed linear spaces and a characterization of real inner product spaces. Math. Nachr. 1986;129:197-204.

[2] Diminnie CR, Andalafte EZ, Freese RW. Generalized angles and a characterization of inner product spaces. Houston J. Math. 1988;14(4):457-480.

[3] Froda A. Sur l'angle complexe, orienté, de deux vecteurs d'un espace unitaire. Atti Accad. Naz. Lincei Cl. Sci. Fis. Mat. Natur. Rend. Lincei, Classe di Scienze Fisiche, Matematiche e Naturali, Ser. 8. 1961;30:845-853.

[4] Galántai A, Hegedüs C.J. Jordan's principal angles in complex vector spaces. Linear Algebra Appl. 2006;13:589-598.

[5] Gunawan H, Lindiarni J, Neswan O. P-, I-, g-, and D-Angles in Normed Spaces, Institute of Technology Bandung (Indonesia), J. Sci. 2008;40A(1):24-32.

[6] Jeffrey A. Complex Analysis and Applications, 2. Edition, Chapman and Hall/CRC, Boca Raton; 2006.

[7] Miličić PM. Sur le g-angle dans un espace norme. Mat. Vesnik. 1993;45:43-48.

[8] Miličić PM. On the B-Angle and g-Angle in Normed Spaces. J. Inequal. Pure Appl. Math. 2007;8(4):1-18.

[9] NIST Digital Library of Mathematical Functions; 2014.
Available:http://dlmf.nist.gov/

[10] Rudin W. Functional Analysis, 2. Edition, McGraw-Hill; 1991.

[11] Scharnhorst K. Angles in complex vector spaces. Acta Appl. Math. 2001;69:95-103.

[12] Singer I. Unghiuri Abstracte şi Funcţii Trigonometrice în Spaţii Banach, Buletin Ştiinţific, Secţia de Ştiinţe Matematice şi Fizice, Academia Republicii Populare Romîne. 1957;9:29-42.

[13] Thürey VW. A generalization of the euclidean angle. J. of Convex Analysis. 2013;20(4):1025-1042.

[14] Thürey VW. Angles and a classification of normed spaces. Ann. Funct. Anal. 2013;4(1):114-137.

[15] Thürey VW. The complex angle in normed spaces. Revue Roumaine De Mathématique Pures Et Appliquées, TOME LX, Nr. 2015;2:177-197.

[16] Valentine JE, Martin C. Angles in metric and normed linear spaces. Colloq. Math. 1976;34:209-217.

[17] Valentine JE, Wayment SG. Wilson angles in linear normed spaces. Pacific J. Math. 1971;36(1):239-243.

[18] Werner D. Funktionalanalysis. 7. Ausgabe, Springer; 2011.

[19] Wikepedia (German).
Available:http://de.wikipedia.org/wiki/Arkussinus und Arkuskosinus.

Biography of author(s)

Volker W. Thürey
Hegelstr. 101, 28201 Bremen, Germany.

He was born in Bremen, Germany on the 12 of September in the year 1955. After going the usual way of education in a primary school and a high school, he passed the graduation, which in Germany is called 'Abitur'. After this he made a first attempt to get an academic degree, and he studied some chemistry. Afterwards he worked one year in the woods, besides shorter activities. Finally he made an apprenticeship as a mathematical technical assistent at the company Messerschmitt-Bölkow-Blohm. This meant that he learned to program computers. After successfully finishing the apprenticeship he worked in the company for a few years. He started a study at the open university in Hagen, Germany. This was the only possible way to do both mathematics and to earn money. In Hagen he made his Intermediate diploma. He finished the study in Bremen in 1995. The thesis was published in 1998. He continued to focus on mathematics. Finally he received a doctor title in 2018 at the University of Bremen, although he did not planed that when he have started with mathematics 30 years ago. As a result he achieved 8 publications in different scientific journals. The topic was mainly functional analysis.

© Copyright (2021): Authors. The licensee is the publisher (B P International).

DISCLAIMER
This chapter is an extended version of the article published by the same author(s) in the following journal.
Journal of Physics: Conference Series, 490: 012038, 2014.

Print ISBN: 978-93-91312-26-8, eBook ISBN: 978-93-91312-34-3

Assessment of Prospective Physics Teachers' Energy Literacy: A Recent Approach

Muhamad Yusup[1*], Agus Setiawan[2], Nuryani Y. Rustaman[2] and Ida Kaniawati[2]

DOI: 10.9734/bpi/nupsr/v9/9820D

ABSTRACT

Energy literacy is one of the keys to addressing the energy problems in the world today, along with efforts to develop green energy technologies. We need to know how energy-literate the citizens are. Measuring literacy energy among prospective physics teachers is essential because they are the next generation of educators responsible for this problem. Nevertheless, there is no assessment instrument to measure how literate they are. This study aims to develop a framework for the assessment of the prospective physics' teacher. Sample of items developed based on the framework also included in this article.

Keywords: Energy; energy literacy; prospective teachers; assessment framework; physics education.

1. INTRODUCTION

Energy literacy is a growing topic in science education research over the last few decades. The majority of research has concentrated on either determining attitudes toward energy conservation and education or attempting to change attitudes toward energy conservation and education through courses and workshops [1]. Researchers then broadened the domain of energy literacy. DeWaters, Powers, and Graham [2] developed an energy literacy scale for a written Energy Literacy Questionnaire survey. The scale measures energy literacy for secondary students in three domains: cognitive, affective, and behavioral outcomes. Many researchers used this scale in different countries [3–7].

Other researchers [8] developed a framework for energy literacy in four domains by adopting and extending the framework developed by DeWaters and Powers [3]: energy concepts, energy reasoning, low carbon lifestyle, and civic responsibility for a sustainable society. These frameworks, like the former, were designed to be used adequately for assessing energy literacy among middle and high school students.

A pre-service teacher is an essential intervention for the next generation of citizens confronted with sustainability challenges [9]. As a result, addressing energy literacy as part of future teacher preparation is critical. Teacher preparation education has the potential to change human behavior and increase energy literacy [10]. Pre-service teacher education is a good program for effecting this change [9].

The National Science Teachers Association established Science Teacher Preparation Standards [11]. One of the standards stated that science teachers should understand that educated people must be prepared to make decisions and take action on current science-and-technology-related topics of societal concern of general societal interest. For this reason, we believe that an assessment framework to assess physics pre-service teachers' energy literacy is required. The existing frameworks are not adequate because of their intended purpose for middle and high school students.

---

[1] *Physics Education Department, Universitas Sriwijaya, Palembang, Indonesia.*
[2] *Postgraduate School of Universitas Pendidikan Indonesia, Bandung, Indonesia.*
**Corresponding author: E-mail: m_yusup@fkip.unsri.ac.id;*

2. METHOD

We developed the assessment framework in the following steps. Firstly, we established the concept of energy literacy and the characteristics of those who possess it. We used concepts of literacy, several national frameworks for energy education, and relevant studies to create a working concept of energy literacy that can be used to construct an assessment. Secondly, we developed a framework model by matching the criteria with a model of the taxonomy of educational objectives we selected. In selecting the taxonomy of educational objectives, we applied the following procedures. (1) We considered cognitive processes and knowledge domains that former researchers [8,12,13] identified as relevant for energy literacy. (2) We searched among taxonomies of educational objectives [14–20] and chose one that appropriates to be applied for energy literacy assessment.

2.1 Energy Education and Energy Literacy

The role of energy education in instilling knowledge, making connections with the environment and society, cultivating responsibility, and shaping behavior regarding energy issues has gotten a lot of attention [5]. There is no agreement among researchers or curriculum developers about energy education definition. One definition of energy education is a vehicle to help students respond to present and future energy-related concerns, including the political, social, economic, and environmental dimensions [1]. The broad objectives of energy education for students are as follows [21,22].

a) They are becoming acquainted with various forms of energy and their interconversion.
b) They are learning about the role of energy in their daily lives.
c) They are becoming aware that energy is not infinitely available—through this, the methods of conserving energy, augmenting it.
d) They are developing awareness about the nature, cause of energy crises, and methods of overcoming them.
e) They are aware of various types of non-renewable and renewable sources of energy, their resource potential, existing technologies to harness them, the economics and energetics of these technologies, and their socio-cultural and environmental aspects.
f) Making the students appreciate the consequences of various energy-related policy measures.
g) Making the students appreciative of the energy-environment nexus and enable them to evolve holistic solutions to ensure sustainability

The goal of energy education is to develop energy-literate citizens. Energy literacy is an understanding of the nature and role of energy in the universe and our lives. Energy literacy can also apply this understanding to answer questions and solve problems [23]. By reviewing literature [12], [23], we defined an energy-literate person as one who:

a) can trace energy flows and think in terms of energy systems;
b) knows how energy is used in everyday life;
c) can assess the credibility of information about energy;
d) can communicate about energy and energy use in meaningful ways;
e) can make informed energy and energy use decisions and take action based on an understanding of impacts and consequences;
f) understands the impacts that energy production and consumption have on all spheres of environment and society;
g) is aware of the need for energy conservation and the need to develop renewable energy resources; and
h) continues to learn about energy throughout his or her life.

2.2 Choosing an Appropriate Taxonomy for Assessment Framework

We did not use those aforementioned energy-literacy-related assessment frameworks [8, 12] because for three reasons. Firstly, they did not represent a model or a theory of human thought instead of a taxonomy [24]. Secondly, they did not give clear information about at what level of thinking the item of assessment would be addressed. Thirdly, they did not clear about how knowledge type and context are integrated into assessment items.

We examined among the taxonomies [14–20] that could be categorized as a framework, because of their broad use in the world. The criteria we used to select the taxonomy that appropriate for our purpose were:

(1) addresses cognitive, as well as affective, behavioral, and knowledge domain in one integrated model;
(2) makes a clear distinction between the thinking processes and the knowledge; and
(3) be able to predict phenomena of energy behavior.

Employing the above criteria, we found that only Marzano's taxonomy [20], named The New Taxonomy that fulfilled both criteria (1) and (2). The New Taxonomy also gave us a model of behavior that satisfied our criteria (3) and was in line with our definition of energy literacy.

Briefly, The New Taxonomy is a two-dimensional framework having three systems of thinking as one dimension and three types of knowledge as the other dimension. The three systems of thinking are ordered in the following six levels:

Level 6: Self-system
Level 5: Metacognitive system
Level 4: Knowledge utilization (cognitive system)
Level 3: Analysis (cognitive system)
Level 2: Comprehension (cognitive system)
Level 1: Retrieval (cognitive system)

For the purpose of our work, we did not include all three types of knowledge in The New Taxonomy, which are information, mental procedures, and psychomotor procedures. We substituted them with system knowledge, action-related knowledge, effectiveness knowledge [25], and pedagogical content knowledge (PCK) [26]. The first three are forms of declarative knowledge, which is akin to information knowledge in The New Taxonomy. We included PCK in this framework because PCK is a unique type of knowledge to teachers, as this framework is intended. The elaboration of these systems of thinking and types of knowledge are presented in the following section.

3. ORGANIZING THE DOMAINS

The way the domain of energy literacy is organized determines the assessment design, including the test items. As we presented in the previous section, we decided to use The New Taxonomy as a basis of the framework we will develop. The framework comprises five interrelated components: self-system, metacognitive system, cognitive system, knowledge, and contexts. Fig. 1 presents these components.

3.1 Knowledge Domain

Knowledge is needed to solve a particular task. A review of the knowledge domain from existing frameworks for environmental literacy provided the basis for this framework. We adopted the forms of environmental knowledge proposed by Frick et al. [25]. The first form of knowledge is system knowledge. System knowledge is defined as "knowing what." This knowledge usually relates to the question of how energy systems operate or knowledge about energy issues. A typical example is knowledge of the relationship between carbon dioxide (CO_2) and global climate change.

The second form of knowledge is action-related knowledge, defined as ''knowing how'' or knowledge of behavioral options and possible courses of action. Unlike factual knowledge, action-related knowledge is more likely to affect behavior. For example, even if people are aware that CO_2 leads to global warming, they may not be aware of their actions to reduce their CO_2 emissions. The third form of knowledge is effectiveness knowledge, which addresses the relative gain or benefit (i.e., the relative conservational effectiveness) associated with a particular behavior. With this form of knowledge, the focus on action-related knowledge has been extended from mere knowing-how-to conserve to knowing-how-to get the most significant environmental benefit. For example, buying an energy-efficient light bulb is a better way to reduce energy consumption than an incandescent light bulb.

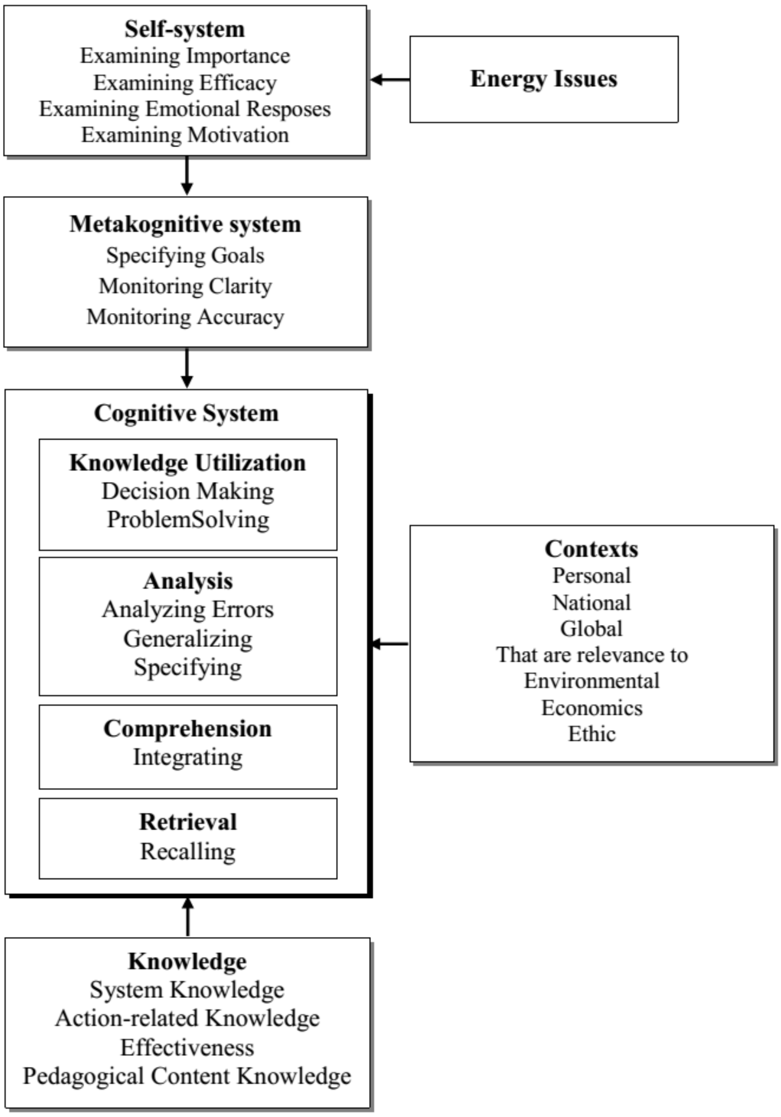

Fig. 1. A framework for assessing energy literacy of pre-service physics teachers (adapted from [20]). Some components from the original framework are excluded due to the purpose of our framework

3.2 Contexts for the Assessment Item

Individuals confront their everyday life situations in which they must use knowledge. Context refers to these situations in which knowledge about energy issues must be applied, ranging from personal to global, combined with environmental, economic, and ethical aspects. The combinations are shown in Table 1. Energy literacy assessment does not assess contexts; instead, it assesses competencies and knowledge in *a* particular context.

Table 1. Contexts for the assessment of energy literacy of preservice physics teachers

	Personal	Local/National	Global
Environment	Environmental impact of energy use	Renewable energy technologies	Climate change
Economics	Energy efficiency	Energy policy	Energy resources and global development
Ethics	Green lifestyle, energy conservation	Energy exploration and production	Global consumption of energy

3.3 Thinking System and Competencies

Competencies are defined as clusters of skills and abilities that may be called upon and expressed in real-world and assessment settings for a specific purpose [27]. Table 2 describes the competencies of energy literate person relate to the six levels of thinking system in The New Taxonomy.

Table 2. The six levels of thinking and competencies relate to each level

System of thinking	Competencies
Level 1: Retrieval	Recognizing nonrenewable and renewable energy resources.
Level 2: Comprehension	Explaining that energy dissipation occurs in every energy transfer. Counting energy consumption of electrical equipment.
Level 3: Analysis	Identifying logic error of information provided about energy. Analyzing the environmental impact of fossil fuel usage.
Level 4: Knowledge utilization	Using information to decide on energy use and purchase. Using information to solve the problem about energy. Proposing personal action to conserve energy.
Level 5. Metacognition	Specifying goals of conserving energy. Specifying the learning objective of the energy concept.
Level 6. Self-system	Examining the importance of energy conservation. Identifying beliefs about one ability to conserve energy. Identifying own emotional response related to energy use. Identifying the overall level of motivation to take action in energy conservation.

4. SAMPLE ITEMS

In this section, examples of the item of energy literacy assessment for pre-service physics teachers are presented.

Question 1: Air Conditioner (AC)

I feel annoyed to find AC in the classroom is on whereas no people there.

A. Always B. Often C. Sometimes C. Never

The categorization for sample Question 1 is presented in Table 3.

Table 3. Framework categorization for sample Question 1

Categories	Framework
Knowledge type	Action-related knowledge.
Competency	Identifying own emotional response related to energy use.
Context	Personal, economics.

Question 2: Air Conditioner (AC)

The human body uses energy at the rate of approximately 100 W when at rest. From chemical energy in our body's stores, this energy is ultimately converted entirely to thermal energy, which is then transferred as heat to the environment. Estimate what BTU/hour of AC you need for a lecture room if its capacity is about a hundred people to take account of transferred thermal energy.

The categorization for sample Question 2 is presented in Table 4.

Table 4. Framework categorization for sample Question 2

Categories	**Framework**
Knowledge type	System knowledge.
Competency	Using information to decide on energy use and purchase.
Context	Personal, economics.

Question 3: Air Conditioner (AC)

One day, you are asked by your father, who is with no science background, to accompanying him to buy an AC that will be used in the small guest room of your home. He tells you that he wants to buy it cash and he has IDR 3.000.000 for its budget. At the electronic store, you find many kinds of AC with a similar specification but differ in power consumption and price, as shown in the table below.

Brand	**Power (watts)**	**Price (IDR)**
A	795	2.900.000
B	840	2.700.000
C	900	2.600.000
D	925	2.500.000

Based on the table above, and only consider both its power consumption and price, which brand of AC will you recommend your father to buy? Give your reason.

The categorization for sample Question 3 above is presented in Table 5.

Table 5. Framework categorization for sample Question 3

Categories	**Framework**
Knowledge type	Effectiveness knowledge
Competency	Using information to decide on energy use and purchase.
Context	Personal, Economics

5. SUMMARY

The purpose of this paper is to develop an assessment framework to measure prospective physics teachers' energy literacy. Due to an energy literate person who has energy knowledge and can use his/her knowledge, we chose The New Taxonomy of Educational Objectives [20], which satisfied our criteria, as a basis for the framework. The framework comprises knowledge domain, context, and three systems of thinking. For the knowledge domain, we substituted the original in The New Taxonomy with system knowledge, action-related knowledge, and effectiveness knowledge, which is akin to declarative knowledge. Assessment items are constructed in the personal, local/national, and global context related to the environment, economics, and ethical aspects. Competencies are assessed with relation to the six levels of the thinking system (i.e., self-system, metacognition, knowledge utilization, analysis, comprehension, and retrieval). Sample items show that the framework developed applicable for assessment items to measure the energy literacy of prospective physics teachers.

COMPETING INTERESTS

Authors have declared that no competing interests exist.

REFERENCES

1. Morrisey JT, Barrow L. A review of energy education: 1975 to NEED 1981. Sci. Educ. 1984;68(4):365–379.
2. DeWaters JE, Powers SE, Graham M. Developing an energy literacy scale; 2007.
3. DeWaters JE, Powers SE. Energy literacy of secondary students in New York State (USA): A measure of knowledge, affect, and behavior. Energy Policy. 2011;39(3):1699–1710, Mar. DOI: 10.1016/j.enpol.2010.12.049.
4. Lay YF, Khoo CH, Treagust DF, Chandrasegaran AL. Assessing secondary school students' understanding of the relevance of energy in their daily lives. Int. J. Sci. Educ. 2013;8(1):199–215.
5. Chen SJ, Chou YC, Yen HY, Chao YL. Investigating and structural modeling energy literacy of high school students in Taiwan. Energy Effic. 2015;8(4):791–808, Jul. DOI: 10.1007/s12053-015-9327-5.
6. Lee LS, Lee YF, Altschuld JW, Pan YJ. Energy literacy: Evaluating knowledge, affect, and behavior of students in Taiwan. Energy Policy. 2015;76:98–106. DOI: 10.1016/j.enpol.2014.11.012.
7. Bodzin AM, Fu Q, Peffer TE, Kulo V. Developing energy literacy in us middle-level students using the geospatial curriculum approach. Int. J. Sci. Educ. 2013;35(9):1561–1589. DOI: 10.1080/09500693.2013.769139.
8. Chen K, Huang S, Liu S. Devising a framework for energy education in Taiwan using the analytic hierarchy process. Energy Policy. 2013;55:396–403.
9. Warren AEFRWALM. Building sustainability literacy among preservice teachers: An initial evaluation of a sustainability courses designed for K-8 educator. in Educating science teachers for sustainability, S. K. Stratton, R. Hagevik, A. Feldman, and M. Bloom, Eds. New York: Springer. 2015;49–67.
10. Zografakis N, Menegaki AN, Tsagarakis KP. Effective education for energy efficiency. Energy Policy. 2008;36:3226–3232. DOI: 10.1016/j.enpol.2008.04.021.
11. National Science Teachers Association. Standards for science teacher preparation; 2003. Available:http://www.nsta.org/pdfs/NSTAstandards2003.pdf.
12. DeWaters J, Powers S. Establishing measurement criteria for an energy literacy questionnaire. J. Environ. Educ. 2013;44(1):38–55.
13. James EO, Robinson M, Powell RR. Beyond STS : An energy education curriculum context for the 21st century. J. Sci. Teacher Educ. 1994;5(1):6–14.
14. Bloom BS, Engelhart MD, Furst EJ, Hill WH, Krathwohl DR, Eds., Taxonomy of educational objectivities: The classification of educational goals. Handbook I: Cognitive domain. New York: David McKay; 1956.
15. Krathwohl BB, Bloom DR, Masia BS. Taxonomy of educational objectives Book 2 Affective Domain. New York: Longman; 1964.
16. Haladyna TM. Writing Test items to evaluate higher order thinking. Boston, MA: Allyn & Bacon, 1997.
17. Hannah LS, Michaelis JU. A comprehensive framework for instructional objectives: A guide to systematic planning and evaluation. Reading, MA.: Addison Wesley; 1977.
18. Biggs J, Collis K. Evaluating the quality of learning: The SOLO taxonomy. New York: Academic Press; 1982.
19. Anderson LW, et al. A taxonomy for learning, teaching and assessing. A Revision of Bloom's Taxonomy of Educational Objectives. New York: Addison Wesley; 2001.
20. Marzano RJ, Kendall JS. The new taxonomy of educational objectives, Ed. Kedua. Thousand Oaks: Corwin Press; 2007.
21. Baluragi DR. Teaching methodology in energy education. in Energy Resources in Science Education, D. F. Kirwan, Ed. Oxford: Pergamon Press. 1987;21–22.
22. Kandpal TC, Garg HP. Energy education. Appl. Energy. 1999;64:71–78.

23. U.S. Department of Energy. Energy literacy: Essential principles and fundamental concepts for energy education. The U.S Department of Energy, Washington; 2012.
24. Anderson JR. The adaptive character of thought. Hillsdale, New Jersey: Lawrence Erlbaum, 1990.
25. Frick J, Kaiser FG, Wilson M. Environmental knowledge and conservation behavior: Exploring prevalence and structure in a representative sample. Pers. Individ. Differ. 2004;37(8):1597–1613.
26. Shulman LS. Those who understand: Knowledge growth in teaching. Educ. Res. 1986;15(2):4–14.
27. Hollweg KS, Taylor JR, Bybee RW, Marcinkowski TJ, McBeth WC, Zoido P. Developing a framework for assessing environmental literacy. North American Association for Environmental Education, Washington, DC; 2011, [Online].
Available: http://www.naaee.net.

Biography of author(s)

Muhamad Yusup
Physics Education Department, Universitas Sriwijaya, Palembang, Indonesia.

Research and Academic Experience: He completed his doctorate in science education from Universitas Pendidikan Indonesia in 2018. He is a lecturer in the physics education department at Universitas Sriwijaya. The disciplines covered include physics teaching and learning, as well as assessment. The research conducted is mainly on these topics.

Research Area: Energy literacy, socioscientific issues, assessment in science education, and Rasch model.

Number of Published papers: Fourteen articles have been published in Indonesian national journals and international proceedings.

Agus Setiawan
Postgraduate School of Universitas Pendidikan Indonesia, Bandung, Indonesia.

Research and Academic Experience: He holds a PhD in material physics from Tohoku University and actively conducts teaching and research in the field of material physics, physics education and TVET. He has attended various professional trainings as follows: (1) Applied Approach for Professional Lecturer- UPI Indonesia (1994) (2) Training for advising and supervising Master and PhD students - Monash University (2011), (3) Site Visit to 8 most outstanding TVET Institution in Germany- RCP Project-GIZ Germany (2012). (4) Training on change management for TVET institutions- NYP Singapore & GIZ Germany (2013).

Research Area:
1. Materials Physics, especially physics of electronic materials.
2. Physics education, especially higher order thinking skills (HOTS) development.
3. TVET (Technical and Vocational Education and Training) development.

Number of Published papers: Scopus: 96 Articles, 510 Citations, 12 H-Index, 14 i10-Index
Google Scholar: 250 Articles, 1156 Citations, 19 H-Index, 36 i10-Index

Special Award: The Best UPI-researcher for fundamental research scheme in 2006

Any other remarkable point(s):
1. Vice Dean for Academic and Student Affairs, Faculty of Technology and Vocational Education Universitas Pendidikan Indonesia (2009-2012).
2. Dean of Faculty of Technology anf Vocational Education Universitas Pendidikan Indonesia (2012-2016)
3. Vice Director for Academic and Student Affairs, School of Postgraduate Studies, Universitas Pendidikan Indonesia (2021-2024)
4. Vice President of RAVTE (Regional Association for Vocational and Technical Education) in Asia (2014- now)

© Copyright (2021): Author(s). The licensee is the publisher (B P International).

DISCLAIMER
This chapter is an extended version of the article published by the same author(s) in the following conference proceeding.
IOP Conf. Series: Journal of Physics: Conf. Series, 877 (2017) 012014.

Print ISBN: 978-93-91312-26-8, eBook ISBN: 978-93-91312-34-3

Recent Development of Intelligent Shunt Fault Classifier for Nigeria 33-kV Power Lines

A. A. Awelewa[1] and P. O. Mbamaluikem[2*]

DOI: 10.9734/bpi/nupsr/v9/8877D

ABSTRACT

This paper presents a new approach to using artificial neural networks (ANNs) in improving the protection of transmission lines. The proposed method uses instantaneous values of voltages and currents during normal and fault conditions on a transmission line as inputs to four different neural network structures. The structures are then aptly combined to yield a system that can detect and classify shunt faults with improved efficiency. The details of the design procedure as well as various simulations carried out are provided in the paper. The performance of the developed system is evaluated using two performance indices, viz., accuracy and mean square error (MSE), and the results show that this approach is capable of detecting and classifying all possible shunt faults on the 33-kV Nigeria power lines in less than 1ms with high level of accuracy. The performance of the system, when tested under various shunt fault types with varying resistances and distances, shows that the system can be used to improve distance line protection in 33-kV Nigeria power line.

Keywords: Artificial neural network; fault detection; fault classification; transmission line; distance protection.

1. INTRODUCTION

Electric power systems generally have maintained a sustained rate of development due to increased usage of electrical energy and this has partly given rise to erection and installation of more power lines – both in number and length [1]. Amongst all the possible solutions, Electrical Energy Storage (EES) has been recognized as one of the most promising approaches [2-4]. The steady and reliable supply of this electrical energy from the power plants to the end users is paramount to utility operators. In conveying the power generated via the power lines (networks of interconnected electrical conductors that convey electrical power from different generating plants to the grid and from the grid to different substations in a varying degree of voltages in order to meet the extremely large number of load demands), the network sometimes encounters faults. These Faults are unavoidable sudden disturbances that can cause an abnormally high amount of current to flow on the power lines, and if left for a while, it may cause severe damage to the entire power system network [5]. Overhead power line (OHPL) faults may be broadly classified into series faults and shunt faults. These faults may be triggered by lightning strokes, dropping of jumper cable, sudden removal of a load from a line, wind storms, trees growing up to or falling across power lines, vehicles running into the towers or poles, birds short circuiting the conductor lines, vandalism, etc. These systems do not perform well with branched transmission lines because of line reflections at the branching points, and neither with parallel lines because of the mutual coupling of adjacent circuits [6]. Furthermore, the overview of faults classification on power lines is depicted in Fig. 1.

1.1 Series or Open Circuit Faults

A fault is said to be an open circuit or series fault if there is an unbalanced series impedance condition in the lines due to one or two broken lines. Practically speaking, open circuit faults occur when one or

---

[1] *Department of Electrical and Information Engineering, Covenant University, Ota, Ogun State, Nigeria.*
[2] *Department of Electrical/Electronics Engineering, Federal Polytechnic Ilaro, Ilaro, Ogun State, Nigeria.*
**Corresponding author: E-mail: peter.mbamaluikem@federalpolyilaro.edu.ng;*

two lines that are controlled by breakers open as against the three lines opening simultaneously. Also, whenever one or two electric power lines are broken or whenever one or two jumper cables of power lines are opened, the series fault is said to have occurred.

1.2 Shunt or Short Circuit Faults

Shunt faults occur as a result of insulation breakdown between the lines, and/or between the lines and the earth. Sequel to this, the three lines short circuit fault is the insulation breakdown between all the three lines. The line-to-line faults are a short circuit or insulation breakdown between either of the two phases. This may be caused by ionization of air around the line conductors or when lines come into physical contact with each other. The single line-to-ground fault is a shunt circuit or insulation breakdown between one of the phases and ground which often results from physical contact. The double line-to-ground fault is an insulation breakdown between any of the two phases and the earth i.e. a situation where any two of the lines come into contact with each other and the ground. Shunt faults are further classified as symmetrical or asymmetrical faults. Fig. 2 illustrates single line diagram of different types of shunt faults.

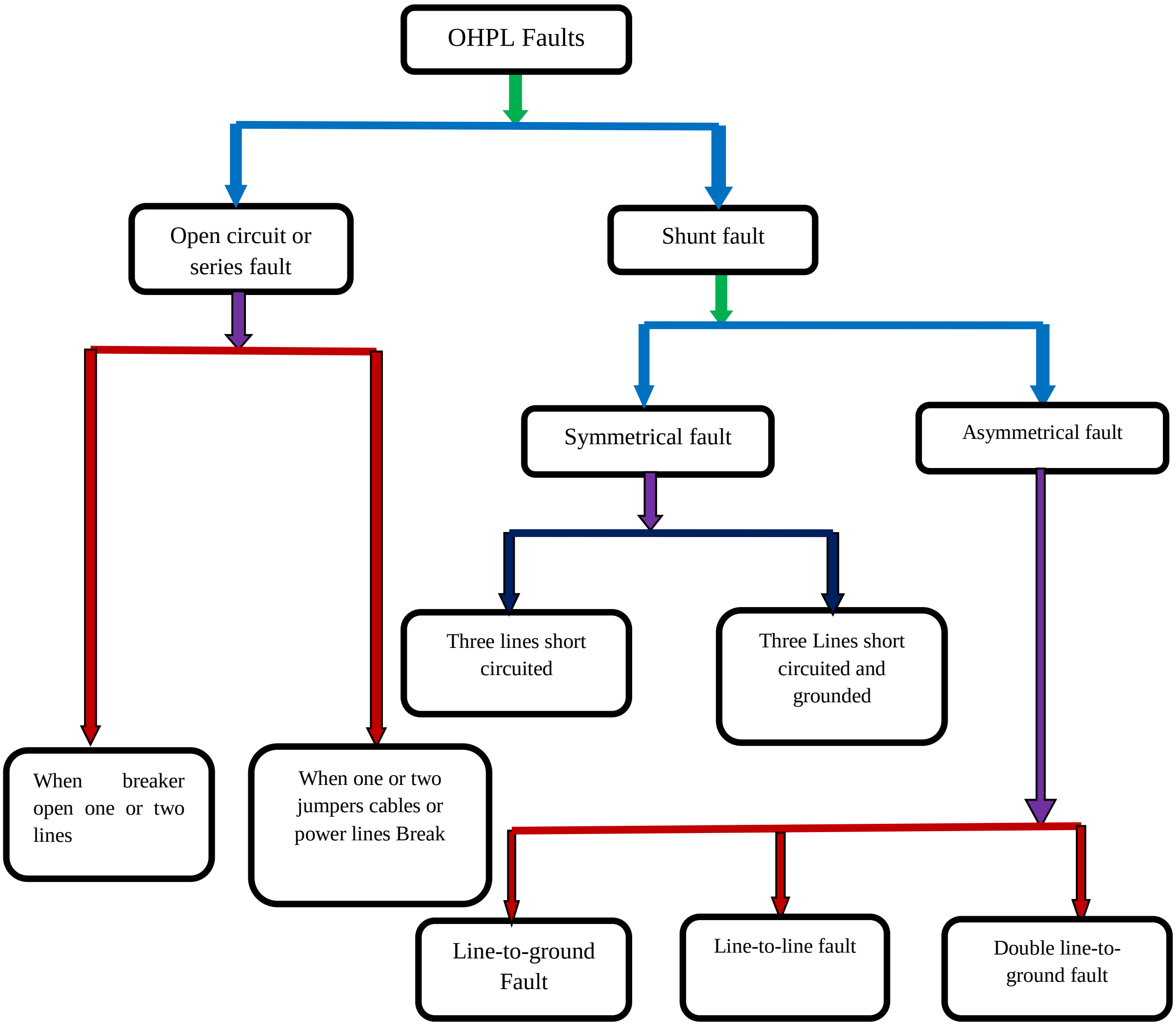

Fig. 1. Categories and subcategories of shunt faults

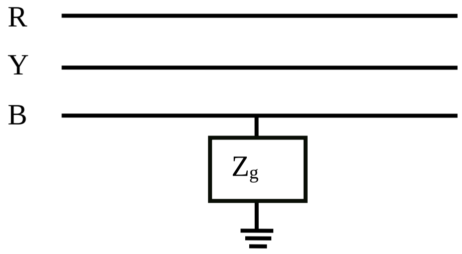

(a): Line-to-ground fault

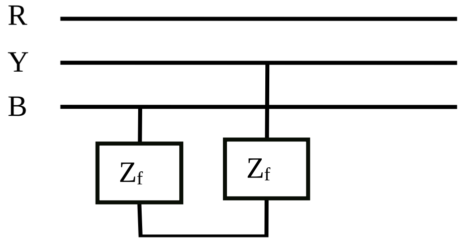

(b): Line-to-line fault

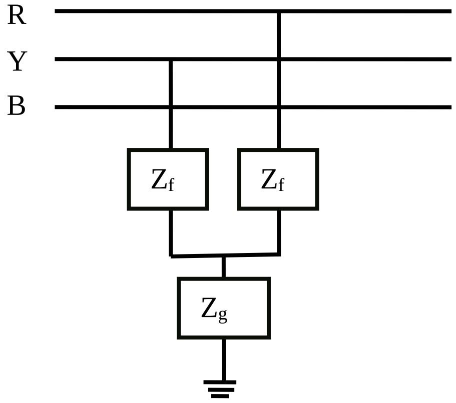

(c): Double line-to-ground fault

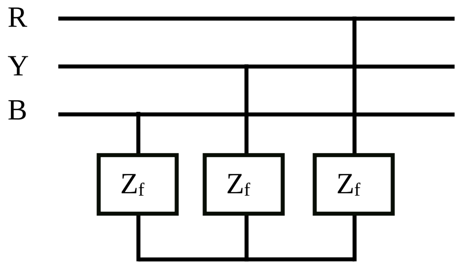

(d): All the lines short

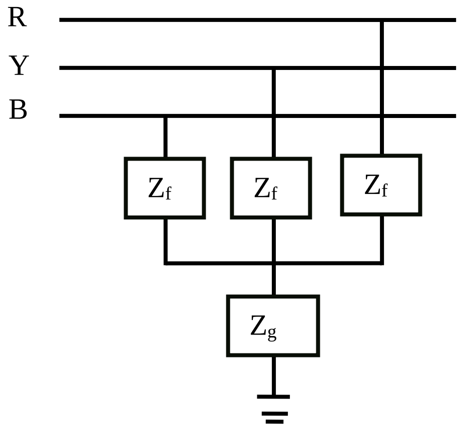

(e): All the lines short circuited to

Fig. 2. Single line representation of shunt faults

The probable occurrence of faults on transmission lines has necessitated the use of a detection and classification system that can aid speedy restoration of power supply on an event of power outage, thereby bringing about optimal utilization of electric power generated and consequent reduction in economic loss. In Nigeria, power outages along the 33-kV power lines (the main link between the 11-kV distribution lines and the 132-kV sub-transmission lines) are very high and it can stay for days or even months before such can be noticed and power restored by the distribution company of Nigeria (DISCO) [7]. This is because the 33-kV Nigerian power network is characterized with long lines which often pass through bushes far off from sight, and there is no system to detect the occurrence of faults on it. To this end, an intelligent system that is capable of detecting and classifying faults is needed, hence the artificial neural network (ANN).

2. ARTIFICIAL NEURAL NETWORK

Artificial Neural Network (ANN) is inspired by the way biological neural systems work. They are parallel computational systems and are made of several processing elements connected together in a particular way, to perform a particular task. ANNs are massively paralleled and have the ability to learn from training data and generalize to new situations. This makes them efficient and robust for real-world applications, hence, they are configured to perform tasks analogous to biological brains.

The structure of a biological neuron is as shown in Fig. 3 and Table 1 depicts an analogy between the biological neuron and the artificial neuron.

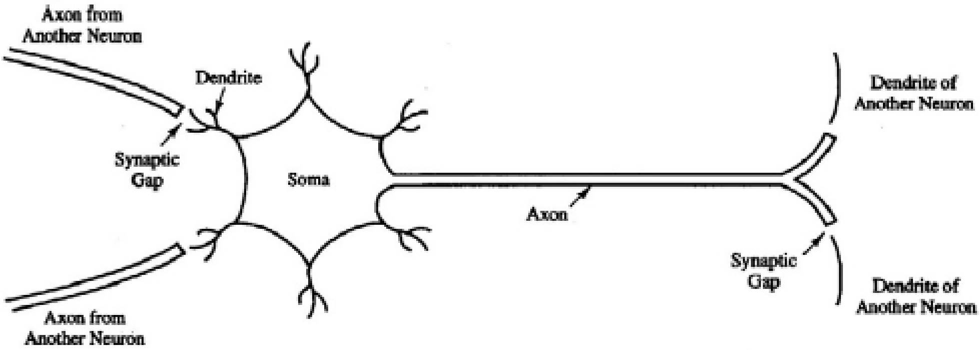

Fig. 3. Typical biological neuron

Table 1. Analogy between biological and artificial neural network

S/N	Biological neural network	Artificial neural network
1	Soma	Neuron
2	Dendrite	Input
3	Axon	Output
4	Synapse	Weight

Over the years, the popularity of ANNs vis-a-vis other methods for fault diagnosis in overhead electrical power lines has steadily increased. The following unique characteristics gave ANN an edge in the artificial intelligent world:

i. Information processing can be carried out in a parallel distributed manner because it is made of massive interconnection of elementary processing units
ii. ANN can be used to solve problems that are inherently nonlinear
iii. ANN approach requires no prior knowledge functions relating the problem variables.
iv. ANN is more tolerant to noise.
v. ANN has the ability to handle situations of incomplete information and corrupt data.

Besides all these, the typical characteristic of ANNs to capture and retain dynamic changes in the power systems and be retrained online makes any ANN-based relaying protection system insusceptible to system parameter variations [8,9]. Hence, ANN learns to produce an output based on a given input data. The training of the network is accomplished by sequentially applying input vectors while adjusting network weights accordingly. The network weight converges gradually as the training (adjustment of different weights) progresses to values that will enable each input vector to produce the target. Fig. 4 illustrates the model of a neuron.

Fig. 4 consists of an input layer, P_1 - P_n representing the input data to the model, a processing neuron and an output layer, γ representing the response of the model. The input is connected to the neuron via the adaptable weights, W_1 - W_n and bias, b. This neuron model can be illustrated by a function that calculates its output as a function of the inputs to it. Thus, the output of the neuron is given as:

$$\mathrm{Z} = \sum \mathrm{W_i P_i} + \mathrm{b}$$

Afterward, a nonlinear transfer function, *f* is applied to the weighted sum and this produces the artificial neuron's output, γ as:

$$\gamma = f(\mathrm{Z})$$

The transfer function is one of the major key factors that determine the capability of an artificial neural network to approximate functions. The appropriate transfer function is chosen based on the application's requirements. The commonly used types of activation functions are; linear activation function, sigmoid activation function, and radial activation function. The sigmoid transfer function was chosen for this work since the work is a nonlinear problem.

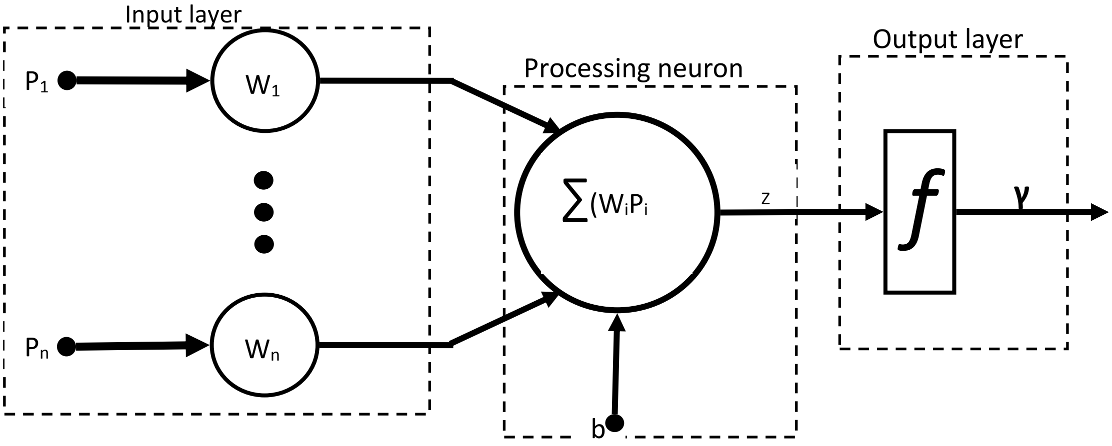

Fig. 4. The model of a neuron

2.1 Artificial Neural Network Topology

Artificial neural network (ANN) topology is simply patterns of connections between the neurons and the transmission of data. It is of two types (1) Recurrent network topology (2) Feed-forward network topology.

Recurrent Networks Topology: Here, neurons are interconnected in such a way that data can flow back from one into another. This means that there are feedback connections.

Feed-Forward Network Topology: In the feed-forward network topology, flow of data from input to output is purely in a forward direction (i.e. unidirectional flow of information). Hence, there is no room for feedback connection between the input and the output. In this study, feed-forward neural network topology (Multi-layer Perceptron being one of the most commonly used feed-forward network topologies) was used due to its simplicity of connection with a well-known learning algorithm.

2.2 Multi-Layer Perceptron

Perceptron is dated back to the McCulloch-Pitts model in the 1940's and it is the simplest and easiest kind of a single layer network of artificial neural network. Rosenblatt worked on this model and in 1961 created many versions of it. Perceptron is the network whose weights and biases could be adjusted accordingly to learn to produce the correct target or output corresponding to the input vector. This network became accepted because of its capability to generalize. In the perceptron model, each outer input is weighted with an appropriate weight, and the sum of the weighted inputs is sent to the linear transfer function, which also has an input of unity as the bias. The linear transfer function is used to return output as a 0 or 1. The perceptron neuron produces the output 1 if the net input into the transfer function is equal to or greater than 0; otherwise, it produces 0. The principal weakness of the perceptron being a single layer network is that it can only solve problems that are linearly separable. But in reality, the real world problems are nonlinear in nature. This limitation was overcome by the development of multi-layer perceptron. The connection of one input layer of McCulloch-Pitts neurons feeding forward to one output layer of McCulloch-Pitts neurons is referred to as Multi-Layer Perceptron (MPL). The MLP consists of at least three layers of neurons fully interconnected together.

A typical example of MLP is the three layer network of Fig. 5, which contains the input layer, hidden layer, and output layer.

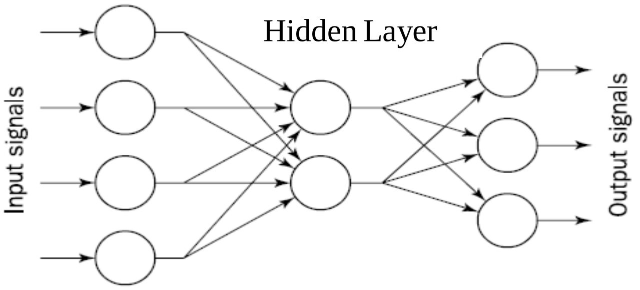

Fig. 5. Structure of a simple MLP

MLP uses learning algorithm during its training process. Hence, the three (3) most widely used MLP algorithms by researchers for fault detection, classification, and location in electric power lines are: scaled conjugate gradient, gradient descent, and the Levenberg-Marquardt algorithm. The basic MLP algorithm follows these procedures:

1. Set all the weights to random numbers between −1 and +1 to initialize the network.
2. Present the first training pattern, and get the output.
3. Compare the output of the network with the target.
4. Compute the error by taking the average difference between the target and the output vector and transmit it back to the hidden and input layer if need be.
5. Repeat step 2 and step 3 for each pattern in the training set to complete one epoch (iteration) and for a designated number of epochs, until the error drops down to a specified limit.

2.3 The Learning Approach

The successful application of a neural network in any field is dependent on the weights to achieve the target. This process of weight determination is known as learning or training. Training is one of the two important steps towards building an intelligent fault locator using the artificial neural network and it is the process whereby the neural network learns to map the input into the output based on a given input data. Hence, a set of data referred to as the training data set is needed, to train the neural network. The training of the network is accomplished by sequentially applying input vectors while adjusting network weights accordingly. The network weight converges gradually as the training (adjustment of different weights) progresses to values that will enable each input vector to produce the target. In this way, the neural network learns what the output should be when a particular set of input is fed into it. The ANN gradually learns the training set and bit by bit develop an ability to generalize upon this data. Having generalized, the ANN will in due course be able to produce an output when a new data set is provided to it. As the training progresses, the ANN minimizes the performance function which in this case is the Mean Square Error. This is so because it is a feedforward network and usually feedforward networks make use of Mean Square Error for its performance characteristic evaluation. For fault detection and classification on power lines, the input data are the three phase voltages and currents which are scaled with respect to their corresponding post and pre-fault values. The outputs of each of the training depend upon what the neural network was trained for.

In this work, the output may either be the fault condition (i.e. Fault or no fault), or the type of fault (i.e. R-G, Y-G, etc) on the power line. The data set for training is obtained by each fault case at a varying resistance of (0.25, 0.5, 0.75, 5, 10, 20, 30 and 50) Ohms respectively and at different locations (at an interval of 2 km) along the 140 km transmission line under consideration. Thus, 560 different fault cases for each of the ten (10) kinds of faults were obtained by simulation. In training the ANN to perform different tasks, sequential feeding of the input-output pair was adopted with the supervised learning. In supervised learning (learning where the input data set and the target values are both known before the training of the ANN), the network weights are modified iteratively with the aim of minimizing the error between a given set of input data and their corresponding target values. Fig. 6 shows the supervised learning approach for a feedforward neural network.

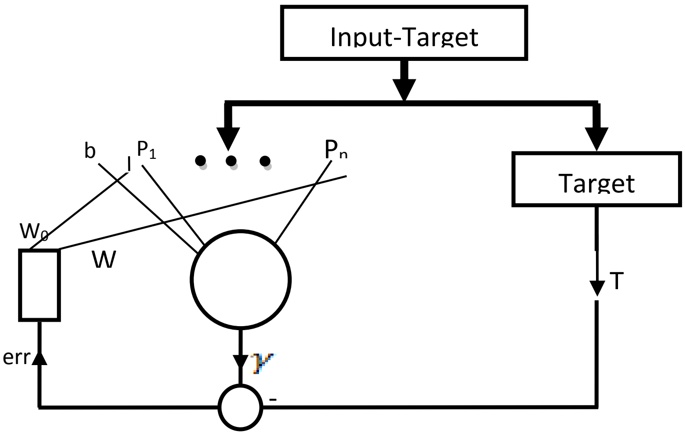

Fig. 6: The supervised learning approach for a feedforward NN

Moreover, the set of input-target data pair that will be used to train the neural network is obtained using the modeled 33-kV Nigeria power lines in Simulink/Matlab 2015a.

2.4 The Testing Process

Testing of the ANN is of key importance to ensure that the trained network can generalize well enough to produce the desired target when new set of data outside the one used in training the model is presented to it. The Neural Network toolbox in Simulink/Matlab partitions the acquired set of data provided to it, into training data set, validation data set, and the testing data set in 70:15:15 percent ratio respectively. The training data set as earlier mentioned is used to train the network. The validation data set is provided to the network input only during the training process. The error in validation data set is monitored throughout the training process and this error increases whenever the network starts overfitting the data. Moreover, if the number of validation fails increase beyond a particular set value, the training process stops and the network returns to the minimum number of validation errors. Furthermore, the test data set is used by the system to test the performance of the trained network. If the minimum value of MSE is reached by the test data set at an appreciably different iteration than the validation data set, perhaps, the neural network may likely not be able to perform satisfactorily. Finally, there are several methods that are used to test the performance of a trained neural network but the four most commonly used methods for fault detection, classification and location include:

a. the plot of the best linear regression fit
b. the plot of the confusion matrix
c. the plot of the Receiver Operating Characteristics (ROC)
d. to present the ANN with a new set of data outside the one used for training

2.4.1 The linear regression Plot

The linear regression plot is the plot of the actual neural network's outputs and the desired targets. The analysis of the slope of this line gives an idea of the training process. The output of a linear regression is between 0 and 1. Ideally, the slope of the plot should be one (1). However, how well the ANN outputs track the targets is determined using the correlation coefficient (r). The closer the correlation coefficient (r) is to 1, the better the performance of the ANN. Fig. 7 depicts an ideal linear regression plot.

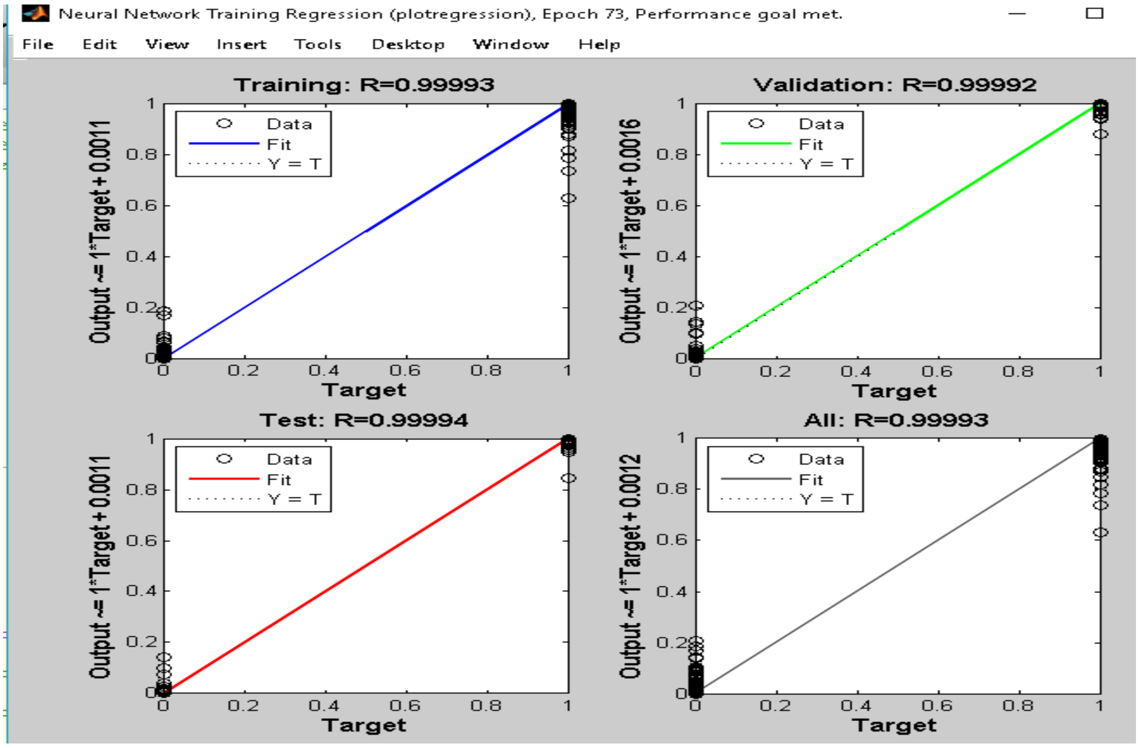

Fig. 7. The linear regression plot

2.4.2 The confusion matrix

Another method employed to test the performance of the artificial neural network is to plot the confusion matrix. The confusion matrix is a plot of the three phases of training, testing and validation. Thus, it shows the percentages of the correct and incorrect classifications of any given target. A percentage of 100 means there has been no confusion in the detection, and classification. A low positive classification rate indicates that the neural network might probably not perform well. Fig. 8 illustrates the confusion matrix. The green square boxes show the correct classifications while the pink boxes show the incorrect classifications.

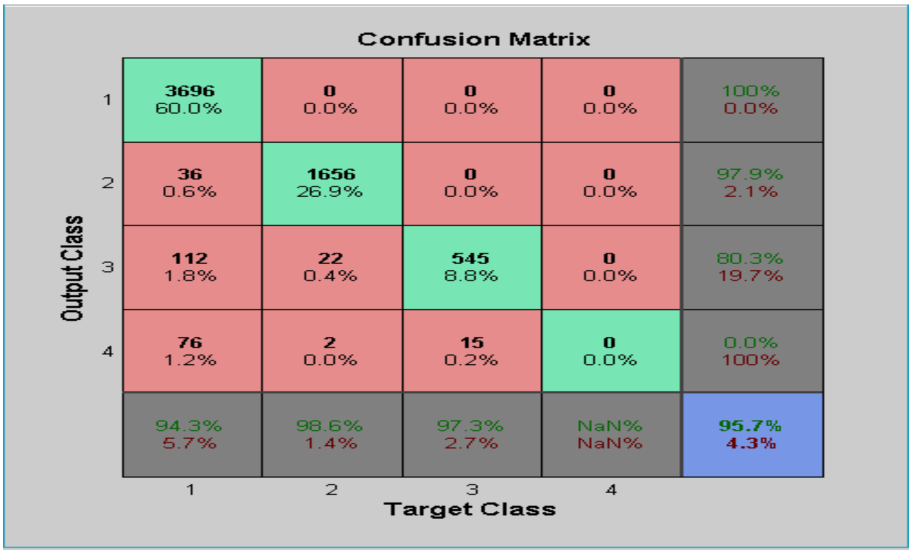

Confusion Matrix

Output Class	1	2	3	4	
1	**3696** 60.0%	**0** 0.0%	**0** 0.0%	**0** 0.0%	100% 0.0%
2	**36** 0.6%	**1656** 26.9%	**0** 0.0%	**0** 0.0%	97.9% 2.1%
3	**112** 1.8%	**22** 0.4%	**545** 8.8%	**0** 0.0%	80.3% 19.7%
4	**76** 1.2%	**2** 0.0%	**15** 0.2%	**0** 0.0%	0.0% 100%
	94.3% 5.7%	98.6% 1.4%	97.3% 2.7%	NaN% NaN%	**95.7%** **4.3%**

Target Class

Fig. 8. The confusion matrix plot

2.4.3 The receiver operating characteristics

The Receivers Operating Characteristics plot shows the relationship between the false positive and the true positive rates as the threshold of the outputs varies from 0 to 1 for classification purposes. The past left and up the line is, the higher the true positive and the fewer the false positive. Fig. 9 illustrates this plot.

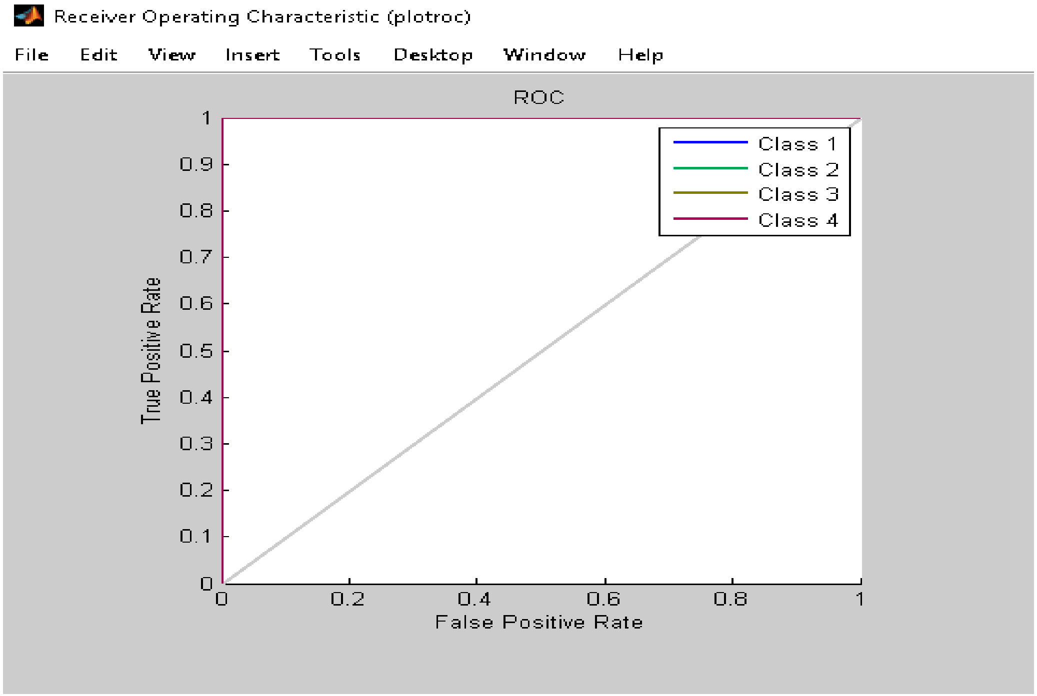

Fig. 9. The receivers operating characteristics

2.4.4 Testing the ANN with a new data set

Finally, the more practical and last means of testing the neural network model developed is to present it with a new set of known inputs and targets outside the ones used in the training of the system. Then, with known inputs and targets, the percentage error in the output of the neural networks can be calculated. The developed ANN system passes the test if the average percentage error in the ANN's output is within the acceptable limit. The test data for this work was generated for each of the fault conditions and No-Fault case. The distance was varied between 8 km to 140 km in the step of 8 km. The fault resistance was varied between 0.25, 0.5, 0.75, 5, 10, 20, 30 and 50 Ohms.

3. REVIEW OF RELATED LITERATURE

Applications of ANNs to power systems have been demonstrated in the areas of security assessment; load forecasting, control, protection, economic dispatch and harmonic analyses. A review of the transmission line protection using ANN is given in [10,11]. The use of ANN as distance relaying algorithm is demonstrated in [12] where an ANN-based scheme is proposed to improve the sensitivity and selectivity of protection systems using samples of current and voltage signals as direct inputs to ANNs as opposed to some other techniques in which preprocessed signals are employed as inputs. A multilayer feed forward ANN is used by [13] to develop a fault detector on transmission lines. The paper employs phase voltage and current signals as input to the neural network. In [8] feed forward ANN with back-propagation algorithm is developed for detection and classification of faults in power transmission lines. The ANN-based algorithm proposed in [14] for transmission lines distance protection, according to the authors, this can be used in any transmission line not considering its configuration or voltage level. According to the study presented in [15], an ANN technique for fault detection and classification is capable of identifying faults within 5 to 7 ms, making the technique very suitable for high speed protective relaying. [16] develops ten ANNs to identify faults type using current and voltage phasors after fault initiation, with each ANN trained to identify one of the types of faults. Also, the author [17], trained a single ANN to identify different fault types using three samples of current and voltage signals sampled at 800 Hz as inputs to the ANN. In this paper, a novel method which uses Multilayer Perceptron feed-forward neural network is proposed for shunt faults classification on the 33 -kV Nigeria power line. The ANN-based fault classifier in this study uses four ANNs to accomplish its classification task. The preprocessed sampled current and voltage values are used as inputs to each of the ANN.

4. THE MODELED POWER SYSTEM

The studied power system network in this paper is the 33-kV power line, which is approximately 140 km length, running from Isolo sub-transmitting station to NEPA axis in Lagos, Nigeria. Modeled in MATLAB 2015a, the single line diagram and parameters of the network are depicted in Fig. 10 and Table 2, respectively.

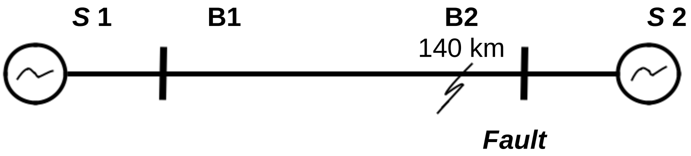

Fig. 10. Studied power system single line diagram

Table 2. Line parameters of the studied system

S/N	Line Property	Value
1	Line Length (km)	140
2	Positive- and zero-sequence resistances (Ohms/km)	[0.18446 0.39072]
3	Positive- and zero-sequence inductances (H/km)	[0.0010981 0.0024668]
4	Positive- and zero-sequence capacitances (F/km)	[1.0865e-08 6.6177e-09]
5	Fault Starting	0.020 seconds
6	Type Conductor	ACSR

From Fig. 10, S1 has a reference voltage of 33 kV, while S2 has a reference voltage of 11 kV. The input data (currents and voltages) for training the ANN are extracted from the power system by simulation due to insufficient real-time data. In the model, the current and voltage measurements are carried out at B1 (see Fig. 10). The instantaneous values of voltages and currents obtained are preprocessed and transmitted to MATLAB to build an ANN-based system for fault detection and classification. Ten different fault scenarios are simulated at varying distance and resistance values. Moreover, the values of the parameters used in generating the data for the proposed ANN-based intelligent shunt fault classifier are shown in Table 3.

Table 3. Training and test data generation parameters

Fault inception angle (^{0})	30, 60
Fault Resistance (Ohms)	0.25, 0.5, 0.75, 5, 10, 20, 30 and 50
ANN Test Data Generation Parameters	
Fault Location (km)	8, 16, 24, …, 138
Fault inception angle (^{0})	20, 90

Fig. 11 depicts the snapshot of the modeled 33-kV Nigeria power line network used in this study. The network consists of 140 km, 33-kV power lines, two transformers, one reference generator at the sending end of the power lines, and a three-phase fault simulator. The lines were modeled using Pi model. The three-phase load 1 and 2 represent the transformers respectively and the power line conductors (line 1 and line 2) together is 140 km long.

The voltage and current signals were measured using the three-phase V-I measurement block. The various shunt faults were simulated at different locations and resistances using the three-phase fault simulator block. The model was used to generate the whole set of data for training the neural network for the development of the intelligent fault classifier.

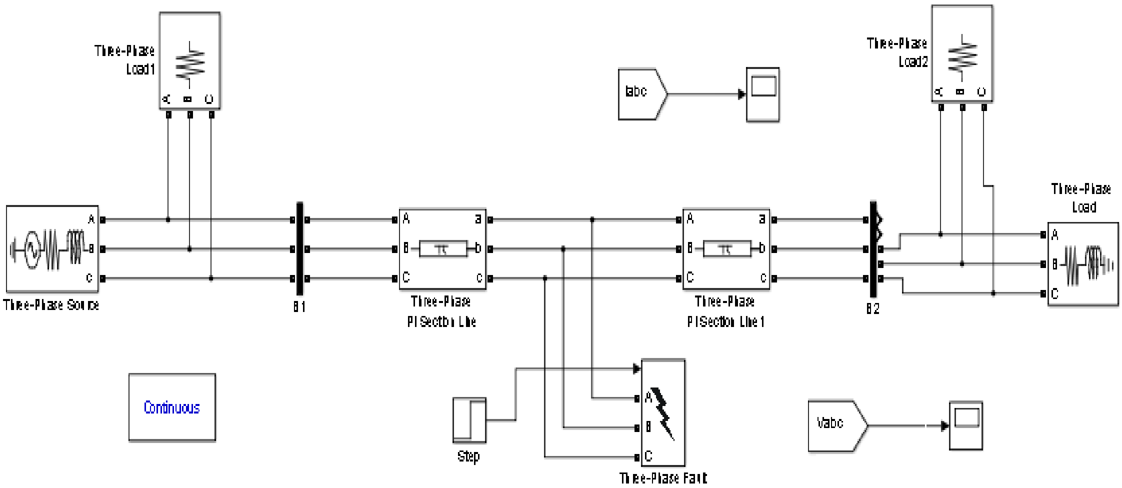

Fig. 11. Snapshot of the modeled 33-kV Isolo Power line in Simulink

4.1 Sampling Frequency

Signal sampling in the electric power system power lines can be described as the reduction of a continuous-time signal to a discrete-time signal. Sampling frequency, therefore, defines the number of samples per second taken from a continuous signal to make a discrete or digital signal. The ratio of it to the main frequency gives the number of samples per second. The choice of the sampling frequency in this work is done based on the results of the experiments that were carried out using 500 Hz, 800 Hz, 1000 Hz, 1200 Hz, 1350 Hz, and 1500 Hz, which are at least twice the fundamental frequency (50 Hz). The result of each was plotted and the shape compared to the shape of the original signal. The one that best replicated the shape of the original signal was chosen. Based on the result of the experiment, 1.5 kHz was chosen as the sampling frequency for the entire simulation in this study.

4.2 Simulation/Data Acquisition

The model was simulated and the three-phase voltage and current waveforms were generated and sampled at a frequency of 1.5 kHz. Consequently, there are 30 samples per cycle. These samples are much; hence feature extraction and scaling were done. This effectively extracts relevant information in the voltage and current signals, which in turn will reduce the overall size of the neural network and advance the time performance of the network. Meanwhile, the fault was created at 0.04s which corresponds to the 55th sample. The scaling was done using the 12th sample before and after the occurrence of the fault. Hence, the inputs to the ANN for detector-classifier are the ratios of the post-fault and pre-fault instantaneous voltages and currents in each of the phases, which correspond to the 67th sample and 43rd sample after and before the occurrence of the fault respectively. The scaling can be done mathematically, using the following generalized expression:

$$\mathrm{V}_{\mathrm{i}}^{\mathrm{abc}} = \frac{\mathrm{V}_{\mathrm{s}}^{\mathrm{RYB}}(n+12)}{\mathrm{V}_{\mathrm{s}}^{\mathrm{RYB}}(n-12)}$$

$$I_i^{abc} = \frac{I_s^{RYB}(n+12)}{I_s^{RYB}(n-12)}$$

Where,

V_i = instantaneous voltage inputs to ANN;
I_i = instantaneous current inputs to ANN;
V_s^{RYB} = Sampled voltage phases;
I_s^{RYB} = sampled current phases
n = Sample number corresponding to the instantaneous time where the fault occurred

4.3 Pre-Processing of Data

Pre-processing within this context is simply the normalization of the scaled data to obtain a conformable input data for ANN that varies between -1 and 1. These data were normalized to suit the ANN input data using the min-max method.

The MATLAB code used for data extraction and pre-processing is:

```
%%MATLAB Code for Generating Training and Test Data for Detection and classification

        clc
        tic
        classification_input = zeros(6,560);
        TTL = 140; %total transmission length
        a = 1:2:140; %varying distance of line 1 in km
        m = 1;
        % code that will make L1 and L2 to iterate
        for j = 1:length(a);
        L1 = a(j);
        L2 = TTL - L1;
        % code to vary the resistance
        b = [0.25 0.5 0.75 5 10 20 30 50];
        for i = 1:length(b);
        R = b(i);
        % code to simulate the model
        sim('Namemodel')

%creating values to read out and write to a variable

        Va1 = Va(post_fault,2)/Va(pre_fault,2);
        Vb1 = Vb(post_fault,2)/Vb(pre_fault,2);
        Vc1 = Vc(post_fault,2)/Vc(pre_fault,2);
        Ia1 = Ia(post_fault,2)/Ia(pre_fault,2);
        Ib1 = Ib(post_fault,2)/Ib(pre_fault,2);
        Ic1 = Ic(post_fault,2)/Ic(pre_fault,2);
        values = [Va1;Vb1;Vc1;Ia1;Ib1;Ic1];

% % write into an excel sheet

        sampledinput(1:6,m) = values; % stuff your 6 elements into one column
         m = m + 1;

end
end
 toc
```

```
%% for normalization

        Classification_input = normc(sampledinput);
```

Or

```
         classificationnorm = zeros(6,560); % create the row by column table size


        c =1:560;
        m = 1;
        for i = 1:560;
        d = c(i);

        table = sampledinput(1:6,m)./norm(sampledinput(1:6,m));
        classificationnorm(1:6,m) = table;
        m = m + 1;
end
```

5. THE PROPOSED INTELLIGENT SHUNT FAULT CLASSIFIER

The developed intelligent shunt fault classifier (ISFC) is designed to detect the presence of a fault and afterward classify the fault using four different modular artificial neural networks. The developed system has two stages – the detection stage and the classification stage. The three-phase fault detectors (IFD_R, IFD_Y, and IFD_B) are to indicate the presence (1) or the absence (0) of shunt faults on lines R, Y, and B respectively, while the detector IFD_G is to signify the involvement of ground. For ease, accuracy, and efficiency of fault classification, the logic behind the proposed system (as shown in Fig. 12) is to use a single ANN to detect a fault on each phase in combination with a ground ANN to show if the ground line is affected. The result is that if the outputs of the four ANNs read 'RYBG: 0 0 0 0', then the system is in a normal state; otherwise, the system is in an abnormal state, and the outputs indicate which lines are responsible for the abnormality (fault). By this method, the occurrence/non-occurrence of faults and the type of faults are captured precisely. For instance, a readout of 'RYBG: 1 0 0 1' implies an occurrence of a line (Phase R)-to-ground fault, while a readout of 'RYBG: 0 1 1 0' means a line-to-line fault has occurred on Phase Y and Phase B.

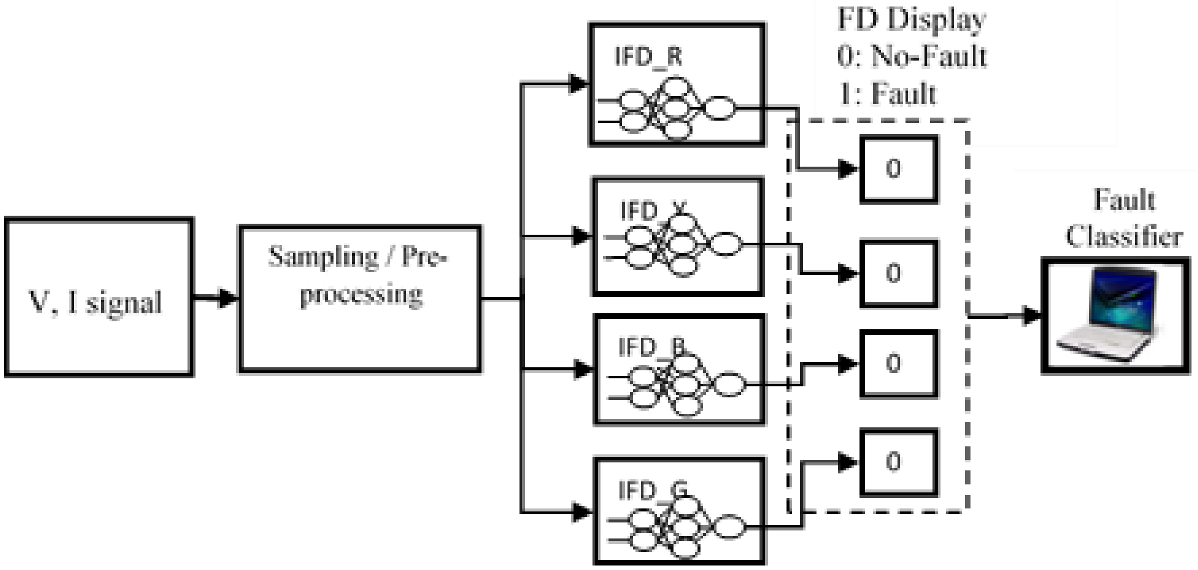

Fig. 12. Block diagram of ISFC in a no-fault state

Fig. 13 is a flowchart showing the developmental process involved in building ISFC

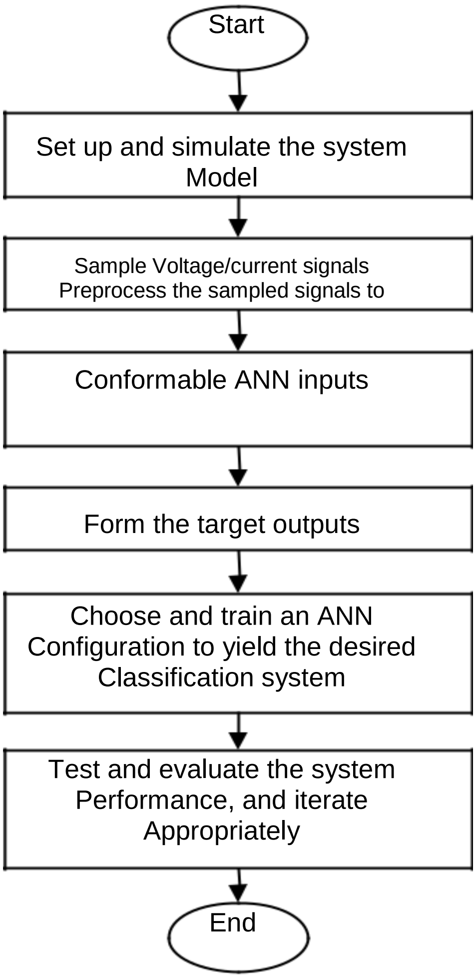

Fig. 13. Developmental process of the proposed ISFC

The proposed ISFC accepts six parameters as inputs, which correspond to the number of phase voltages and currents, and one output (either 0 or 1), which corresponds to the number of target outputs. Also, the number of hidden layers, the number of hidden layer neurons and the activation functions are all determined experimentally. As given in Table 4, all fault scenarios (ten cases of shunt fault and one no-fault case) are considered. For each fault scenario, the power network is simulated severally by varying the fault distance, resistance and inception angle so as to realize sufficient data for training and testing the ANNs. The training set consists of 6 x 6,160 input data sets and 1 x 6,160 target output data. This together forms a 6 x 1 input-output pattern for each of the module. It is important to note that, before they are presented to the ANN, the generated instantaneous current and voltage values are preprocessed and normalized to match the ANN input pattern of 0’s and 1’s. This is an essential stage in the development of the classifier which involves the reduction of the size of the input data sets to correspond to the neural network input pattern. It reduces the magnitude of the input data to the neural networks to a maximum value of + 1 and a minimum value of -1, hence improving the rate of the training process [18].

Table 4. The target truth table for the ANN-based ISFC

Module	**Fault type**										
Code	**R-G**	**Y-G**	**B-G**	**R-Y-G**	**R-B-G**	**Y-B-G**	**R-Y**	**R-B**	**Y-B**	**R-Y-B**	**No-**
ANN_R	1	0	0	1	1	0	1	1	0	1	0
ANN_Y	0	1	0	1	0	1	1	0	1	1	0
ANN_B	0	0	1	0	1	1	0	1	1	1	0
ANN_G	1	1	1	1	1	1	0	0	0	0	0

Table 5 shows a sample of the scaled Voltage and Current values used for phase R. The fault has been simulated at a distance of 60 km from bus B1 on a 140 km, 33-kV electric power lines.

Table 5. Sample of the scaled voltage and current values for ANN

S/N	V_R	V_Y	V_B	I_R	I_Y	I_B
1	0.3253	0.2693	0.3471	0.4805	0.4861	0.4835
2	0.3979	0.3383	0.3955	0.4336	0.4385	0.4362
3	0.4472	0.3923	0.4380	0.3868	0.3912	0.3891
4	0.5715	0.5604	0.5677	0.1104	0.1114	0.1109
5	0.5755	0.5720	0.5748	0.0604	0.0608	0.0606
6	0.5765	0.5759	0.5765	0.0340	0.0342	0.0341
7	0.5766	0.5767	0.5769	0.0252	0.0253	0.0252
8	0.5768	0.5771	0.5772	0.0183	0.0184	0.0183
9	0.4765	0.4397	0.4906	0.3339	0.3377	0.3361
10	0.4964	0.4599	0.5039	0.3080	0.3115	0.3100

6. RESULTS AND EVALUATION

The supervised learning is employed in training extensively several configurations of the ANN with varying number of hidden layers, hidden layers neurons and activation functions for each of the modular ANNs with their corresponding target outputs. It is observed after series of training and testing of various combinations of hidden layers that the ANN with two hidden layers results in the best performance for all the ANN modules. The results of the configurations are summarized in Table 6.

Table 6. The ANN modular architecture

ANN	Layer neurons				Activation Function	Performance
Module	**Input**	**Hidden layer 1**	**Hidden layer 2**	**Output**	**Combination**	**MSE**
ANN_R	6	10	10	1	tan-sigmoid/purelin/log-sigmoid	0.00551
ANN_Y	6	10	12	1	Log-sigmoid/tan-sigmoid/tan-sigmoid	0.000638
ANN_B	6	10	12	1	log-sigmoid/purelin/tan-sigmoid	1.888e-8
ANN_G	6	10	18	1	tan-sigmoid/log-sigmoid/log-sigmoid	0.00381

More so, the performance MSE, confusion matrix, regression plot and the generalization capability are used as performance indicators for the trained ANNs. Fig. 14 to Fig. 16 show the performance MSE, confusion matrix and regression plot respectively for ANN_R.

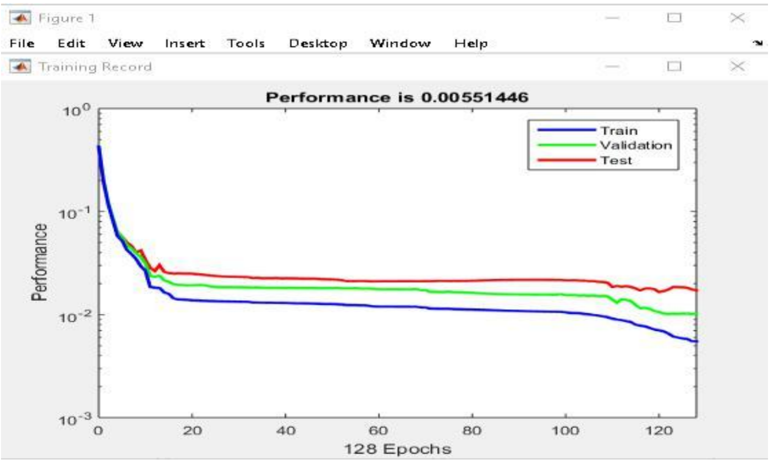

Fig. 14. Performance Plot for ANN_R mode

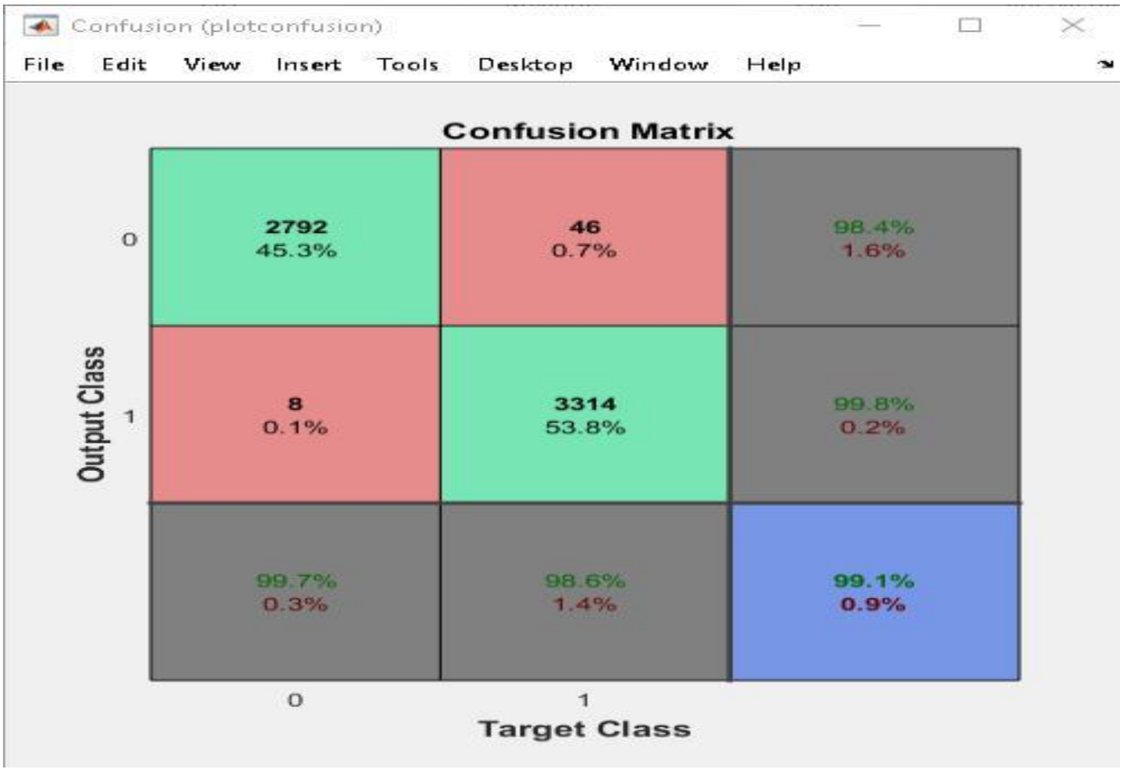

Output Class \ Target Class	0	1	
0	**2792** 45.3%	**46** 0.7%	98.4% 1.6%
1	**8** 0.1%	**3314** 53.8%	99.8% 0.2%
	99.7% 0.3%	98.6% 1.4%	**99.1%** **0.9%**

Fig. 15. The confusion matrix of ANN_R model

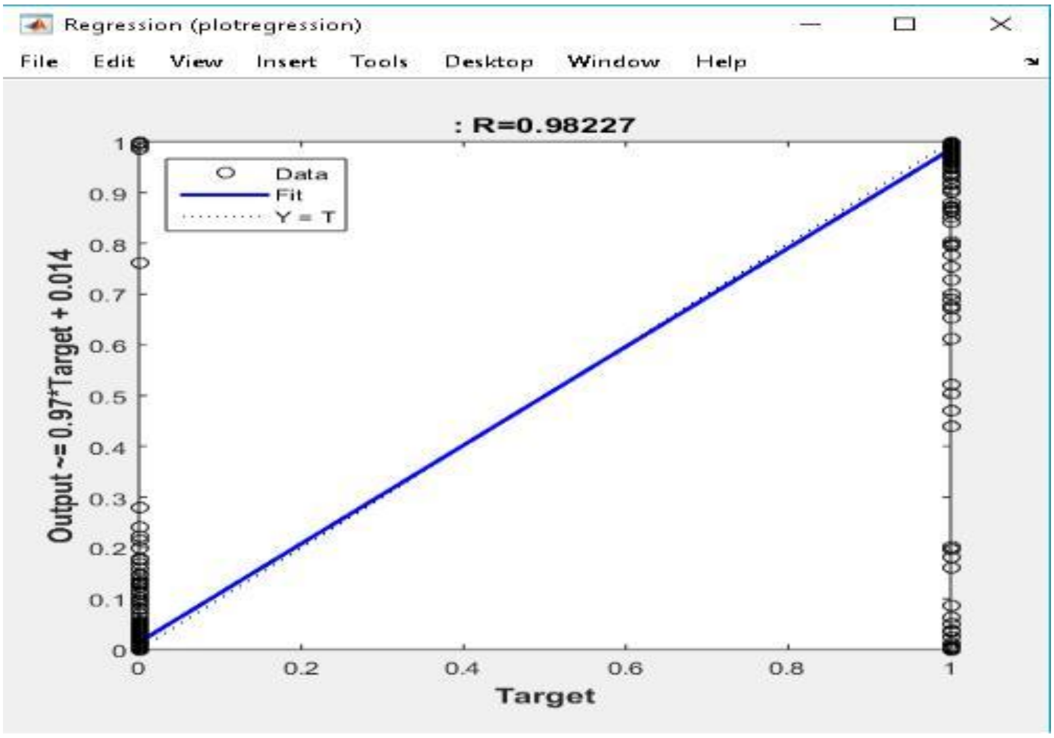

Fig. 16. The regression plot of ANN_R model

Furthermore, Fig. 17 to Fig. 19 depicts the performance MSE, confusion matrix and regression plot respectively for ANN_Y.

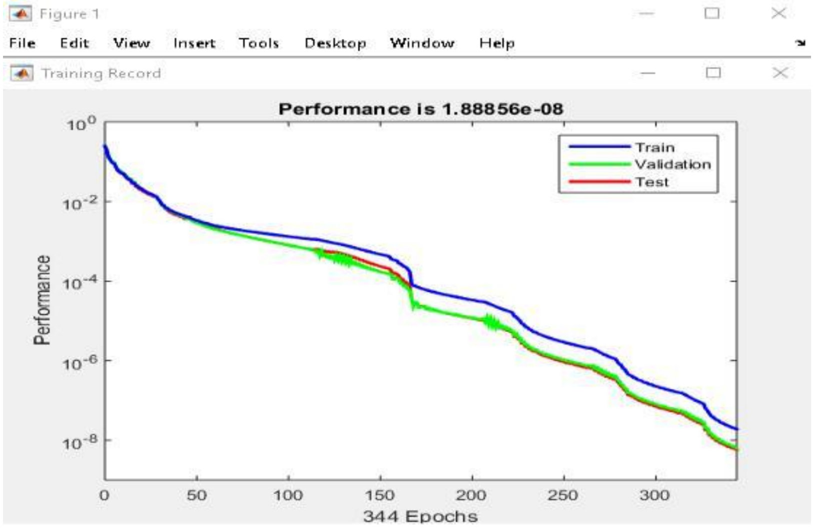

Fig. 17. Performance plot for ANN_Y model

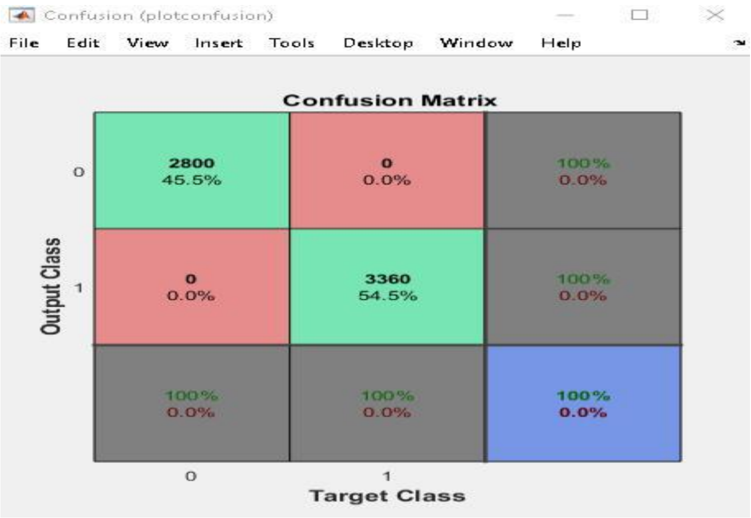

Output Class	0	1	
0	2800 45.5%	0 0.0%	100% 0.0%
1	0 0.0%	3360 54.5%	100% 0.0%
	100% 0.0%	100% 0.0%	100% 0.0%

Target Class

Fig. 18. The confusion matrix of ANN_Y model

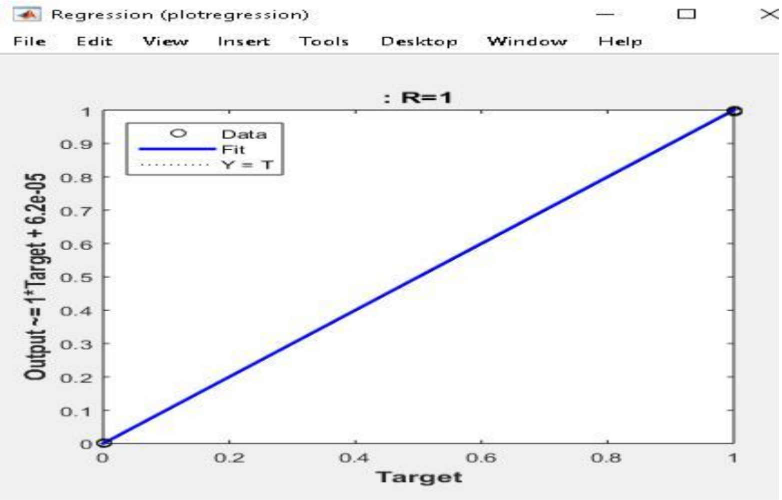

Fig. 19. The regression plot of ANN_Y model

Fig. 20 to Fig. 22 illustrates in that order the performance MSE, confusion matrix, and regression plot for the trained ANN_B.

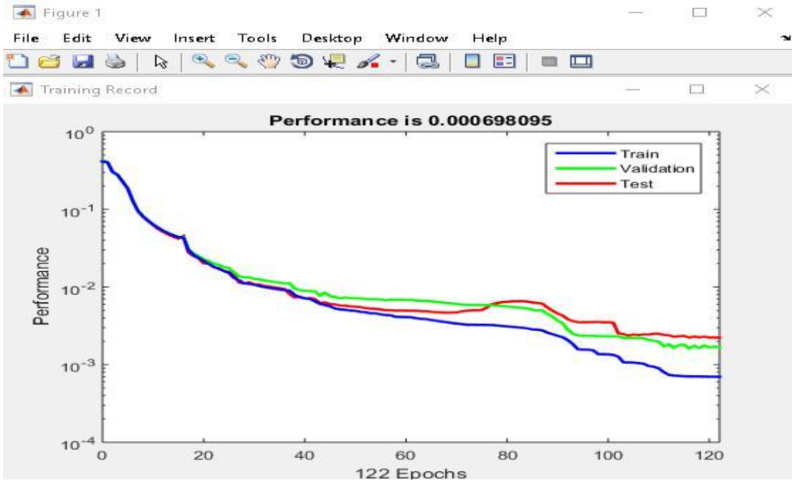

Fig. 20. Performance plot for ANN_B model

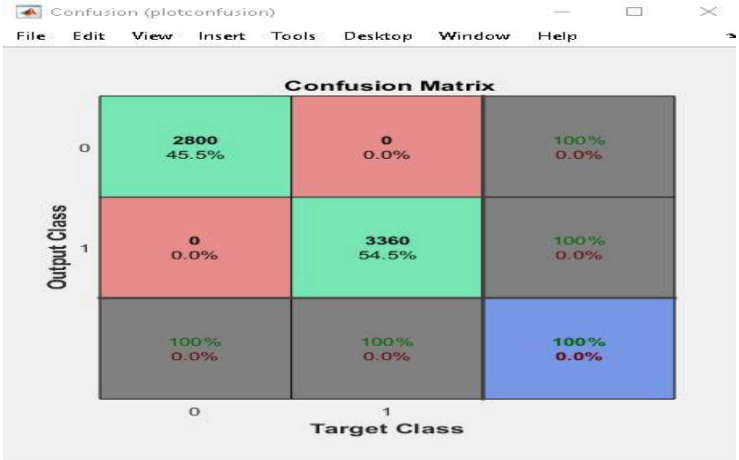

	0	1	
0	2800 45.5%	0 0.0%	100% 0.0%
1	0 0.0%	3360 54.5%	100% 0.0%
	100% 0.0%	100% 0.0%	100% 0.0%

Fig. 21. The confusion matrix of ANN_B model

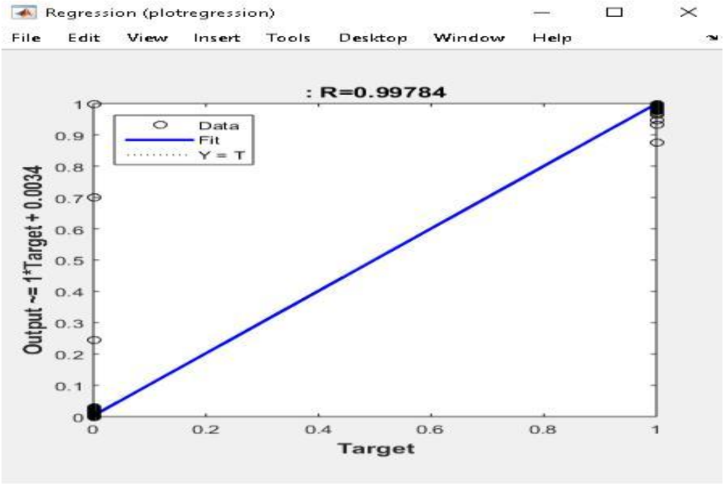

Fig. 22. The regression plot of ANN_B model

The performance MSE, confusion matrix and the regression plot for ANN_G is shown in Fig. 23 to Fig. 25.

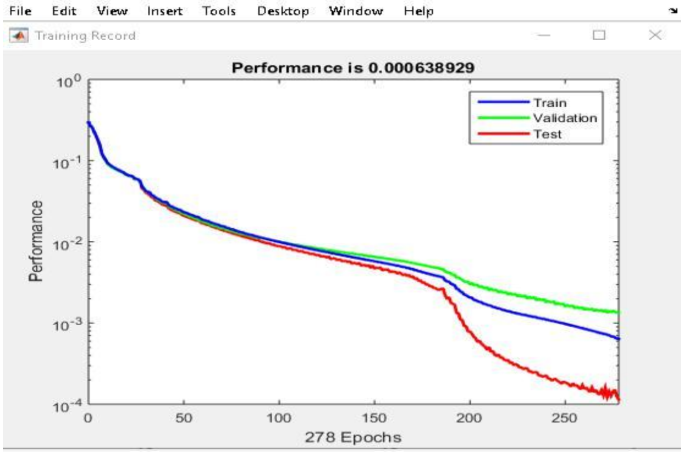

Fig. 23. Performance plot for ANN_G model

Output Class \ Target Class	0	1	
0	2800 45.5%	4 0.1%	99.9% 0.1%
1	0 0.0%	3356 54.5%	100% 0.0%
	100% 0.0%	99.9% 0.1%	99.9% 0.1%

Fig. 24. The confusion matrix of ANN_G model

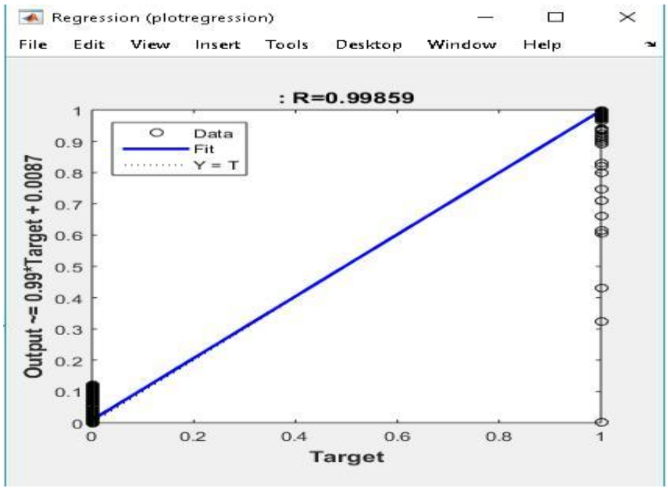

Fig. 25. The regression plot of ANN_G model

Moreover, the developed ISFC capability to generalize is tested with 10 new fault instances for each fault type, amounting to 110 new fault scenarios. Fig. 26 to Fig. 29 represent the Simulink models that show the responses of the developed intelligent shunt fault classifier for some selected fault types.

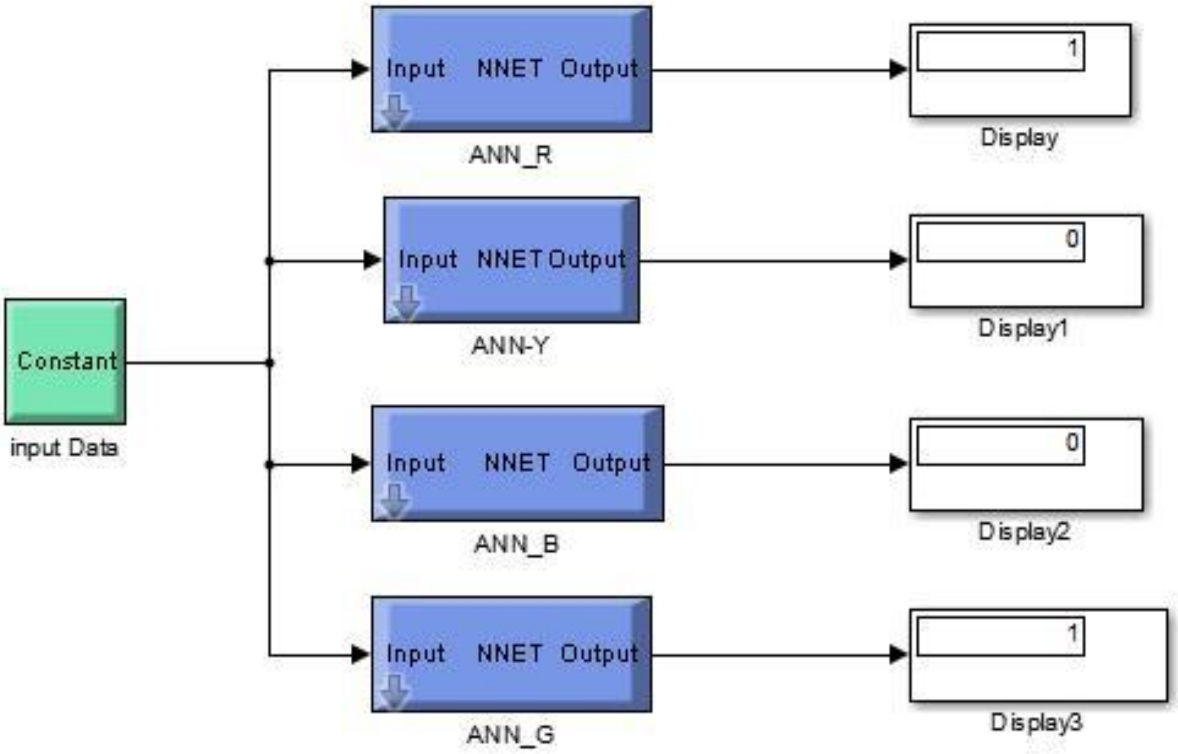

Fig. 26. ISFC output for R-G fault with fault occurring at 48 km

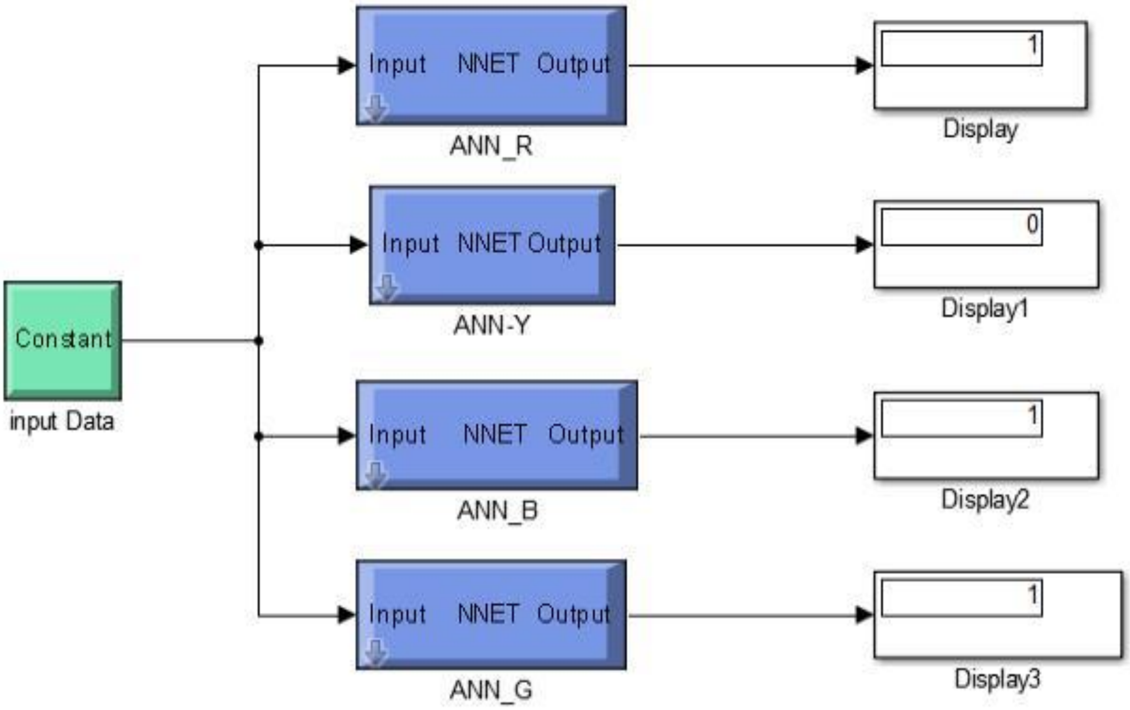

Fig. 27. ISFC output for Line-line-to-ground fault for R-B-G fault with fault occurring at 56 km

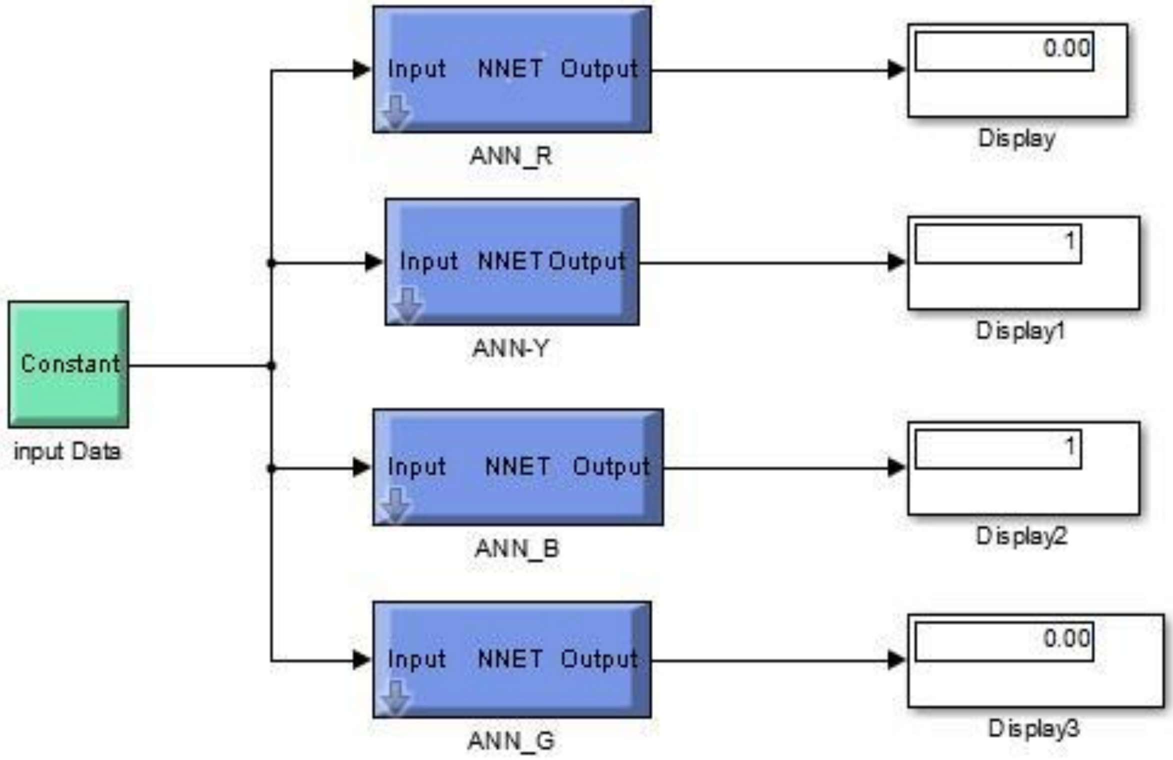

Fig. 28. ISFC output for line-to-line fault for Y-B fault with fault occurring at 48 km

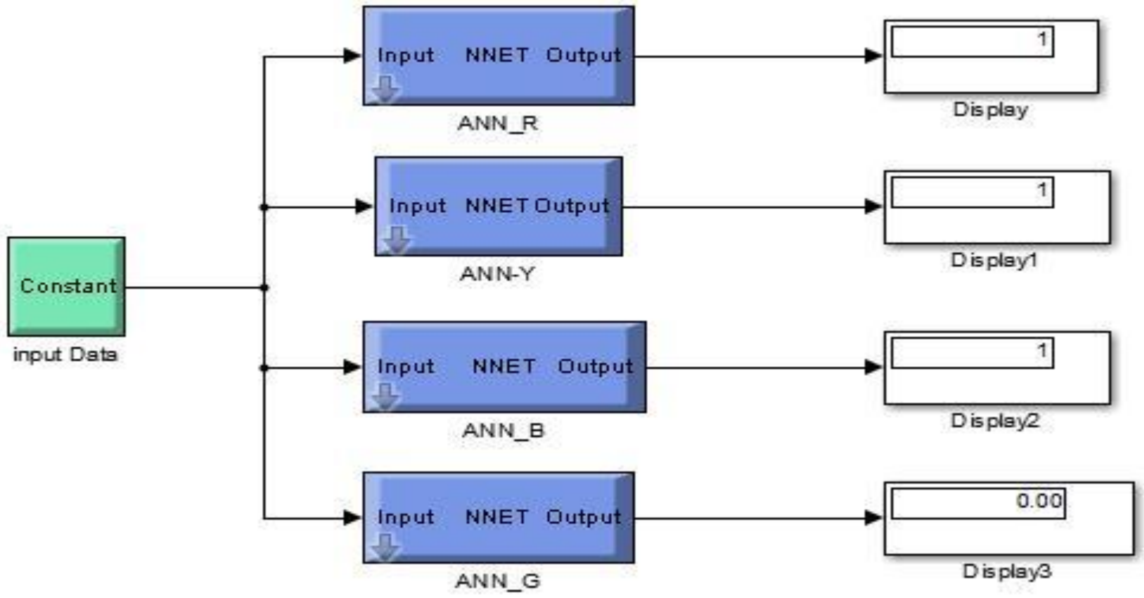

Fig. 29. ISFC output for three lines shunt fault (R-Y-B) with fault occurring at 72 km

It can be seen from the performance plots (Fig. 14, Fig. 17, Fig. 20 and Fig. 23) which show the mean square error, that the testing and the validation curves have similar characteristics. Hence, it can be said that the ISFC has an efficient training, testing and validation. The satisfactory accuracy (Fig.15, Fig. 18, Fig. 21 and Fig. 24) and the accurate correlation (Fig. 16, Fig. 19, Fig. 21 and Fig. 25) shown by the confusion matrixes and the regression plots respectively by the developed ISFC proof that this system can be deployed for the purpose for which it is developed. Finally, based on the results presented in Fig. 26 to Fig. 29, the ISFC developed can effectively and efficiently classify all the ten possible types of shunt faults and No-fault condition considered on the 33-kV Nigeria transmission line. The Simulink results presented demonstrate the ability of the intelligent shunt fault classifier to accurately indicate and classify all shunt fault types in all the considered simulation tests.

7. CONCLUSION

A new approach for shunt fault classification has been demonstrated in this paper. The model employs preprocessed and normalized instantaneous values of currents and voltages generated from one terminal datum as inputs to four independent ANN modules corresponding to the three phases and the ground, respectively of an electric power transmission line. After suitably training the modules (ANN_R, ANN_ Y, ANN_B, and ANN_G), their outputs are appropriately gated to visually indicate the fault types. The performance of the system, when tested under various shunt fault types with varying resistances and distances, shows that the system can be used to improve distance line protection in 33-kV Nigeria power line.

COMPETING INTERESTS

Authors have declared that no competing interests exist.

REFERENCES

1. Hosseini E. Short circuit fault classification and location in transmission lines using a combination of wavelet transform and support vector machines. International Journal on Electrical Engineering and Informatics. 2015;7(2):353–365.
2. Chen H , Cong TN, Yang W, Tan C, Li Y, Ding Y. Progress in electrical energy storage system: A critical review. Prog Nat Sci. 2009;19:291-312.
3. Status of electrical energy storage systems. Dti report. DG/DTI/00050/00/00, urn no. 04/1878. UK Department of Trade and Industry. 2004;1–24.
4. Luo X, Wang J, Dooner M, Clarke J. Overview of current development in electrical energy storage technologies and the application potential in power system operation. Applied Energy. 2015;137:511-536.
5. Martín F, Aguado JA. Wavelet based ANN approach for transmission line protection. IEEE Transactions on Power Delivery. 2003;18(4):1572-1574.
6. IEEE Power Engineering Society. IEEE Guide for Determining Fault Location on AC Transmission and Distribution Lines; 2005.
7. Oluwole A, Samuel O, Festus O, Olatunji O. Electrical power outage in Nigeria: History, causes and possible solutions. Journal of Energy Technology Policy. 2012;2(6):18–24.
8. Phyo ET. Fault Detection and classification for transmission line protection system using artificial neural network. Journal of Electrical/Electronics Engineering. 2016;4(5):89.
9. Sanaye-Pasand M, Khorashadi-Zadeh H. An extended ANN-based high speed accurate distance protection algorithm. International Journal Electrical Power Energy System. 2006;28(6):387–395.
10. Yadav A, Dash Y. An overview of transmission line protection by artificial neural network: fault detection, fault classification, fault location, and fault direction discrimination. Advances in Artificial Neural Systems, Hindawi Publishing Corporation. 2014;1–20.
Available:http://dx.doi.org/10.1155/2014/230382
11. Kezonuic MA. Survey neural net application to protective relaying and fault analysis. Engineering International System. 1997;5(4):185-92.
12. Kesharwani S, Singh DK. Simulation of Fault Detection for Protection of Transmission. 2014;3(5):1367–1371.
13. Santos RC, Senger EC. Transmission lines distance protection using artificial neural networks. International Journal of Electrical Power Energy System. 2011;33(3):721–730.
14. Dalstein T, Kulicke B. Neural network approach to fault classification for high speed relaying. IEEE transactions on Power Delivery PWRD. 1995;10(2):1002-1011.
15. Poelt A, Frohlich K. Two new methods for very fast type detection by means of parameter fitting and artificial neural networks. IEEE transactions on Power Delivery PWRD.1999;14(4):1269-1275.

16. Aggarwal RK, Xuan QY, John AT, Bennett A. A Novel fault classification technique for double-circuit lines based on a combined unsupervised/supervised neural network. IEEE transactions on Power Delivery PWRD. 1999;14(4):1250-1255.
17. Sanaye-Pasand M, Khorashadi-Zadeh H. An extended ANN-based high speed accurate distance protection algorithm, Electrical Power and Energy Systems. 2006;28(2006):387–395.
18. Awelewa AA, Mbamaluikem PO, Samuel IA. Artificial neural networks for intelligent fault location on the 33-kV Nigeria transmission line. International Journal of Engineering Trends and Technology (IJETT). 2017;54(3):147–155.

Biography of author(s)

A. A. Awelewa
Department of Electrical and Information Engineering, Covenant University, Ota, Ogun State, Nigeria.

He holds a doctoral degree in Electrical and Electronics Engineering. He has taught a great deal of courses at undergraduate and postgraduate levels, and carried out research resulting in numerous publications in peer-reviewed international journals. His research interests involve modeling, analysis, and control of dynamical systems; power system analysis, stability, and control, including voltage instability/collapse prediction; and energy utilization and efficiency, including analysis and design of renewable energy systems. He is a corporate member of the Nigerian Society of Engineers (NSE), member of the Institute of Electrical and Electronics Engineers (IEEE), and registered member of the Council for the Regulation of Engineering in Nigeria (COREN).

P. O. Mbamaluikem
Department of Electrical/Electronics Engineering, Federal Polytechnic Ilaro, Ilaro, Ogun State, Nigeria.

He obtained his Bachelor of Engineering (B.Eng.) and Masters of Engineering (M.Eng.) Degree from Enugu State University of Science and Technology, Enugu and Covenant University, Ota, Ogun State, Nigeria respectively. He is a Lecturer in the Department of Electrical/Electronics Engineering at the Federal Polytechnic, Ilaro since 2010. One of his major researches was on the Development of an intelligent Fault Locator for the 33-kV Nigeria Power lines from where this piece of work was birth. As an Engineer with twelve (12) year Teaching/working experience in the field of Electrical/Electronics Engineering at Federal Polytechnic, Ilaro, he has experienced working/consulting with students/Colleagues on different projects and has several Journal publications and conference papers in reputable peer-reviewed international journals. His research interests encompasses power system analysis, power system stability, energy utilization and efficiency, power system protection and artificial intelligence. He is a corporate member of International Association of Engineers (IAENG), and registered member of the Council for the Regulation of Engineering in Nigeria (COREN).

© Copyright (2021): Author(s). The licensee is the publisher (B P International).

DISCLAIMER
This chapter is an extended version of the article published by the same author(s) in the following journal.
International Conference on Engineering for Sustainable World, 1378 (032098), 2019.

Chapter 10

Print ISBN: 978-93-91312-26-8, eBook ISBN: 978-93-91312-34-3

The Effect of Alpha Oscillation Network Decoding on Driver Alertness

Chi Zhang[1*], Jinfei Ma[2], Jian Zhao[3], Pengbo Liu[3], Fengyu Cong[1,4,5,6], Tianjiao Liu[7], Ying Li[1], Lina Sun[1] and Ruosong Chang[2]

DOI: 10.9734/bpi/nupsr/v9/10102D

ABSTRACT

The countermeasure of driver fatigue is valuable for reducing the risk of accidents caused by vigilance failure during prolonged driving. Listening to the radio (RADIO) has been proven to be a relatively effective “in-car” countermeasure. However, the connectivity analysis, which can be used to investigate its alerting effect, is subject to the issue of signal mixing. In this study, we propose a novel framework based on clustering and entropy to improve the performance of the connectivity analysis to reveal the effect of RADIO to maintain driver alertness. Instead of reducing signal mixing, we introduce clustering algorithm to classify the functional connections with their nodes into different categories to mine the effective information of the alerting effect. Differential entropy (DE) is employed to measure the information content in different brain regions after clustering. Compared with the Louvain-based community detection method, the proposed method shows superior ability to present RADIO effect in the confused functional connection matrices. Our experimental results reveal that the active connection clusters distinguished by the proposed method gradually move from the frontal region to the parieto-occipital region with the progress of fatigue, consistent with the alpha energy changes in the two brain areas. The active clusters in the parieto-occipital region significantly decrease and the most active clusters remain in the frontal region when RADIO is taken. The estimation results of DE confirm the significant change ($p<0.05$) of information content due to the cluster movements. Hence, preventing the movement of the active clusters from the frontal region to the parieto-occipital region may correlate with maintaining driver alertness. The revelation of the alerting effect is helpful for the targeted upgrade of the fatigue countermeasures.

Keywords: Driver fatigue; alerting effect; EEG; clustering; differential entropy.

1. INTRODUCTION

Fatigue is a phenomenon that reduces and weakens physical, mental, and emotional exertion and often entails decreased physiological functions (including speed, strength, coordination, reaction time, balance, and decision) [1]. In the transportation system, fatigue decreases drivers’ alertness level and gives rise to road accidents. According to the related road crash investigations, about 10–20% of all the crashes and 40% of the fatal crashes are caused by the driver fatigue [2-5]. Car crash is the number one reason for the teen deaths in the U.S., and driver fatigue is reported to be responsible for

---

[1] *Faculty of Electronic Information and Electrical Engineering, School of Biomedical Engineering, Dalian University of Technology, Dalian 116024, China.*
[2] *School of Psychology, Liaoning Normal University, Dalian 116029, China.*
[3] *Faculty of Vehicle Engineering and Mechanics, School of Automative Engineering, Dalian University of Technology, Dalian 116024, China.*
[4] *School of Artificial Intelligence, Faculty of Electronic Information and Electrical Engineering, Dalian University of Technology, Dalian, China.*
[5] *Key Laboratory of Integrated Circuit and Biomedical Electronic System, Liaoning Province. Dalian University of Technology, Dalian, China.*
[6] *Faculty of Information Technology, University of Jyvaskyla, Jyvaskyla, Finland.*
[7] *School of Psychology, Shandong Normal University, Jinan 250358, China.*
**Corresponding author: E-mail: chizhang@dlut.edu.cn;*

more than 57% of the traffic accident deaths [6]. Therefore, safe and affordable countermeasures are worthy of being explored.

In real-world driving conditions, drivers take various countermeasures to relieve fatigue and maintain mental and physical performance, such as caffeine consumption, napping, opening a window, listening to the radio, talking, and parking to take a walk. Among them, opening a window and listening to the radio are considered to be effective ways to stay awake by most professional and nonprofessional drivers [7]. A previous study restricted young adult drivers' sleep to 5h at night and exposed them to cold air (AIR), listening to the radio (RADIO), or nil treatment during driving [8]. Of all the countermeasures, only RADIO significantly decreased the drowsiness level represented by Karolinska Sleepiness Scale (KSS) score. Nevertheless, the effect of AIR is transient and non-significant. Even though RADIO has been proven to be a relatively effective "in-car" countermeasure, the brain mechanism underpinning its alerting effect is still unknown. This paper aims to develop a method to explore the RADIO effect so that the precision of countermeasures can be improved to maintain driver alertness more effectively.

An important advancement in neuroscience research, reflecting the modern concept of the brain as a highly integrated and dynamic system, is the assessment of functional connectivity in brain networks (i.e., increase or decrease of the correlation from brain activities in different areas) [9]. Changes in the functional connectivity across the mental states can provide richer information about human cognition than the simpler univariate approaches [10], but communication between brain circuits is also reflected in neural oscillations, which can be measured through spectrum analysis of electroencephalography (EEG) recordings in the frequency domain [11]. In the frequency domain, previous studies have demonstrated that the power of alpha and theta oscillations predominantly in the central and posterior brain regions (parietal-occipital) is generally increased when the subjects are fatigued or tired, in contrast to a decrease in the higher frequency bands [12,13]. Therefore, the oscillatory information, especially the alpha-band indicator, has been considered as one of the most prominent EEG-indicators [14,15]. Alpha oscillations play a prominent role in the control of cortical excitability [16]. Alpha-band power (8–13 Hz) has been shown to be sensitive to the early stage of fatigue and applied in fatigue assessment by many real-traffic and simulated driving studies. Recent research has demonstrated that alpha spindles, which consist of short (0.5–2s) bursts of high frequency alpha activity, in the parietal/occipital area are significantly correlated with fatigue and drowsiness [17]. In connectivity analysis, several studies have reported that the functional brain networks become more integrated during task performance in comparison with the resting state, but linearly decrease with the ongoing time-on-task [10,18]. In the prolonged visuomotor vigilance task, Gaggioni et al. [19] suggested that decreased propagation of EEG response evoked by transcranial magnetic stimulation within the fronto-parietal cortex was related to the failure of the increased vigilance. Under the simulated driving condition, Kong et al. [20] also revealed the degraded performance of small-world features of brain networks under the fatigue state, providing further support for the presence of a reshaped global topology in connectivity networks when drivers shifted from the alert stage to the drowsy stage. Zhao et al. [21] attributed the shift to a more economic but less efficient configuration, or an inability to retrieve the resources related to mental fatigue. Obviously, the interaction analysis of functional connectivity and the oscillations like alpha waves can provide more adequate and reliable information for exploring the neural mechanism of the alerting effect of RADIO.

However, the connectivity analysis of time series will encounter significant challenges in practical applications. Traditional approaches of connectivity analysis, which can be used to estimate the changes of signal coupling across mental states, usually characterize either different single connections or the system's average behavior [22]. Recent studies have shown that these approaches ignore the complex spatiotemporal patterns of activity, for example, the global signal changes to propagating waves [23-25]. Additionally, the connectivity analysis from sensor space data isnon-robust and it is sometimes difficult to obtain results that are statistically significant in cognitive studies. This issue is also serious for the measure of EEG, which records brain electrical activities non-invasively at a millisecond time scale. Owing to signal mixing, which translates to volume conduction in the case of EEG recordings and to signal leakage in source reconstructed EEG data, the activity of any single neuronal source is detected by a spatially widespread group of sensors [26].

From the perspective of individual sensors, the same sensor mayalso pick up multiple sources. Thus, EEG-based connectivity analysis suffers from two types of false positives—artificial and spurious interactions. Artificial interactions directly caused by signal mixing neglecting real interactions between neuronal groups at the considered locations can be reduced by a number of binarized connectivity matrices that typically aim to remove linear coupling terms [27]. Spurious interactions arising from the leakage of signals from a true link of sources to the surrounding links are more difficult to process due to multivariate mixing effects [28,29]. Up to now, steps towards addressing the problem have been taken for suppressing spurious interactions, such as oscillation-based and phase-based estimates [30,31]. Even though some improvements are achieved, all the interaction measures are still sensitive to spurious interactions with residual signal mixing in the source space [26].

In this context, we are not seeking to further suppress spurious interactions, but to mine effective information with the false positives. A single link in a brain network may be spurious link, but we view the problem from a different angle. Two distinct groups of connections with spurious links can be classified by machine learning method automatically. As signal mixing does not vary over time [27,31-33], the change of pattern classification of connection groups over time is considered to reflect the shift of the mental states. In this study, the smallest group of connections is defined as a connection cluster composed of a node and all the connections linked to it. Since the definition includes node, the classification changes manifest the evolution of spatiotemporal patterns. Accordingly, we propose the clustering algorithm implemented in brain networks. In order to verify that the spatiotemporal evolution indeed generates the information content change, entropy is calculated in different brain areas after clustering. In information theory, entropy represents the complexity and the uncertainty of the information source and embodies the information content through the probability distributions that underlie the process of communication [34]. As a nonlinear estimation of the dynamical EEG activity, entropy-based algorithms have been proven to be useful and robust estimators for evaluating regularity or predictability [28,35,36]. For example, Shi et al. [37] utilized differential entropy (DE) to extract the EEG features of driver alertness and found it was more accurate and stable compared with energy spectrum, autoregressive parameters, fractal dimension, and sample entropy. Therefore, DE was selected to implement the entropy estimation.

This paper is organized as follows. In Section 2, we describe the experimental details and EEG data preprocessing to extract alpha oscillations (see Sections 2.1 and 2.2), illustrate the functional connectivity analysis to construct brain networks (see Section 2.3), explain clustering algorithm implemented in the constructed brain network (see Section 2.4), elaborate the DE-based information content evaluation method (see Section 2.5), and provide the statistical analysis process (see Section 2.6). Results of the study are presented in Section 3 and discussed in Section 4.

2. MATERIALS AND METHODS

The signal flowchart of the proposed methodology is shown in Fig. 1. The analysis is based on clustering algorithm implemented in the brain networks and entropy assessment in the alpha band. The EEG data come from the prolonged driving experiments described in Section 2.1. In the frequency domain, alpha oscillations are extracted by discrete wavelet transform, which is included in data preprocessing (see Section 2.2). In the spatial dimension, the brain networks of alpha oscillations are constructed based on connectivity estimation in alpha band (see Section 2.3). The nodes of the classified clusters are extracted through the hierarchical clustering algorithm so that the labels of the classification outputs manifest the enrichment levels of alpha interactions (see Section 2.4). Clustering evolved at the data of different stages indicates spatiotemporal changes. Finally, according to the spatiotemporal patterns, the statistical analysis of DE in the alpha band is made in the corresponding brain areas (see Section 2.5). The spatiotemporal patterns and the DE values are used to assess the alerting effect of the fatigue countermeasure.

2.1 Experiments and Data

This study was conducted in accordance with the Declaration of Helsinki, and the protocol was approved by the Ethics Committee of Dalian University of Technology (protocol number: 2018-040). All subjects gave their informed consent for inclusion before they participated in the experiments. Twenty-eight healthy subjects aged from 20 to 30 years old were recruited in the study. None of the subjects reported mental disorders or neurological disorders. They had normal sleeping patterns, normal vision or corrected to normal with glasses or contact lenses, without prescription, without alcohol and caffeine 24h before the experiment. Each subject drove along at daytime for more than one hour under monotonous highway environment produced in a driving simulator (QJ-3A1). The interactive display system of the simulator was developed based onvirtual reality (VR). The VR scenes were displayed on the car-like three-sided screen with an angle of 120° (see Fig. 2). The subjects were divided into the following two groups according to whether the countermeasure was implemented.

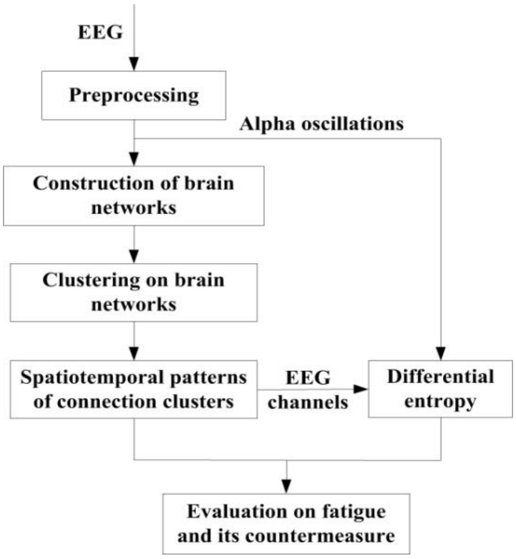

Fig. 1. Flowchart of the data-driven methodology

The control group was composed of 14 male subjects with a mean age of 25.64 years. In the control group, no countermeasure was taken. The subjects just drove under the simulated driving environment to induce fatigue.

The experimental group was also composed of 14 male subjects with a mean age of 22.57 years. In the experimental group, the subjects were exposed to RADIO during driving. They chose the talk show radio station that they would normally select on such journeys. Volume was at their discretion.

Nineteen standard electrodes (i.e., Fp1, Fp2, F7, F3, Fz, F4, F8, T3, C3, Cz, C4, T4, T5, P3, Pz, P4, T6, O1, and O2) mounted on a cap (eego™mylab from ANT Neuro, Berlin, Germany) were attached to the scalps following the International 10–20 System to collect the EEG data of the subjects during driving. The EEG's sampling frequency is 500Hz.

Fig. 2. Experimental setting

2.2 Data Preprocessing

The original EEG signals are inevitably disturbed by a large quantity of high frequency and low frequency noise (i.e., artifact), such as power frequency noise, body movement and blinking, which needs to be removed. In addition, various aspects of the signals, such as trends, sudden changes, and start/end tag information, may be useful for alerting effect analysis in the time domain and need be retained. Wavelet transform is an effective tool to analyze the various components of a non-stationary signal due to its attractive properties such as good local representation in both time and frequency domains and multi-rate filtering (differentiating the signals with various frequencies) [38]. Referring to [39], the raw EEG data were filtered by wavelet decomposition with 9 levels; after that, wavelet coefficients (7.8–15.6Hz) at fifth level were used to reconstruct alpha waves. Moreover, the wavelet-based threshold technique in [28] was used to correct the filtered signals.

On account of the staged and accumulative properties of fatigue [40,41], the continuous data after artifact removal were epoched into segments of 10min. Segments 1–6 correspond to the data within 0–10min, 10–20min, 20–30min, 30–40min, 40–50min, and 50–60min, respectively.

In the frequency domain, alpha ratio was calculated in each segment and group for the oscillation analysis. The alpha ratio is defined as the energy of the alpha frequency band divided by the total energy of the EEG frequency band. Therefore, it reflects the change of the alpha activity level.

2.3 Construction of Brain Networks

In accordance to graph theory [42], a brain network can be represented by a graph G(N,E), where N and E are the node and edge (or link) sets, respectively. We assigned EEG electrodes to the elements of N. The edges reflecting the adjacency relations among the nodes in the networks can be described by the functional connectivity matrix *F,* whose element *F*(*i*,*j*) shows the edge between nodes (electrodes) *i* and *j*. To show that the effective information of the networks on maintaining driver alertness can be dug out with spurious interactions, the cross-correlation method, which has been proven to suffer from primary and secondary leakage [26], is adopted in the estimation of the edges. The correlation between the EEG signals s_i and s_j can be calculated by the following equations:

$$\gamma_{ij} = \left| \frac{CC(s_i, s_j)(\tau)}{\sqrt{CC(s_i, s_i)(0)CC(s_j, s_j)(0)}} \right|, \tag{1}$$

$$CC(s_i, s_j)(\tau) = \begin{cases} \sum_{t=1}^{N-\tau} s_i(t+\tau)s_j(t), & \tau \geq 0 \\ CC(s_j, s_i)(-\tau), & \tau < 0 \end{cases}, \tag{2}$$

where time delay τ is set to zero. γ_{ij} corresponds to the element in *i*th row and *j*th column of the functional connectivity matrix *F*, which presents. To exclude self-connections of nodes, the elements on the main diagonal of *F* are set to zero. The other elements of *F* reflect functional coupling (i.e., functional connectivity) of the signals in different channels. Here, the signals were selected as the alpha oscillations after preprocessing to construct alpha oscillation networks.

As a measure of overall connectivity strengths in a brain network, the global connectivity energy has been used to assess fatigue during driving. The previous studies have demonstrated that its staged change is associated with the accumulation of fatigue [43,44]. The global connectivity energy is defined as the total energy of all the connectivity matrix elements. In this work, the global connectivity energy was calculated tocompare the alertness level both between the segments and between the two groups in the experiments.

2.4 Clustering on Brain Networks

In the constructed brain networks, an unsupervised clustering algorithm was employed to search the significant connectivity information at group level (connection cluster). Since every connection cluster has only one node, the classification of the clusters equals the classification of their nodes in a brain network. Thereafter, the connections of a connection cluster are defined as the attributes of its node.

Mathematically, we re-express the constructed brain network $G(N,E)$ with N nodes as $X=\{X_1, X_2, \ldots, X_N\}^T$, where $X_i=\{x_i^1, x_i^2, \ldots, x_i^M\}$ with M links ($M=N-1$ for weighted network) is a vector denoting the ith node whose attribute $x_i^j = \boldsymbol{F}(i,j)$ ($j\neq i$) is a scalar representing the strength of the functional connectivity between Node i and Node j. The spatial connectivity information is searched based on agglomerative hierarchical clustering, which establishes the foundations for inducing a hierarchical clustering from a newly represented, or newly encoded, mapping of functional connectivity matrix F.
To begin with, each node and the connections linked to it in a constructed brain network are considered as a single-element cluster group at the lowest level, i.e., $C_i=\{X_i\}$, $1\leq i\leq N$. Dendrogram$_k=\{C_1, C_2, \ldots, C_N\}$, $k=N$. Then, based on the distance (similarity function) calculation, two closest cluster groups are successively merged to reduce the number of cluster groups by 1 until a single cluster group remains at the highest level (i.e., $k=1$):

$$(a,b) = argmin_{(i,j)}\{d(\boldsymbol{C}_i,\boldsymbol{C}_j):\ 1\leq i<j\leq k\}, \tag{3}$$

$$\text{merge}(\boldsymbol{C}_a,\boldsymbol{C}_b) = \boldsymbol{C}_{2N+1-k}, \tag{4}$$

$$\boldsymbol{Dendrogram}_{k-1} = \boldsymbol{Dendrogram}_k - \{\boldsymbol{C}_a,\boldsymbol{C}_b\} + \{\boldsymbol{C}_{2N+1-k}\}, \tag{5}$$

where C_i and C_j denote two different clusters; k is the level number; Dendrogram indicates the cluster set and its element number is reduced by 1 to reach a higher level in Equation (5); and d represents Euclidean distance between two clusters. The Euclidean distance can be calculated by the following expressions:

$$d(\boldsymbol{C}_i,\boldsymbol{C}_j) = d(\boldsymbol{X}_a,\boldsymbol{X}_b), \tag{6}$$

$$d(\boldsymbol{X}_a,\boldsymbol{X}_b) = \sqrt{\sum_{m=1}^{M}(x_a^m - x_b^m)^2}, \tag{7}$$

where M denotes the number of attributes of the node vectors $\boldsymbol{X}_a$ and $\boldsymbol{X}_b$. x_a^m and x_b^m indicate the attributes (corresponding to functional connectivity) of the two node vectors.

Finally, we cut the dendrogram to complete clustering on brain networks to obtain different node groups (i.e., cluster groups), number (Z) of which is predetermined. As the number of the cluster groups contained in Dendrogramis equal to the level number k, Z cluster groups will be left by the Zth level cut through the dendrogram. That means we classify the nodes of the brain networks into Z groups according to the elements of Dendrogram$_Z$.

In this study, Z is set to 4 to acquire class pattern changes associated with fatigue in the control group and the alerting effect of RADIO in the experimental group. As shown in Fig. 3, four cluster groups are left by the fourth level cut. Because the cluster groups are merged based on the distance, the later the cluster group is involved in the merged operation, the more different the cluster group will be. The four cluster groups (i.e., C_6, C_3, C_4 and C_5) are labeled as Class 1, Class 2, Class 3, and Class 4 with the increase of difference.

2.5 Differential Entropy

DE is considered as a univariate and non-linear measure of information content in a given time series X. It quantifies information in an arbitrary time series X of length N as the probability that the value x of

X within a certain area. The probability is represented by the integral of the probability density function in the area. Its calculation formula can be expressed as:

$$DE(X) = -\int_X p(x)\log p(x)\,\mathrm{d}\,x\,, \tag{8}$$

where *X* represents the time series, $p(x)$ denotes the probability density function of *X*.

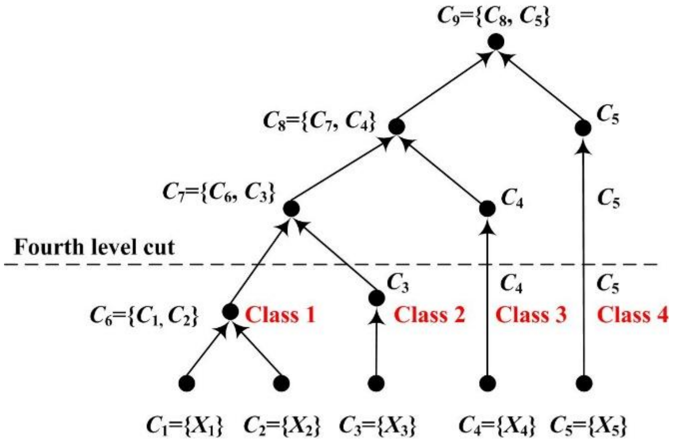

Fig. 3. An exemplar dendrogram representing a possible hierarchical clustering process for five connection clusters

In this work, the alpha oscillations after preprocessing were used as thetime series to calculate the DE values. DE was performed on all the nodes of the brain networks constructed in Section 2.3. The nodes which were used for DE statistical analysis were determined by the spatiotemporal patterns of connection clusters.

2.6 Statistical Analysis

To compare alertness evaluation performance, the EEG features (i.e., global connectivity energy, alpha ratio, and DE) of the subjects in the control and experimental groups were averaged for each driving stage (Segments 1–6). The standard deviations were calculated to measure their variability (see Figs. 6 and 7 and Table 3). When the staged changes of the feature meansare acquired, it needs to be confirmed whether the observed difference between group means reflects actual difference in the sample population of both groups. The Wilcoxon rank-sum test, also called the Mann–Whitney U test, is a non-parametric test used to determine whether two independent sample populations follow the same distribution [45]. It does not require the data normality assumption and is suitable for small samples (such as subject number <30). Hence, the Wilcoxon rank-sum test was selected for statistical analysis to check whether the EEG features can reflect the actual differences between the two groups in Section 2.1. The significance level α was set to 0.05. Values of $p<0.05$ (with a confidence interval of 95%) indicate that the samples in the two groups come from different distributions—the group means are different.

3. RESULTS

Figs. 4 and 5 show the matrices of the averaged functional connectivity of the control group and the experimental group across the subjects, respectively. Nodes Fp1, Fp2, F7, F3, Fz, F4, F8, T3, C3, Cz, C4, T4, T5, P3, Pz, P4, T6, O1, and O2 are numbered 1–19. Each small square surface in a matrix represents a connection between two nodes. Color indicates the value of the correlation coefficient reflecting connectivity strength. The correlation coefficients on the main diagonal were set to zero (deep blue) to exclude self-connection. All the functional connectivity analyses are based on the functional connectivity matrices. The traditional approaches of connectivity analysis suffer from spurious interactions. As demonstrated in Figs. 4 and 5, from Segment 1 to Segment 6, the changes in vigilance affect the functional connectivity. The overall connectivity strength of both the control and experimental groups becomes weaker (more blue surfaces) after Segment 1. However, there is almost no change after Segment 1 and no difference between inter- and intra-groups through observation.

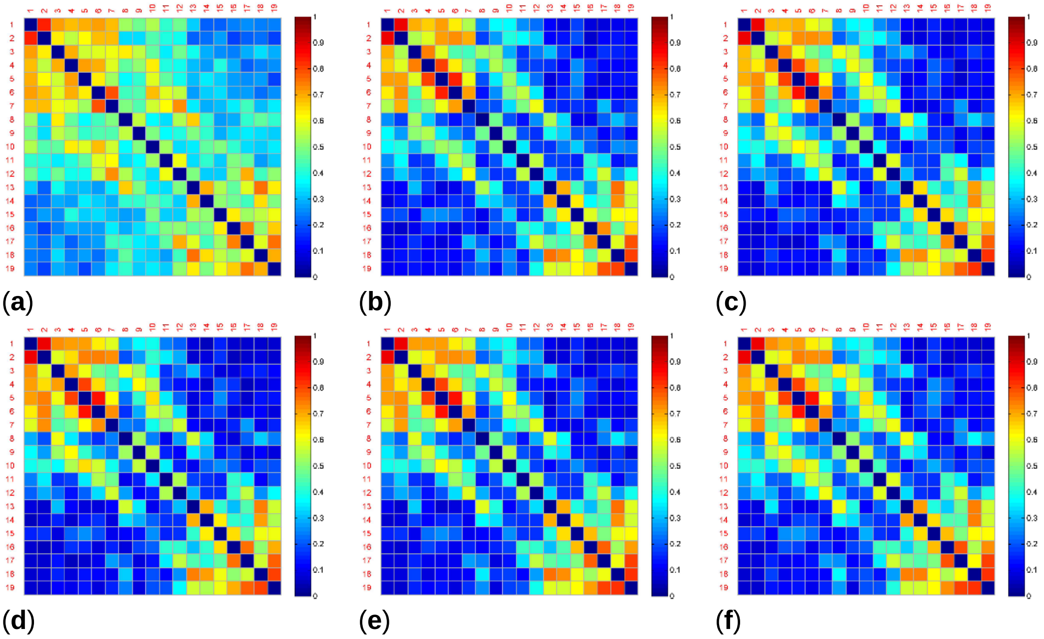

Fig. 4. Averaged functional connectivity matrices of the control group, (a) Functional connectivity matrix in Segment 1; (b) Functional connectivity matrix in segment 2; (c) Functional connectivity matrix in segment 3; (d) Functional connectivity matrix in segment 4; (e) Functional connectivity matrix in segment 5; (f) Functional connectivity matrix in segment 6

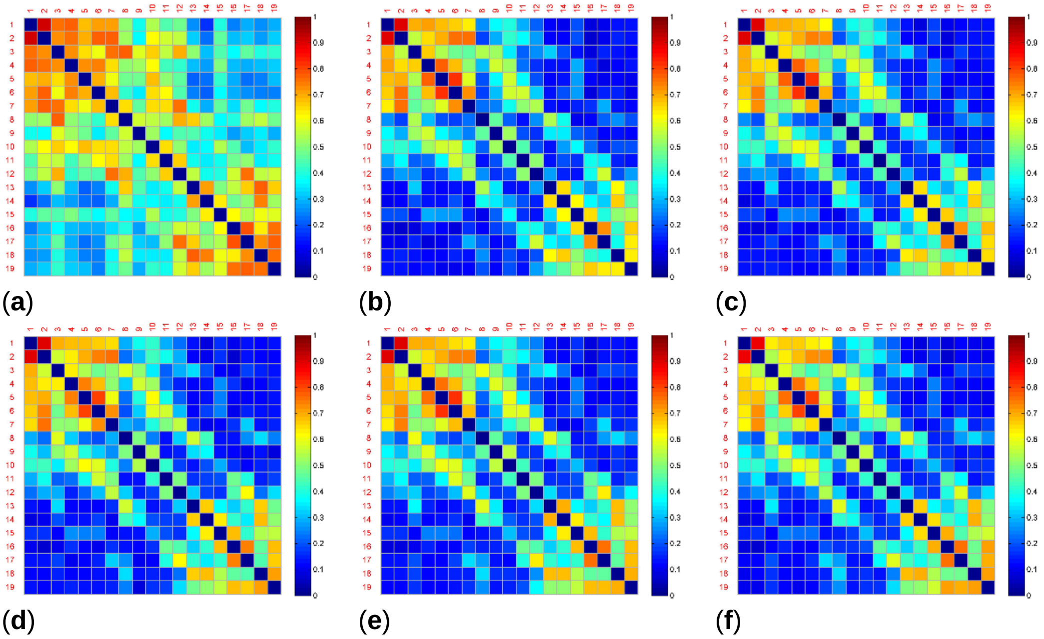

Fig. 5. Averaged functional connectivity matrices of the experimental group, (a) Functional connectivity matrix in segment 1; (b) Functional connectivity matrix in segment 2; (c) Functional connectivity matrix in segment 3; (d) Functional connectivity matrix in segment 4; (e) Functional connectivity matrix in segment 5; (f) Functional connectivity matrix in segment 6

The global connectivity energy was used to measure the overall functional connectivity of each brain network in different stages. The energy of all the elements of the functional connectivity matrix F was calculated and the results of statistical analysis are shown in Fig. 6. The curves of the averaged global connectivity energy of both the experimental group and the control group decline in the second segment. Table 1 presents the results of the Mann–Whitney U test for the global connectivity energy. There is no statistically significant difference between the two groups, but with large standard deviations for the subjects in each group. It illustrates that the networks' average behavior is largely affected by the individual differences of the subjects. The pivotal information of fatigue and alerted effect of the countermeasure is concealed.

One of the reasons for the poor results is that the brain networks may contain false positives. For example, it is uncertain which the connections are true interactions among the red surfaces in the top left corner in Fig. 4b. Nevertheless, the blue and red surfaces in the top left and in the bottom right corner of this figure can be classified into different groups by observation. Therefore, dividing into subsets of electrodes may obtain a more powerful result.

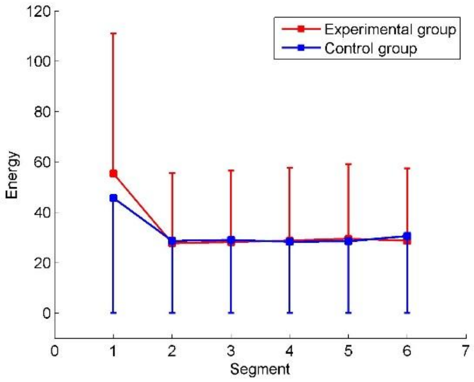

Fig. 6. Global connectivity energy, The averages andstandard deviations are plotted

Table 1. Results of the Mann–Whitney U test for differences in the global connectivity energy

Segment	**Control Group vs. Experimental Group**	
	Z	***p***
1	−1.13	>0.05
2	1.04	>0.05
3	1.36	>0.05
4	0.57	>0.05
5	1.17	>0.05
6	1.77	>0.05

Fig. 7 confirms that the activities of the different brain regions (nodes) can be classified. After wavelet decomposition implemented in data preprocessing, the wavelet coefficients in the alpha band and the total band of EEG can be obtained (refer to Section 2.2). To quantify the alpha activity level in EEG, the energy of the wavelet coefficients in the alpha band was calculated and converted to the energy ratio, which was divided by the total energy of the EEG band. Fig. 7 shows the energy ratios of the two brain areas in the control and experimental groups. The frontal and parieto-occipital ratios are acquired by averaging ratios across the frontal channels (i.e., Fp1, Fp2, F7, F3, Fz, F4, and F8) and the parieto-occipital channels (i.e., T5, P3, Pz, P4, T6, O1, and O2), respectively. In contrast with the increase of the parieto-occipital ratios, the frontal ratios drop gradually in both groups from Segment 1 to Segment 6. As shown in Table 2, the Mann–Whitney U test revealed that the alpha energy ratios between the frontal region and the parieto-occipital region were significantly different in every segment. The alpha energy ratios with significant differences between the two regions were marked with asterisks in Fig. 7. The mark ** represents $p<0.01$. Therefore, the frontal and parieto-occipital ratios can be classified into two categories over time in both groups. However, the differences between the two groups are not significant (see control group vs. experimental group in Table 2). Hence, simply dividing into the subsets of electrodes is not enough. The differences between the two groups are explored by the proposed clustering algorithm and DE.

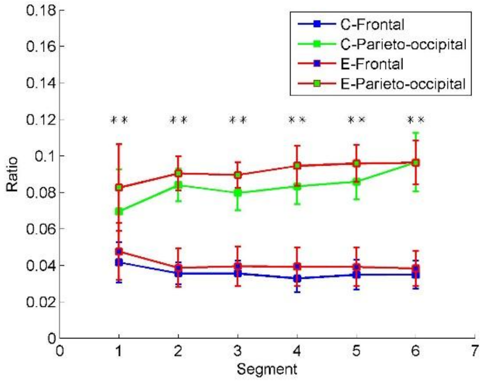

Fig. 7. Alpha energy ratios in the control and experimental groups. The averages and standard deviations from the subjects are plotted. C-Frontal and C-Parieto-occipital represent the frontal and parieto-occipital ratios in the control group. In contrast, E-Frontal and E-Parieto-occipital represent the frontal and parieto-occipital ratios in the experimental group. ** denotes *p*<0.01

Table 2. Results of the Mann–Whitney U test for differences in the alpha energy ratios

Segment	**Frontal area vs. Parieto-occipital area**				**Control group vs. Experimental group**			
	Control group		**Experimental group**		**Frontal area**		**Parieto-occipital area**	
	Z	***p***	***Z***	***p***	***Z***	***P***	***Z***	***p***
1	−4.02	<0.01	−4.20	<0.01	0.07	>0.05	−1.77	>0.05
2	−3.70	<0.01	−3.88	<0.01	−0.34	>0.05	−0.48	>0.05
3	−3.56	<0.01	−4.30	<0.01	−1.03	>0.05	−0.94	>0.05
4	−3.93	<0.01	−4.20	<0.01	−1.45	>0.05	−1.26	>0.05
5	−3.97	<0.01	−4.11	<0.01	−0.99	>0.05	−0.16	>0.05
6	−3.97	<0.01	−4.39	<0.01	−0.76	>0.05	−0.16	>0.05

Figs. 8 and 9 show the clustering results of the brain networks in the control and experimental groups, respectively. The element size of functional connectivity matrices in Figs. 4 and 5 are represented by the link thickness of the brain networks. Every node represents a connection cluster. Different colors (blue, cyan, green, and yellow) on the nodes indicate different classes (Classes 1–4). As the hierarchical clustering algorithm was adopted, the connection clusters with the shortest distance between each other (blue nodes) were classified as Class 1 first, and the yellow nodes whose attributes were 'farthest' from the others were finally sifted out and labeled as Class 4 by using Equations (3)–(7). That means that the higher the class is, the more different or active the cluster will be. Since the subjects in the control group drove without any extra stimulus from countermeasure and induced fatigue in Segment 1, the brain network with the classification of the connection clusters presented in Fig. 8a was considered as the default mode network of driving in the experiments of this study (DMND). Compared to DMND, in the other segments of Fig. 8, the strong connections are concentrated in the frontal region and the parieto-occipital region and the connectivity between the frontal and parieto-occipital regions significantly reduces, which corresponds to the trend in Fig. 6. Particularly, the classification changes of the connection clusters (or nodes) in the brain networks are staged with fatigue accumulation. As shown in Fig. 8a–f, the nodes labeled as high classes (i.e., cyan, green, and yellow nodes) move to the parieto-occipital region step by step. In Fig. 9a, the nodes (T3, T4, and Fz) in the auditory and frontal areas of brain are labeled as Classes 2–4 (high classes), respectively, when the drivers were exposed to RADIO. It reveals that there are intermediately active clusters in the auditory area. Hence, the brain network in Fig. 9a was considered as the default mode network of RADIO (DMNR). Compared to DMNR, the superficial connectivity in the other segments of

Fig. 9 seems to return to fatigue mode with weak links between the frontal region and the parieto-occipital region. In addition, the cyan nodes move to the parieto-occipital region. However, the most active clusters labeled as Classes 3 and 4 remain in the frontal area in Segments 2 to 6.

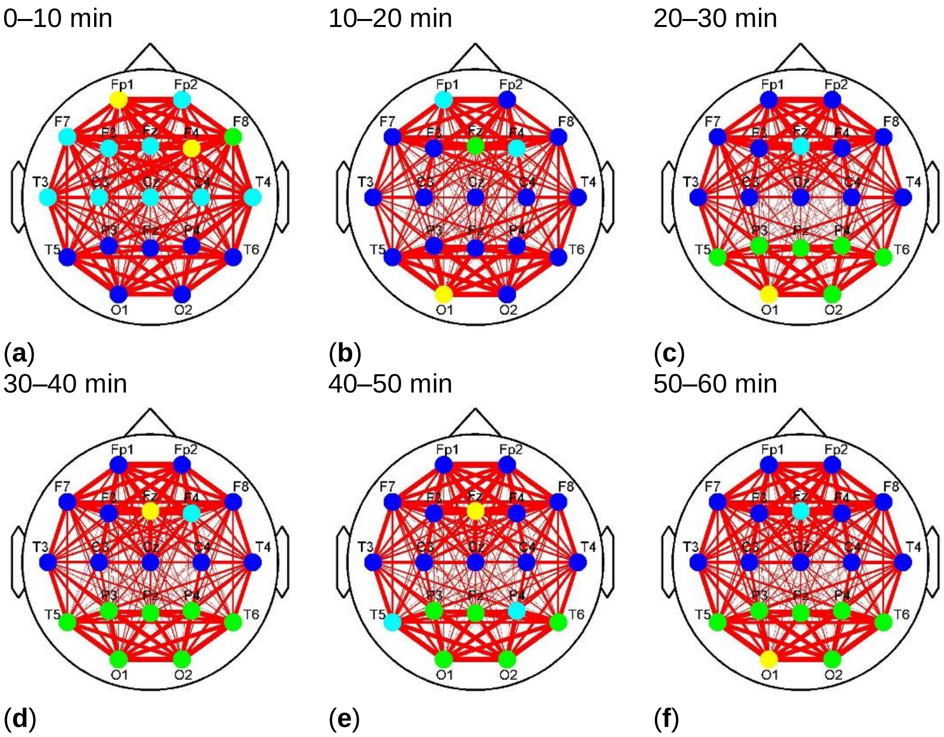
0–10 min (a)
10–20 min (b)
20–30 min (c)
30–40 min (d)
40–50 min (e)
50–60 min (f)

Fig. 8. Classification of connection clusters in each stage brain network of the control group, (a) Classification in Segment 1; (b) Classification in Segment 2; (c) Classification in Segment 3; (d) Classification in Segment 4; (e) Classification in Segment 5; (f) Classification in Segment 6. Classes 1–4 was represented by blue, cyan, green, and yellow, respectively

Fig. 10 shows the class change on each node corresponding to Figs. 8 and 9. In Fig. 10a, high class (Class 3) is mainly marked in the parieto-occipital region (Nodes 13–19) by the clustering algorithm implemented in the brain networks after Segment 2. Compared to Fig. 10a, the active level of the most clusters (represented by the nodes) of the parieto-occipital region in Fig. 10b reduces by one grade to Class 2. By contrast, Nodes 5 and 6 in the frontal regionmaintain high class. It reveals a shift tendency of the active connection clusters constructed based on alpha oscillations from the parieto-occipital region to the frontal region, when RADIO was taken during the prolonged driving task.

To demonstrate the superiority of the proposed clustering method, the widely used Louvain algorithm was adopted to detect the community in the brain networks. According to the community, the subsets of electrodes can also be distinguished. However, because too much connectivity information is confused (see Fig. 6), there is no change in the community division over time in both groups in Fig. 11, if the community change of T3 in Fig. 11b is neglected.

Fig. 12 confirms that the spatiotemporal evolution of the connection clusters in Figs. 8 and 9 generate the information content change. DE was calculated on all the nodes in Figs. 8 and 9. According to the movements of the connection clusters between the frontal region and the parieto-occipital region, DE values were averaged across Nodes Fp1, Fp2, F7, F3, Fz, F4, and F8 and across Nodes T5, P3, Pz, P4, T6, O1, and O2 to quantify information content of the frontal and parieto-occipital regions, respectively. Fig. 12 presents the averaged DE curves across subjects in each group. The shaded area indicates the standard deviation. As shown in Fig. 12a, the trend of the frontal entropy values in the control group is declining over time, whereas the parieto-occipital entropy curve has a significant upward trend. Overall, the DE values of the experimental group in Fig. 12b present the opposite trend compared with Fig. 12a. The entropy values in Fig. 12, which were expressed as mean±standard deviation (SD) across the subjects, are presented in Table 3. As shown in Table 3, the average entropy values of the experimental group are larger than those of the control group. Through the Mann–Whitney U test, the DE differences between groups present statistical significance for all the segments (see Table 4). The DE values with significant differences between groups were marked with asterisks in Table 3. The asterisks * and ** indicate $p<0.05$ and $p<0.01$, respectively. Since all the p-values are less than 0.05, the proposed method contributes to the evaluation of the alerting effect in the experimental group.

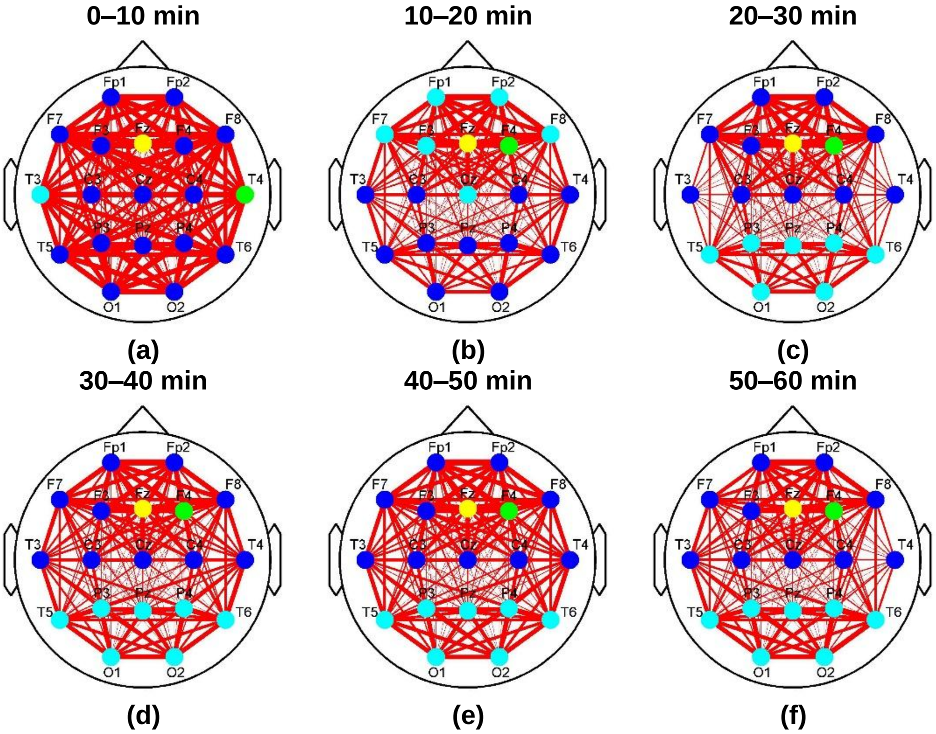

Fig. 9. Classification of connection clusters in each stage brain network of the experimental group. (a) Classification in Segment 1; (b) Classification in Segment 2; (c) Classification in Segment 3; (d) Classification in Segment 4; (e) Classification in Segment 5; (f) Classification in Segment 6. Classes 1–4 was represented by blue, cyan, green, and yellow, respectively

4. DISCUSSION

Fatigue is multifaceted in nature [15,46]. It not only brings the simple increase of alpha activity level and decoupling between different brain regions, but also changes wave propagation, hemispheric symmetry, and modular network properties. In Fig. 7, the alpha energy ratios in the parieto-occipital region presented a gradual increase trend during the prolonged driving task, which was consistent with the previous studies, where oscillatory activity at the alpha band had been observed to increase in the posterior brain regions (parietal-occipital) during attentional lapses [47] and during the states of drowsiness relative to the states of alertness [14,17]. As is known to us, alpha oscillations occur during wakefulness, particularly over the occipital cortex, appear markedly at eye closure and decrease at eye opening [48]. Thus, the increase of the alpha energy ratios probably indicates more eye closures and driver drowsiness. Nevertheless, the alpha energy ratios of the frontal region showed the opposite trend. The frontal regionis involved in the higher cognitive functions, such as working memory, selective attention, error detection, and behavior control [49-51]. As pointed out by Sadaghiani et al. [16], alpha oscillations is also involved in the mechanism that gates and controls sensory information processing as a function of cognitive relevance. Therefore, the opposite trend in the frontal region may correspond to the weakening of motivation and wakefulness. It seems that there was an alpha wave propagation between the frontal region and the parieto-occipital region. As one fell, another rose.

Table 3. DE values in every segment. *denotes *p*<0.05. ** represents *p*<0.01

Group	**Brain Area**	**DE (Mean ±SD)**					
		Segment 1	**Segment 2**	**Segment 3**	**Segment 4**	**Segment 5**	**Segment 6**
Control	Frontal	1.90±0.46**	1.92 ± 0.31**	2.02 ± 0.55**	1.89 ± 0.51**	1.91 ± 0.30**	1.41 ± 0.36**
	Parieto-occipital	1.55±0.61**	2.81 ± 0.62**	3.03 ± 0.82*	2.95 ± 0.74**	2.93 ± 0.50*	2.76 ± 0.65**
Experiment	Frontal	6.66 ± 2.30**	6.09 ± 1.68**	6.12 ± 1.73**	5.95 ± 1.19**	6.37 ± 1.60**	8.57 ± 4.17**
	Parieto-occipital	9.76 ± 2.98**	3.98 ± 1.02**	4.15 ± 1.28*	4.25 ± 1.37**	4.08 ± 1.44*	4.21 ± 1.15**

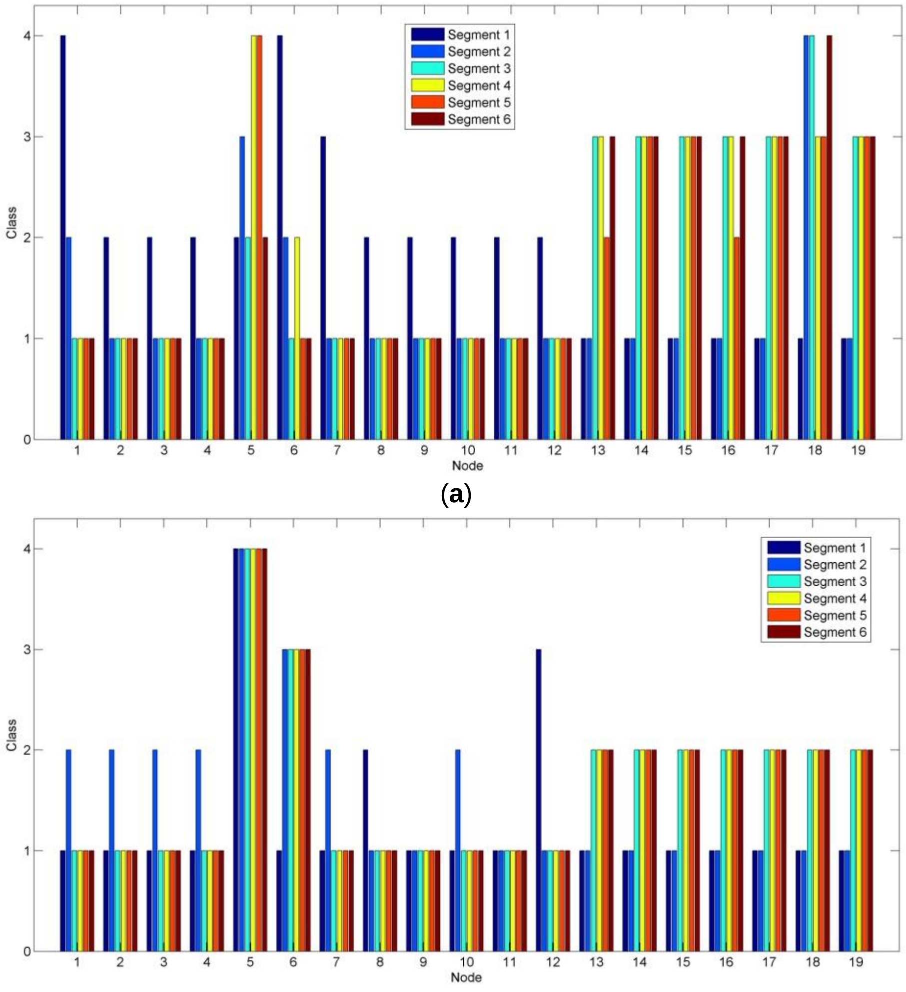

(**a**)

(**b**)

Fig. 10. Class sets from all the nodes and segments. (a) Class set of the control group; (b) Class set of the experimental group. Nodes Fp1, Fp2, F7, F3, Fz, F4, F8, T3, C3, Cz, C4, T4, T5, P3, Pz, P4, T6, O1 and O2 are numbered 1–19

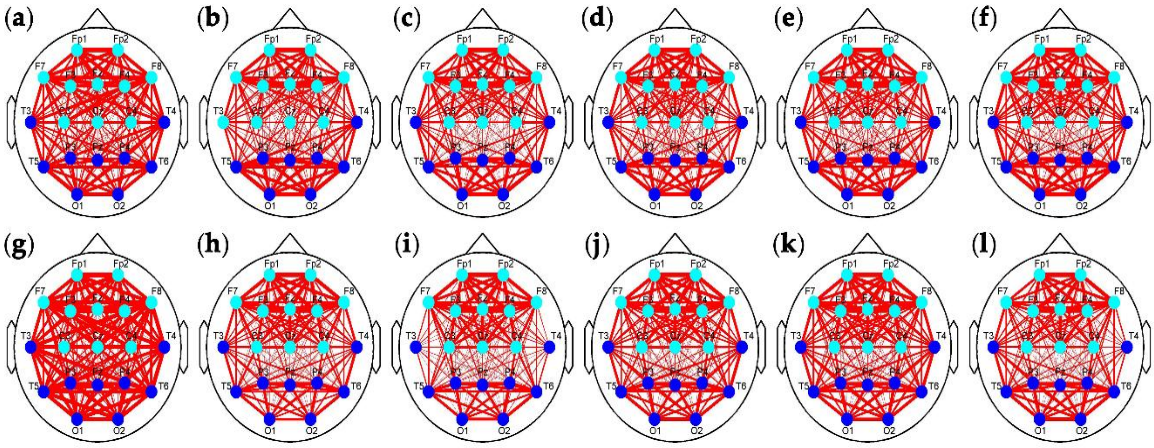

Fig. 11. Community detected by Louvainalgorithm. (a–f) Community detected in Segments 1–6 of the control group; (g–l) Community detected in Segments 1–6 of the experimental group

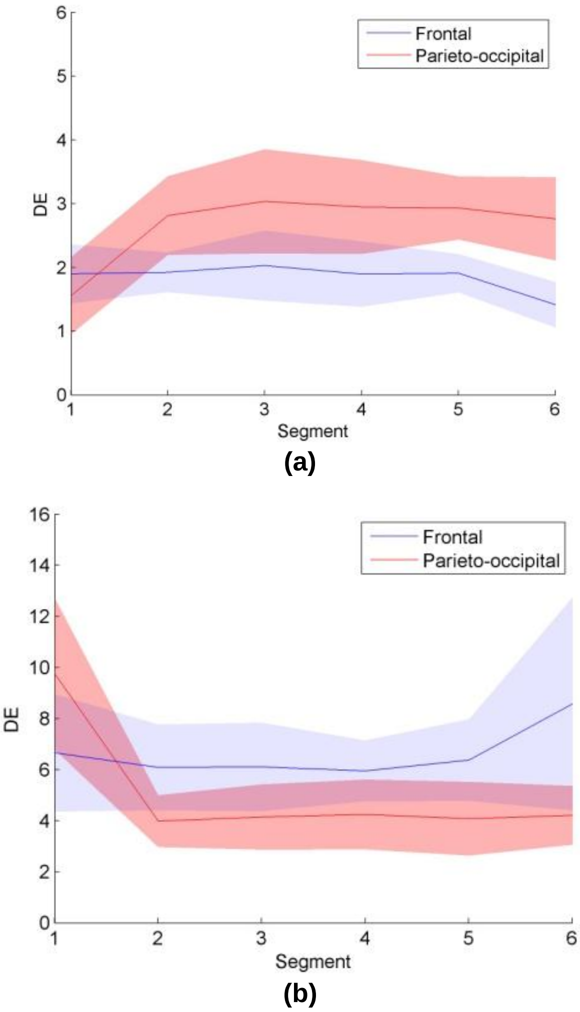

Fig. 12. DE change during driving. (a) Averaged DE across subjects in the control group; (b) Averaged DE across subjects in the experimental group. All the DE values of the subjects in each group were averaged and the shaded area indicates the standard deviation

Table 4. Results of the Mann–Whitney U test for differences in DE

Segment	**Control Group vs. Experimental Group**			
	Frontal Area		**Parieto-Occipital Area**	
	Z	***p***	***Z***	***p***
1	−4.48	<0.01	−4.48	<0.01
2	−4.48	<0.01	−2.96	<0.01
3	−4.48	<0.01	−2.55	<0.05
4	−4.48	<0.01	−2.60	<0.01
5	−4.48	<0.01	−2.37	<0.05
6	−4.30	<0.01	−3.52	<0.01

However, for the analysis of the functional connections, a wide variety of information underlying fatigue and alerting effect of the fatigue countermeasure was still implicit, due to false positives. As shown in Figs. 4–6, the strong connectivity in Segment 1 may just reflect the difference of the initial state. The curve of the averaged global connectivity energy was relatively flat after Segment 1, which cannot reveal the fatigue information or concur with the fatigue assessment of the alpha energy ratios. More importantly, it lost the countermeasure information without statistically significant intergroup difference. The previous studies have already proven the effectiveness of RADIO as an "in-car" countermeasure [8]. Such informationmust be involved in the experimental group somehow but implicated by signal mixing.

Under the condition of no significantly statistical difference using the traditional connectivity analysis (see Figs. 4–6), the proposed methodology was applied to mining the spatiotemporal information (see Figs. 8–10 and 12). Particularly, we employed clustering algorithm performed in the brain networks with false positives to try to point out what happened in the brain after RADIO was taken. We considered that all the links connected to a node was basic unit (connection cluster) of connectivity analysis, not a single link or the node itself. Even though false positives exist in the connection clusters, the clusters can be classified into different groups with different labels. Compared with the Louvain-based community detection method, the proposed clustering method shows more superior ability to mine the effective information with the confused functional connection matrices (see Figs. 8, 9 and 11). In Louvain algorithm, the community is formed according to the largest modularity increment [52]. The modularity is defined as the difference between the connection weights of nodes in the community and the connection weights in a random case. The algorithm cannot make sure that the community of the chosen neighbor is the most appropriate community in which the current node *i* ought to be. This may lead to instability of the performance. Additionally, it requires the assumption that a random neighbor is likely to be in a good community, which may not be appropriate for the brain networks in Fig. 11.

Unlike Louvain, the proposed clustering method mainly calculates the distance between each connection cluster to classify the nodes into different groups. The classification mode changes with the progress of fatigue or reflects the alerting effect of RADIO. As shown in Fig. 8, the active connection clusters labeled as high classes moved from the frontal region to the parieto-occipital region with the accumulation of driver fatigue. Since the brain networks were constructed in the alpha band, it reveals a coupling effect between the alpha connection clusters and the alpha oscillations. That is to say that the decrease of the active level of the connection clusters in the frontal region may also correspond to the weakening of motivation and wakefulness and the increase of the active level of the connection clusters in the parieto-occipital region can indicate more eye closures and driver drowsiness. Therefore, the clustering algorithm based on functional connectivity can reveal fatigue information. The analysis of alpha oscillations provides a clue for the interpretation of the active cluster movement, and in other words, the change of the active level of the alpha oscillations in the frontal and parieto-occipital regions may be caused by the active cluster movement. We then took the change of classification mode in Fig. 8 as a reference to analyze the alerting effect of RADIO. In DMNR, the most active clusters were distributed in the auditory and frontal areas of the brain. It illustrates that the brain indeed reacts when the drivers are listening to the radio. Acoustic information may enter the brain through the clusters in the auditory area and the accompany driving information may be comprehensively processed by the cluster in the frontal region. As the prolonged driving task progressed, only the clusters containing cyan nodes moved to the parieto-occipital region in Fig. 9, which reflected relatively low-class fatigue information. Particularly, the most active clusters labeled as Classes 3 and 4 remained in the frontal area, after cyan nodes moved to the parieto-occipital region. Because the frontal region is responsible for the higher cognitive functions, the motivation and wakefulness of the drivers in the experimental group were probably enhanced during the prolonged driving task. The entropy-based analysis confirmed the movement of the connection clusters accompanied with the information content change. As shown in Fig. 12, the overall DE values of the experimental group were larger than those of the control group, indicating that the fatigue countermeasure was effective. Entropy measures the average uncertainty of event set to embody information content. Therefore, it revealed the recovery of the complexity of the brain activity when RADIO was taken. The recovery of the activity complexity brought the larger information content. Throughout the control and experimental groups, the trend of DE curves in the frontal and parieto-occipital regions was consistent with the movement of the connection clusters. The DE rise of the frontal region and the decline of the parieto-occipital region in the experimental group may be a result of the movement of the connection clusters.

Comparing Figs. 9 and 12b with Figs. 8 and 12a, we draw conclusions about the alerting effect of RADIO. Although the alpha connection clusters and the alpha oscillations are coupled with each other to some extent, RADIO relieves fatigue by preventing the active cluster movement from the frontal region to the parieto-occipital region, not the alpha propagation. Making the active clusters stay in the frontal area may maintain alertness.

Note that all the subjects in the experiments were males. In the control group, it requires the subjects to drive a long time without any fatigue countermeasure. We did not recruit female subjects. Even if this study focuses on the methods to investigate the effect of RADIO to maintain driver alertness, the gender factor is not considered. This is a result limitation.

Future work will concern the improvement of localization precision of the active clusters. High-density electrode setting will be adopted so that the default network of driving and the neural mechanism of alerting effect can be explored in depth.

5. CONCLUSION

In this paper, a new framework to improve the performance of connectivity analysis for RADIO effect exploration has been proposed. Instead of analyzing the network system behavior, dividing the electrodes into subsets obtains a more powerful result. The subsets are classified by the clustering algorithm implemented in brain networks automatically. The quantitative analysis based on DE proves the effectiveness of the method and the active clustermovement after classifying generates the information content change. The alerting effect of RADIO is related with suppressing the active cluster movement from the frontal region to the parieto-occipital region, which is helpful for maintaining driver alertness during prolonged driving. The limitation of this study is that only male subjects participated in the experiments. Whether the effect holds with females is unknown.

AUTHOR CONTRIBUTIONS

This work was carried out in collaboration among all authors. ‘Author CZ conceived the methodology and developed the algorithm; Authors JM and RC designed the experiment. Authors JM and TL performed the experiment; Author CZ analyzed the data and wrote the paper. L.S. finished editing and proof reading. Authors JM, JZ, PL, FC, and RC were in charge of the supervision of this research and helping in revising. All the authors have read and agreed to the published version of the manuscript.

ACKNOWLEDGMENTS

We gratefully acknowledge the financial support from the National Foundation in China (No. JCKY2019110B009; 2020-JCJQ-JJ-252) and the Fundamental Research Funds for the Central Universities [DUT21GF301; DUT20LAB303; DUT20LAB308] in Dalian University of Technology in China. This research received no external funding.

COMPETING INTERESTS

Authors have declared that no competing interests exist.

REFERENCES

1. Borragán G, Guerrero-Mosquera C, Guillaume C, Slama H, Peigneux P. Decreased prefrontal connectivity parallels cognitive fatigue-related performance decline after sleep deprivation. An optical imaging study. Biological Psychology. 2019;144:115-124.
2. Anund A, Kecklund G, Vadeby A, Hjälmdahl M, Åkerstedt T. The alerting effect of hitting a rumble strip—A simulator study with sleepy drivers. Accident Analysis & Prevention. 2008;40(6):1970-1976.
3. Fu R, Wang H, Zhao W. Dynamic driver fatigue detection using hidden Markov model in real driving condition. Expert Systems with Applications. 2016;63:397-411.
4. Administration NHTS. Asleep at the wheel: A national compendium of efforts to eliminate drowsy driving; Washington. DC., U.S; 2017.

5. Qiong W, Jingyu Y, Mingwu R, Yujie Z. In Driver Fatigue Detection: A Survey, 2006 6th World Congress on Intelligent Control and Automation. 2006; 8587-8591.
6. Sun W, Zhang W, Zhang X, Lü C, Chen G. Development of Fatigue Driving Detection Method Research. Automobile Technology. 2009;2:1-5.
7. Gershon P, Shinar D, Oron-Gilad T, Parmet Y, Ronen A. Usage and perceived effectiveness of fatigue countermeasures for professional and nonprofessional drivers. Accident Analysis & Prevention. 2011;43(3):797-803.
8. Reyner L, Home J. Evaluation of 'in-car'countermeasures to sleepiness: Cold air and radio. Sleep. 1998;21(1):46-51.
9. Imperatori C, Farina B, Adenzato M, Valenti EM, Murgia C, Marca GD, et al. Default mode network alterations in individuals with high-trait-anxiety: An EEG functional connectivity study. Journal of Affective Disorders. 2019;246:611-618.
10. Sun Y, Lim J, Kwok K, Bezerianos A. Functional cortical connectivity analysis of mental fatigue unmasks hemispheric asymmetry and changes in small-world networks. Brain and Cognition. 2014;85:220-230.
11. Trainor L. Using electroencephalography as a tool to understand auditory perception: Event-related and time-frequency analyses. The Journal of the Acoustical Society of America. 2017;141(5):3559-3559.
12. Lal SK, Craig A. Driver fatigue: electroencephalography and psychological assessment. Psychophysiology. 2002;39(3):313-321.
13. Charbonnier S, Roy RN, Bonnet S, Campagne A. EEG index for control operators' mental fatigue monitoring using interactions between brain regions. Expert Systems with Applications. 2016;52:91-98.
14. Simon M, Schmidt EA, Kincses WE, Fritzsche M, Bruns A, Aufmuth C, et al. EEG alpha spindle measures as indicators of driver fatigue under real traffic conditions. Clinical Neurophysiology. 2011;122(6):1168-1178.
15. Culp J, El Gindy M, Haque A. Driver alertness monitoring techniques: A literature review. International Journal of Heavy Vehicle Systems. 2008;15(2-4):255-271.
16. Sadaghiani S, Scheeringa R, Lehongre K, Morillon B, Giraud AL, D'Esposito M, et al. Alpha-Band Phase Synchrony Is Related to Activity in the Fronto-Parietal Adaptive Control Network. Journal of Neuroscience. 2012;32(41):14305-14310.
17. Lawhern V, Kerick S, Robbins KA. Detecting alpha spindle events in EEG time series using adaptive autoregressive models. BMC Neuroscience. 2013;14(1):101.
18. Qi P, Ru H, Gao L, Zhang X, Zhou T, Tian Y, et al. Neural Mechanisms of Mental Fatigue Revisited: New Insights from the Brain Connectome. Engineering. 2019;5(2):276-286.
19. Gaggioni G, Ly JQM, Chellappa SL, Coppieters 't Wallant D, Rosanova M, Sarasso S, et al. Human fronto-parietal response scattering subserves vigilance at night. NeuroImage. 2018;175:354-364.
20. Kong W, Lin W, Babiloni F, Hu S, Borghini G. Investigating Driver Fatigue versus Alertness Using the Granger Causality Network. Sensors. 2015;15(8):19181-19198.
21. Zhao C, Zhao M, Yang Y, Gao J, Rao N, Lin P. The Reorganization of Human Brain Networks Modulated by Driving Mental Fatigue. IEEE Journal of Biomedical and Health Informatics. 2017;21(3):743-755.
22. Argollo de Menezes M, Barabasi AL. Fluctuations in Network Dynamics. Physical Review Letters. 2004;92(2):287011-287014.
23. Abbas A, Belloy M, Kashyap A, Billings J, Nezafati M, Schumacher EH, et al. Quasi-periodic patterns contribute to functional connectivity in the brain. NeuroImage. 2019;191:193-204.
24. Cole MW, Ito T, Bassett DS, Schultz DH. Activity flow over resting-state networks shapes cognitive task activations. Nature Neuroscience. 2016;19:1718.
25. Matsui T, Murakami T, Ohki K. Transient neuronal coactivations embedded in globally propagating waves underlie resting-state functional connectivity. Proceedings of the National Academy of Sciences. 2016;113(23):6556-6561.
26. Palva JM, Wang SH, Palva S, Zhigalov A, Monto,S, Brookes MJ, et al. Ghost interactions in MEG/EEG source space: A note of caution on inter-areal coupling measures. NeuroImage. 2018;173:632-643.
27. Palva S, Palva JM. Discovering oscillatory interaction networks with M/EEG: challenges and breakthroughs. Trends in Cognitive Sciences. 2012;16(4):219-230.

28. Zhang C, Cong F, Kujala T, Liu W, Liu J, Parviainen T, Ristaniemi T. Network Entropy for the Sequence Analysis of Functional Connectivity Graphs of the Brain. Entropy. 2018;20(5):311.
29. Wang SH, Lobier M, Siebenhühner F, Puoliväli T, Palva S, et al. Hyperedge bundling: A practical solution to spurious interactions in MEG/EEG source connectivity analyses. NeuroImage. 2018;173:610-622.
30. Vinck M, Oostenveld R, van Wingerden M, Battaglia F, Pennartz CMA. An improved index of phase-synchronization for electrophysiological data in the presence of volume-conduction, noise and sample-size bias. NeuroImage. 2011;55(4):1548-1565.
31. Nolte G, Bai O, Wheaton L, Mari Z, Vorbach S, Hallett M. Identifying true brain interaction from EEG data using the imaginary part of coherency. Clinical Neurophysiology. 2004;115(10):2292-2307.
32. Brookes MJ, O'neill GC, Hall EL, Woolrich MW, Baker A, Corner SP, et al. Measuring temporal, spectral and spatial changes in electrophysiological brain network connectivity. Neuroimage. 2014;91:282-299.
33. Drakesmith M, El-Deredy W, Welbourne S. Reconstructing coherent networks from electroencephalography and magnetoencephalography with reduced contamination from volume conduction or magnetic field spread. PloS One. 2013;8(12):e81553.
34. Shannon CE. A mathematical theory of communication. Bell System Technical Journal. 1948;27(3, 4):379-423, 623-656.
35. Takahashi T, Cho RY, Mizuno T, Kikuchi M, Murata T, Takahashi K, et al. Antipsychotics reverse abnormal EEG complexity in drug-naive schizophrenia: A multiscale entropy analysis. Neuroimage. 2010; 51(1):173-182.
36. Kar S, Bhagat M, Routray A. EEG signal analysis for the assessment and quantification of driver’s fatigue. Transportation research part F: Traffic Psychology and Behaviour. 2010;13(5): 297-306.
37. Shi LC, Jiao YY, Lu BL. Differential Entropy Feature for EEG-based Vigilance Estimation. In 35th Annual International Conference of the IEEE Engineering in Medicine and Biology Society, Osaka, Japan. 2013;6627-6630.
38. Gurudath N, Riley HB. Drowsy driving detection by EEG analysis using wavelet transform and k-means clustering. Procedia Computer Science. 2014;34:400-409.
39. Zhang C, Wang H, Fu R. Automated Detection of Driver Fatigue Based on Entropy and Complexity Measures. IEEE Transactions on Intelligent Transportation Systems. 2014;15(1): 168-177.
40. De Gennaro L, Ferrara M, Curcio G, Cristiani R. Antero-posterior EEG changes during the wakefulness–sleep transition. Clinical Neurophysiology. 2001;112(10):1901-1911.
41. Tanaka H, Hayashi M, Hori T. Statistical features of hypnagogic EEG measured by a new scoring system. Sleep. 1996;19(9):731-738.
42. Onias H, Viol A, Palhano-Fontes F, Andrade KC, Sturzbecher M, Viswanathan G, et al. Brain complex network analysis by means of resting state fMRI and graph analysis: Will it be helpful in clinical epilepsy? Epilepsy & Behavior. 2014;38:71-80.
43. Wang H, Zhang C, Shi T, Wang F, Ma S. Real-time EEG-based detection of fatigue driving danger for accident prediction. International Journal of Neural Systems. 2015;25(2):1-14.
44. Zhang C, Sun L, Cong F, Ristaniemi T. Spatio-temporal dynamical analysis of brain activity during Mental Fatigue Process. IEEE Transactions on Cognitive and Developmental Systems; 2020.
DOI: 10.1109/TCDS.2020.2976610
45. Maior de Barros RS, Gonzalez Hidalgo JI, de Lima Cabral DR. Wilcoxon Rank Sum Test Drift Detector. Neurocomputing. 2018;275:1954-1963.
46. Hopstaken JF, van der Linden D, Bakker AB, Kompier MAJ. A multifaceted investigation of the link between mental fatigue and task disengagement. Psychophysiology. 2015;52(3):305-315.
47. Peiris MT, Davidson PR, Bones PJ, Jones RD. Detection of lapses in responsiveness from the EEG. Journal of Neural Engineering .2011;8(1):016003.
48. Lal SKL, Craig A. A critical review of the psychophysiology of driver fatigue. Biological Psychology. 2001;55(3):173-194.
49. Gehring WJ, Knight RT. Prefrontal–cingulate interactions in action monitoring. Nature Neuroscience. 2000;3(5):516.

50. Lin CT, Chuang CH, Wang YK, Tsai SF, Chiu TC, Ko LW. Neurocognitive characteristics of the driver: A review on drowsiness, distraction, navigation, and motion sickness. Journal of Neuroscience and Neuroengineering. 2012;1(1): 61-81.
51. Cohen JD, Botvinick M, Carter CS. Anterior cingulate and prefrontal cortex: Who's in control? Nature Neuroscience. 2000;3(5):421.
52. Zhang Z, Pu P, Han D, Tang M. Self-adaptive Louvain algorithm: Fast and stable community detection algorithm based on the principle of small probability event. Physica A: Statistical Mechanics and its Applications. 2018;506:975-986.

Biography of author(s)

Chi Zhang
Faculty of Electronic Information and Electrical Engineering, School of Biomedical Engineering, Dalian University of Technology, Dalian 116024, China.

He has received the B.S., M.S., and Ph.D degree of Science in Engineering from Northeastern University, China, in 2010, 2012 and 2016, respectively. He is currently a lecturer with the School of Biomedical Engineering, Faculty of Electronic Information and Electrical Engineering, Dalian University of Technology, Dalian, China. His research interests include biomedical signal processing, brain–computer interface, and artificial intelligence. He has published over 30 technological papers. He has received various academic awards including the second and third prizes of Liaoning Provincial Natural Science Academic Achievement Award, the second prize of Shenyang City Natural Science Academic Achievement Award, and Excellent Poster Awards of Liaoning Neuroscience Society Seminar.

Jinfei Ma
School of Psychology, Liaoning Normal University, Dalian 116029, China.

Research and Academic Experience: He has completed his PhD and working as an Assistant Professor in the College of Psychology , Liaoning Normal University.
He has completed the courses of General Psychology (graduate level); Traffic Psychology (graduate level)
His research includes the following publications:
The Relationship Between Drivers' Cognitive Fatigue and Speed Variability During Monotonous Daytime Driving, Frontiers in psychology,2018(9).
Lane-changing-decision characteristics and the allocation of visual attention of drivers with an angry driving style, Transportation Research Part F: Traffic Psychology and Behaviour,2020(05).
The exceptionists of Chinese roads: The effect of road situations and ethical positions on driver aggression, Transportation Research Part F: Psychology and Behaviour,2018(58).
The interactive effect of vehicle signals and sensation-seeking on driver hazard perception, Transportation Research Part F: Psychology and Behaviour, 2020(08).
Funding:
Preside the Humanity and Social Science Youth Foundation of Ministry of Education of China (Research on Psychological Mechanism and Regulation of Passive Fatigue of L3 Autonomous Vehicle's Drivers;grant numbers 20YJC190015).
Presided and fulfilled a Humanities and Social Science Project 'The influence of drivers' attribution tendency on aggressive driving behavior', numbered W201683617.

Research Area: Social Psychology; Safety Psychology.

Number of Published Papers: SSCI: 4; CSSCI:4.

Jian Zhao
Faculty of Vehicle Engineering and Mechanics, School of Automative Engineering, Dalian University of Technology, Dalian 116024, China.

He received his PH.D degree in mechanical engineering in 2008 from the Xidian University, also received the Excellent PH.D Graduate Award from Xidian University. He had been a research scientist in the mechatronics department of Johannes Kepler University Linz. Currently, he is a full professor at School of Automotive Engineering, Dalian University of Technology. He was granted 30 innovation Patents, and has published over 50 technological papers. His current research interests include autonomous driving, MEMS sensors, compliant mechanics, and nonlinear dynamics. He has received various academic awards including the Second Class Award of Science and Technology from Chinese Institute of Electronics, Best report award of ICMT 2016, Best paper award of 2018 ASME IDETC, Annual best paper award in Chinese Journal of Scientific Instrument.

Pengbo Liu
Faculty of Vehicle Engineering and Mechanics, School of Automative Engineering, Dalian University of Technology, Dalian 116024, China.

Research and Academic Experience: He was born in Xian, China. He received the B.Tech. degree in electrical engineering from the Dalian Polytechnic University, and the M.Tech. and Ph.D. degrees from Dalian University of Technology. He is currently working as an Engineer with the School of Automotive Engineering, Dalian University of Technology, China.

Research Area: Sensors, Intelligent Car, Internet of vehicles.

Number of Published Papers: 20.

Fengyu Cong
Faculty of Electronic Information and Electrical Engineering, School of Biomedical Engineering, Dalian University of Technology, Dalian 116024, China and School of Artificial Intelligence, Faculty of Electronic Information and Electrical Engineering, Dalian University of Technology, Dalian, China and Key Laboratory of Integrated Circuit and Biomedical Electronic System, Liaoning Province. Dalian University of Technology, Dalian, China and Faculty of Information Technology, University of Jyvaskyla, Jyvaskyla, Finland.

He received the B.S. degree in Power and Thermal Dynamic Engineering and the Ph.D. degree in Mechanical Design and Theory from the Shanghai Jiao Tong University, China, in 2002 and 2007, and the Ph.D. degree in Mathematical Information Technology from the University of Jyväskylä, Finland, in 2010. From December 2013, he has been working as a professor in the Department of Biomedical Engineering in the Dalian University of Technology at Dalian in China. His research interests include brain signal processing, acoustic signal processing, independent component analysis, tensor decomposition, and pattern recognition/machine learning/data mining. He has published over 100 technological papers and 1 English monograph. His Google Scholar H-index is 20 (February 2021).

Tianjiao Liu
School of Psychology, Shandong Normal University, Jinan 250358, China.

Research and Academic Experience: Liaoning Normal University, Dalian, China
College of Ps Aychology, undergraduate, Sep. 2015-- June 2019
Shandong Normal University, Jinan, China
School of Psychology, postgraduate, Sep. 2019.

She was mainly engaged in psychological research on fatigue driving and risk-taking behavior.

Research Area: Fatigue driving ; adolescents' risk-taking behavior.

Number of Published Paper: one paper(the first author).

Ying Li
Faculty of Electronic Information and Electrical Engineering, School of Biomedical Engineering, Dalian University of Technology, Dalian 116024, China.

Research and Academic Experience: Dalian University of Technology, Dalian, China.
Department of Biomedical Engineering, postgraduate, Sep. 2018-- June 2020.
RWTH Aachen University, Aachen, Germany.
Medicine, accepted as a doctor, April 2021— till date.

Research Area: Cognitive neuroscience (EEG, ERP, fMRI).

Number of Published Paper: 1.

Any Other Remarkable Point: The study of mental fatigue in patients with Fibromyalgia, Brain Network.

Lina Sun
Faculty of Electronic Information and Electrical Engineering, School of Biomedical Engineering, Dalian University of Technology, Dalian 116024, China.

She received the B.S. degree from Harbin Normal University, Harbin, China and M.S. degree from Dalian University of Technology, Dalian, China in 2015 and 2018 respectively. She is currently working in the International office, Dalian University of Technology, Dalian, China. Her research interests are language learning and cognitive science. She has published 6 technological papers. She has received various academic awards including the University Outstanding Scholarship in Dalian University of Foreign Languages and the Third Prize in National Teaching Skills Competition for the English Majors of Higher Normal Schools.

Ruosong Chang
School of Psychology, Liaoning Normal University, Dalian 116029, China.

He has received the B.S. degree in Education from Northeast Normal University. He is currently a professor and doctoral supervisor of Liaoning Normal University, and the director of Liaoning Collaborative Innovation Center of Children and Adolescents Healthy Personality Assessment and Cultivation. He has been long engaged in the teaching and research of theoretical psychology, healthy personality theory and traffic psychology. He has published over 10 books and textbooks, and 70 papers. He has received various academic awards including the first prize of National Teaching Reform Achievement Award, Liaoning Provincial Teaching Achievement Award, and the Advanced Individual in Education and Research of Liaoning Province.

© Copyright (2021): Author(s). The licensee is the publisher (B P International).

DISCLAIMER
This chapter is an extended version of the article published by the same author(s) in the following journal.
Entropy, 22, 2020.

London Tarakeswar

Registered offices
India: Guest House Road, Street no - 1/6, Hooghly, West Bengal, PIN-712410, India, Corp. Firm
Registration Number: L77527, Tel: +91 7439016438 | +91 9748770553, Email: director@bookpi.org,
(Headquarters)
UK: 27 Old Gloucester Street London WC1N 3AX, UK
Fax: +44 20-3031-1429 Email: director@bookpi.org,
(Branch office)

View publication stats